Deep foundations of a high-rise building : An in-situ testing and numerical study

Rosy Milane

N°d'ordre NNT : 2021LYSEI028

THESE de DOCTORAT DE L'UNIVERSITE DE LYON
Opérée au sein de
INSA Lyon

Ecole Doctorale ED162
MEGA : Mécanique – Energétique – Génie civil – Acoustique

Spécialité/ discipline de doctorat : Génie civil

Soutenue publiquement le 27/5/2021 par :
Rosy MILANE

Deep foundations of a high-rise building: an *in-situ* testing and numerical study

---

Devant le jury composé de :

FRANK, Roger	Directeur de recherche Émérite	ENPC	Rapporteur
JARDINE, Richard	Professeur des Universités	Imperial college	Rapporteur
SALCIARINI, Diana	Professeur des Universités	University of Perugia	Examinatrice
MANIN, Lionel	Maître de Conférences	INSA Lyon	Examinateur
DAOUADJI, Ali	Professeur des Universités	INSA Lyon	Directeur de thèse
BRIANCON, Laurent	Maître de Conférences	INSA Lyon	Co-directeur de thèse
GRANGE, Stéphane	Professeur des Universités	INSA Lyon	Invité
CAZES, Pierre	Ingénieur	Antea Group	Invité
LOUVARD, Clémence	Ingénieure	Antea Group	Invitée

Département FEDORA – INSA Lyon - Ecoles Doctorales

SIGLE	ECOLE DOCTORALE	NOM ET COORDONNEES DU RESPONSABLE
CHIMIE	**CHIMIE DE LYON** **https://www.edchimie-lyon.fr** Sec. : Renée EL MELHEM Bât. Blaise PASCAL, 3e étage secretariat@edchimie-lyon.fr	**M. Stéphane DANIELE** C2P2-CPE LYON-UMR 5265 Bâtiment F308, BP 2077 43 Boulevard du 11 novembre 1918 69616 Villeurbanne **directeur@edchimie-lyon.fr**
E.E.A.	**ÉLECTRONIQUE, ÉLECTROTECHNIQUE, AUTOMATIQUE** **https://edeea.universite-lyon.fr** Sec. : Stéphanie CAUVIN Bâtiment Direction INSA Lyon Tél : 04.72.43.71.70 secretariat.edeea@insa-lyon.fr	**M. Philippe DELACHARTRE** INSA LYON Laboratoire CREATIS Bâtiment Blaise Pascal, 7 avenue Jean Capelle 69621 Villeurbanne CEDEX Tél : 04.72.43.88.63 **philippe.delachartre@insa-lyon.fr**
E2M2	**ÉVOLUTION, ÉCOSYSTÈME, MICROBIOLOGIE, MODÉLISATION** **http://e2m2.universite-lyon.fr** Sec. : Sylvie ROBERJOT Bât. Atrium, UCB Lyon 1 Tél : 04.72.44.83.62 secretariat.e2m2@univ-lyon1.fr	**M. Philippe NORMAND** Université Claude Bernard Lyon 1 UMR 5557 Lab. d'Ecologie Microbienne Bâtiment Mendel 43, boulevard du 11 Novembre 1918 69 622 Villeurbanne CEDEX **philippe.normand@univ-lyon1.fr**
EDISS	**INTERDISCIPLINAIRE SCIENCES-SANTÉ** **http://ediss.universite-lyon.fr** Sec. : Sylvie ROBERJOT Bât. Atrium, UCB Lyon 1 Tél : 04.72.44.83.62 secretariat.ediss@univ-lyon1.fr	**Mme Sylvie RICARD-BLUM** Institut de Chimie et Biochimie Moléculaires et Supramoléculaires (ICBMS) - UMR 5246 CNRS - Université Lyon 1 Bâtiment Raulin - 2ème étage Nord 43 Boulevard du 11 novembre 1918 69622 Villeurbanne Cedex Tél : +33(0)4 72 44 82 32 **sylvie.ricard-blum@univ-lyon1.fr**
INFOMATHS	**INFORMATIQUE ET MATHÉMATIQUES** **http://edinfomaths.universite-lyon.fr** Sec. : Renée EL MELHEM Bât. Blaise PASCAL, 3e étage Tél : 04.72.43.80.46 infomaths@univ-lyon1.fr	**M. Hamamache KHEDDOUCI** Université Claude Bernard Lyon 1 Bât. Nautibus 43, Boulevard du 11 novembre 1918 69 622 Villeurbanne Cedex France Tél : 04.72.44.83.69 **hamamache.kheddouci@univ-lyon1.fr**
Matériaux	**MATÉRIAUX DE LYON** **http://ed34.universite-lyon.fr** Sec. : Yann DE ORDENANA Tél : 04.72.18.62.44 yann.de-ordenana@ec-lyon.fr	**M. Stéphane BENAYOUN** Ecole Centrale de Lyon Laboratoire LTDS 36 avenue Guy de Collongue 69134 Ecully CEDEX Tél : 04.72.18.64.37 **stephane.benayoun@ec-lyon.fr**
MEGA	**MÉCANIQUE, ÉNERGÉTIQUE, GÉNIE CIVIL, ACOUSTIQUE** **http://edmega.universite-lyon.fr** Sec. : Stéphanie CAUVIN Tél : 04.72.43.71.70 Bâtiment Direction INSA Lyon mega@insa-lyon.fr	**M. Jocelyn BONJOUR** INSA Lyon Laboratoire CETHIL Bâtiment Sadi-Carnot 9, rue de la Physique 69621 Villeurbanne CEDEX **jocelyn.bonjour@insa-lyon.fr**
ScSo	**ScSo*** **https://edsciencessociales.universite-lyon.fr** Sec. : Mélina FAVETON INSA : J.Y. TOUSSAINT Tél : 04.78.69.77.79 melina.faveton@univ-lyon2.fr	**M. Christian MONTES** Université Lumière Lyon 2 86 Rue Pasteur 69365 Lyon CEDEX 07 **christian.montes@univ-lyon2.fr**

*ScSo : Histoire, Géographie, Aménagement, Urbanisme, Archéologie, Science politique, Sociologie, Anthropologie

“What we think, we become...”

Buddha

To my beloved parents, Georges and Souad,

Who believed in me.

To the soul of my uncle Youssef.

Acknowledgments

It takes two hands to clap.

Accordingly, I would like to express my gratitude towards all those who helped to make this dream come true.

Firstly, I would like to thank my director Ali Daouadji and my supervisors Laurent Briançon and Stéphane Grange for their help and big support during the last three years and from Day one. A very big thank you to Laurent Briançon for his help particularly in the experimental part of the thesis and his guidance, be it on a professional or personal level. I also want to thank Pierre Cazes, my supervisor from the company Antea Group, for all his useful advices.

I would also like to thank Pr. Daniel Dias for the many discussions we have had and all his technical advices.

The experimental work in this thesis could not have been accomplished without the assistance of the technicians in the laboratory GEOMAS. I would like to thank in particular Jostar Laforet, Mario Masapollo and Stéphane Vacherie for their help and assistance.

I thank also the "Région Auvergne-Rhône-Alpes" for the funding they provided, which made our project possible.

Furthermore, I wish to thank "Itasca" for their trust in our project and for providing us with their Pre-release version 7.0 of FLAC3D which served as a support for the numerical modeling in this thesis.

I would also like to thank Pr. Roger Frank and Pr. Richard Jardine who accepted to review this manuscript as well as Mrs. Diana Salciarini and Mr. Lionel Manin for being members in the jury.

I also wish to extend my thanks most especially my friends and colleagues who have always assured me of their support during the last three years in the laboratory GEOMAS: Alexios, Adnan, Atéfé, Danai, Gianluca, Joao, José, Nour and Thomas. Thank you all for the warm atmosphere, the laughter, the coffee breaks and all the beautiful memories. I will miss you very much.

There are friends, there is family and there are friends that become family.

Elie, François, Jérôme, Zeina, Peter, Christine, Maha C., Maha R., Maria, Nicole, Miled and David. I am grateful for your presence in my life. Your encouragement helped me to overcome all the difficult obstacles during this journey.

And last but not least, I would like to express my gratitude to my parents Georges and Souad and my sisters Tracy and Valery. Thank you for believing in me and for always being my source of motivation. Without you, I have no idea how I could have made it.

Abstract

The construction of high-rise buildings in urbanized area can be subject to several constraints. When the loads transferred to the foundations become high a shallow foundation becomes insufficient. This is where piles or pile groups are used to transfer the loads to deeper soil layers or to reduce the settlement. The design of the structure and the foundations starts by a good understanding of the behavior of the ground, the piles and the pile-soil interface subjected to high loads. This analysis allows to determine the bearing capacity and the settlement of single piles. It becomes more challenging in case of pile groups.

In the framework of the project "Fondasilex", this thesis proposes the study of the pile foundations in the tower "Silex^2" built in the Part-Dieu district in Lyon, France. It is founded on 20 piles, 1.22 m in diameter and 15.5 m deep, which are bored into three layers of fluvial alluviums and anchored in the Miocene molasse. The soil in Lyon is poorly characterized in the literature, which is likely to lead to an oversizing of the foundations and consequently a high increase in construction costs.

This thesis offers some important elements to improve the design of piles; it presents the geotechnical auscultation and numerical modeling performed within this project which aim to characterize the soil of Lyon and the pile-soil interaction, to predict the long-term behavior of the structure, the foundations and the soil and then to constitute a base of experience to help in the study of other towers planned on the Part-Dieu neighborhood. This work was accompanied by laboratory testing carried out on the alluvial and molasse samples extracted from the site.

In the first part, an instrumentation of the foundations and the soil was set up to enable the real-time monitoring of their behavior. It consists of a fiberglass rod extensometer connected to six displacement sensors that measure the settlement of the soil at six different depths, concrete pressure cells and strain gages of two types (electrical resistance and vibrating wire) which measure respectively the stress on the head of the piles and the deformation at three positions. At the same time, the pile deformation was also measured using fiber optic sensors interrogated by the ODiSI 6100 which uses the OFDR (Optical Frequency Domain Reflectometry) technique based on Rayleigh scattering. These measurements were analyzed in the light of the construction progress of the steel structure.

In the second part, numerical models were carried out on FLAC3D, based on the finite difference method. A sensitivity analysis performed on an isolated pile model helped to understand the influence of each of the model parameters on the pile's response. Models with two or more piles were also used to study the group effect that may occur. All these models helped to understand the behavior of the structure, the soil and the soil-structure interface. A perfectly plastic elastic law with a Mohr-Coulomb criterion and the Plastic-

Hardening Model were found suitable to represent the behavior of the alluviums and molasse respectively. These laws have been calibrated and validated using the instrumentation and laboratory tests (triaxial, oedometer and shear box tests) carried out, due to the absence of a static pile load test.

These two studies carried out in parallel allowed to establish a methodology to optimize the design in future projects and to evaluate the response of the foundations and the soil on the Part Dieu site.

Keywords: Piles, pile-soil interface, fluvial alluviums, Miocene molasse, instrumentation, fiberglass rod extensometer, fiber optic sensors, electrical resistance strain gages, vibrating wire strain gages, concrete pressure cells, finite difference method, FLAC3D, Mohr-Coulomb, Plastic-hardening Model.

Résumé

La construction de tours de grande hauteur dans les grandes villes fortement urbanisées peut être sujet à plusieurs contraintes. Dans ce type de constructions, on a en général recours à des fondations profondes pour transférer les charges à des couches de sol plus profondes ou pour réduire le tassement. Un bon dimensionnement de la structure et des fondations et par conséquent une optimisation des coûts exige alors une bonne compréhension du comportement du sol, des pieux ainsi que l'interface sol-pieu. Cette analyse se base sur une évaluation de la capacité portante et du tassement des pieux qui devient plus délicate quand l'effet de groupe est à considérer.

Dans le cadre du projet « Fondasilex », cette thèse propose l'étude des fondations de la tour silex^2 qui est construite dans le quartier de la Part-Dieu à Lyon. Celle-ci est fondée sur 20 pieux de 1.22 m de diamètre et 15.5 m de long et qui traversent trois couches d'alluvions du Rhône pour s'ancrer dans une couche de molasse du Miocène. L'absence de caractérisation précise des sols rencontrés dans la littérature peut entraîner un surdimensionnement des fondations et par conséquent une augmentation des coûts de construction.

Cette thèse essaie d'apporter des éléments pour améliorer le dimensionnement de ce type de fondations ; elle présente l'auscultation géotechnique et la modélisation numérique réalisées au sein de ce projet dans le but de mieux comprendre le mécanisme de transfert des charges dans le cas de pieux. Il permet ainsi de caractériser le sol lyonnais et l'interaction pieux-sol, de prédire le comportement à long terme de la structure, des fondations et du sol et par la suite constituer une base de données pour les autres tours prévues sur le site de la Part-Dieu. Ce travail a été accompagné d'essais de laboratoire sur les échantillons d'alluvions et de molasse prélevés du site.

En première partie, une instrumentation des fondations et du sol a été mise en place afin de suivre leur comportement pendant la construction de l'ouvrage et lors de sa mise en service. Elle est constituée d'un extensomètre multipoint pour mesurer le tassement des alluvions et de la molasse à six profondeurs, de capteurs de pression totale, des capteurs de déformation (électriques ou à corde vibrante) qui ont mesuré respectivement la contrainte sur la tête des pieux et la déformation qui en résulte sur toute la longueur du pieu. Cette dernière a été en même temps mesurée à l'aide de fibres optiques interrogées par la centrale ODiSI 6100 qui utilise la réflectométrie fréquentielle avec diffusion de Rayleigh. Les mesures effectuées par ces capteurs ont été analysées à la lumière de l'avancement de la construction de la charpente métallique.

En deuxième partie, des modèles numériques ont été réalisés sur FLAC3D, basés sur la méthode des différences finies. Une étude paramétrique sur un modèle de pieu isolé a permis d'analyser l'influence de chacun des paramètres du sol sur la réponse du pieu. Dans le but d'évaluer et analyser l'effet de groupe qui pourra avoir lieu dans le projet, des modèles qui comportent deux pieux ou plus ont été établis. Tous ces modèles ont permis de comprendre le comportement de la structure, du sol et de l'interface sol-structure. Une loi élastique parfaitement plastique avec un critère de Mohr-Coulomb et le Plastic-Hardening Model ont été jugés bien adéquats aux alluvions et à la molasse respectivement. Ces modèles ont été calibrés et validés à l'aide de l'instrumentation et des essais de laboratoire (triaxiaux, œdométriques et à la boîte de cisaillement) qui ont été réalisés sur des échantillons d'alluvions et de molasse, en raison de l'absence d'un essai de chargement statique.

Ces deux études menées en parallèles ont permis d'établir une méthodologie pour optimiser la conception dans les futurs projets et l'évaluation de la réponse des fondations et du sol sur le site de la Part Dieu.

Mots clés : pieux, interface sol-structure, alluvions du Rhône, molasse du miocène, instrumentation, extensomètre multipoint, fibre optique, jauges de déformation, extensomètre à corde vibrante, capteur de pression totale, différences finies, FLAC3D, Mohr-Coulomb, Plastic-Hardening Model.

Table of contents

List of figures

List of tables

List of symbols and abbreviations

The symbols that are used locally are defined in the text.

The superscripts "1" and "2" after the word "Silex" allow to refer to the name of the two buildings in Part-Dieu area.

The dates are given in the following format: dd/mm/y.

List of abbreviations

BEM	Boundary element method
CPC	Concrete pressure cell
CPT	Cone penetration test
ERSG	Electrical resistance strain gage
FDM	Finite difference method
FEM	Finite element method
FOS	Fiber optic sensor
NGF	General levelling of France
PMT	Pressuremeter test
POT	Potentiometer (displacement sensor)
SPT	Standard penetration test
TS	Transfer structure
VWSG	Vibrating wire strain gage

List of symbols

Greek letters

α	Interaction factor in a pile group / or the rheological coefficient of the soil in pressuremeter theory
γ	Effective unit weight of soil
$\gamma_{0.7}$	Shear strain magnitude at 72.2%G_0 in PH-S soil model
δ_{ij}	Kronecker tensor
δ'	Soil-pile friction angle
ε	Strain
ε_{ij}	Strain second order tensor
ε_1	Principal strain in direction 1
ε_2	Principal strain in direction 2
ε_3	Principal strain in direction 3
ε^e	Elastic component of the deformation
ε^p	Plastic component of the deformation
$\dot{\varepsilon^p}$	Plastic deformation rate
ε_v	Volumetric deformation

ε_v^p	Plastic component of the volumetric deformation
η	Group efficiency factor
με	Deformation measured in μm/m
ν	Poisson's ratio of a material
ν_s	Poisson's ratio of soil
ν_{ur}	Unloading/reloading Poisson's ratio in PH model
σ	Stress
σ_{ij}	Stress second order tensor
σ_1	Major effective principal stress
σ_2	Intermediate effective principal stress
σ_3	Minor effective principal stress
σ_n	Normal stress
σ'_h	horizontal effective stresses in soil
σ'_v	vertical effective stresses in soil
τ	Mobilized unit skin friction
ϕ	Soil friction angle
ϕ_{int}	Friction angle of the interface in FLAC3D
ψ	Dilation angle
ψ_{int}	Dilation angle of the interface in FLAC3D

Roman letters

A_b	Area of pile tip
A_s	Area of pile shaft
$A_{s,i}$	Area of pile shaft at layer i
B_g	Width (breadth) of the block formed by a pile group
c	Drained cohesion of soil
c_{int}	Cohesion of the interface in FLAC3D
c_u	Undrained cohesion of the soil
D	Diameter of a pile
d	Spacing between the piles in a group
E	Young modulus of a material
E_i	Initial tangent Young modulus
E_M	Menard's pressuremeter modulus
E_p	Young modulus of the pile
E_b	Bearing stratum Young's modulus
E_c	Young modulus of the concrete
E_{cm}	Secant elastic modulus of the concrete defined between the origin and $0.4f_{cm}$
$E_{c,eff}$	Effective modulus of concrete
E_s, E_y	Modulus of elasticity of the soil
E_{50}^{ref}	Reference secant stiffness from drained triaxial test (at p_{ref})
E_{50}	Secant stiffness from drained triaxial test
E_{ur}^{ref}	Reference unloading/reloading stiffness in PH model (at p_{ref})
E_{ur}	Unloading/reloading stiffness in PH model
E_{oed}^{ref}	Reference tangent stiffness for oedometer primary loading (at p_{ref})
E_{oed}	Tangent stiffness for oedometer primary loading
E_0^{ref}	Reference initial stiffness modulus in PH-S soil model
E_y	Deformation moduli of the soil

F	Applied load on the head of the pile (It can be referred in some paragraphs as Q)
F_b	Mobilized load at pile tip (It can be referred in some paragraphs as Q_b)
F_G	Total load applied on a pile group
F_s	Mobilized load at pile shaft (It can be referred in some paragraphs as Q_s)
f	Yield surface
f_{cm}	Mean compressive strength of the concrete
f_{ck}	Characteristic cylinder compressive strength of the concrete
G	Shear modulus of a material
G_{ur}	Unloading/reloading shear modulus
G_0	Shear stiffness modulus at very small strain in PH-S soil model
G_s	Shear modulus of soil
g	Plastic potential
K	Bulk modulus of a material
K'	Pile stiffness factor
K_0	Coefficient of earth pressure for the soil at rest
K_{nc}	Normal consolidation coefficient
k_n	Normal stiffness of the interface in FLAC3D
k_s	Shear stiffness of the interface in FLAC3D
L	Length of the pile
L_g	Length of the block formed by a pile group
m	Power for stress-level dependency of stiffness in PH model
n	Number of piles in a group
n_1	Number of piles in horizontal side
n_2	Number of piles in vertical side
OCR	Over consolidation ratio
P	Perimeter of the pile section
p'	Mean effective stress (or hydrostatic pressure)
p_c	Preconsolidation pressure
p_l^*	Limit pressure from PMT
p_{ref}	Reference pressure in PH model
q	Deviatoric stress
q_b	Ultimate tip resistance pressure
q_c	Tip resistance from CPT test
q_f	Ultimate deviatoric stress
q_s	Ultimate unit skin friction
$q_{s,i}$	Ultimate unit skin friction at layer i
R	Resistance of a strain gage
R_b	Ultimate base resistance
R_c	Ultimate Compressive pile resistance
$R_{c,cr}$	Creep resistance
R_f	Failure ratio in PH model
R_{gu}	Ultimate bearing capacity of the pile group
R_{iu}	Ultimate bearing capacity of a single pile
R_s	Ultimate shaft resistance
S	Settlement of a single pile
S_g	Average settlement of a pile group
s_i	Pile-soil relative displacement

General introduction

The world's largest cities are tending to build high-rise buildings that are symbols of economic and financial power. Sites located in high urbanized areas may be subject to some problems and constraints such as excessive loads or bad soil quality. A poor understanding of the behavior of the soil and the structure may lead to an oversizing and significant costs afterwards or in the opposite case to underestimated settlements that may cause safety issues.

Pile foundations are adopted in such huge projects to transfer the loads to deeper levels or to reduce the settlement. Thus, the applied load from the superstructure can be carried by the shaft or the tip or both. Accordingly, the piles are qualified as floating or end-bearing piles. The analysis of the piles' behavior, or that of pile groups, starts by the evaluation of their bearing capacity and their settlement. Besides, this should be accompanied by the estimation of the shear stress mobilized at the pile's shaft and consequently, the load transferred to the tip. Therefore, a good characterization of the soil and the soil-pile interface is much needed.

To improve the knowledge of the soil, the structure and the interface between them, several methods were developed and are being used. They are either analytical, experimental or numerical.

Several analytical methods were developed to help estimate the bearing capacity of piles. Among others are the empirical methods that use the rigid plastic theory, which were blamed for overlooking the elastic and strain hardening behavior that occur in piles. Other theoretical approaches are based on experimental tools such as the pressuremeter tests or the cone penetration tests for the calculation of the bearing capacity of the piles. These methods are in general suitable for single pile analysis and are based on experimentally determined parameters which are not always well estimated. On the other hand, there are analytical methods that estimate the piles' settlements such as the method based on the elastic theory or the load transfer method. The former was developed by Poulos and Davis (1980). It only uses elastic parameters thus it cannot describe the non-linear behavior. It is adequate for representing the elastic behavior of piles at small loads. However, the latter gives more realistic results but it requires the construction of load transfer curves. There are already in the literature some theoretical curves that were developed based on previous experience such as the tri-linear curves of Frank and Zhao (1982). Others are based on pile load tests.

Pile load tests are experimental tests performed on real sites that allow to determine the response of single piles to several types of loading. In such tests, a geotechnical instrumentation program is essential. The experience showed that the instrumentation in geotechnical projects is important during the site investigation stage, the construction stage or during the operating phase (Nicholson et al., 1999).

Finally, numerical methods were conceived to apply the previously cited methods in a computed manner, where more complex geometries can be adopted and the parameters and the constitutive laws can be easily modified. Several numerical methods are in general used for piles such as the BEM, FEM and FDM. Numerical methods do not always describe the real behavior of the structure and/or the soil. For example, in the case of piles, it is recommended to calibrate these models using experimental tools (laboratory tests or geotechnical instrumentation).

In the framework of the "Pack ambition 2017" funded by the region "Auvergne-Rhône-Alpes", the project "Fondasilex" is intended to study the behavior of the soil and the pile foundations of the Silex^2 tower, constructed at the Part-Dieu business district in Lyon which is showing a great dynamism. The tower is founded on 20 piles of 1.22 m diameter which are bored into the alluvial deposits of the Rhône and are anchored in the Miocene molasse. The soil in Lyon is characterized by layers of alluviums which are formed by sands and gravels, above a thick layer of molasse which consists of sandy-silty to sandy-gravelly beige sands. Both soils are not well characterized in the literature. The alluviums have been the subject of few studies in the 70s and 80s that allowed to determine the cohesion and the friction angle at shallow depths only, while for the molasse of the Part-Dieu there is nothing to mention. Therefore, the behavior of the soil and the pile foundations could not be studied.

The main objectives of this work were the following:

- To have a good knowledge of the soil's characteristics in the Part-Dieu neighborhood
- To understand the behavior of the soil when subjected to loads
- To analyze and understand the load transfer mechanism of the piles and the pile-soil interaction
- To try to predict their behavior over the long term
- To obtain a data base for the other towers planned on the same region

Therefore, a geotechnical instrumentation was carried out to measure in real time the deformation of the piles over their entire lengths, the stress transferred at their head and the ground settlement at 6 different depths as well. Laboratory experiments (triaxial, shear box and oedometer tests) were carried out on some soil samples extracted from the site with the aim to determine some parameters. Finally, numerical models were then calibrated on FLAC3D based on the actual observed behavior of the foundations and the soil.

In order to deal with these various points, this thesis was divided into four chapters.

The literature review of Chapter 1 presents the load transfer mechanisms of axially loaded piles. It provides a detailed overview on the existing analytical, experimental and numerical methods developed to calculate the bearing capacity and the settlement of piles and pile groups as well. Some of the available constitutive laws were also detailed with a view to choose the best for the soil in this project. Finally, the geotechnical instrumentation was presented with its benefits, objectives and historical aspects.

Chapter 2 introduces the project Silex^2 and shows the foundation plan and the applied load at the head of the piles. Crushing tests on concrete samples were performed allowing to determine the Young modulus. Besides, the characteristics of the existing soil formations are shown together with some experimental tests from the literature.
On the other hand, this chapter presents the experimental and numerical tools used in this project. Firstly, the geotechnical instrumentation performed on the piles and the soil is detailed showing the schedule, the characteristics of the used sensors and the installation procedure.
Secondly, the numerical tool FLAC3D that employs the finite difference method is presented. Three different models were performed allowing to study the case of isolated piles, pile groups and global models. In this chapter, only the geometry of these models was shown. The analysis was kept for the third and fourth chapters.

Chapter 3 is devoted to presenting the results of the numerical models of FLAC3D. A sensitivity analysis was first performed on the isolated pile models to study the effect of each of the parameters on the behavior of the piles:

- Parameters of the soil (Young modulus, cohesion, friction angle, dilatancy angle)
- Parameters of the interface
- Young modulus of the pile

Then a comparison was made with the pile group and the global models to show the variation of the settlement. Besides, the influence of the water table and the concrete's Young modulus on the response of the pile was studied.
Finally, two analytical methods were tested on this project. The Load transfer method (Frank and Zhao, 1982) and the theory of elasticity (Poulos and Davis, 1980) were used in an attempt to prove their efficiency in this case.

Chapter 4 presents the results of the characterization of the alluviums and the molasse by performing experimental tests (shear box, triaxial and oedometer tests). These tests allowed to determine the soil parameters that served as the basis for the numerical models. On the other hand, the parameters measured by the sensors such as the deformation along the piles, the stress at their top and the soil's settlement were analyzed and presented in this same chapter. The results of this experimental work were confronted with the findings of the numerical section.

Chapter 1: Literature review

1- Introduction

The first use of pile foundations in history goes back to thousands of years ago. Phoenicians, for example, have used sheet piles for dock and shore constructions with their expanding sea trade, a method that appears to be derived from the skill of boat builders in the planking of ships. Steel and wood piles were then used by Egyptians, Greeks and Romans for shore works (Fleming et al., 2008). Ever since, the usage of pile foundations has been largely expanded and the use of concrete piles has become more and more common worldwide mainly with the introduction of reinforced concrete by the French contractors Coignet and Hennebique. During the last decades, the design of piles has advanced steadily, especially due to the development of analytical methods and computer-based techniques. Various standard codes were then suggested in many countries to design and construct pile foundations such as the Eurocode 7 (2005) and the ACI Committee 543R-12 (2012).

This chapter is devoted to providing a better understanding of pile foundations, their design and their behavior when subject to axial loads in particular. Besides, an overview of the numerical experiences available in the literature will be presented without forgetting the geotechnical instrumentation that in many projects has been carried out in parallel.

2- Axially loaded piles

Piles are generally used as a replacement of shallow foundations when the bearing capacity of the soil is insufficient, or to reduce the settlement, especially if the load from the superstructure is very important or if the soil beneath the structure is not able to resist to it. They are categorized according to several criteria:

- Their constitutive material: concrete, steel, timber or composite
- Their geometry (shape and size): Timber piles can be rectangular or circular in shape. Their size or diameter can vary from 3 to 5 m. On the other hand, driven steel piles may be of I-section or hollow pipe filled afterward with concrete and their diameter and thickness may go up to 1.2 and 0.023 m respectively. Precast concrete piles are available in rectangular, octagonal, triangle or circular shapes. However, cast-in place concrete piles are circular in general and their diameter can go up to 1.2 m.
- The applied load on the piles: Depending on the use-case (high-rise buildings, highways, bridges, wind turbines...), they can be subject to axial, lateral or combined load. In the following, only axially loaded piles will be studied.
- Their function: end-bearing and/or friction piles
    - Friction piles carry the load in majority by means of the skin friction mobilized along their shaft. Piles installed in cohesive soils are good examples of friction piles in general.
    - End-bearing piles transfer the loads to a stiffer stratum located at a greater depth in a way that the load is carried by means of bearing resistance at the pile tip only.
    - Piles with both skin friction and end-bearing resistance simultaneously.

According to the French standard NF P 94-262 (2012), piles are qualified as friction (or floating) when under creep load, the effort mobilized by skin friction is higher than the effort mobilized at the pile's tip.

The pile's function can also vary depending on the method used to construct the pile.

- The method of construction used:
  - Driven piles which can be executed using various methods (dropping weight, vibration and jacking against a reaction)
  - Bored piles which can be executed with or without casing.

All these methods are explained in Fleming et al. (2008). Particularly, the Continuous Flight Auger (CFA) technique, which is used in the project associated with this thesis, will be detailed in Chapter 2. This is an important factor that affects the load transfer occurring between the pile and the adjacent soil layers. Based on this classification, piles can be qualified as "displacement" on "non-displacement" which correspond generally to driven and bored piles respectively.

2-1- Load transfer mechanisms of axially loaded piles

When a pile is loaded, it stresses the adjacent soil near the shaft causing its settlement. This vertical load "F" is in general carried by the shaft as skin friction, the soil below pile's tip as end-bearing pressure or both simultaneously, depending on the soil layers characteristics as well as the type of the pile (Figure 1.1).

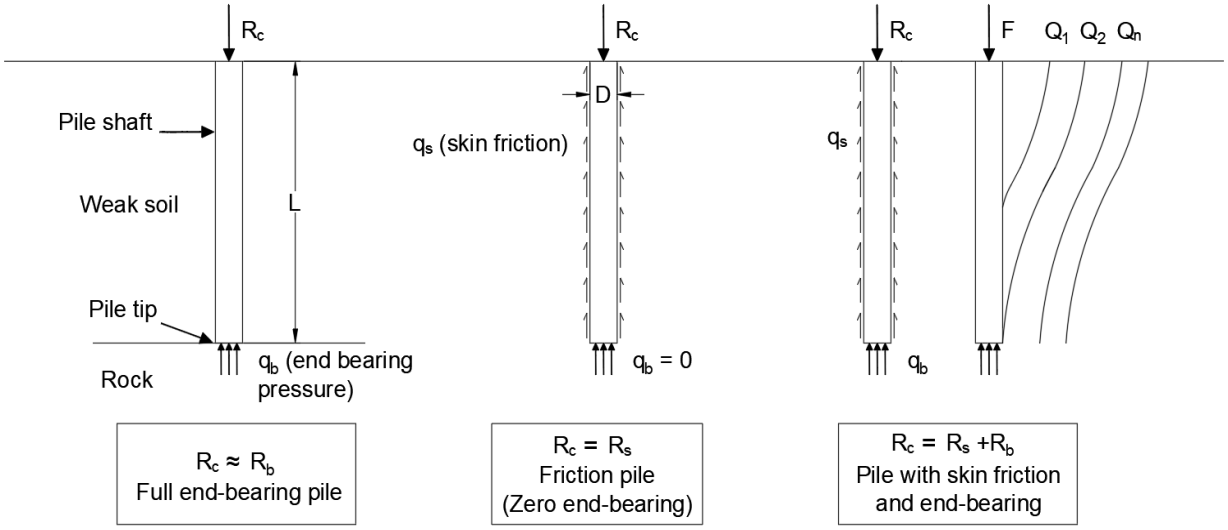

Figure 1.1 Different load transfer mechanisms in axially loaded piles

The skin friction along the pile's shaft is the main responsible of the transfer of the stresses to the soil. The movement of the pile causes the soil to move in the direction of the applied load. The sign of the relative movement between the pile and the adjacent soil produces skin friction along the shaft that can thus be either positive or negative.

In a normal case, when the pile settles more than the soil, the relative movement is positive and the skin friction on the pile's shaft is in upward direction. However, as long as the pile is loaded, if the soil near the surface is softer, the latter will settle more and consequently the relative displacement between the pile and the soil becomes oriented downward. This is called "negative skin friction" or "down drag" and it results in the reduction of the effective bearing capacity of the pile. At a certain depth in the soil, the shear stress becomes positive again locating the "neutral plane" which is defined as the position where the soil does not exert any force on the pile. The location of the neutral plane varies from case to case depending on the type of the pile, the construction method and the applied load. In a pure floating pile, its location may be estimated at two-thirds of the pile length, whereas in an end-bearing pile, it is usually at the rigid stratum level (Rajapakse, 2016).

Negative skin friction has been discussed by many researchers (Johannessen and Bjerrum, 1965; Fellenius, 1969; Combarieu, 1985; Poorooshasb et al., 1996; Comodrosmos and Bareka, 2005).

2-2- Calculation of pile capacity using theoretical approaches

In the literature, there are numerous published works for pile capacity calculations. The used methods can be classified into two main sections: field or theoretical approaches. The former includes among others static or dynamic pile load tests, which are not always possible. That is where methods based on theoretical approaches are used. They will be presented in the following paragraph.

The first equation for bearing capacity of foundations was given by Terzaghi (1943) for a long strip footing. Many authors have tried to improve it by including geometrical factors such as the inclination angle of the load and the shape of the foundation (Caquot and Kerisel, 1953; Meyerhof, 1963; Hansen, 1970; Vesić, 1973). Later on, this equation was improved so it can estimate the ultimate bearing capacity of deep foundations as the summation of R_s the ultimate shaft resistance which is the shear force developed along the pile shaft and R_b the ultimate tip resistance generated at the pile tip. It may be written as follows:

$$R_c = R_b + R_s = A_b * q_b + A_s * q_s \qquad \text{Eq. 1.1}$$

When the soil is heterogeneous, the ultimate shaft resistance has to be estimated at the different layers allowing to express the ultimate pile resistance as follows:

$$R_c = R_b + R_s = A_b * q_b + \Sigma A_{si} * q_{si} \qquad \text{Eq. 1.2}$$

Where A_{si} and q_{si} correspond to the area of the shaft and the unit skin friction at the *i*-layer.

Additionally, a new resistance load is defined which is the ultimate creep resistance $R_{c,cr}$ of piles. It is the load below which the load transfer curve is quasi-linear. There are equations relating this resistance to R_b and R_s for different type of piles. As an example, for a non-displacement pile under compression, this relation is given by:

$$R_{c,cr} = 0.5R_b + 0.7R_s \qquad \text{Eq. 1.3}$$

In the literature, there are different methods used to evaluate the ultimate capacity of piles. Some are empirical and others are based on laboratory or in-situ tests (SPT, CPT and PMT).

2-2-1- Empirical equations - Rigid-plastic theory

In deep foundations, only punching shear failure occurs as long as the length to width ratio is greater than 4 (Vesić, 1967). Rigid-plastic theory assumes that the material exhibits plastic deformation with no elastic component. In this context, many researchers have calculated the pile capacity, which is only valid at failure. The failure surfaces were predicted differently by these authors as presented in Figure 1.2. Although these methods overlook the elastic and strain hardening behavior that occur in piles, they can still be considered as good methods for performing preliminary calculations.

It turned out that the bearing capacity of piles depends on the friction angle ϕ of the soil and the ratio L_c/D where L_c refers to the critical depth, which is defined as the depth of the pile up to which the effective stress will increase linearly. It was shown that after this depth, the effective stress and thus the skin friction become constant. The critical depth is estimated at 10 to 20 times the diameter of the pile depending on the density of the sand. According to Poulos and Davis (1980), this ratio is calculated as follows:

$$\begin{cases} L_c/D = 5 + 0.24\,(\phi - 28) & for \quad 28° < \phi < 36.5° \\ L_c/D = 7 + 2.35\,(\phi - 36.5) & for \quad 36.5° < \phi < 42° \end{cases} \qquad \text{Eq. 1.4}$$

The friction angle to be used in the previous formulas is calculated based on ϕ_0 the angle of internal friction prior to the installation of the pile as follows:

$$\begin{aligned} \phi\,(°) &= 0.75\,\phi_0 + 10 && for\ driven\ piles \\ \phi\,(°) &= \phi_0 - 3 && for\ bored\ piles \end{aligned} \qquad \text{Eq. 1.5}$$

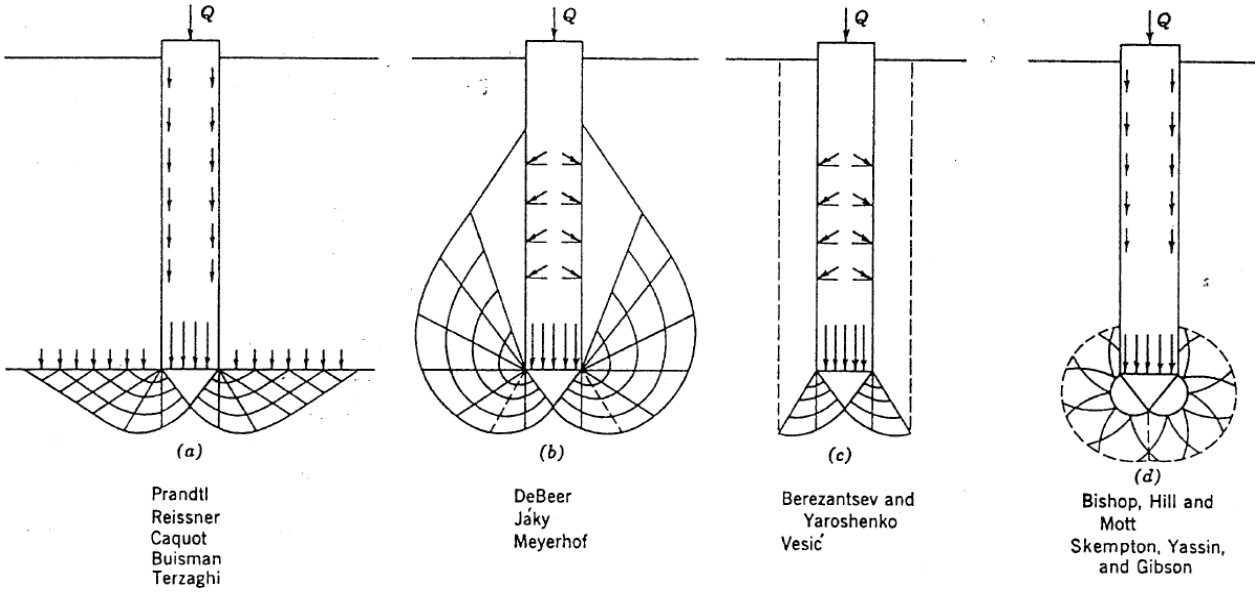

Figure 1.2 Failure patterns under piles (Vesić, 1967)

2-2-1-1- Calculation of the tip resistance

Identically to a shallow foundation, the ultimate tip resistance pressure of a pile may be expressed using Eq. 1.6 which can be changed into Eq. 1.7 by the simple assumption of a small diameter to length ratio.

$$q_b = \gamma\, D\, N_\gamma^* + \sigma_v'\, N_q^* + \mathrm{c}\, N_c^* \qquad \text{Eq. 1.6}$$

$$q_b = \sigma_v'\, N_q^* + \mathrm{c}\, N_c^* \qquad \text{Eq. 1.7}$$

Where N_γ^*, N_q^* and N_c^* are the modified bearing capacity factors that include all shape factors and σ_v' is the effective overburden pressure at the tip of the pile.

There are many methods used to calculate these factors. For example, Berezantsev et al. (1961) as cited in Tomlinson (1986) proposed solutions for sandy soils. Meyerhof (1976), on the other hand, suggested equations for both sands and clays and Vesić (1977) and Janbu (1976) developed a method suitable for different types of soils. Three of these methods are presented in the following.

- Meyerhof (1976)

Meyerhof (1976) calculates the tip resistance as follows:

$$\begin{cases} R_b = \sigma_v'\, N_q^*\, A_b \le 50 N_q^*\, tan\,\phi\, A_b \quad (for\ dense\ sand) \\ R_b = \sigma_v'\, N_q^*\, A_b \le 25 N_q^*\, tan\,\phi\, A_b \quad (for\ loose\ sand) \end{cases} \qquad \text{Eq. 1.8}$$

$$R_b = N_c^*\, C_u\, A_b = 9 C_u\, A_b \ \textit{(for clay)} \qquad \text{Eq. 1.9}$$

Where N_q^* is determined for driven piles by using some charts. However, for bored piles, q_b has to be reduced by one-third to one-half.

- Vesić (1977)

This method is based on the theory of expansion of cavities. The ultimate tip resistance is calculated using the equation:

$$R_b = (c\, N_c^* + \sigma_m N_\sigma^*)\, A_b \qquad \text{Eq. 1.10}$$

Where σ_m is the mean effective normal ground stress.

N_c^*, σ_m and N_σ^* are calculated using Eq. 1.11 to Eq. 1.17.

$$\sigma_m = \frac{1 + 2K_0}{3}\sigma_v' \qquad \text{Eq. 1.11}$$

$$N_c^* = \left(N_q^* - 1\right) cot\phi \qquad \text{Eq. 1.12}$$

$$N_\sigma^* = \frac{3N_q^*}{1 + 2K_0} = \alpha_1 e^{\alpha_2} N_\phi (I_{rr})^{\alpha_3} \qquad \text{Eq. 1.13}$$

$$\alpha_1 = \frac{3}{3 - sin\phi}, \quad \alpha_2 = \left(\frac{\pi}{2} - \phi\right) tan\phi, \quad \alpha_3 = \frac{1.33 sin\phi}{1 + sin\phi} \qquad \text{Eq. 1.14}$$

$$N_\phi = \left(tan\left(45° + \frac{\phi}{2}\right)\right)^2 \quad \text{Eq. 1.15}$$

$$I_{rr} = \frac{I_r}{(1 + I_r)\Delta} \quad \text{Eq. 1.16}$$

$$I_r = \frac{E_s}{2(1+\nu)(c' + \sigma'_v\, tan\,\phi)} = \frac{G_s}{c' + \sigma'_v\, tan\,\phi} \quad \text{Eq. 1.17}$$

In the previous equations, I_r and I_{rr} are respectively the rigidity and the reduced rigidity indices of the soil. Δ is the average volumetric strain in the plastic zone below the pile tip, which can be considered as zero for a dense soil simplifying the formula into $I_r = I_{rr}$, or it can be determined from triaxial tests. There are tables and charts that give the values of N_c^* and N_σ^* for various values of I_{rr} and ϕ.

- Janbu (1976)

The failure surface according to Janbu (1976) is characterized by an angle ψ (which is different from the dilation angle) as shown in Figure 1.3. It varies from 60° in soft compressible soil to 105° in dense sand.

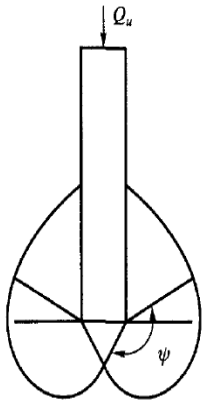

Figure 1.3 Failure pattern as described by Janbu (1976)

The ultimate resistance may be expressed as follows:

$$R_b = \left(c' N_c^* + \sigma'_v N_q^*\right) A_b \quad \text{Eq. 1.18}$$

$$N_q^* = \left[tan\,\phi + \sqrt{1 + tan^2\,\phi}\right]^2 e^{2\psi tan\phi} \quad \text{Eq. 1.19}$$

$$N_c^* = \left(N_q^* - 1\right) cot\phi \quad \text{Eq. 1.20}$$

There are tables used to determine N_q^* and N_c^* for different values of ψ and ϕ.

Janbu's method presents many uncertainties due to the difficulty in determining the value of ψ at the base level and because for a full development of a plastic zone at the base, the settlement of the pile should be at least equal to 10 to 20% of the pile diameter which is not always achievable.

2-2-1-2- Calculation of the shaft resistance

The ultimate shaft resistance may be expressed as follows:

$$R_s = A_s * q_s = P\ \Delta L\ q_s \quad \text{Eq. 1.21}$$

$$q_s = K_0\ \sigma_v'\ tan\ \delta' \quad \text{Eq. 1.22}$$

Where ΔL is the pile length over which P and q_s are taken as constant and σ_v' is the effective vertical stress at corresponding depth. In France, the soil-pile friction angle δ' is often estimated at 2/3 of the friction angle of the soil.

Identically to the tip resistance, many equations were developed to express the ultimate shaft resistance of a pile in a homogeneous soil. They will not be detailed in this thesis.

2-2-2- Calculation of pile capacity based on pressuremeter tests (PMT)

This is one of the most used method in France for calculating the ultimate resistance of piles. Based on the French standard NF P 94-262 (2012), the total ultimate tip resistance may be calculated as in Eq. 1.23.

$$R_b = \mathrm{k_p}\ A_b\ p_{le}^* \quad \text{Eq. 1.23}$$

Where p_{le}^* is the equivalent net limit pressure and k_p is a pile bearing factor. They are determined as follows:

$$p_{le}^* = \frac{1}{3a+b} \int_{L-b}^{L+3a} p_l^*(z)\ dz \quad \text{Eq. 1.24}$$

$$\begin{cases} a = D/2 & for\ D > 1\ m \\ a = 0.5\ m & for\ D < 1\ m \end{cases} \quad ; \quad b = \min\{a, h\} \quad \text{Eq. 1.25}$$

$$k_p = \min\left\{1 + \left[k_{pmax} - 1\right] \frac{D_{eff}}{5D}; k_{pmax}\right\} \quad \text{Eq. 1.26}$$

$$D_{eff} = \frac{1}{p_{le}^*} \int_0^L p_l^*(z) dz \quad \text{Eq. 1.27}$$

Where $p_l^*(z)$ is the net limit pressure, calculated as the difference between the measured limit pressure and the horizontal pressure at rest and h is defined locally as the embedment of the pile in the stratum. k_{pmax} can be determined from tables for different categories of soils.

The total ultimate shaft resistance may be calculated using the Eq. 1.28 to Eq. 1.30.

$$R_s = P \int_0^h q_s(z)\ dz \quad \text{Eq. 1.28}$$

$$q_s = min\{\alpha_{pile-soil}\ f_{soil}; q_{smax}\} \quad \text{Eq. 1.29}$$

$$f_{soil} = (\mathrm{a}\ p_l^* + b)(1 - e^{-c\ p_l^*}) \quad \text{Eq. 1.30}$$

The coefficients a, b, c and $\alpha_{pile-soil}$ are determined from specific tables for different types of soils.

2-2-3- Calculation of pile capacity based on cone penetration tests (CPT)

Another method based on the cone penetration tests is also suggested by the French standard NF P 94-262 (2012). It calculates the total ultimate tip resistance as follows:

$$R_b = k_c \, A_b \, q_{ce} \qquad \text{Eq. 1.31}$$

Where q_{ce} is the equivalent cone resistance and k_c is a pile bearing factor that are determined based on the following equations:

$$q_{ce} = \frac{1}{3a+b} \int_{L-b}^{L+3a} q_{cc}(z)\, dz \qquad \text{Eq. 1.32}$$

Where q_{cc} is the tip resistance capped at $1.3q_{cm}$ (defined in Eq. 1.33) and a and b are similar to those in the pressuremeter based method (Eq. 1.25).

$$q_{cm} = \frac{1}{3a+b} \int_{L-b}^{L+3a} q_c(z)\, dz \qquad \text{Eq. 1.33}$$

The pile bearing factor used in Eq. 1.31 is a function of the embedment length D_{eff} of the pile and its diameter. It can be calculated based on the following equations.

$$D_{eff} = \frac{1}{q_{ce}} \int_{0}^{L} q_{cc}\,(z) dz \qquad \text{Eq. 1.34}$$

k_c is estimated based on the value of D_{eff}/D ratio. If it is higher than 5, then:

$$k_c = k_{cmax} \qquad \text{Eq. 1.35}$$

k_{cmax} is determined from tables for different categories of soils.

Otherwise,

$$k_c = \begin{cases} 0.3 + (k_{cmax} - 0.3)(D_{eff}/D)/5 & for\ clays\ and\ silts \\ 0.2 + (k_{cmax} - 0.2)(D_{eff}/D)/5 & for\ medium\ soils \\ 0.1 + (k_{cmax} - 0.1)(D_{eff}/D)/5 & for\ sands\ and\ gravels \\ 0.15 + (k_{cmax} - 0.15)(D_{eff}/D)/5 & for\ marls\ and\ altered\ rocks \end{cases} \qquad \text{Eq. 1.36}$$

On the other hand, R_s may be calculated identically to the previous method (Eq. 1.28). However, q_s is calculated based on the cone resistance.

$$q_s(z) = \alpha_{pile-soil}\, f_{soil}\, q_c(z) \qquad \text{Eq. 1.37}$$

$$f_{soil} = (\mathrm{a}\, q_c + b)(1 - e^{-c\, q_c}) \qquad \text{Eq. 1.38}$$

The coefficients a, b, c and $\alpha_{pile-soil}$ are determined from specific tables for different types of soils.

2-3- Settlement analysis of piles

Since the primary objective of using piles foundations is to reduce the deformation of the structure, the evaluation of the pile settlement is a key study.

When a load is applied on the head of the pile, it compresses and settles into the soil. In the last century numerous methods have been developed to estimate the settlement of axially loaded piles. Traditional methods have been used such as the conventional one-dimensional theory (Terzaghi, 1943) and the empirical correlations for sands and clays (Meyerhof, 1959; Focht, 1967).

Later, more advanced methods were developed, especially with the growth of sophisticated computer programs. These methods are various and are based on one or more of the following detailed approaches.

2-3-1- Semi-empirical approach

The total settlement of a single pile may be divided into three main components (Vesić, 1977):

- The elastic settlement of pile shaft due to axial deformation

$$S_e(1) = \frac{\left(Q_{wp} + \xi Q_{ws}\right) L}{A_b \, E_p} \qquad \text{Eq. 1.39}$$

- The settlement of pile caused by the load at its tip

$$S_e(2) = \frac{q_{wp} D}{E_s} (1 - \nu_s^2) \, I_{wp} \qquad \text{Eq. 1.40}$$

- The settlement of pile due to skin friction

$$S_e(3) = \left(\frac{Q_{ws}}{P \, L}\right) \frac{D}{E_s} (1 - \nu_s^2) \, I_{ws} \qquad \text{Eq. 1.41}$$

$$I_{ws} = 2 + 0.35 \sqrt{\frac{L}{D}} \qquad \text{Eq. 1.42}$$

Where Q_{wp} and Q_{ws} are the load carried at the pile tip and pile shaft respectively under working load condition, q_{wp} is the ultimate tip resistance pressure, ξ is a factor that depends on the nature of the skin friction distribution along the pile shaft (1/2 for clay and 2/3 for sand) and I_{wp} and I_{ws} are influence factors.

2-3-2- Experimental methods

This method is based on data measured on real instrumented piles or on model piles in the laboratory. As examples of available studies in the literature are the instrumented full-scale pile load tests (Neves et al., 2001b; McCabe and Lehane, 2006; Mattsson et al., 2013) and the centrifugal models for piled raft foundation (Horikoshi et al., 2003). Standard codes for pile load tests are available and are being used nowadays (NF P 94-150-1, 1999; International Organization for Standardization, 2005). Examples of piles instrumentation will be addressed later in Section 5 of this chapter.

2-3-3- Analytical methods

The analytical evaluation of pile settlements is generally done using various methods such as theoretical load transfer curves, discrete layer approach, elastic solutions or hybrid approaches. In the following section, some of these will be detailed.

2-3-3-1- Elastic theory

In the framework of the elastic theory, many models were developed based on Mindlin's equations (Mindlin, 1936), that calculate the stresses and deformations generated at any point of an elastic solid subject to a point load at another location.

The method consists in dividing the pile in a number of elements and imposing a compatibility between the displacement of the pile, obtained by considering the compressibility of the pile under axial loading and that of the adjacent soil calculated by using Mindlin's equation. In other words, this method considers an incompressible pile in a half space and then uses many correction factors to take the compressibility into account.

The use of 10 elements turns to give acceptable accuracy unless the pile is long (L/D > 50) or very compressible (K' < 100).

K' is the pile stiffness factor calculated according to Eq. 1.43. It measures the relative compressibility of the pile and the soil.

$$K' = \frac{E_p \, R_A}{E_s} \qquad \text{Eq. 1.43}$$

Generally, the area ratio R_A is estimated at 1 for a solid pile.

Besides, this method offers the possibility to study the behavior of pile groups subject to axial loads (Poulos, 1968; Poulos and Davis, 1968), but it also presents some limitations. It oversimplifies the pile behavior and cannot describe its non-linear response because it only uses elastic parameters (elastic modulus and Poisson's ratio).

Elastic based methods have been largely used on both floating and end-bearing piles (D'Appolonia and Romualdi, 1963; Poulos and Davis, 1968; Poulos and Mattes, 1969; Mattes and Poulos, 1969; Butterfield and Banerjee, 1971; Banerjee and Davies, 1978). The differences between those applications lie in the equations of the shear stress distribution along the pile.

Poulos and Davis (1980) made some modifications to consider the slip at the pile-soil interface, the piles with non-uniform shaft diameters and the case of piles with rigid caps resting on soil surface. Their method can estimate the load distribution along the pile shaft, the load transferred to the pile tip and the settlement of the pile, based on some easily determined parameters (pile diameter and depth, Young moduli of the pile and soil), and some correction factors presented in their textbook. These factors consider, among others, the effect of the relative pile-soil stiffness, the substratum and the Poisson's ratio of the soil layers. In the elastic theory method as suggested by Poulos and Davis (1980), the assumption of floating or end-bearing pile should be initially taken (Figure 1.4). The parameters and equations of the settlement vary accordingly.

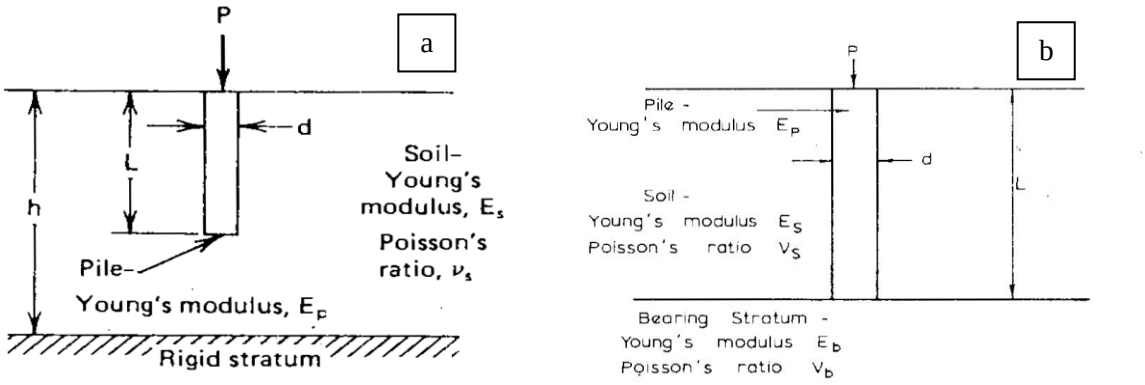

Figure 1.4 Example of (a) floating pile and (b) end-bearing pile (Poulos and Davis, 1980)

The settlement at the top of the pile is calculated as follows:

$$S = \frac{FI}{E_s D} \qquad \text{Eq. 1.44}$$

I is a parameter that includes many correction factors and may be expressed as follows:

$$I = \begin{cases} I_0 R_k R_h R_\upsilon & \text{Floating pile} \\ I_0 R_k R_b R_\upsilon & \text{End-bearing pile} \end{cases} \qquad \text{Eq. 1.45}$$

Where I_0 is a settlement-influence factor and R_k, R_v, R_h and R_b are correction factors for compressibility, Poisson's ratio, depth and base moduli that can be determined from graphs according to the type of the pile. These factors depend among others on K' (defined in Eq. 1.43), the pile length and the pile diameter.

It was shown that the settlement of the pile decreases when its length increases for constant diameter. It increases if the pile is more compressible, i.e., for a lower value of K'. In a floating pile in particular, the settlement decreases for a finite layer, i.e., when L/h is big. On the other hand, the settlement of an end-bearing pile is affected by its slenderness, its compressibility K' and the stiffness of the bearing stratum.

Eq. 1.44 initially calculates the settlement of a pile in a homogeneous soil. However, since this is not always the case, Poulos and Davis (1980) suggested to use the weighted average modulus E_{av} for a non-homogeneous soil with a varying modulus.

$$E_s = E_{av} = \left(\frac{1}{L}\right)\sum_{j=1}^{n} E_i h_i \qquad \text{Eq. 1.46}$$

2-3-3-2- Load transfer method

Another recognized method is the load transfer method (LTM). It was first proposed by Seed and Reese (1957) and Coyle and Reese (1966) and it is based on load transfer curves obtained at different depths of the pile, from instrumented pile load tests or laboratory tests. These curves are called t-z and q-z curves, relating respectively the mobilized unit skin friction to the pile shaft settlement at different depths and the pile end resistance to the pile end displacement.

Contrarily to elastic theory method, the load transfer method is capable of modeling the non-linear behavior of the piles.

In this method, the pile is divided into segments and it was shown that a large number of segments gives better results (Bowles, 1996). It is an uncoupled approach, where the pile-soil interaction is characterized by springs distributed along the pile shaft and at the pile tip and are considered as independent (Figure 1.5). Their behavior can be determined from empirical or theoretical formulas (Eq. 1.47 to 1.49), relating the vertical load at each segment to the mobilized shaft resistance and to the settlement (Coyle and Reese, 1966). Load transfer factors are used to calculate the stiffness of the elastic springs and they usually depend on the pile and the soil characteristics.

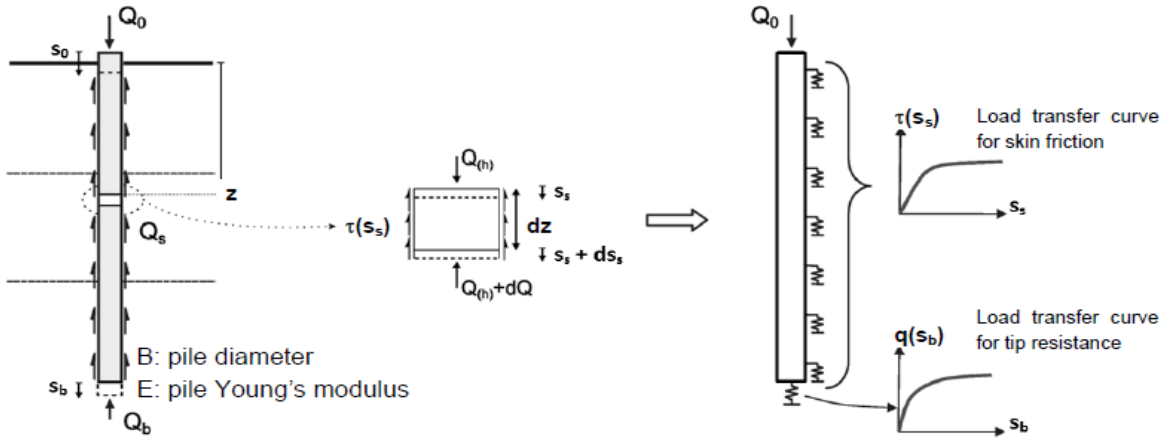

Figure 1.5 Load transfer method and spring mass model for an axially loaded pile (Bohn, 2015)

$$\frac{dQ(z)}{dz} = -\pi\, D\, \tau(s_s(z)) \qquad \text{Eq. 1.47}$$

$$\frac{\mathrm{d}s_s(z)}{dz} = -\frac{Q(z)}{E_p \pi \left(\frac{D}{2}\right)^2} \qquad \text{Eq. 1.48}$$

$$\mathrm{E_p}\, \pi \left(\frac{D}{2}\right)^2 \frac{d^2 s_s(z)}{dz^2} - \pi\, D\, \tau(s_S(z)) = 0 \qquad \text{Eq. 1.49}$$

Considering that load transfer curves are avilable for the shaft and the tip, the settlement of the pile is estimated according to the following procedure:

A tip displacement is assumed and the corresponding curve is used to calculate the load at the tip. The displacement of the first element above the tip is estimated allowing to calculate the unit skin friction by using the appropriate curve. The load transferred by the side shaft is then evaluated. The previous step is repeated for all the pile elements until the top is reached allowing to determine the head load corresponding to the assumed tip movement. This procedure allows the determination of the load-settlement curve of the pile by repeating it for different tip displacement values.

The load transfer behavior in piles varies with the Poisson's ratio and shear modulus of the soil and the pile geometry (Guo, 1997). In the literature, there are available curves that can be used automatically for particular types of piles and soils (Coyle and Reese, 1966 for pipe piles in clay; Coyle and Sulaiman, 1967 for steel piles in sand; Reese et al., 1969 for bored piles in clay). Besides, empirical 1D load transfer curves exist which are based on direct measurements of load and displacement at different depths along the pile (Guo, 1997).

Since pile load tests are not always possible, many authors worked on theoretical load transfer curves for single layered soils (Kraft et al., 1981, Liu et al., 2004). Others have searched for analytical solutions for axially loaded piles embedded in a non-homogeneous soil deposit to get closer to reality (Randolph and Wroth, 1978; Rajapakse, 1990; Lee, 1991; Seo and Prezzi, 2007; Zhang and Zhang, 2012 and Zhang et al., 2014). Load transfer functions can be elastoplastic, bilinear, tri-linear (Frank and Zhao, 1982), exponential (Liu and Meyerhof, 1987), parabolic, softening and hyperbolic models for non-linear behavior (Hirayama, 1990; Zhang et al., 2016)... Although the modeling of nonlinear behavior of the soil was made possible, these methods have some limitations. By using load transfer curves, the displacement of the pile at any point is only related to the shear stress at that point and is independent of the stresses elsewhere in the pile (Poulos and Davis, 1980).

Guo (1997) and Hemaida (2007) gave a broader overview on empirical and theoretical load transfer methods. In this thesis, we will just go through the method developed by Frank and Zhao (1982) which is the most widespread in France for pile settlement estimation.

- The load transfer method as described by Frank and Zhao (1982)

This method uses the pressuremeter moduli (E_M) obtained from PMT to build load transfer curves for different soil layers. These curves are tri-linear as shown in Figure 1.6. The slopes of the branches are calculated according to Table 1.1 and the ultimate values q_b and q_s are determined as suggested by the standards NF P 94-262 (2012).

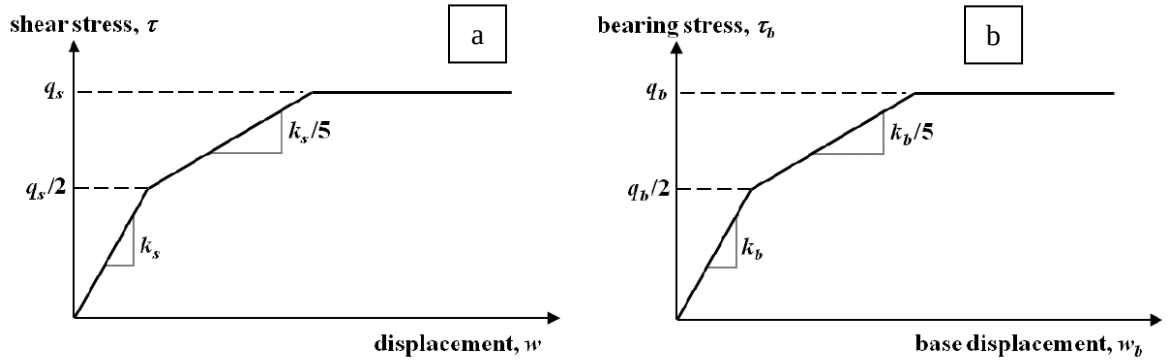

Figure 1.6 Load transfer curves for (a) skin friction and (b) tip resistance based on Frank and Zhao (1982)

Table 1.1 summarizes the different values of stiffnesses k_s and k_b based on the type of soil.

The main advantage of this method is that it is based on the pressuremeter tests that are in general easily performed. It was tested on 90 pile load tests carried out in France and it showed satisfactory outcomes regardless the type of soil (Abchir et al., 2014). It was also implemented in many software such as Foxta for example where friction and base resistance mobilization laws are automatically defined based on the pressuremeter modulus E_M required as an input.

Table 1.1 Slopes of the load transfer curves in the LTM method of Frank and Zhao (1982)

	Shaft friction curve	**End-bearing curve**
Fine soils	$k_s = 2\frac{E_M}{D}$	$k_b = 11\frac{E_M}{D}$
Granular soils	$k_s = 0.8\frac{E_M}{D}$	$k_b = 4.8\frac{E_M}{D}$

2-3-4- Numerical methods

Generally, in analytical methods, a large number of simplifying assumptions are made regarding geometry and material properties. Therefore, the calculated settlements are not accurate. Researchers started using numerical approaches in geotechnical as a means to apply their analytical theories in a computed manner so they can change parameters easily or because of the variety of constitutive models and the complexity of the geometry they offer. Guo (1997) reviewed in details several numerical methods used for single pile analyses and found that the majority of the results were compatible.

- Boundary Element Methods (BEM) may use load transfer functions, described in the previous section, to represent the pile-soil interaction (Coyle and Reese, 1966 based on Seed and Reese, 1957; Randolph, 1986; Kraft et al., 1981). Others are based on elastic continuum theory that represent the soil mass response, by using Mindlin's equation (Butterfield and Banerjee, 1971; Poulos, 1979; Poulos and Davis, 1980; Poulos, 1989), or Chan's solution (Chan et al., 1974).

- The Finite Element Method (FEM) has been largely used in geotechnical engineering in general and in pile foundations in particular. The main advantage of FEM is that even complex constitutive models can be used for soils and piles, provided that the meshes are well developed (Hong et al., 2003). FEM was used by many authors (Ottaviani, 1975; Comodromos et al., 2009; Xue et al., 2011; Alnuaim et al., 2013; Ju, 2015). It was shown that up to a load well beyond half the failure load, the load settlement behavior of piles is linear even though the soil behaves in a non-linear way (Ellison et al., 1971; Desai et al., 1974). Balaam et al., (1975) found a close agreement between the elastic theory (Mindlin's solutions) and the numerical approach. Al-Obaidi et al. (2016) compared a numerical model performed in Plaxis with the theoretical method of Berezantsev et al. (1961) and they also found good agreement.

- The Finite difference method (FDM) is one of the oldest techniques used in science that includes solving differential equations together with boundary and initial conditions (Christian and Desai, 1977). While in FEM, the stress, strain and displacements are defined everywhere and a rigidity

matrix is calculated, in FDM the derivatives are replaced by algebraic expressions written in terms of variation at discrete locations in space only that are reformulated at every step without the need of matrices (Billaux and Cundall, 1993). More details about FDM are shown in Chapter 2.

Although they still can be better than conventional methods, the results of numerical models do not always describe the real behavior of the structure depending on the accuracy of the chosen parameters and constitutive models. It has to be said that the numerical methods by themselves are sometimes not enough. For example, in foundation settlement analysis, these models might require the assignment of unrealistic values of cohesion and friction angle in order to get the expected behavior. For a good and effective use of these tools, it is nowadays recommended to use instrumented static pile load tests to complete it.

3- Axially loaded pile groups

In the majority of the projects, a group of piles is used to transfer the load from the superstructure to the soil instead of a single pile. There is thus a need to evaluate their bearing capacity and axial settlement.

In the literature, there are several approaches used to decide whether the pile-soil-pile interaction is important or not. In fact, the distance between the piles is a very important factor that affects the response of the pile group. If the spacing between the piles is more than 3 times the pile diameter, they behave as individual piles (Reese et al., 2005). On the other hand, other authors consider that the group interaction is not to be considered when spacing exceeds 8 time the pile diameter (CGS, 1992). In France, the bearing capacity of the pile groups should be verified if the axis-to-axis pile spacing is less than 3 times the pile diameter. However, in order to be able to abstain settlement verification, a minimum spacing of 8D is required (Frank et al., 2019).

According to Geotechnical Engineering Office (2007), the behavior of pile group is influenced among others by the pile installation method, the load transfer mode, the nature of the substratum and the pile-soil relative stiffness. It is also affected by the presence or not of a pile cap and its characteristics if present. In other words, if the load is symmetrical and the pile cap is rigid, all the piles will settle in the same amount whereas it is not the case if it is flexible. In addition, if the cap rests on the ground surface, the bearing pressure on the cap will sustain a part of the load, which is not always easily evaluated. However, as soon as the ground begins to settle, this contact may be lost and the load will be taken then by the piles exclusively (Reese et al., 2005).

We will consider in the following, a general layout of a pile group with (n_1 x n_2) piles as in Figure 1.7.

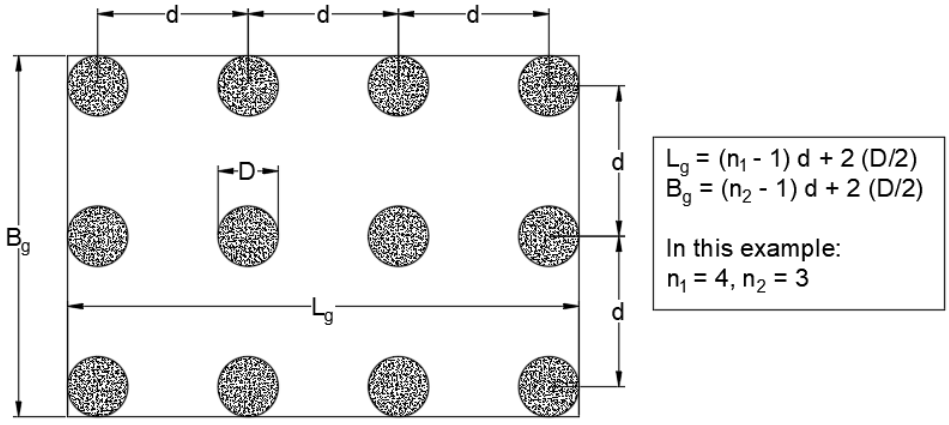

Figure 1.7 General plan view of a pile group

3-1- Ultimate axial capacity and efficiency of pile groups under axial load

Due to the pile-soil-pile interaction that may occur if the piles are closely spaced, there is a high need to evaluate the efficiency of these piles, in order to determine whether the piles are reacting to the loading individually or as a group.

The bearing capacity of a pile group is generally different from the sum of the capacities of the individual piles. This is caused by the overlapping of stresses in the zone between the foundations, affecting not only a bigger radius around the piles but also the soil at a higher depth (Figure 1.8). In these cases, the soil contributes as well to the load transfer mechanisms.

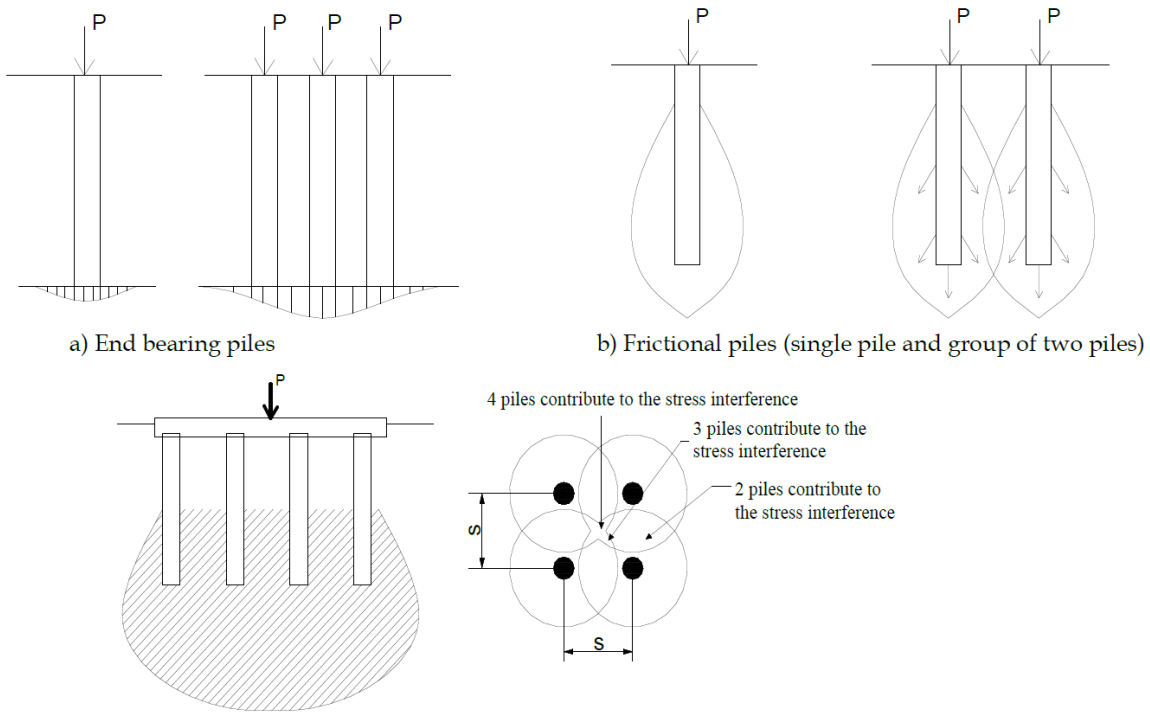

Figure 1.8 Interferences of stresses in pile groups (Tuan, 2016)

Different failure mechanisms are available as shown in Figure 1.9. It should be noted that for granular soils, the three failure mechanisms need to be checked.

The concept of block failure consists in creating an imaginary block (Figure 1.9-c). The ultimate load is calculated as the sum of the friction on the perimeter of the block and the load carried by its base. In this case, the axial capacity may be calculated similarly to individual piles, by using the base area of the block as A_b and the block surface area as A_s in Eq. 1.2. The minimum settlement needed to mobilize the base capacity of the block is 5 to 10% of the breadth B_g (Figure 1.7) of the group (Fleming et al., 2008). In general, this failure mode occurs when the ratio q_b/q_s is small like for clays.

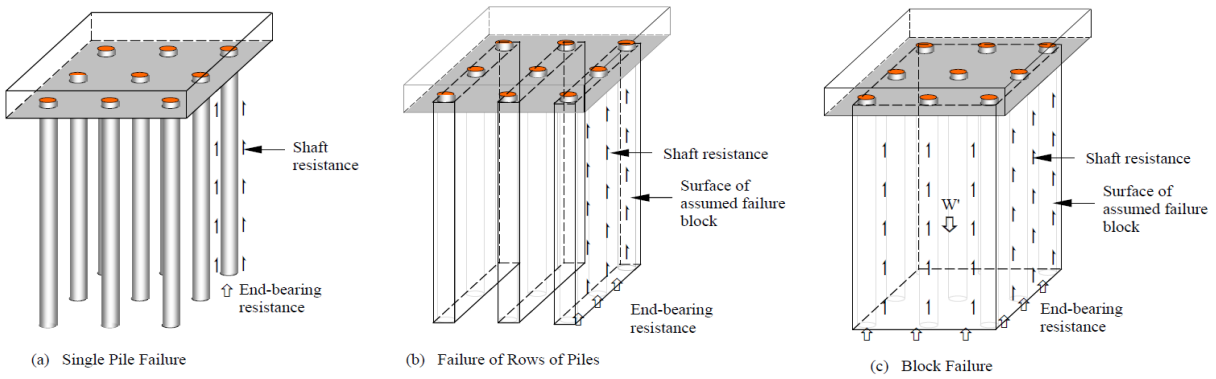

Figure 1.9 Failure mechanisms of Pile groups (Fleming et al., 2008 as cited in Geotechnical Engineering Office, 2006)

On the other hand, a group efficiency (or reduction) factor η is defined as the ratio between the ultimate bearing capacity of the pile group and the sum of the ultimate bearing capacity of individual piles.

$$\eta = \frac{R_{gu}}{n\,R_{iu}} \qquad \text{Eq. 1.50}$$

- Pile groups in granular soils

Generally, in driven piles, the group efficiency is higher than 1 due to the soil densification that may likely occur. As an example, Vesić (1969) suggests a factor of 3. For the sake of safety, designers tend to consider a factor of unity unless the pile is driven in very dense sands, where the dilatancy phenomenon may cause its increase.

In bored piles, the group efficiency is much lower due to loosening and disturbance of granular soils that comes with their construction. This factor is 2/3 in Meyerhof (1976) and 0.7 in O'Neill (1983). It may be assumed as 0.85 in floating piles and 1 in end-bearing piles.

- Pile groups in cohesive soils

Based on cases of pile groups in clay investigated by many researchers, it can be concluded that the group efficiency depends on the spacing, the number and the length of piles and is usually less than unity (De Mello, 1969; O'Neill, 1983). It is higher in stiff clays than in soft clays and it can be higher than unity if the cap is in contact with the soil. The probability of failure of pile group becomes important if the pile spacing is less than two pile diameters (De Mello, 1969). The capacity of a pile group in clay is calculated as the minimum of the sum of the ultimate capacity of individual piles and the capacity of the group acting as a block as defined previously. It is recommended to use a large fictive pile if the spacing between the piles is smaller than 3 times the pile diameter. Otherwise, Converse-Labarre formula can be used if the spacing is up to 8 times the diameter (Frank, 1999).

The capacity of pile groups in all type of soils have been studied and analyzed all over the years using many empirical and analytical methods (Converse-Labarre method, Los Angeles group action method and Seiler and Keeney, 1944 as cited in Das, 2007). However, in these methods, some discrepancies were found because they overlook many parameters such as the pile installation method, its pile length and the soil characteristics (O'Neill, 1983).

Some of the equations that calculate group efficiency of friction piles are presented in the following.

- Converse-Labarre equation

$$\eta = 1 - \left[\frac{(n_1 - 1)\, n_2 + (n_2 - 1)\, n_1}{90\, n_1 n_2}\right]\theta \quad ; \quad \theta(deg) = \tan^{-1}(\mathrm{D/d}) \qquad \text{Eq. 1.51}$$

Where n_1 and n_2 are non-zero values that represent the number of piles in each direction.

In France, Converse-Labarre equation is used to reduce the ultimate skin friction as follows:

$$R_{gu} = n_1 * n_2 (R_b + \eta R_s) \qquad \text{Eq. 1.52}$$

- Los Angeles Group Action equation

$$\eta = 1 - \frac{D}{\pi\, d\, n_1 n_2}[n_1(n_2 - 1) + n_2(n_1 - 1) + \sqrt{2}(n_1 - 1)(n_2 - 1)] \qquad \text{Eq. 1.53}$$

Another method was suggested by Tuan (2016) to estimate the ultimate axial capacity of a group piles when they act as a block. Firstly, it calculates the efficiency η_S of the skin friction part, as in Eq. 1.54.

$$\eta_S = \frac{q_s[2(n_1 + n_2 - 2)d + 4D]L}{n_1 n_2 P L q_s} = \frac{2(n_1 + n_2 - 2)d + 4D}{n_1 n_2 P} \qquad \text{Eq. 1.54}$$

Another component was suggested to calculate the group efficiency related to pile tip η_b, as follows:

$$\eta_b = \begin{cases} 0.5 + 0.05\ (d/D) & 1 \le d/D \le 5 \\ 1 & d/D > 5 \end{cases} \qquad \text{Eq. 1.55}$$

The average of both values is then determined allowing the calculation of the ultimate axial capacity of the pile group.

$$\eta = \frac{\eta_s + \eta_b}{2} = \frac{1}{2}\left[\frac{2(n_1 + n_2 - 2)d + 4D}{n_1 n_2 P} + \eta_b\right] \qquad \text{Eq. 1.56}$$

$$R_{gu} = \eta\ (n\ R_{iu}) = \frac{1}{2}\left[\frac{2(n_1 + n_2 - 2)d + 4D}{n_1 n_2 P} + \eta_b\right]\ (n\ R_{iu}) \qquad \text{Eq. 1.57}$$

3-2- Settlement analysis of pile groups

The settlement of a pile group subject to a given load per pile is generally larger than the settlement of a single pile under the same load. In the literature, various approaches exist to evaluate this settlement.

3-2-1- Elastic and consolidation settlement of pile groups (Vesić, 1969)

- Elastic settlement of pile groups $S_{G(e)}$

Elastic settlement is the immediate settlement of the pile group under service working load. The ratio of immediate to total settlement in pile groups is less than that for a single pile. It is in the range of two-third to three-quarter for typical friction pile group configurations in granular soils (Poulos and Davis, 1980).

It may be expressed by the following equation.

$$S_{G(e)} = \sqrt{\frac{B_g}{D}} S_e \qquad \text{Eq. 1.58}$$

Where S_e is the settlement of each pile at a comparable working load.

- Consolidation settlement of pile groups $S_{c(i)}$

This method assumes that the load is transmitted to the soil starting from a depth of 2L/3 from the top of the pile. The consolidation settlement of each layer "i" is calculated by the following equation:

$$S_{c(i)} = \frac{\Delta e(i)}{1 + e_0(i)} H_i \qquad \text{Eq. 1.59}$$

Where H_i is the thickness, $e_0(i)$ is the initial void ratio and $\Delta e(i)$ the change of void ratio caused by the stress increase in layer i.

The total consolidation settlement of a pile group is then calculated as the sum of the components calculated in each layer.

3-2-2- Simplified approaches based on 1D consolidation theory

3-2-2-1- Equivalent raft method

This is a very simplified method that consists in substituting the pile group by a fictive equivalent flexible raft foundation (Randolph, 1994). The position of the raft strongly depends on the soil layers as shown in Figure 1.10 and its area is calculated based on the pile length and the embedment in the rigid stratum.

In France, the standard NF P 94-262 (2012) suggests using the method of Terzaghi. It assumes a raft with an area equal to the pile group section located at two third of the total pile length from the top of the pile group. Frank (1999) has proposed a diffusion ratio of 1:2 under this raft which defines the affected zone under this raft.

Based on these assumptions, the settlement of this fictive raft can now be calculated using either elastic or consolidation theory for granular and cohesive soils respectively. It should be added to the elastic compression of the pile's section located above the raft, in order to obtain the total settlement of the pile group (Viggiani et al., 2012).

Equivalent raft method does not take the influence of pile spacing into account and it gives only a rough estimate of the pile group settlement especially for complex geometries or non-uniform loads (Geotechnical Engineering Office, 2006).

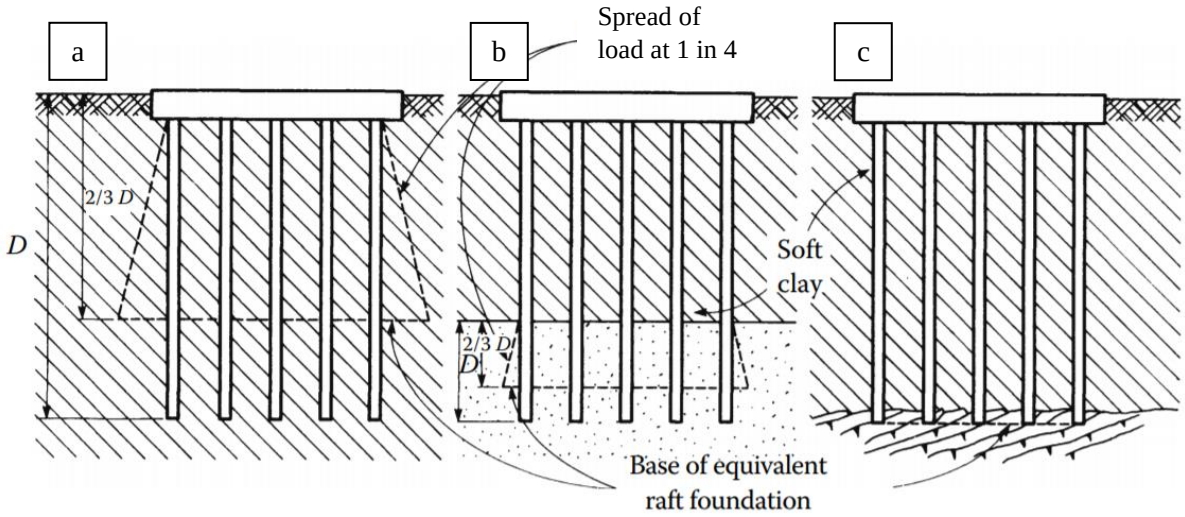

Figure 1.10 Equivalent raft method applied on: (a) friction piles in dense granular soil; (b) piles with combined shaft friction and end bearing in stratum of dense granular soil; (c) end bearing piles on hard rock stratum (Tomlinson and Woodward, 2014)

3-2-2-1- Equivalent pier method

The equivalent pier method consists in replacing the pile group by an equivalent pier that has the same length and an equivalent diameter. The settlement of the pier is then determined similarly to single piles. In opposition to the previous method, the equivalent pier approach is the best used when the breadth of the group is smaller than its length (Poulos and Davis, 1980 as cited in Viggiani et al., 2012). The modulus of the pier should be calculated in this case as the weighted average between pile and soil moduli (Bohn, 2015).

3-2-3- Empirical approaches

Empirical formulas were developed by several researchers in order to quantify the interaction between piles in a group. Two new ratios were suggested, relating the average settlement of a pile group S_g to the settlement S of a single pile when the latter is subject to a load equal to the average load per pile in the group.

These ratios satisfy the following equations:

$$S_G = R_S S = n R_G S \quad \text{Eq. 1.60}$$

$$R_S = n\,R_G \quad ; 1/n \leq R_G \leq 1 \quad \text{Eq. 1.61}$$

- The group settlement ratio R_S

$$R_S = \frac{Average\ group\ settlement}{Settlement\ of\ single\ pile\ at\ same\ average\ load\ as\ a\ pile\ in\ the\ group} \quad \text{Eq. 1.62}$$

- The group reduction factor R_G

$$R_G = \frac{Average\ group\ settlement}{Settlement\ of\ single\ pile\ at\ same\ total\ load\ as\ the\ group} \quad \text{Eq. 1.63}$$

3-2-4- Analytical methods

It was found that the conventional load transfer method is not suitable for pile groups. Therefore, Poulos (1968) was the first to introduce the interaction factor "α" in a two-pile interaction analysis before it was used by others (Randolph and Wroth, 1979a; Poulos and Davis, 1980; Mandolini and Viggiani, 1997).

$$\alpha = \frac{additional\ settlement\ caused\ by\ an\ adjacent\ pile}{settlement\ of\ pile\ under\ its\ own\ load} \quad \text{Eq. 1.64}$$

For floating piles, there are charts relating the pile group interaction factor to the spacing between the piles "d" for several values of slenderness ratio and K' (defined in Eq. 1.43). It can be seen that the interaction factor decreases with increasing spacing and with decreasing L/D and K' (Poulos and Mattes, 1971). For end-bearing piles, this factor decreases with increasing spacing, L/D and K'. It is proven that no interaction occurs when K' approaches infinity.

Many adjustments were done in order to take into account the effect of finite layers, an enlarged pile tip, the variation of Poisson's ratio, a nonuniform soil modulus and a finite compressibility of bearing stratum (Poulos and Davis, 1980).

Several analytical methods based on elastic continuum approaches are available in the literature. They can either use closed analytical solutions (Randolph and Wroth, 1978; Randolph and Wroth, 1979a) or boundary element methods (Poulos, 1968; Poulos and Davis, 1980; Caputo, 1984).

In the following, only two of these methods will be explained.

- The method by Poulos and Davis (1980)

In the framework of the elastic theory, a method was developed to address general cases including more than two piles, regardless of their number, provided that they are symmetrical, equally spaced and carry the same load. The concept of superposition of interaction factors is applied and the piles are considered to be free-standing. Thus, this superposition principle may be concretized by the following generalized formula that calculates the settlement of the pile "k" based on the interaction taking place with nearby piles. For a group of "n" identical piles, "n" equations of this type can be written.

$$S_k = S \sum_{j=1, j\neq k}^{n} (F_j \, \alpha_{kj}) + S \, F_k \qquad \text{Eq. 1.65}$$

Where S is the displacement of a single pile under unit load, F_j and F_k are the loads applied to piles "j" and "k" and α_{kj} is the interaction factor between them.

In any pile group, the total load may be calculated as in Eq. 1.66.

$$F_G = \sum_{j=1}^{n} F_j \qquad \text{Eq. 1.66}$$

The settlement of the piles in the group is evaluated by solving these "n+1" equations. To do so, an assumption should be made:

- Equal loads for a flexible cap
- Equal settlements for a rigid cap

For most cases, especially when the piles are symmetric and equally loaded, the average settlement of the pile group is equal to that of a group with a rigid cap.

Charts are used to determine the interaction factors according to values of d/D, L/D and K' reflecting the spacing, the slenderness and the stiffness of the pile group. It was noticed in these charts that the longer and the more deformable the piles are, the more they interact with each other. For floating piles, a higher pile-soil stiffness ratio leads to higher interaction effects. Besides, it was shown that the settlement increases due to piles interaction in floating piles is higher than that in end-bearing piles.

- The method by Randolph and Wroth (1978, 1979a) as cited in (Bohn, 2015)

Another method for determining the settlement of pile groups was proposed by Randolph and Wroth (1978, 1979a) in which the concept of interaction factors for equally loaded rigid piles was modified. The authors defined a closed-form solution that evaluates the radial distribution of shear stresses around the pile. A magical radius r_m was defined as the minimum distance from the center of the pile after which the shaft skin stress induced by the pile becomes negligible. The expressions differ from a homogeneous to a non-homogeneous soil.

- For a homogeneous or Gibson soil (with E varying linearly with depth):

$$r_m = 2.5\ L\ (1 - \nu_s) \qquad \text{Eq. 1.67}$$

For a single pile in a homogeneous soil, the settlement of the pile shaft due to skin friction S_s and the settlement of the tip S_b, are calculated using the following equations:

$$S_s = \frac{q_s(D/2)}{G_s} ln\left(\frac{r_m}{(D/2)}\right) \qquad \text{Eq. 1.68}$$

$$S_b = \frac{F_b(1-\nu)}{4\left(\frac{D}{2}\right)G_s} \qquad \text{Eq. 1.69}$$

The total settlement of the pile in a homogenous elastic soil is then calculated as follows:

$$S = \frac{\frac{F}{\left(\frac{D}{2}\right)G_s}}{\frac{4}{1-\nu_s} + \frac{2\pi\ L}{\left(\frac{D}{2}\right)\ln\left(\frac{r_m}{(D/2)}\right)}} \qquad \text{Eq. 1.70}$$

In order to take into consideration, the case of two identical piles with a spacing "d" subject to equal load "F", the following equations of the settlement may be used.

$$S_{sG} = \frac{q_s(D/2)}{G_s}\ln\left(\frac{r_m}{(D/2)}\right)\left[1 + \frac{\ln\left(\frac{r_m}{s}\right)}{\ln\left(\frac{r_m}{(D/2)}\right)}\right] = S_s\left[1 + \frac{\ln\left(\frac{r_m}{s}\right)}{\ln\left(\frac{r_m}{(D/2)}\right)}\right] \qquad \text{Eq. 1.71}$$

$$S_{bG} = \frac{F_b(1-\nu)}{4\left(\frac{D}{2}\right)G}\left(1 + \frac{2(D/2)}{\pi d}\right) = S_b\left(1 + \frac{2(D/2)}{\pi d}\right) \qquad \text{Eq. 1.72}$$

$$S_G = \frac{\frac{F}{\left(\frac{D}{2}\right)G_s}}{\frac{4}{1-\nu_s}\ \frac{s}{\frac{2}{\pi}\left(\frac{D}{2}\right)+S} + \frac{2\pi L}{\left(\frac{D}{2}\right)\left[\left(\frac{r_m}{(D/2)}\right)+\ln\left(\frac{r_m}{d}\right)\right]}} \qquad \text{Eq. 1.73}$$

- For a non-homogeneous soil (Lee, 1993 as cited in Zhang and Zhang, 2012):

$$r_m = 2.5L\ \rho_m\left(1 - \nu_{avg}\right) \qquad \text{Eq. 1.74}$$

$$\rho_m = \frac{\sum_{i=1}^{n_s} G_{si}h_i}{G_{sm}L} \qquad \text{Eq. 1.75}$$

$$\nu_{avg} = \frac{\sum_{i=1}^{n_s} \nu_i h_i}{L} \qquad \text{Eq. 1.76}$$

Where i is the layer index, ρ_m the modified inhomogeneity factor and G_{sm} the maximum shear modulus of the soil layers.

Other equations exist in the literature for end-bearing piles (Randolph and Wroth, 1979b as cited in Lee, 1991).

3-2-5- Numerical methods

Several researchers have developed numerical approaches that help analyzing the behavior of pile groups.

- Based on the same approaches used for singles piles, BEM was used by may authors as summarized by Butterfield and Douglas (1981). Another method is based on the non-linear behavior of soil below yield was validated later by Mandolini and Viggiani (1997) via a BEM analysis on a batch of pile load tests.
- In the discrete element analysis (Chow, 1986b), the piles are modeled using discrete elements and the interaction occurs only between two segments of the same layer because the layers are independent. This is called a layer model. However, in a hybrid load transfer approach, the interaction is possible between the layers, and it is called the continuum model (Figure 1.11-b).
- The infinite layer approach (Guo et al., 1987; Cheung et al., 1988) consists in representing each soil layer by an infinite layer element and the pile by a solid bar. In every step, one pile is subject to a load while the second is replaced by a soil column of the same properties as the surrounding soil. The force acting along pile 2 is calculated as the induced settlement multiplied by its stiffness. Residual forces are then calculated as the difference between the force on the pile and that calculated from infinite layer model and are hence applied in the opposite direction along pile 2 to maintain equilibrium, while pile 1 is now replaced by a soil column. This procedure is repeated until the displacement of both piles become negligible (Figure 1.11-a).

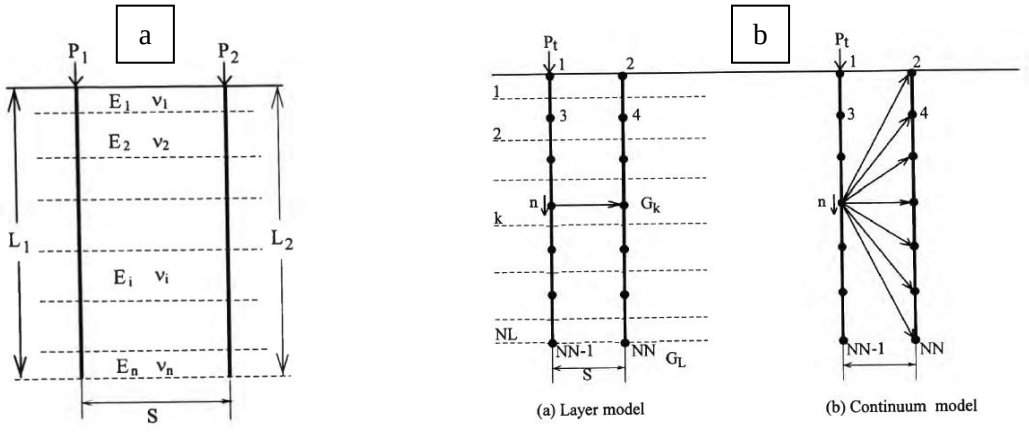

Figure 1.11 Pile discretization methods: (a) Guo et al. (1987) and (b) Chow (1986a)

- Randolph (2003) developed a methodology through a program named RATZ to predict the behavior of pile groups. In this method, a parabolic or hyperbolic load transfer curve describes the behavior of single piles and the group effects are considered by multiplying the elastic part of this curve determined from Randolph and Wroth (1979a), by the group settlement R_s and by adding the non-linear component to it afterwards. Figure 1.12 shows the load transfer curves for a single pile and pile group.

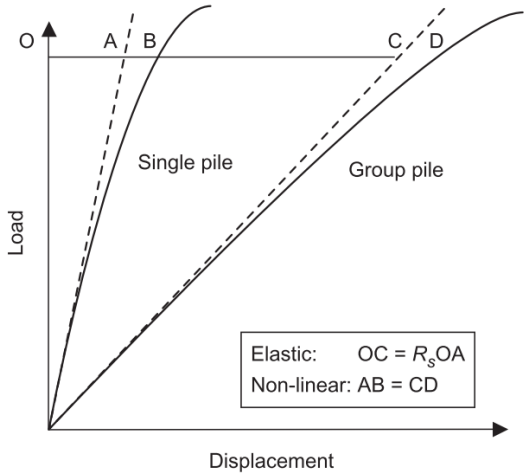

Figure 1.12 Calculations of a non-linear transfer response (Fleming et al., 2008)

4- Soil constitutive models

The soil consists of a solid skeleton of grains in contact with each other surrounded by air and water. When subject to a load, the soil behaves in a complex way since its three components obey different laws. This makes it difficult to establish a behavioral model that is reliable for the actual reaction of the soil. Usually, laboratory tests help to determine the necessary parameters and in geotechnical engineering, the triaxial and isotropic compression tests are mainly used. A constitutive law describes the variation of the deformations as a function of variations in the stress sensor and it has the following form:

$$\sigma_{ij} = F(\varepsilon_{ij}) \qquad \text{Eq. 1.77}$$

It is essential, while modeling deep foundations problems to find a constitutive law capable of describing the behavior of the soil at small strains, which is characterized by stiffness variation. Lade (2005) presented an overview of the majority of the available models in the literature with their attributes and capabilities.

In the following paragraph, some models are explained in details.

4-1- Elastic models

4-1-1- Linear elastic behavior (Hooke's law)

A material is linear elastic if it is deformed by a stress and then returns to its initial state when this stress ceases to be applied. The relationship between the stress and the elastic deformation tensors is linear (Eq. 1.78). Moreover, the state of stress depends only on the state of deformation and vice versa and therefore, the history of loads applied to a soil does not affect its behavior.

$$\sigma_{ij} = C_{ijkl}\,\varepsilon_{kl} + \sigma_{ij}^{0} \qquad \text{Eq. 1.78}$$

Where σ_{ij} and ε_{kl} are second order tensor and C_{ijkl} is a fourth order tensor.

If σ_{ij}^{0} is zero which is the stress state at an initial state of null deformation, this equation becomes as follows:

$$\sigma_{ij} = C_{ijkl}\varepsilon_{kl} \qquad \text{Eq. 1.79}$$

This relation can be expressed in terms of:

- Young modulus and Poisson's ratio:

$$\sigma_{ij} = \frac{E}{(1+\nu)}\varepsilon_{ij} + \frac{\nu E}{(1+\nu)(1-2\nu)}\varepsilon_{kk}\delta_{ij} \qquad \text{Eq. 1.80}$$

$$\varepsilon_{ij} = \frac{1+\nu}{E}\sigma_{ij} - \frac{\nu}{E}\sigma_{kk}\delta_{ij} \qquad \text{Eq. 1.81}$$

- Bulk and shear moduli:

$$K = \frac{E}{3(1-2\nu)} \qquad \text{Eq. 1.82}$$

$$G = \frac{E}{2(1+\nu)} \qquad \text{Eq. 1.83}$$

The linear elastic model will be used for concrete structures (piles, transfer structure, raft foundation…), since a linear elastic behavior is expected under working loads.

In the literature, an inadequacy of this model has emerged mainly by comparing theoretical calculations with experimental results, especially when approaching failure (Lade, 2005). Lade gave examples that prove how the matrix used in elastic calculation cannot always be representative of soil behaviors. In fact, according to this theory, normal strains are caused by normal stresses only and the same is applicable for shear stresses and strains. However, experience shows that when the soil is subject to shear stresses, it may expand, i.e., the normal (and volumetric strain) increases and on the other hand, shear strain increments can result from changes in normal stress. Therefore, models based on a non-linear elastic behavior were developed to get closer to real behavior of soils.

4-1-2- Non-linear behavior (Hyperelastic and hypoelastic models)

Among others, examples include hyper-elastic, also called Green elastic (Boyce, 1980; Cambou and Jafari, 1988) and hypo-elastic models such as the hyperbolic models (Duncan and Chang, 1970; Hardin and Drnevich, 1972). These two types differ from each other by the way they are formed. While in a hyper-elastic material the stress-strain law derives from a strain energy density function, hypo-elastic models relate the stress increment not only to the strain increment but also with the actual stress (Eq. 1.84).

$$d\sigma_{ij} = C_{ijkl}\,(\sigma_{mm})\,d\varepsilon_{kl} \qquad \text{Eq. 1.84}$$

Where C_{ijkl} is the tangent behavior tensor.

A hyperbolic stress-strain relation as shown in Figure 1.13 characterizes the hyperbolic models, as follows:

$$\sigma_1 - \sigma_3 = \frac{\varepsilon_1}{a + b\varepsilon_1} \qquad \text{Eq. 1.85}$$

Where ε_1 is the axial deformation and the coefficients a and b are determined by a simple triaxial test.

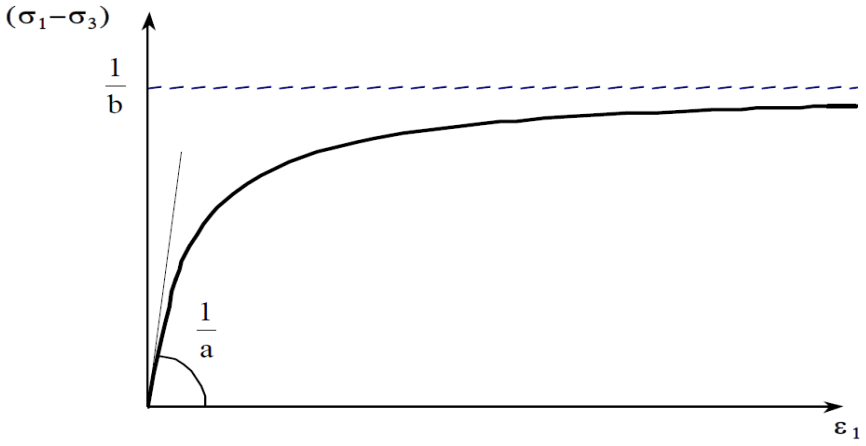

Figure 1.13 Hyperbolic law (Kondner, 1963)

The initial tangent Young modulus may be expressed as follows:

$$E_i = \frac{d(\sigma_1 - \sigma_3)}{d\varepsilon_1} = \frac{a}{(a + b\varepsilon_1)^2} = \frac{1}{a} \quad \text{Eq. 1.86}$$

This equation was later developed by Duncan and Chang (1970) to express a stress-dependent stiffness as in Eq. 1.87.

$$E_i = K_h P_a \left(\frac{\sigma_3}{P_a}\right)^n \quad \text{Eq. 1.87}$$

Where P_a is the atmospheric pressure and K_h and n are parameters obtained from drained triaxial tests.

This model considers the Mohr-Coulomb failure criterion in Eq. 1.88. Therefore, the equation of the tangent modulus becomes as follows:

$$\left(\sigma_1 - \sigma_3\right)_f = \frac{2(c\cos\phi + \sigma_3 \sin\phi)}{1 - \sin\varphi} \quad \text{Eq. 1.88}$$

$$E_t = E_i \left(1 - \frac{\sigma_1 - \sigma_3}{\left(\sigma_1 - \sigma_3\right)_{ult}}\right)^2 = K_h p_a \left(\frac{\sigma_3}{p_a}\right)^n \left[1 - \frac{R_f(1 - \sin\phi)(\sigma_1 - \sigma_3)}{2(c\cos\phi + \sigma_3 \sin\phi)}\right]^2 \quad \text{Eq. 1.89}$$

A new parameter R_f is then defined as the ratio between the deviatoric stress at failure and the asymptotic one.

$$R_f = \frac{(\sigma_1 - \sigma_3)_f}{(\sigma_1 - \sigma_3)_{ult}} \quad \text{Eq. 1.90}$$

In fact, the Duncan-Chang model serves as a basis for the Plastic Hardening model that will be presented in Section 4-2-3.

4-2- Plastic models

4-2-1- Definition of plastic behavior

In opposition to elasticity, plasticity is the term used when irreversible deformations occur in a material subject to stress. The total deformation tensor has in fact two components as follows:

$$\varepsilon = \varepsilon^e + \varepsilon^p \quad \text{Eq. 1.91}$$

Any model describing the behavior of a material should have a linear or a non-linear elastic law and a plastic law characterized by a yield surface, a flow rule and a hardening rule.

- Yield surface:

It is also known as the plasticity criterion and it represents the limit of the elastic range in the stress space. Above this limit, the behavior of the material becomes irreversible. The yield surface is a scalar function f that depends on the stress state and the hardening parameters as in Eq. 1.92 and 1.93.

$$f(\sigma_{ij}, R) = 0 \qquad \text{Eq. 1.92}$$

$$\begin{cases} f < 0 \ \text{Elastic domain} \\ f > 0 \ \text{Impossible domain} \\ f = 0 \ \text{The state of stress is on the boundary of the elastic domain} \end{cases} \qquad \text{Eq. 1.93}$$

- Flow rule

It is an expression of the variation of plastic deformation as a function of stress and strain variations. It shows how the plastic deformation evolves. Based on the principle of maximum plastic work described by Hill (1950), at any point of the border the Eq. 1.94 is applicable.

$$\dot{\varepsilon^p} = \dot{\lambda}\frac{\partial f}{\partial \sigma} \qquad \text{Eq. 1.94}$$

Where $\lambda \geq 0$ is called a plastic multiplier.

In this case, the deformation rate is normal to the yield surface and the law is called associated. However, for soils, experience does not validate this principle. Hence the need to introduce a new plastic potential g with a new concept, which is the flow rule that corresponds to a non-associated law as follows:

$$\dot{\varepsilon^p} = \dot{\lambda}\frac{\partial g}{\partial \sigma} \qquad \text{Eq. 1.95}$$

This considers the dilatancy of the material.

- Hardening rule

For some types of soils, experience showed that when the state of stress is on the yield surface, this latter tends to change during the loading. It is called hardening when the surface increases or softening in the opposite case. This surface depends thus on the stress and the deformation of the material. The hardening can have different aspects. They are presented in Figure 1.14.

- Isotropic hardening: the yield surface undergoes a change in size controlled by a scalar variable
- Kinematic hardening: the yield surface undergoes a rotation, translation or distortion controlled by a tensor of second or fourth order
- Mixed hardening: the yield surface can undergo rotation and deformation at the same time

Plenty of models were developed in the literature. Some were used for metals and others for coherent or cohesionless soils. They can be elastic perfectly plastic models, elastoplastic models with hardening, critical state models, bounding surface models, multisurface models, double hardening models…

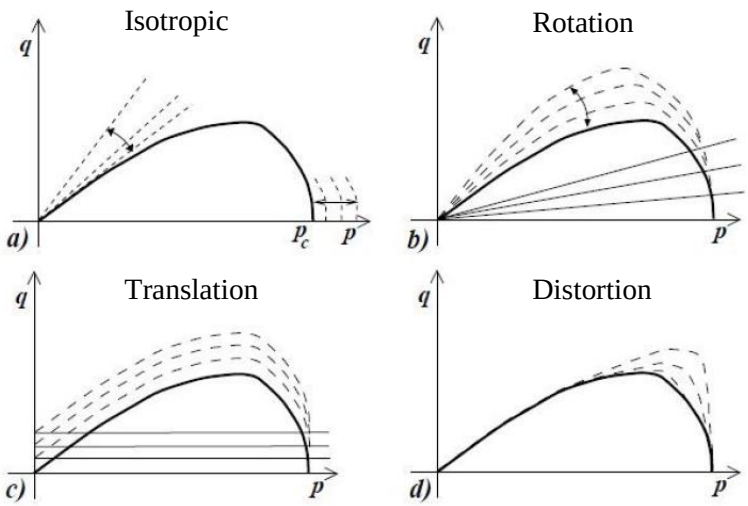

Figure 1.14 Different types of hardening (Jeremic et al., 2009 as cited in Foucault, 2010)

4-2-2- Elastic perfectly plastic model – Mohr-Coulomb (MC) failure criterion

In this model, the yield surface depends only on the state of stress. It is fixed in the stress space and represents a failure criterion at the same time. In the literature, many failure criteria are available: Tresca, Von Mises, Mohr-Coulomb, and Drucker Prager… They do not represent the hardening property of the material and cannot be used for cyclic loadings. Plastic deformations are possible only on the peak level or if the final stress level is reached.

In particular, Mohr-Coulomb model joined Hooke's elastic law with Coulomb's failure criterion dating from 1776 which is presented in Eq. 1.96 and 1.97.

$$\tau = \sigma_n \, tan\phi + c \qquad \text{Eq. 1.96}$$

$$f = \sigma_1 - \sigma_3 + (\sigma_1 + \sigma_3) \, sin\phi - 2c \, cos\phi \qquad \text{Eq. 1.97}$$

The stress-strain curve has a linear elastic section that has as a slope the Young's modulus E and a perfectly plastic section for yield. By drawing the failure criterion in the (σ_n, τ) plane, it is possible to determine the friction angle and the cohesion as the slope of the line and the y-intercept respectively based on Eq. 1.96. Other parameters are obtained by triaxial tests as shown in Figure 1.15.

Computations with this model are relatively fast since the stiffness is constant. It can be used for all types of soils and it is generally considered as a first approximation of real soil behavior. One main advantage of this model is its simplicity of formulation. It consists of only five parameters: ϕ, c, E, ν and ψ, which are easily determined by simple drained triaxial tests.

The drawback of the Mohr-Coulomb model is that it assigns a constant stiffness to the material so that there is no difference between initial loading and unloading-reloading and it also cannot reproduce strain-dependent stiffness behavior. For example, while studying examples of deep excavation in the sand, it was shown that the deformation modulus was underestimated at small loads where the strain was too small.

Besides, even at larger strain levels, this model was not suitable because it was not able to consider unloading stiffness during excavations (Brinkgreve et al., 2006; Schweiger, 2009; Khoiri and Ou, 2013; Hsiung and Dao, 2014). On the other hand, it is not able to describe the behavior of the soils under cyclic loading.

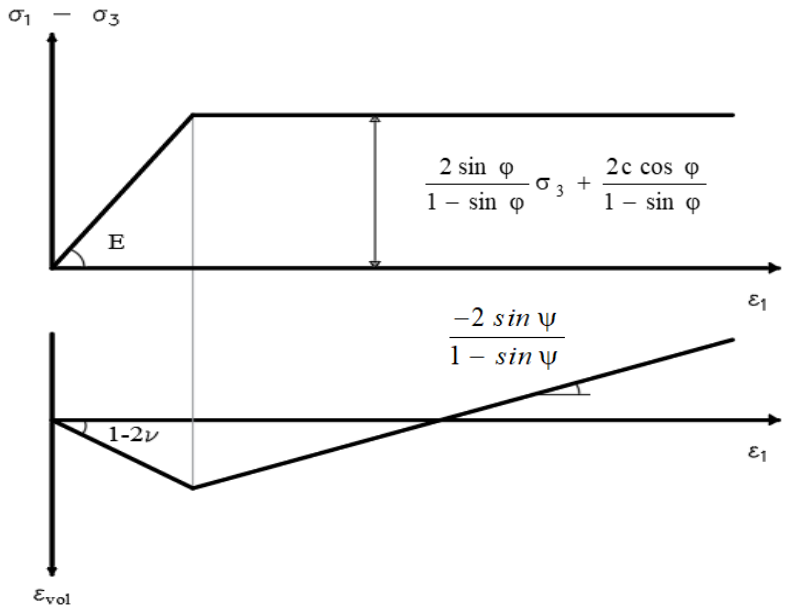

Figure 1.15 Mohr-Coulomb failure criterion based on triaxial test results

4-2-3- Plastic Hardening Soil Model (PH)

Experience showed that the soil's response is nonlinear even at small loads. In the framework of the classical theory of plasticity, an advanced isotropic non-linear elastoplastic model was formulated by Schanz et al. (1999). It is the hardening soil model which uses Mohr-Coulomb as a failure criterion and is characterized by a hyperbolic stress-strain relationship based on the hyperbolic model of Duncan and Chang (1970). The PH model supersedes Duncan-Chang model because it uses the theory of plasticity and it can reflect the soil dilatancy during shearing. Besides, the yield surface can expand due to plastic straining and two types of hardening: the shear and compression hardening (Schanz et al., 1999). Therefore, two independent yield criteria can also be defined.

The following description of the PH model and the determination of its parameters is based on the standard drained triaxial test so all stresses are effective. Stress components are positive in tension.

- Definition of the stiffness moduli

The stiffness of the soil depends on the stress level via a power law defined by the parameter m. Three different stiffness parameters are therefore defined as follows:

- Triaxial stiffness modulus for primary deviatoric loading (E_{50}) which is used instead of the initial modulus E_i to describe the shear hardening for small strains

$$E_{50} = E_{50}^{ref}\left(\frac{c\ cot\phi - \sigma_3}{c\ cot\phi + p_{ref}}\right)^m \quad \text{Eq. 1.98}$$

- Triaxial stiffness modulus for unloading/reloading (E_{ur}), knowing that this path is purely elastic. In this case, the elastic strains are calculated based on the following equations.

$$E_{ur} = E_{ur}^{ref}\left(\frac{c\ cot\phi - \sigma_3}{c\ cos\phi + p_{ref}}\right)^m \quad \text{Eq. 1.99}$$

$$G_{ur} = \frac{E_{ur}}{2(1+\nu_{ur})} \quad \text{Eq. 1.100}$$

$$\varepsilon_1^e = \frac{q}{E_{ur}};\ \varepsilon_2^e = \varepsilon_3^e = \nu_{ur}\frac{q}{E_{ur}} \quad \text{Eq. 1.101}$$

- Tangent stiffness modulus for primary compressive loading (E_{oed}), used to describe the compression hardening

$$E_{oed} = E_{oed}^{ref}\left(\frac{\sigma_1 + c\ cot\phi}{p_{ref} + c\ cot\phi}\right)^m \quad \text{Eq. 1.102}$$

Where E_{50}^{ref}, E_{ur}^{ref} and E_{oed}^{ref} are reference stiffness moduli corresponding to the reference stress p_{ref}, considered generally equal to 100 kPa or determined by the means of drained triaxial tests calibrated on a numerical program such as FLAC3D.

- Shear yield criterion and flow rule

The hyperbolic stress-strain relationship, shown in Figure 1.16, reflects the decrease of stiffness that occurs when the soil is subject to primary deviatoric loading. It is also accompanied by the emergence of irreversible plastic strains. The yield curve is described as follows:

$$\varepsilon_1 = \frac{q_a\ q}{E_i\ (q_a - q)} \quad for\ q < q_f \quad \text{Eq. 1.103}$$

Where the ultimate deviatoric stress q_f is related to the stress q_a by the means of the failure ratio R_f.

$$q_f = \frac{c\ cot\phi - \sigma_3}{1-sin\phi}\frac{2sin\phi}{2-sin\phi} = \frac{6sin\phi}{3-sin\phi}(p' + c\ cot\phi) \quad \text{Eq. 1.104}$$

$$p' = (\sigma_1 + 2\sigma_3)/3 \quad \text{Eq. 1.105}$$

$$R_f = \frac{q_f}{q_a} < 1 \quad \text{Eq. 1.106}$$

$$E_i = \frac{2E_{50}}{2 - R_f} \quad \text{Eq. 1.107}$$

The shear yield function is defined in Eq. 1.108.

$$f^s = \frac{E_{ur}}{E_i}\frac{q_a q}{(q_a - q)} - q - \frac{E_{ur}\gamma^p}{2} = 0 \qquad \text{Eq. 1.108}$$

Where γ^p is a shear hardening parameter defined as follows:

$$\Delta\gamma^p = -(\Delta\varepsilon_1^p - \Delta\varepsilon_2^p - \Delta\varepsilon_3^p) \qquad \text{Eq. 1.109}$$

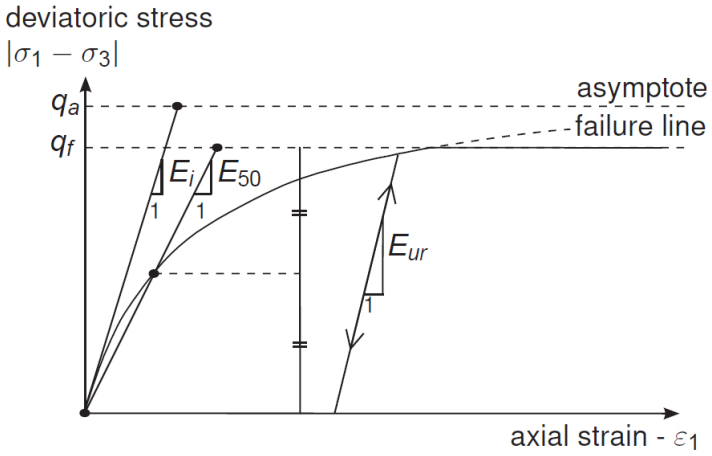

Figure 1.16 Hyperbolic stress strain-diagram (Brinkgreve et al., 2010)

For a given value of the parameter γ^p, the yield function $f^s = 0$ can be presented in the (p'- q) plane as a multisurface yield criterion (Figure 1.17). The shape of the yield loci varies depending on the value of m so that straight lines correspond to a value of m equal to unity and curves reflect lower values of m.

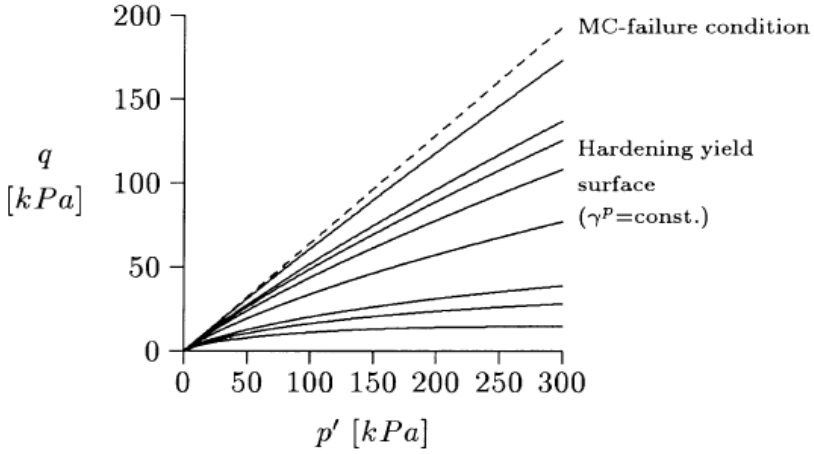

Figure 1.17 Shear hardening yield surface for various values of γ^p (Schanz et al., 1999)

A non-associated flow rule is used and the shear potential function is given by the following equation.

$$\dot{\varepsilon}_v^p = sin\psi_m \dot{\gamma}^p \qquad \text{Eq. 1.110}$$

The plastic potential and the different parameters are defined as follows:

$$g^s = m_1\sigma_1 + m_3\sigma_3 \qquad \text{Eq. 1.111}$$

$$m_1 = \frac{-1 + sin\psi_m}{2} \quad ; \quad m_3 = \frac{1 + sin\psi_m}{2} \qquad \text{Eq. 1.112}$$

$$sin\psi_m = \frac{sin\phi_m - \sin\phi_{cv}}{1 - sin\phi_m sin\phi_{cv}} \qquad \text{Eq. 1.113}$$

$$sin\phi_m = \frac{\sigma_1 - \sigma_3}{\sigma_1 + \sigma_3 - 2c\ cot\phi} \qquad \text{Eq. 1.114}$$

$$sin\phi_{cv} = \frac{sin\phi - \sin\psi}{1 - sin\phi\ sin\psi} \qquad \text{Eq. 1.115}$$

Where ϕ_m and ψ_m are the mobilized friction and dilation angles and ϕ_{cv} is the critical state friction angle (at failure).

If the mobilized friction angle is smaller than ϕ_{cv}, the material contracts. Otherwise, it dilates (Schanz et al., 1999).

- Volumetric cap criterion and flow rule

The second yield surface is a cap type that passes through the initial stress state. Any variation in the average stress p' leads to the activation of this mechanism. In their definitions, the two mechanisms are independent from each other.

This criterion reflects the volumetric isotropic hardening and controls the plastic volume strain. Besides, an associated flow rule is combined with the yield surface.

$$f^v = g^v = \frac{\tilde{q}^2}{\alpha^2} + p'^2 - p_c'^2 = 0 \qquad \text{Eq. 1.116}$$

$$\tilde{q} = -[\sigma_1 + (\delta - 1)\sigma_2 - \delta\sigma_3] \qquad \text{Eq. 1.117}$$

$$\delta = \frac{1 + sin\phi}{1 - sin\phi} \qquad \text{Eq. 1.118}$$

$$p_{c,ini} = OCR\sqrt{\left(\frac{\tilde{q}_{ini}^2}{\alpha^2}\right) + p_{ini}^2} \qquad \text{Eq. 1.119}$$

$$\Delta\gamma^v = -\Delta\varepsilon_v^p = -(\Delta\varepsilon_1^p + \Delta\varepsilon_2^p + \Delta\varepsilon_3^p) \qquad \text{Eq. 1.120}$$

Where α is a constant derived internally from other material parameters such as K_0^{nc} and p_c is the isotropic preconsolidation pressure that determines also the magnitude of the yield cap, presented by an ellipse in the (p'- q) plane.

For a triaxial compression condition, the following simplification may be done:

$$\tilde{q} = -[\sigma_1 - \sigma_3] \qquad \text{Eq. 1.121}$$

A big number of parameters characterizes the PH model. However, they can be easily determined from triaxial and oedometer tests. In some cases, the parameters are determined by back-analysis (Hsiung and Dao, 2014). Experience allows also to assume some preliminary values for certain types of soils. For example, the default value of R_f is 0.9 in the manual of FLAC3D (Itasca, 2019). The exponent m varies from 0.4 (sands) to 1 (clays). Also for sands, the unloading reloading Poisson's ratio is usually taken as ν_{ur} = 0.2 (Schanz et al., 1999; Brinkgreve et al., 2010; Khoiri and Ou, 2013).

Besides, in case of uncertainty or insufficiency in laboratory tests, the oedometric and the unloading-reloading stiffness moduli may be calculated from the secant stiffness modulus (Schanz et al., 1999; Schanz and Vermeer, 1998; Brinkgreve et al., 2010).

$$E_{ur}^{ref} = (3 - 5)\, E_{50}^{ref} \qquad \text{Eq. 1.122}$$

$$E_{oed}^{ref} = E_{50}^{ref} \qquad \text{Eq. 1.123}$$

The classical PH model presents always a good improvement in comparison with Mohr-Coulomb but settlements are still overestimated because it does not consider strain dependent stiffness. The option of small strains helps to overcome this problem (Hsiung and Dao, 2014). It will be explained in the following section.

4-2-4- Plastic Hardening Soil-Small (PH-S)

4-2-4-1- Non-linear behavior at small strains

At small-strain level, most of the soils show higher stiffness values and non-linear stress-strain response (Burland, 1989). In this framework, Jardine et al. (1986) used a new stress-strain equation (Eq. 1.124) to express the undrained behavior of a material they named LPC2.

$$\frac{E_u}{C_u} = A + B\cos\left\{\alpha\left[\log_{10}\left(\frac{\varepsilon_a}{C}\right)\right]^{\gamma}\right\} \qquad \text{Eq. 1.124}$$

Where the empirical constants A, B, C, α and γ can be determined from experimental tests.

This material was then compared by these authors to linear elastic model. They showed the effect of the non-linear behavior of soils in different applications (footings, cavity, excavation and piles).

In piles, in particular, the authors showed the impact of the small strain characteristics and local failure on the behavior of soil. Using the constitutive models where an elasto-plastic (non-linear) was assigned to the soil, local plastic failure was observed for small settlements (less than 2 mm) especially near the ground surface. Small strains, less than 0.05% were detected everywhere except immediately near the pile.

In other studies, experimental observations showed the presence of a small zone where the behavior is linear elastic (Jardine, 1992; Clayton and Heymann, 2001). This was observed on different soil types. This zone is governed by G_{max}, the initial shear modulus also called small-strain shear modulus.

The limit of this zone is not exact; It corresponds to a 0.0006% strain for Toyoura sand (Teachavorasinskun, 1989), while for Magnus till and London clay, resonant column gave a small strain stiffness G_{max} at 0.002 % and 0.02% respectively, which is considered overestimated for many reasons (Jardine, 1992).

For higher strain levels, the stiffness decreases according to a degradation curve specific to each soil as shown in Figure 1.18. The decrease of the soil modulus combined with the increase of stress and/or strain levels is the reason behind the non-linear stress-strain curves. Many equations were developed by different researchers (Kondner, 1963; Hardin and Drnevich, 1972; Jardine et al., 1986; Puzrin and Burland, 1996).

An example used for monotonic loads is given in the following equation (Fahey and Carter, 1993):

$$\frac{G_{sec}}{G_{max}} = 1 - f\left(\frac{\tau}{\tau_{max}}\right)^{g} \qquad \text{Eq. 1.125}$$

Where f and g are parameters and G_{sec} and G_{max} are the secant and the maximum shear modulus which correspond to τ and τ_{max} respectively.

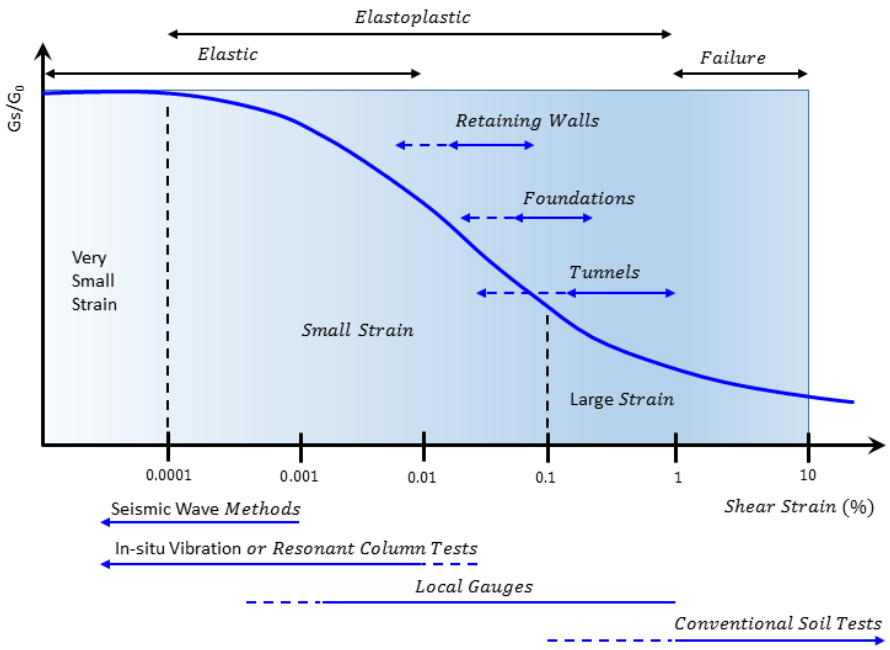

Figure 1.18 Stiffness modulus degradation curve and pical strain ranges (Modified from Atkinson and Sallfors, 1991 as cited in Itasca, 2019)

Classic experimental tests (oedometer, direct shear, triaxial…), do not show the non-linear behavior of the soil due to the inaccuracy of used sensors, load cell compressibility, misalignment or lack of homogeneity of strain and stress fields in samples as cited by Cazacliu and Di Benedetto (1998). Therefore, in such cases, dynamic tests are important and can be performed in the laboratory or in-situ as follows:

- **Laboratory tests** using bender elements, resonant column or local strain measurements. Bender element is a technique suggested for geotechnical applications by Shirley and Hampton (1978) and is used to measure shear wave velocity and small strain stiffness of soils. It is popular since it can be used for triaxial, oedometer of torsional shear tests.

  Some applications are presented in Table 1.2.

Table 1.2 Some examples of precision tests performed on soils

Test	Authors
Simple shear on hollow cylinder	Ampadu and Tatsuoka, 1993
Roscoe type test	Dorudian and Vucetic, 1995
Torsion, Compression, Confinement tests on hollow cylindrical sample in static and dynamic loading (T4C StaDy)	Developed at ENTPE Lyon (Cazacliu and Di Benedetto, 1998; Geoffroy et al., 2003; Sauzéat et al., 2003)

It should be noted that these tests are not suitable for coarse grain material and undisturbed or cemented material (Pokhrel et al., 2015).

- **In-situ tests** used to estimate shear wave velocity V_s at different depths. These are more reliable that laboratory tests since they prevent disturbance of samples. The most common method is the downhole testing DHT.

The small-strain stiffness depends on various factors such as the shear and volumetric strains, the stress state, the void ratio… Hardin and Richart Jr (1963) suggested an equation for the small-strain shear modulus of sandy soils relating it to the previously mentioned parameters, as follows:

$$G_0 = G_{max} = \text{A F(e)}(\sigma_0')^{\text{n}} \qquad \text{Eq. 1.126}$$

Where,

- A is a dimensionless number that depends on the mineral composition, size, shape, grading and surface texture of grains
- σ_0' is the mean effective stress
- n is an exponent that varies according to the soil type
- F(e) is a function of the void ratio, which can be expressed as in Eq. 1.127 and Eq. 1.128. These equations were determined based on shear wave velocity measurements using resonant column method.

$$G_0 \propto \frac{(2.17-e)^2}{1+e} \text{ for rounded-grained sands (e<0.8)} \qquad \text{Eq. 1.127}$$

$$G_0 \propto \frac{(2.97-e)^2}{1+e} \text{ for angular-grained sands (e>0.6)} \qquad \text{Eq. 1.128}$$

In addition, if information about the shear wave velocity V_s is available, another equation for the small-strain stiffness can be used as follows:

$$G_0(kPa) = \rho V_s^2 = \frac{\gamma}{g} V_s^2 \qquad \text{Eq. 1.129}$$

4-2-4-2- Plastic Hardening Soil-Small (PH-S)

In this framework, the PH-S model was developed as a new improvement of the classic PH model that includes the small strain feature (Benz, 2007). In addition to the features shown in Section 4-2-3 of Chapter 1, the PH-S uses a modified hyperbolic for the stiffness degradation curve (Hardin and Drnevich, 1972; Fahey and Carter, 1993) and requires 2 additional parameters: the reference stiffness at a very small strain (E_0^{ref}) and the shear strain ($\gamma_{0.7}$) at which the shear modulus is reduced to 72.2% of its initial value (Santos and Correia, 2001).

By default, E_0^{ref} is taken as $3E_{ur}^{ref}$. E_0^{ref} and G_0^{ref} are used to calculate E_0 and G_0 using a power law identically to the moduli defined in PH model (Eq. 1.98 and 1.99). The shear stiffness modulus G_0 at very small strain level may be determined from the corresponding E_0 as follows:

$$G_0 = \frac{E_0}{2(1+\nu)} \qquad \text{Eq. 1.130}$$

On the other hand, the determination of $\gamma_{0.7}$ is not as easy and the values are found to be very scattered for different types of soils. Therefore, Hsiung and Dao (2014) found the value of 10^{-4} in sands by back analysis.

In this thesis, this model was used for the different soil layers in Chapter 4. The determination of the parameters will be shown later.

4-3- Comparison between MC, PH and PH-S and choice of parameters

There are already in the literature many references that compare the three previously cited models in different applications for soils. Hsiung and Dao (2014) studied the movements caused by a deep excavation on sand and showed that Mohr-Coulomb model overestimated the displacements and that PH and PH-S gave similar behavior but the maximum displacement is reduced in PH-S due to small strain stiffness effects. Besides, in a comparison made in Plaxis2D between MC and PH on tunnels excavation, the latter showed more accurate results (Çelik, 2017).

The input parameters of the previously described models are presented in the following table.

Table 1.3 Parameters of the MC, PH and PH-S models (Hsiung and Dao, 2014)

Parameter	MC	PH	PH-S	Parameter	MC	PH	PH-S
ϕ	x	x	x	E_{50}^{ref}		x	x
C	x	x	x	E_{oed}^{ref}		x	x
E	x			E_{ur}^{ref}		x	x
ν	x			**m**		x	x
ψ	x	x	x	ν_{ur}		x	x
K_0	x	x	x	G_0^{ref}			x
R_f		x	x	$\gamma_{0.7}$			x

- Cohesion and angles of friction and of dilatancy

These parameters are easily determined from a standard triaxial performed on the soil sample (Figure 1.15). The friction angle is related to surface roughness, compaction and shape of the grains. Thus, the same state can be easily reproduced in the laboratory in order to evaluate its value.

- Modulus of deformation

The drained deformation modulus in a MC model is defined as the initial slope of the (ε_a, q) curve in a drained triaxial test. Identically, the values of the stress-dependent stiffnesses defined in a PH model are as well determined from triaxial and oedometer tests. An example will be shown in the chapter 4 of this thesis.

However, the determination from laboratory tests of the deformation modulus in sandy soils in particular is not always easy since it is highly affected by the disturbance of the samples unlike other parameters (Hsiung and Dao, 2014). Many researchers used back-analysis or calibration results (Bowles, 1996; Hsiung, 2009) or tried to find correlations between Young modulus and other moduli estimated in in-situ tests. For example, many empirical formulas relate the deformation modulus to the N-index of an SPT because this test is not influenced by soil disturbance (Hsiung and Dao, 2014). In particular, the two moduli E and E_{50}^{ref} of the sand, were evaluated using Eq. 1.131 and 1.132 (Hsiung, 2009).

$$\mathrm{E\ (kPa)} = 2000\ \mathrm{N} \qquad \text{Eq. 1.131}$$

$$E_{50}^{ref}\ \mathrm{(kPa)} = 1200\ \mathrm{N} \qquad \text{Eq. 1.132}$$

It was also shown that the compression modulus of sandy soils linearly increases with pressure and thus with depth (Yang et al., 2013). This is due to the increase of the total stresses. Therefore, some authors proposed a new equation for a deformation modulus that varies with depth (Ma et al., 2014) as follows:

$$E_{s,z} = E_{s,0.1-0.2}\left(\frac{z}{h_0}\right)^{1/\beta} \qquad \text{Eq. 1.133}$$

Where z is the depth of soil layer (m), h_0 a reference depth (1 m for example), β a parameter depending on the soil charcteristics and $E_{s,0.1-0.2}$ the compression modulus measured under 100 - 200 kPa pressure in geologic reports.

This method gave more realistic load settlement curves which were in closer agreements with experimental values (Gowthaman and Nasvi, 2017; Yang et al., 2013). An alternative of this equation can be also the adoption of the PH model which uses a modulus that varies with the pressure.

An equation was also used to estimate the deformation modulus based on the pressuremeter modulus of the soil:

$$E_y = \frac{(1+\nu)(1-2\nu)}{1-\nu}E_{oed} = \frac{(1+\nu)(1-2\nu)}{1-\nu}\frac{E_M}{\alpha} \qquad \text{Eq. 1.134}$$

Where α is a rheological coefficient that characterizes the soil as presented in the following table.

Table 1.4 Value of the rheological coefficient according to the soil type (NF P 94-262, 2012)

Nature of soil	**Peat**	**Clay**		**Silt**		**Sand**		**Gravels**	
	α	E_M/pl	α	E_M/pl	α	E_M/pl	α	E_M/pl	α
I	1	>16	1	>14	2/3	>12	1/2	>10	1/3
II		9 – 16	2/3	8 – 14	1/2	7 – 12	1/3	6 – 10	1/4
II		7 – 9	1/2	5 – 8	1/2	5 – 7	1/3	-	

I: Overconsolidated or very tight *II:* Normally consolidated *III:* Underconsolidated altered and disturbed or loose

On the other hand, a correlation was suggested by Bohn (2015) to calculate the initial stiffness of the soil using the elastic equation of Randolph and Wroth (1978) and the first slope of the non-linear curve of Frank and Zhao (1982). This method contributed to the following formulas:

- Pile shaft:

$$E = \alpha_{pile,s}\,(1+\nu)\ln\frac{2.5L\,(1-\nu)}{D/2}E_M\ ; \qquad \alpha_{pile,s} = \begin{cases} 2 & for\ clay \\ 0.8 & for\ sand \end{cases} \qquad \text{Eq. 1.135}$$

- Pile tip:

$$E = \frac{\alpha_{pile,b}}{4}\,(1-\nu^2)\,\pi\,E_M\ ; \qquad \alpha_{pile,s} = \begin{cases} 11 & for\ clay \\ 4.8 & for\ sand \end{cases} \qquad \text{Eq. 1.136}$$

4-4- Behavior of the soil-pile interface

In the literature, the soil-structure interface was defined differently from an author to another. It is mainly defined as the soil region located between the surface of the structure and the nearby soil mass (De Gennaro, 1999) characterized by a strain localization due to the tangential load transfer from the structure to the soil (Pra-Ai, 2013). The characteristics of the interface are generally determined by experimental tests carried out with several available devices. These tests can be performed according to one of the three following conditions: constant normal stress, constant volume or constant normal stiffness. On the other hand, numerical tools may be also used to understand the behavior of an interface.

In fact, when a pile is axially loaded, the soil located in the shear zone, directly near the shaft, tends to dilate. However, it is blocked by the nearby soil resulting in the increase of the normal stress on the surface of the pile (Schlosser and Guilloux, 1981). It is also shown that, for granular soils, the failure occurs at the pile-soil interface unless the surface of the pile is very rough (Yoshimi and Kishida, 1981). The thickness of this interface varies according to the grains size, the density of the soil and the roughness of the pile (Said, 2006).

The soil-structure interface is generally characterized by a soil-pile friction angle δ' obtained from the friction angle ϕ of the soil depending on the roughness of the pile and the relative settlement between the soil and the structure. The shear resistance may be calculated as follows:

$$\tau = \sigma \tan\delta' \qquad \text{Eq. 1.137}$$

The Eurocode 7 (2005) suggests to use a value of two-third of the friction angle for prefabricated structures and ϕ for cast in place elements such as bored piles. Underestimating the soil-pile friction angle leads to high costs of the project and overestimating may cause safety issues.

Many authors tried to understand the special behavior of the soil-structure interfaces by developing constitutive laws based on the same concepts used for soils. Interface constitutive models include among others the nonlinear elastic model (Clough and Duncan, 1971), the elastic perfectly plastic model (Zhou and Lu, 2009), and the strain softening model (Esterhuizen et al., 2001). These laws were implemented in

many software using different types of interface: zero-thickness elements (Barbas and Frank, 1982; Neves et al., 2001a), thin-layer elements (Madabhushi and Haigh, 1998)…

It should be noted that Mohr-Coulomb failure criterion is the simplest and the most common and it will be used in this thesis due to the absence of experimental testing that help to calibrate advanced models.

5- Geotechnical instrumentation

The complexity of geotechnical structures such as dams, bridges or high-rise buildings requires a sound understanding of the behavior of the soil, the structure itself and the interface. This information can be obtained by doing a list of in-situ and laboratory tests, or by studying the behavior of structures in reduced scale models. However, in many cases, these methods are not sufficient and this is where the geotechnical engineer resorts to an instrumentation program. This section will highlight some of the main aspects of geotechnical instrumentation.

5-1- Benefits and objectives of geotechnical instrumentation

The benefits of the instrumentation in geotechnical vary with the objective and the phase during which it is executed (Dunnicliff, 1988).

- During the design phase, the instrumentation can be performed as site investigation method to help in determining the initial site conditions by measuring groundwater pressures, stresses and deformability conditions… Besides, pile load tests for example, are performed to verify the adequacy of the design.

- During the construction stage, real time measurements can be essential to provide legal protection or to ensure safety by preventing soil collapse during an excavation or by protecting the structure from premature failure. In some cases, it aims to advance the state of the art by improving a construction method or by expanding the existing knowledge on a certain type of soil.
  In addition, the instrumentation plays an active role in the design and the construction, allowing modifications to be carried out (Patel et al., 2007). This is called the observational method and was applied for buildings, excavations, railways and other projects (Peck, 1969; Muir Wood, 1990; Powderham, 1994; Powderham and Nicholson, 1996; Nicholson et al., 1999; Powderham, 2002; Allagnat, 2005). It was also proposed by the Eurocode 7 (2005) as a means of justifying geotechnical structures. The observational method, as described by Nicholson et al. (1999) is "*a continuous, managed, integrated, process of design, construction control, monitoring and review that enables previously defined modifications to be incorporated during or after construction as appropriate. All these aspects have to be demonstrably robust. The objective is to achieve greater overall economy without compromising safety".*

- Finally, during the operating phase, instrumentation aims to study the long-term behavior of the structure, for example long-term measurements of leakage, ground deformations, and long-term performance of rock bolts. It is sometimes called Structural Health monitoring (SHM) and it serves for civil infrastructure maintenance, to ensure quality and safety (Barrias et al., 2016). In this case, the acquisition system gives continuous updates about the structure that may face damages due to the environment.

The instrumentation of piles in particular has many benefits. It can help to verify and optimize the design, or to determine the global pile bearing capacity. I can also allow to determine the subdivision of the ultimate load into shaft friction and end bearing load.

5-2- Metrology vocabulary

For a better understanding, Table 1.5 presents the definition of some of the metrology terms that will be used in this thesis.

Table 1.5 Definition of metrology terms (Potts, 2012)

Category	Property	Designation
Measurement properties	Accuracy	Closeness of agreement between a measurement and a true value of the measurand
	Trueness	Closeness of agreement between the average value obtained from a large number of tests and a reference quantity value
	Precision	Closeness of agreement between independent test results obtained by replicate measurements on the same or similar objects under specified conditions
	Uncertainty	Non-negative parameter characterizing the dispersion of the quantity values being attributed to a measurand, based on the information used
	Reproducibility	Closeness of the agreement between the results of measurements carried out under changed conditions of measurement.
	Repeatability	Closeness to which a measurement instrument will read the same value for a defined measurement when multiple measurements are collected.
Sensors properties	Measuring interval	The set of values that can be measured by the instrument
	Calibration curve	Curve representing the relation between indications and corresponding measured values
	Resolution	The smallest change in the signal that can be detected and accurately indicated by a sensor. Resolution can be expressed either as a proportion of the reading (or the full-scale reading) or in absolute terms.
	Sampling resolution	The distance between two consecutive gages
	Spatial resolution	In a fiber optic sensor, this is the smallest distance over which a variation can be measured
	Stability	A measure of how the metrological properties of an instrument remain constant in time
	Sensitivity	Relationship between the change of the output electrical signal and that of the input physical signal
	Linearity	Closeness of the calibration curve to a straight line. The linearity of the transducer is an expression of the extent to which the actual measured curve of a sensor departs from the ideal curve.
Instrumentation properties	Discretion	The ability of a sensor to give the value of the parameter to be measured without modifying it by its presence
	Redundancy	The use of two sensors or more measuring identical or related parameters

5-3- Sensors classification

Sensors are tools that transform a physical quantity into a parameter that can be measured. They may be classified according to the following criteria:

- The technology used (electrical, electromagnetic, frequency and optical sensors). Voltage sensors are not the best option for cables longer than 100 m. However, current (4 - 20 mA) and frequency sensors are insensitive to electromagnetic disturbances and can use up to 1000-m cables.
- The energy intake (passive or active sensors)
- The output type: analog, numerical or logic signal).
- The type of measured parameters (Table 1.6)

Table 1.6 Summary of sensors and measured parameters (Briançon et al., 2016)

Type of parameter	Parameter / Unit	Measurement	Example of sensors
Mechanical	Stress (Pa, kPa)	Stresses and loads are not directly measured. In general, they are calculated from the deformation of a test body to which the force is applied.	Concrete/earth pressure cells Shaft friction cell for unit shaft friction
	Load (N, kN)		Load sensors (Osterberg cell for pile tip load,
Hydraulic	Water level (NGF)	Ground water table level	Piezometers
	Pore pressure (Pa, kPa)	Pore water pressure exerted by the water in a saturated soil	Pore pressure transducers
Geometric	Displacement (m, mm)	It is measured by the relative displacement between two points	Fiberglass rod extensometers
	Deformation (m/m, μm/m (με))	It can be calculated using the displacement or another parameter like the resistance	Vibrating-wire strain gages Electrical resistance strain gages
	Tilt (Radian)	Angle variation	
Environmental	Temperature (°C)		Thermistor

Ding and Qin (2000) provided in their work an overview of geotechnical instruments used in different applications.

5-4- History of geotechnical instrumentation

5-4-1- Conventional geotechnical instrumentation

Geotechnical Instrumentation began in the 1930s and 1940s with simple programs to assist field observations. In recent years, its role has become more important especially with the progress of technology, which has spawned a remarkable development in sensors that have become more complex and accurate at the same time (Dunnicliff, 1988).

France, among other countries, witnessed the emergence of national projects such as SOLCYP (SOLlicitation CYcliques sur Pieux), a collaborative research project between academia and industries that aims to study the behavior of piles subject to cyclic loading, by the means of sensors installed in the structure.

During the past few decades, pile instrumentation was mainly performed for testing (e.g., low strain integrity test, high strain dynamic testing, cross-hole sonic logging, and static pile load testing), in order to evaluate the settlement and the bearing capacity of the piles. Later, instrumentation was introduced in geotechnical investigations with the intention of collecting some measurements (load, strain, settlement, ground movement, inclination...). Sensors set-up in full-scale piles were becoming more common as they help to evaluate their performance by comparing more realistic measured data with values predicted by pile design methods.

In the early pile load tests carried out on drilled shafts, only applied load could be measured (Reese, 1969). Skempton's formula (Eq. 1.138) has been used to estimate the load carried by the base (Skempton, 1959) and consequently, the mobilized skin friction was calculated as the difference between the two values.

$$Q_b = 9C_u A_b \qquad \text{Eq. 1.138}$$

Attempts were made later to measure the mobilized skin friction of the pile by using an electrical resistance strain gage attached to the reinforcing cage (DuBose, 1956). This method was developed afterwards by putting the same type of gage in a 5 cm diameter pipe embedded in the shaft (Mohan et al., 1963). Concomitantly, vibrating-wire gages started to be used instead of electrical resistance strain gages and they presented a better stability over a long period of time (Whitaker et al., 1962; Osgerby and Taylor, 1968).

Some problems may be encountered in drilled shaft instrumentation. Firstly, the gages are exposed to moisture and chemical action when installed in concrete. Secondly, concrete may have different properties along the pile and may undergo physical changes that can affects readings, assuming that the gages were not damaged during the installation of the reinforcing cage. On the other hand, the real geometry of drilled shafts after execution may differ sometimes from the designed one (Figure 1.19). It can be due to improper excavation, poor quality of concrete or improper placement of concrete (Reese, 1979). The observed abnormalities in the shaft may affect the calculated load especially if the size of the pile is changed at specific locations or may even result in having gages not embedded in the concrete (Hayes and Simmonds, 2002).

In general, it is difficult to measure the stress in piles by the means of sensors. Therefore, sensors measuring the deformations have been used in an attempt to calculate the stress after multiplying by the deformation modulus. Two main problems may be encountered in this case: an uncertainty of the modulus and of the pile section as described earlier. The concrete modulus may vary locally in bored piles due to air voids or moisture for example. In addition, this method neglects strains that are not caused by stress, such as shrinkage and creep stresses. A load cell should be sometimes placed near the gage in order to relate both values measured (Dunnicliff, 1988).

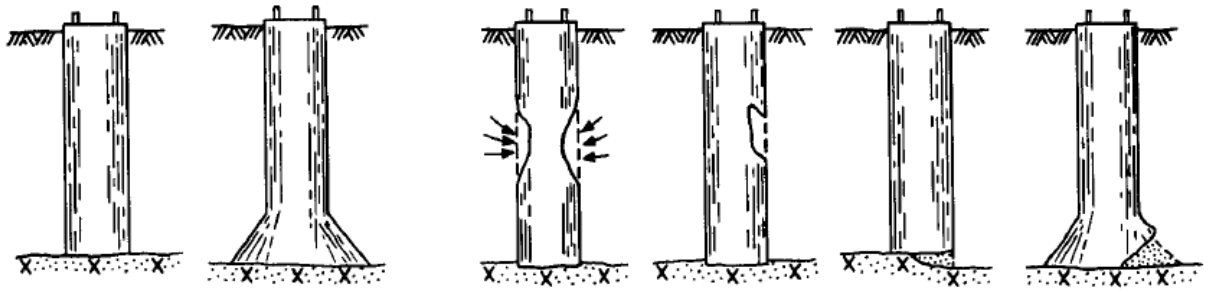

Figure 1.19 Possible abnormalities in drilled shafts (Dibiagio and Myrvoll, 1981 as cited in Dunnicliff, 1988)

Some authors gathered different load test performed on several types of soils and piles. Kulhawy et al. (1983) summarized 410 published and unpublished static load tests in axial compression or uplift. Dunnicliff (1988) showed many history cases for load tests on instrumented drilled shafts and driven piles as well as for embankment dams and underground excavations. On the other hand, several instrumented static pile load tests were carried out in order to study and evaluate pile settlements. They are available in the database of IFSTTAR (Institut français des sciences et technologies des transports, de l'aménagement et des réseaux). Table 1.7 summarizes some of the recent applications in the last few years.

Table 1.7 Recent instrumentation works on piles using conventional instruments

Authors	Objective of the study	Installed sensors
Hajduk and Paikowsky, 2000	Performance evaluation of test piles	Electrical resistance, piezo-electric, piezo-resistive, and vibrating wire instruments
Hayes and Simmonds, 2002	Load tests analysis in bored piles	Vibrating-wire strain gages, sister bars and Osterberg cells
Paikowsky and Hajduk, 2004	Analysis of the time dependent pile capacity gain in closed ended steel pipe and prestressed concrete piles	Strain gages (electrical and vibrating-wire, piezometers, accelerometers, telltales, thermistors, total soil pressure gages
Liew et al., 2004	Load tests analysis in bored piles	Vibrating-wire strain gages, extensometers
Faisal and Lee, 2008	Load tests analysis in driven and jacked-in prestressed spun concrete piles	Global strain extensometer
Fellenius et al., 2009	Load tests analysis in pretensioned spun high strength concrete piles	Vibrating-wire strain gages, sister bars
Mishra et al., 2012	Analysis of the differential movement at railroad bridge	Multidepth deflectometer, strain gages
Bica et al., 2014	Load tests analysis in steel displacement piles	Vibrating-wire strain gages, Electrical resistance strain gages

5-4-2- Optical fiber sensing

As an alternative to classical sensors, optical fibers are being used nowadays in several applications and more particularly in geotechnical. This technique was available in the first half of the twentieth century but its application was limited. However, in the 80s, optical fibers were developed and began to be used for strain and temperature measurements (Giallorenzi et al., 1982; Barrias et al., 2016). The development of the optical fibers in the market is presented in Figure 1.20.

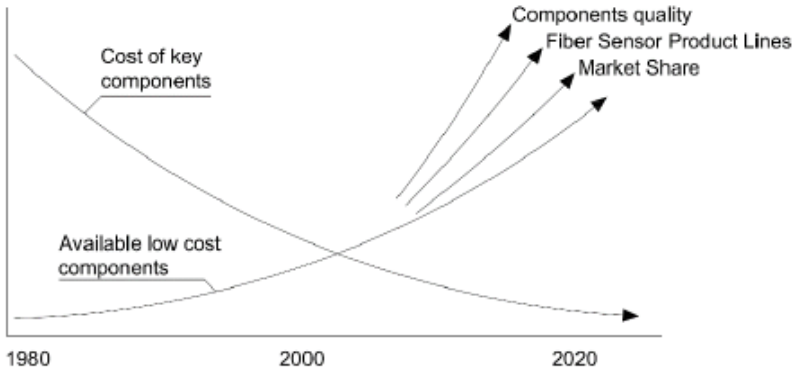

Figure 1.20 Trend for optical fibers (Udd and Spillman Jr, 2011 as cited in Barrias et al., 2016)

It may sound simple, but working on site with a dozen of cables exiting from the piles or the raft foundation is not easy at all, especially because of the high risk of losing them. In general, there is a tendency to reduce the number of cables on site. The main advantage of this technique is that one optical fiber cable can substitute a dozen or so cables. It can be installed anywhere due to its small size and it can resist chemically aggressive environments.

Fiber optic sensors can measure strain or temperature at a particular or at several points over their entire length with a good precision and a high spatial resolution. This technique presents several advantages over conventional sensors, mainly its electromagnetic insensitivity due to the galvanic isolation of the fiber, its flexibility, its reliability, its high bandwidth and the possibility of multiplexing easily in order to enable the measurement over long distances.

In addition, FOSs are able to give a continuous information and allow the construction of a more reliable strain profile in the structure where they are installed. Nowadays, optical fibers are used in piles to assess their integrity and determine their deformation in load and integrity tests, and in anchors and micro piles to evaluate their bearing behavior. It is also used to monitor big geo-structures such as dams by integrating the sensor is geosynthetics for example (Habel and Krebber, 2011).

- Components of a FOS

A fiber optic sensor comprises a silica or plastic core of 4 - 600 µm diameter having a uniform refractive index, surrounded by a 125-µm diameter cladding. The interface between core and cladding serves to trap the light waves being varied in the core by reflection (Barrias et al., 2016). A 250-µm diameter buffer and finally a 400-µm diameter jacket for protection purposes cover the cladding. A typical cross section view of an optical fiber is shown in Figure 1.21. It becomes multicore or multimode by changing the number of cores and the diameter respectively.

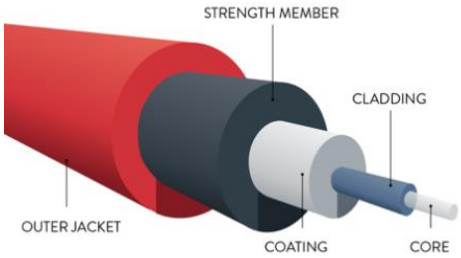

Figure 1.21 Cross sectional view of a fiber optic sensor (https://www.ofsoptics.com/optical-fiber-coatings/)

- Different techniques and scatterings used

In geotechnical monitoring projects, many techniques were developed and are being increasingly used allowing the monitoring of a length of tens of kilometers by a single optical fiber. Commercially available fiber-optic-based instruments include displacement transducers, piezometers, strain gages, and temperature gages.

FOSs can be discrete (point sensors, quasi-distributed) or distributed sensors. On one hand, fiber Bragg gratings (FBG) with quasi-distributed sensors were largely used in piles (Byrne et al., 2015) and tunnels (Guan et al., 2014; Li et al., 2015). On the other hand, many researchers used Distributed Optical Fiber Sensors (DOFS), which are based on reflectometry by either Brillouin, Raman or Rayleigh scattering.

Scattering describes the phenomenon that occurs when an electromagnetic wave interacts with the medium in the optical fiber, generating a secondary wave of the same type. It is the sum of the amplitudes diffused by the elements in a given direction. In a homogeneous medium, this wave is only present in the direction of propagation while due to the heterogeneity of the fibers, the scattered beam can move in all directions and in particular back towards the source, allowing the user to get information about the fiber properties. This is called backscattering (Bao and Chen, 2012). Each fiber has unique silica impurities distributed along its whole length. Its profile can change with any change in strain/temperature applied to the fiber. The spectral shift of the backscatter (Rayleigh for example), is then converted into strain or temperature change.

Rayleigh scattering is based on a quasi-elastic (linear) phenomenon, where the optical properties only vary over space. It is used for temperature, stress and strain measurements. Raman and Brillouin scatterings are inelastic and are a result of a shift in a photon energy and in the frequency of the scattered light wave. These

are called Stokes and anti-Stokes processes and they occur when the photons lose or gain energy respectively. Raman scattering is only sensitive to temperature (Cheng and Xie, 2004; Abalde-Cela et al., 2010; Oakley et al., 2011) while Brillouin scattering may be used for both temperature and stress (Kurashima et al., 1990; Bao et al., 1995; Motil et al., 2016).

Figure 1.22 and Table 1.8 represent some differences between the three cited methods. The data in the table are extracted from Sikali Mamdem (2012) and updated based on the latest FOS technologies.

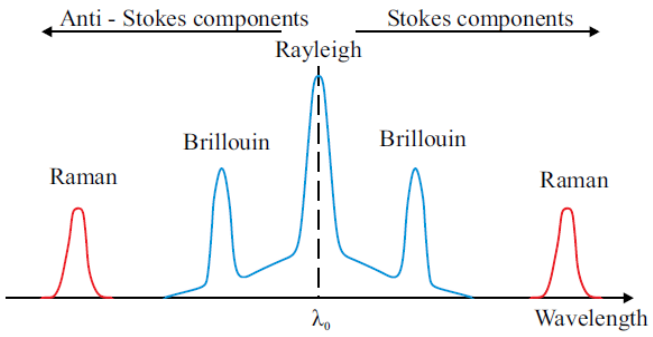

Figure 1.22 Rayleigh, Brillouin and Raman scattering in the optical fibers (Fajkus et al., 2017)

Table 1.8 Comparison of different fiber optic sensors

	Rayleigh	**Brillouin**	**Raman**
Spatial resolution	1 mm	50 cm	1m
Fiber length	2 km*	10 – 50 km	10 – 30 km
Acquisition time	30 s	Few minutes	30 s – few minutes
Strain resolution (με)	1	20	-
Temperature resolution (°C)	0.1	1	0.1
***** *FOSs of 50 m maximum can be connected to OdiSI 6100 (used in this project)*			

- Types of Distributed Optical Fiber Sensors (DOFS)

Different techniques of DOFS are used and they have largely been developed to suit various applications. These include among others, Brillouin Optical Time Domain Analysis (BOTDA), Brillouin Optical Time Domain Reflectometer (BOTDR) and Optical Frequency Domain Reflectometry (OFDR) used in this project to measure piles deformation.

Many civil engineering studies used BOTDR technique:

- Concrete beams (Zeng et al., 2002)
- Bridge monitoring (Bastianini et al., 2007)
- Tunnel deformation (Shi et al., 2005; Qiu et al., 2008; Song et al., 2011; Moffat et al., 2015)
- Applications on piles (Pelecanos et al., 2018; Kechavarzi et al., 2019)

Developed by Eickhoff and Ulrich (1981), the OFDR technique has high sensitivity and high spatial resolution up to 1 mm, with a precision up to 1 με. Instead of reading the intensity of the Rayleigh backscattered signal, the OFDR measures the interference fringes of the Rayleigh scattered light from a tunable laser source and a static reference fiber in frequency domain. By means of the inverse Fourier transformation, the amplitude and phase in frequency domain are converted to the time/spatial domain (Leung et al., 2015). Many OFDR-based interrogators that employ Rayleigh scattering exist in the market and were used by many authors, especially those provided by LUNA.

- OdiSi B was used in full-scale fatigue testing on an aircraft fuselage (Davis et al., 2016) and in piles applications (Kania et al., 2020)
- OBR 4600 was used for diaphragm walls in Grand Paris Express project (Nejjar, 2019) and for load tests on CFA piles using a spatial resolution of 10 mm (Bersan et al., 2018), which is the first documented application of OFDR technique on CFA piles
- OdiSi 6100 which is configured with 1 to 8 active measurement channels and gives the possibility to use a FOS of up to 50m length. To our knowledge, this particular interrogator has never been used in a pile application. It will be used in this thesis.

DOFSs that use Rayleigh scattering can be easily used in case of piles even though they are sensitive to temperature, since the strains due to temperature variations in the concrete are sometimes negligible compared to the mechanical strains. However, whenever needed, a fiber-optic temperature sensor may be installed as well inside the pile which measures the temperature variations and allows to make a temperature compensations (Kania et al., 2020).

6- Conclusion

This chapter is devoted to providing a wide and comprehensive summary of the most important topics on pile foundations.

Firstly, we presented an overview on the available methods used for bearing capacity and settlement analyses of single piles and pile groups. The elastic theory and the load transfer method developed by Frank and Zhao will be used later in this thesis together with numerical methods. Given that the most used method nowadays is based on numerical approaches, a summary of the constitutive models used for soils and pile-soil interfaces was given secondly, which is a very important input of these methods. The PH and MC models were chosen to represent the behavior of the soil and the interface.

Finally, previous instrumentation works carried out on drilled piles especially were presented showing conventional sensors and fiber optic sensors as well. According to previous experience of the authors, an ideal system of instrumentation should be easy to be installed, accurate, durable, stable and economic.

The information in this chapter paved the way for the instrumentation and the numerical modeling done in the framework of our project that will be presented in the following chapters.

Chapter 2: Overview of Silex^2 and presentation of the experimental and numerical tools

1- Introduction

"Fondasilex" is a collaborative research project funded by the "Région Auvergne-Rhône-Alpes" in France. It involves the research unit GEOMAS at INSA Lyon and the company Antea Group, in the framework of the construction project "Silex^2" owned by Covivio, a French Company previously known as "la Foncière des Régions". This project also involves "Group builders and partners" who is the main contractor, "Eiffage Construction Confluences – ECC", the subcontractor responsible for the construction and "Société Générale de Confortement – SGC" the company that executed the deep foundations of the project.

The aim of the project is to be able to gain insight on the mechanical behavior of the foundations and the soil formation in Lyon when they are subject to the load transferred from the superstructure. This chapter sets out all the parts of the project, together with its geotechnical hypotheses. It describes the experimental tests carried out in previous projects located in the same region, that give a close idea about the expected mechanical behavior. However, this was not enough and recourse was made to an in-situ instrumentation that allowed to measure the actual load transferred from the superstructure to the top of the foundations together with the deformation induced in both foundations and soil. On the other hand, a numerical model had to be set and calibrated using a finite difference software named FLAC3D®, and compared against these measured values. Experimental, analytical and numerical results are shown in Chapters 3 and 4.

2- Overview of Silex^2 project

2-1- Presentation of Silex^2

The project is located at "9 rue des cuirassiers", in the area of Part-Dieu in Lyon, France, as shown in Figure 2.1 and consists in the following 4 parts:

- The rehabilitation of the existing EDF tower (in blue) which was built in 1976
- The construction of a new 26-floor high-rise building (in green) of 112 m high up to the highest point of the cap (135 m high with the mast)
- The construction of two small buildings R+8, R+3 (in yellow)
- The construction of a base (R+1 to R+2) and an underground parking

Silex^2 is surrounded by those two buildings and another R+8 building called Silex^1 owned by the same company and constructed back in 2015. The natural ground level in Part-Dieu is 168 m NGF, where NGF is the general levelling of France.

The two towers are linked via two structural connections at the high-floor of the level 20. Two structural joints were used to block the displacements in both horizontal directions authorizing only those in Z direction. The site is located in a low seismicity zone II where liquefaction potential analysis is not required, based on the decree dating from 22 October 2010.

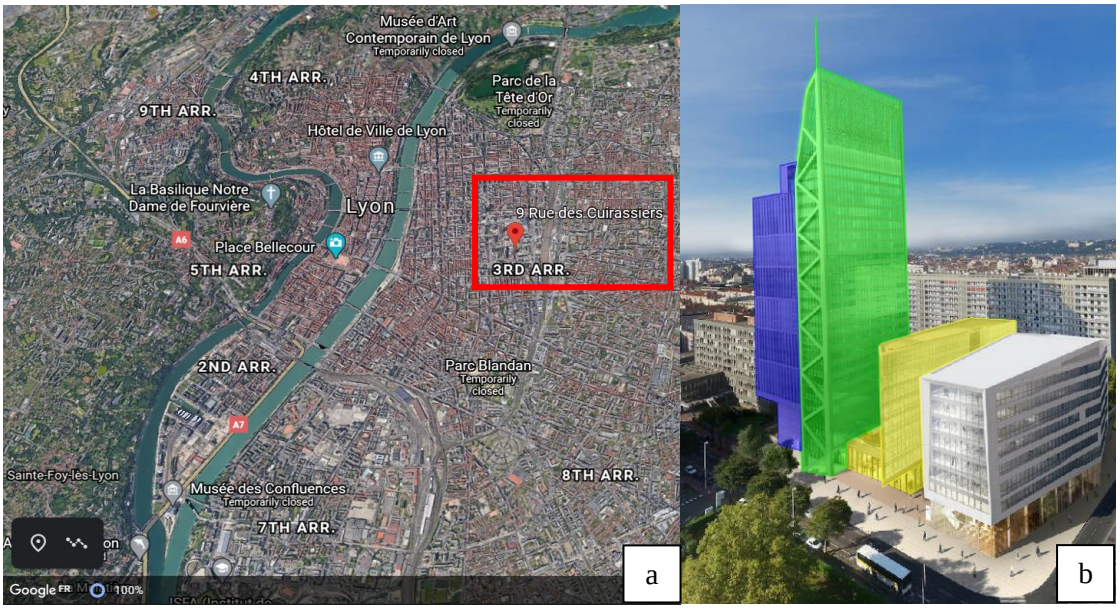

Figure 2.1 (a) Aerial view of the project's location from Google Earth and (b) virtual image of the project

2-2- Historical construction phases of the project

The site of Silex^2 has undergone many transformations. New buildings were constructed and others in the contrary do not exist anymore. Knowing that the soil has a memory, these changes affect its actual state of stress and deformation which make it important to model the loading history in order to have a wider idea about its behavior. For a clearer picture, the loading history is presented in the sketch in Figure 2.2.

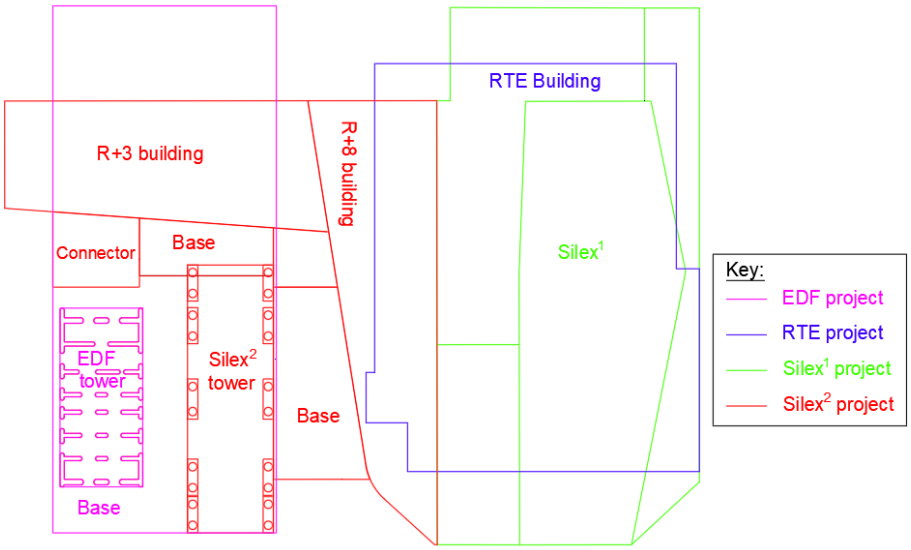

Figure 2.2 Sketch of Silex^2 tower and its neighboring buildings

The phases are summarized as follows:

- Phase 1: EDF project
  - Construction of the RTE building in 1970
  - Construction of the EDF tower in 1976 (rehabilitated later in 2007)
- Phase 2: Silex[1]
  - Demolition of the RTE building in 2015
  - Construction of Silex[1] building in 2015
- Phase 3: Silex[2]
  - Demolition of the base (four parking levels) and high levels of EDF tower in 2018
  - Construction of Silex[2] building and other structures starting 2019

The loads transferred to the soil by each of the cited buildings and structures are summarized in Table 2.1.

Table 2.1 Load transfer values for all construction phases

Phase	Structure/Building	Equivalent surface load
Phase 1: Construction of EDF	EDF tower	Load varies depending on the pile
	RTE building (North)	70 kPa
	EDF tower (base)	48 kPa
Phase 2: Construction of Silex[1]	Silex[1]	175 kPa
	Silex[1] Parking	25 kPa
	Silex[1] base	82 kPa
Phase 3: Construction of Silex[2]	Silex[2] tower	Load varies depending on the pile
	Silex[2] base	79 kPa
	Connector	44 kPa
	R+3 building	89 kPa
	R+8 building	158 kPa

The deconstructed parking was founded on well foundations of a 1 to 1.6 m diameter that carry between 600 to 4 000 kN each. In order to simplify the boundary problem in this work, if a modeling of the construction history is to be considered, a surface load of 48 kPa will be considered, applied on a rectangular area of 33.45 x 19.8 m^2 next to the tower EDF.

2-3- Foundations of Silex[2]

This section contains some of the important information about the pile foundations: the descriptive plan, the load transfer as well as the properties of the used materials. The pile foundations were designed and executed by the French company SGC (Société Générale de Confortement).

2-3-1- Foundation plan and method of construction

The new high-rise building is founded on 10 points of supports, each relying on a pair of 1.22-m diameter piles via a reinforced concrete transfer structure (TS) that is 1.55 m or 1.8 m in height depending on the level of the nearby raft. Based on the French standard NF P 94-262 (2012), a minimum embedment of 1.5 m in the rigid stratum is required. Therefore, the twenty piles are all anchored in the molasse layer reaching 146.5 m NGF.

The piles in Silex^2 were casted using continuous flight auger (CFA) technique, which is suitable for all types of soils especially those characterized by a superficial water table and most importantly, it can be used for piles with up to 1.2-m diameter. Cast in-situ piles have many advantages over driven piles: i) the low disturbance of soil and adjacent structure, ii) the low noise they cause and most importantly iii) the higher bearing capacity they can carry.

The CFA piles are constructed based on the following steps, presented later in Figure 2.3.

- The digging head of the auger is fitted with an expandable cap. The auger is rotated into the ground down to the desired final depth of the pile, while the soil, which is stuck in the flights, provides support for the hole.
- As the auger is withdrawn from the ground, a highly workable concrete mix is pumped down through the hollow center of the auger pipe to the base. This step is done from the base-up to prevent concrete segregation.
- The reinforcement cage is then installed into the wet concrete using a vibrator if needed. In Silex^2, six of the cages were equipped with sensors and will be detailed in Chapter 3.
- Earthworks are done up to the desired level and few days later, the piles head are broken to the same level using a hydraulic hammer.

According to the NF P 94-262 (2012), this type of piles is considered in Class 2 and Category 6.

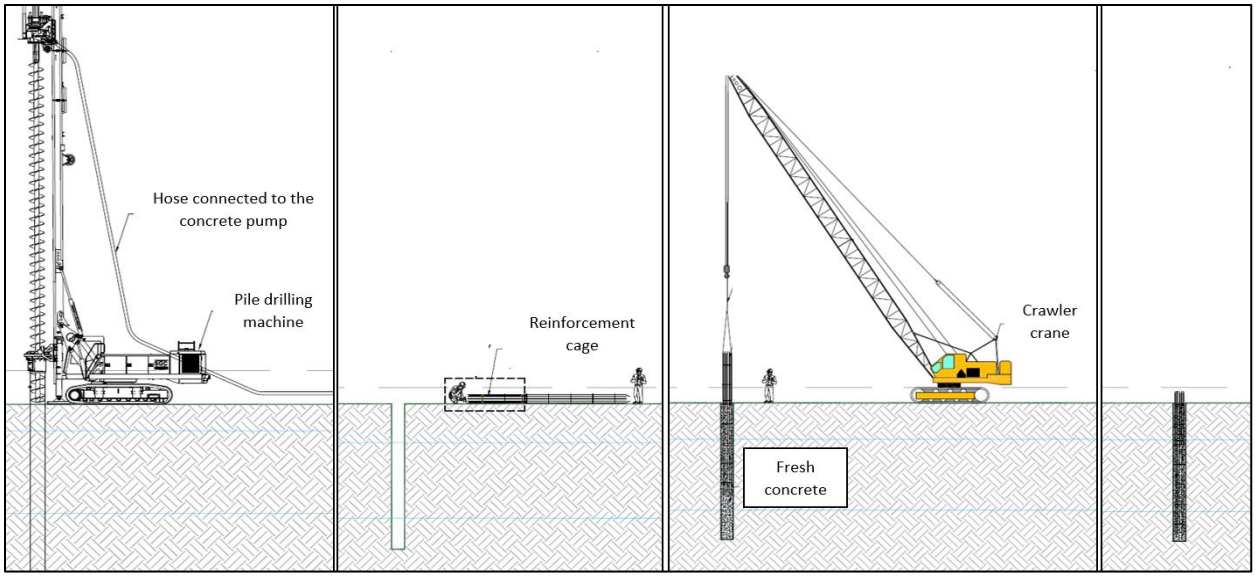

Figure 2.3 Scheme showing the main steps of the CFA technique used in Silex^2

During the construction, the working platform was at 164 m NGF. The foundation plan is presented in Figure 2.4, showing the location of the new tower in comparison to the nearby buildings. It shows also the execution order of the piles which follows the recommendations of the standards in a way it prevents the influence of the execution of any pile on the others.

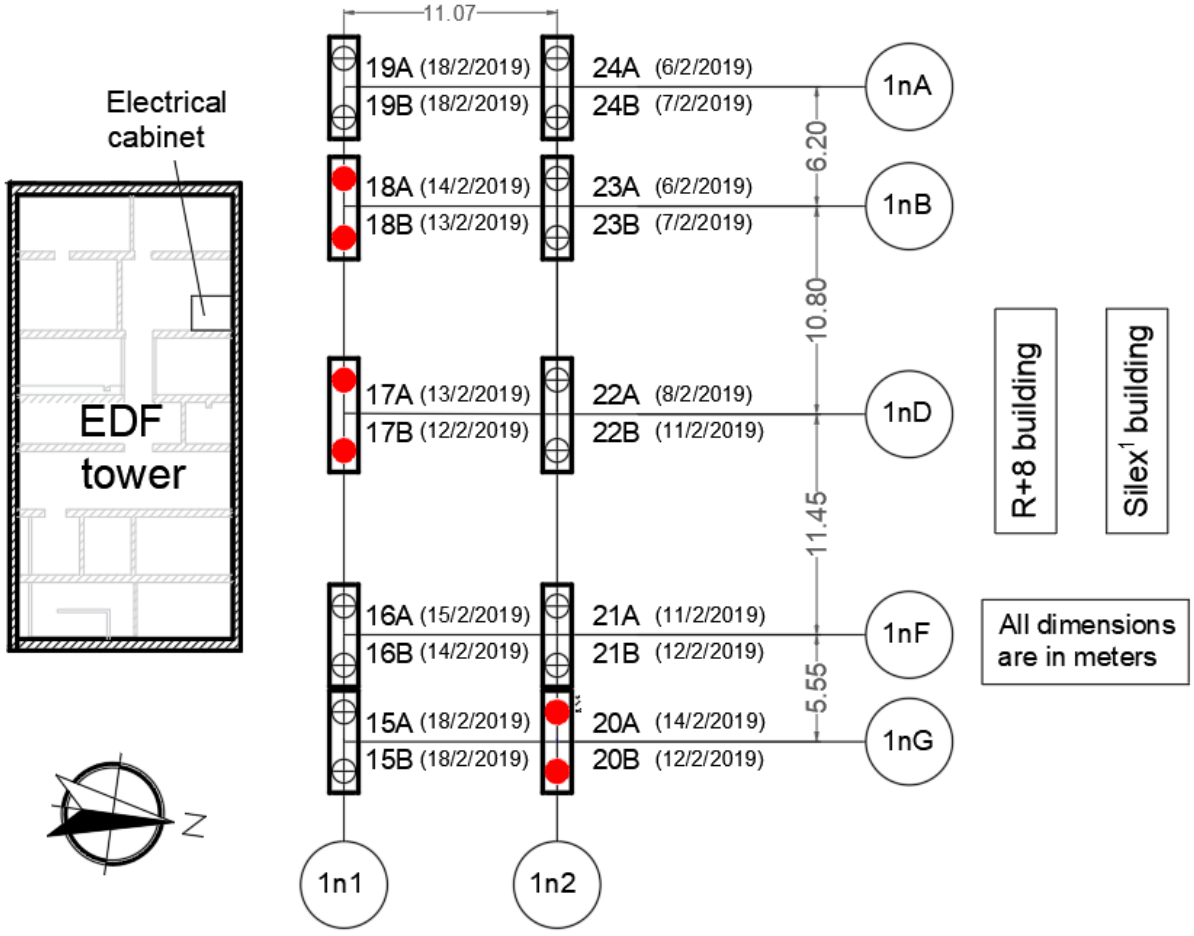

Figure 2.4 Foundation plan in Silex[2]

Table 2.2 and Table 2.3 present also some important geometrical characteristics of the piles and their corresponding transfer structure, showing a "*" sign near the instrumented ones. It should be noted that the bottom level of the used reinforcement cage is at 147.5 m NGF, identically for all the piles.

Table 2.2 Piles characteristics and levels

Pile No (A/B)	Pile tip A_i (m NGF)	Pile head A_s (m NGF)	Pile length (m)	TS level (m NGF)	Spacing between piles A/B (m)
Pi15	146.5	161.19	14.69	162.74	3.06
Pi16	146.5	161.19	14.69	162.74	3.06
Pi17*	146.5	161.19	14.69	162.99	3.66
Pi18*	146.5	161.19	14.69	162.74	3.06
Pi19	146.5	161.3	14.8	162.85	3.06
Pi20*	146.5	162.45	15.95	164	3.06
Pi21	146.5	162.45	15.95	164	3.06
Pi22	146.5	162.15	15.65	163.95	3.66
Pi23	146.5	162.15	15.65	163.7	3.06
Pi24	146.5	161.8	15.3	163.35	3.06

Table 2.3 Characteristics and levels of the transfer structures (TS)

Pile No (A/B)	TS length (m)	TS width (m)	TS height (m)	TS level (m NGF)
Pi15	5.3	1.5	1.55	162.74
Pi16	5.3	1.5	1.55	162.74
Pi17*	5.9	1.5	1.8	162.99
Pi18*	5.3	1.5	1.55	162.74
Pi19	5.3	1.5	1.55	162.85
Pi20*	5.3	1.5	1.55	164
Pi21	5.3	1.5	1.55	164
Pi22	5.9	1.5	1.8	163.95
Pi23	5.3	1.5	1.55	163.7
Pi24	5.3	1.5	1.55	163.35

2-3-1- Load transfer at the foundations

Based on the NF P 94-262 (2012), the bearing capacity of the foundations is only estimated under vertical loads. For design purposes, the load transfer from the superstructure to the foundations was calculated for several load combinations in both serviceability and ultimate limit states. Different cases are available. They either analyze the towers as coupled or consider Silex[2] alone, which is the worst-case scenario that would happen if the joints between the towers were accidentally broken.

Loads were determined at the base level of the TS, knowing that there is an articulated connection between this structure and the piles. The Appendix gives the normative calculation method of the loads and the combinations. The highest values (per pile) are shown in Table 2.4.

Table 2.4 Preliminary Load Transfer used for piles design based on numerical analysis

Pile No	SLS Characteristic		SLS Quasi-permanent		ULS		ULS seismic	
	N_{max}	H_{max}	N_{max}	H_{max}	N_{max}	H_{max}	N_{max}	H_{max}
Pi15	7 586	373.6	5 900	68.2	10 829	557.3	6 955	444.1
Pi16	7 395	259.5	6 001	53.1	10 396	384.7	6 326	243.3
Pi17	8 233	92.2	6 707	32.1	11 558	138.1	6 889	227.7
Pi18	6 989	225.3	5 572	36	9 807	333.8	5 904	227.5
Pi19	7 237	370.4	5 592	55	10 199	530.6	6 552	364.4
Pi20	7 557	407.3	6 014	80.3	10 643	606.6	7 069	431.5
Pi21	7 186	177.7	5 901	33	10 114	263.7	6 225	222.8
Pi22	7 802	97.1	6 447	33.3	10 957	144.7	6 681	221.8
Pi23	6 763	176.9	5 463	30.2	9 482	262.6	5 789	216.1
Pi24	6 913	375.9	5 420	44.5	9 726	559.9	6 366	353.8

Loads are given per pile in Kilonewtons (kN)

According to the previous table, the piles can be considered as axially loaded piles since the horizontal load in comparison to the vertical one is negligible. However, these combinations consider permanent, variable, wind and seismic actions. Their effect cannot be observed in the short term, during the construction of the tower and not even before any seismic or wind event occurs. The loads measured at the head of the piles at the end of the construction correspond to the unfactored permanent dead loads. These values will be presented in Table 4.5 and 4.6 of Chapter 4.

At the time of the construction, some parameters were recorded by the drilling machine (drill rate, torque…) and it was possible as well to monitor the volume of the used concrete. The monitoring records of the 20 piles showed an over-consumption of concrete between 3 and 22% resulting in an actual diameter varying between 1.24 and 1.34 m with an average of 1.3 m.

Besides, pile integrity tests which can generally show any possible flaw that could take place during the execution of the piles were carried out. They can also measure the lengths of the piles and the stiffness at their head. It was observed that the actual lengths were compliant with the theoretical ones. 19 tests out of 20 showed that the low-frequency dynamic stiffnesses were normal to high and reflect thus a good soil-pile connection.

2-3-2- Properties of pile materials

All calculations and measurements were done in accordance with the French standard NF EN 1992-1-1 (2007). High-adherence steel was used for the reinforcement with an elastic limit of 500 MPa. Two concrete classes were used: C50/60 for pile foundations and C30/37 for other structures. Its unit weight is 25 kN/m^3 and the Poisson's ratio is considered 0.2 for uncracked sections since no material failure is expected for the applied load.

The compressive strength and the elastic modulus were evaluated by performing laboratory crushing tests. In this regard, the mean compressive strength f_{cm} is usually defined and determined as the maximum value

in the experimental load deformation curves. It is related to the characteristic cylinder compressive strength as follows:

$$f_{cm}(MPa) = f_{ck}(MPa) + 8 \qquad \text{Eq. 2.1}$$

As an example, the characteristic cylinder compressive strength of a concrete of class C50/60 is 50 MPa.

The experimental secant elastic modulus E_{cm} can be determined from the same curve as the slope of the line connecting the point at $0.4f_{cm}$ to the origin.

It may be expressed alternatively in terms of the theoretical f_{cm} according to the standards as in Eq. 2.2.

$$E_{cm} = 22000 \left(\frac{f_{cm}}{10}\right)^{0.3} \quad (MPa) \qquad \text{Eq. 2.2}$$

The tangent modulus E_i is generally taken as $1.05E_{cm}$.

However, in long-term studies, it was noticed that the creep may generate permanent deformations that could not be evaluated by using the same modulus as before. Therefore, the elastic modulus should be reduced for creep considerations in order to be used in the calculations.

Hence, the "effective modulus" is created to visualize these deformations. It is expressed in terms of $E_{cm}(t_0)$ the modulus after t_0 days and $\phi(\infty, t_0)$ a creep coefficient, as shown in Eq. 2.3.

$$E_{c,eff} = \frac{E_{cm}(t_0)}{1 + \phi(\infty, t_0)} \qquad \text{Eq. 2.3}$$

t_0 is defined as the age of the first loading. $\phi(\infty, t_0)$ is determined using charts provided by the NF EN 1992-1-1 (2007) for internal and external environmental conditions. These charts use the class of the concrete, the average radius h_0 as well as the load application time t_0.

In Figure 2.5, the chart for concrete in an external environment with a relative humidity of 80% is shown given that S, N and R are relative to the cement (slow, normal, rapid).

A more simplistic form exists and is largely used by the design companies. It is expressed as follows:

$$E_{c,eff} = \frac{E_{cm}}{3} \qquad \text{Eq. 2.4}$$

On 14/2/2019, during the construction of the piles, 10 cylindrical samples (11 x 22 cm) were taken from three different concrete mixers. The samples were labeled as follows:

- Mixer 1: Samples 1a / 1b / 1c / 1d
- Mixer 2: Samples 2a / 2b / 2c
- Mixer 3: Samples 3a / 3b / 3c

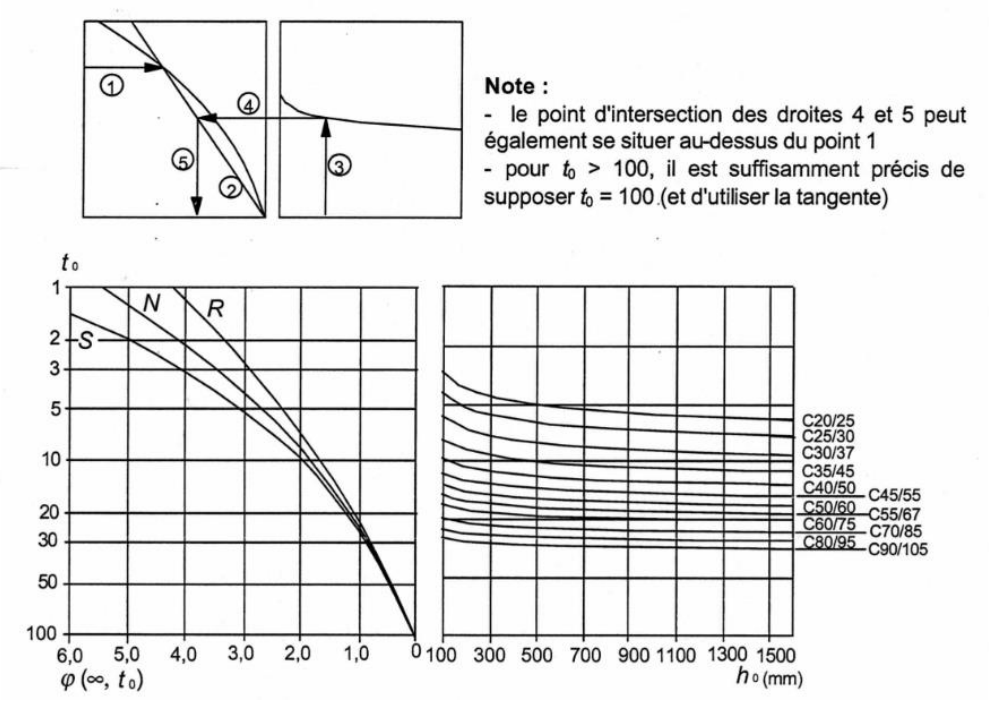

Figure 2.5 Chart used to determine the creep coefficient in an external environment - RH = 80% (Eurocode 2, 2005)

Three groups of tests were planned for different stages i) after 28 days, ii) when half of the total load was applied on the foundations, and iii) at the end of the construction in order to evaluate the maximum compressive strength and the deformation modulus of the concrete. The batches of concrete crushing tests were performed as follows:

- After 28 days approximately (29/3/2019): Samples 1a / 2a / 3a shown in Figure 2.6
- At mid-load (23/7/2020): Samples 1b / 2b / 3b / 1d
- At the end of the construction (10/12/2020): Samples 1c / 2c / 3c

Unfortunately, a technical problem occurred during the second group of tests which gave non-usable results.

Figure 2.6 The three concrete cylindrical samples after the first batch of crushing tests

Three vertical and one horizontal electrical resistance strain gages were installed on each of the samples, measuring the axial and lateral deformations as a function of the applied load and time. The samples were analyzed individually allowing to determine the average characteristics of the concrete (Table 2.5).

Table 2.5 Calculations based on concrete crushing tests

		Batch 1 (1a/2a/3a) 29/3/19	**Batch 2 (1b/2b/3b/1d) 23/7/20**	**Batch 3 (1c/2c/3c) 10/12/20**
f_{cm} (MPa)	***Arithmetic mean***	**54.3**	x	**49.2**
	Std deviation	0.23		3.53
0.4 f_{cm} (MPa)	***Arithmetic mean***	**21.7**		**19.7**
	Std deviation	0.09		1.4
E_{cm} (GPa)	***Arithmetic mean***	**34.5**		**40.4**
	Std deviation	0.845		1.2
E_i (GPa)	***Arithmetic mean***	**39.2**		**44.4**
	Std deviation	0.68		2.4
$E_{cm,theoritcal}$ (GPa)			37.3	
$E_{i,theoritcal}$ (GPa)			39.1	

The tests performed on the 10/12/20 shows the modulus of the concrete at the end of the construction but they do not express the effect of the creep since no load was applied on the sample during that time. The difference between the values may be due to test variability only, not showing necessarily the curing of the concrete. The value 34.5 GPa was adopted in the analysis.

In reference to Eurocode 2 (2005), the concrete modulus used in the calculations depends on the load and the construction phase. For example, for short-term analysis and accidental loads, a short-term modulus equal to E_{cm} is used, more particularly for SLS characteristic, ULS D&T (wind effect) or ULS seismic load combinations. However, in long-term analysis such as SLS Quasi-Permanent combination, a reduced value is generally used.

Based on the results of the first batch of tests, the "effective modulus" can now be calculated using the measured E_{cm} and the $\phi(\infty, t_0)$ given from the curves in Figure 2.5. The age of the first loading t_0 is estimated at 45 days which happened to be the date of the first batch of crushing tests. Therefore, the modulus of the deformation $E_{cm}(t_0)$ is 34.5 GPa and $\phi(\infty, t_0)$ is estimated at 1.2.

$$E_{c,eff} = \frac{E_{cm}(t_0)}{1 + \phi(\infty, t_0)} = \frac{34.5}{1 + 1.2} = 15.7\ GPa \qquad \text{Eq. 2.5}$$

This modulus will be used later in the numerical models in order to be able to visualize the permanent deformations generated due to the creep.

It should be also noted that in the documents circulated by "Eiffage Construction Confluence", the secant and the effective moduli used for short- and long-term analyses were 33 and 10 GPa respectively. This difference will be considered in case of any comparison.

3- Soil formation characteristics

The current paragraph outlines some of the aspects and the characteristics of the soil layers in the Lyon region. It covers also the results of the experimental tests previously carried out in the neighborhood since the 1970s.

3-1- Lyon subsoil conditions

In the geological periods of the Oligocene and Miocene (about 35 to 5 million years ago), the Alps was formed because of the collision between the African and the Eurasian tectonic plates. It was subject to many cycles of erosions that abandoned the materials at the foot of the mountains resulting in the actual subsurface layers (Rousset, 2013).

The geology of Lyon was studied by many authors (Dumollard, 1963; David, 1967; David, 1973; Lareal, 1975). It is characterized by the presence of four main types of soils and rocks that are either primary, secondary, tertiary or quaternary according to their age. In order to study the geotechnical aspect in this project, the focus will be placed on the behavior of the molasse and the alluviums, the shallowest layers which belong to the last two ages respectively.

The layers forming the subsoil in Lyon are listed below, by increasing order of altitude level.

- Embankment: Sandy-Clayey gravels and sandy silts with gravels and pebbles

- Alluviums: Modern and fluvial, they consist of sands and gravels. Some lenses of silty or clayey sands may be found in the middle of the Rhône's alluviums layer. In Part-Dieu, it was noticed that the thickness of these lenses varies between 1 to 4 m.

- Molasse: It represents the substratum in Lyon, especially in the zone located at the left bank of the Rhône River. Dating from the Miocene era, it is formed either by fine sands called in French "Saint-Fons" or by clay and ferruginous stones known as "du Jardin des Plantes" (Lareal, 1975).
  The molasse is the local term for sedimentary rocks formed of sandstone, mudstone and marl. In Part-Dieu, they consist of sandy-silty to sandy-gravelly beige sands that have indurated layers.
  The roof level of the molasse is about 19 m from the natural ground level (168 m NGF). It is not constant as shown in Figure 2.7.
  The substratum is at 70 m from the natural ground level according to the BRGM (Synthèse hydrogéologique de la Molasse miocène 86 SGN 016 RHA de 1986, Bureau de Recherches Géologiques et Minières). It was also estimated at 96 m NGF, according to data collected from a drilled borehole in "Archives départementales" site, hundreds of meters away from Silex[2].

- Clay: This formation dates from the Oligocene period. It consists of highly overconsolidated greyey clay located at 70 m depth approximately.

The following sections present the results of the experimental tests carried out in Part-Dieu and in Bugey, a nearby region.

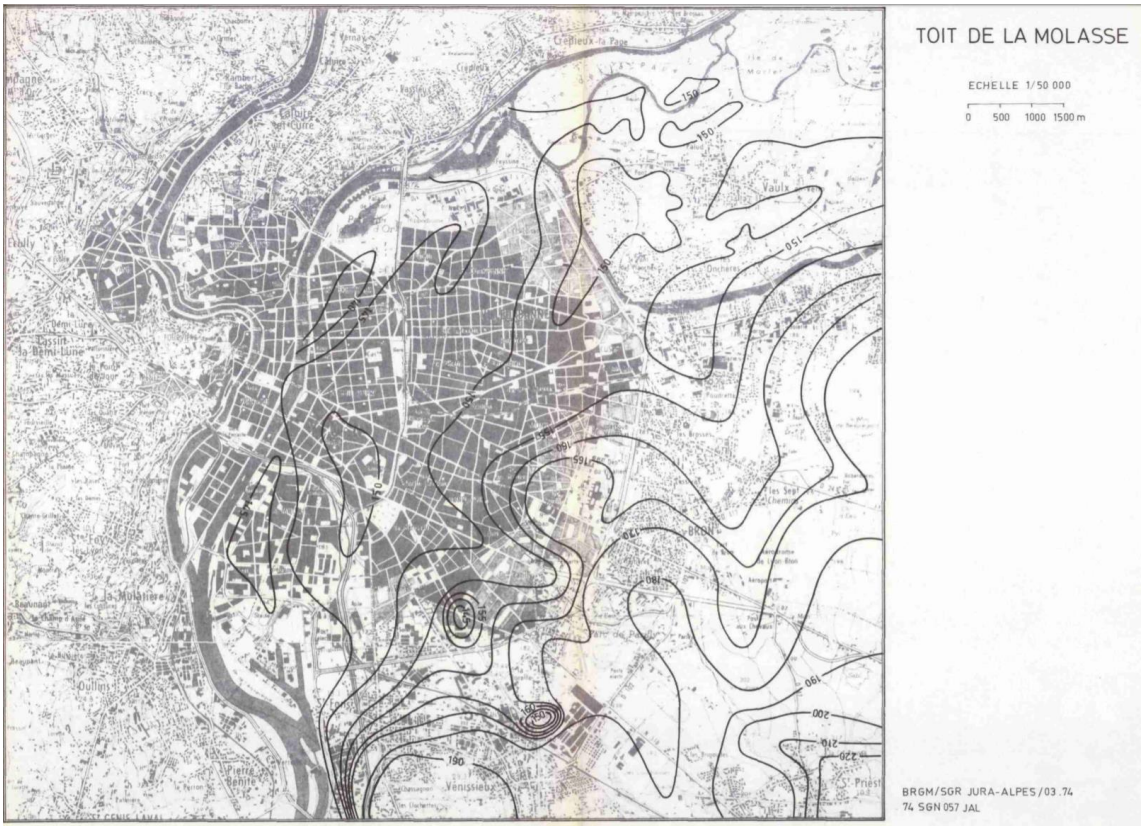

Figure 2.7 Altitude of the molasse layer in Lyon (Gudefin and Rousselot, 1974)

3-1-1- Overview on the previous works in Part-Dieu

The need of experimental sites in Part-Dieu goes back to the construction of the metro lines. Studies were made by many researchers to understand the behavior of the fluvial alluviums especially following the construction of diaphragm walls. Ever since, many studies have emerged in the literature (Waldmann and Ferrand, 1970; Waldmann et al., 1971; Kerisel and Lareal, 1971; Kerisel et al., 1972; Lareal et al., 1973; Lareal, 1975; Kastner and Lareal, 1975).

An instrumentation was carried out by Kastner (1982) during the construction of the metro lines A and B in order to measure the displacement of the soil and the structure, the efforts in the struts, the wall curvature and finally the soil properties at failure.

An experimental device has already been set up to perform direct shear tests on the alluviums on site (Waldmann et al., 1971). It was also used later by many other authors (Lareal, 1975; Kastner, 1982; Bourdeau et al., 1989; Bourdeau, 1997). The main reason to fall back on in-situ tests in case of alluviums is that they can lose easily their cohesion.

As represented in Figure 2.8, the dimensions of the direct shear box were 0.6 m x 0.6 m x 0.4 m. The maximum normal stress that could be applied was 158 kPa and the shear displacement was being controlled at a velocity of 1 mm/min.

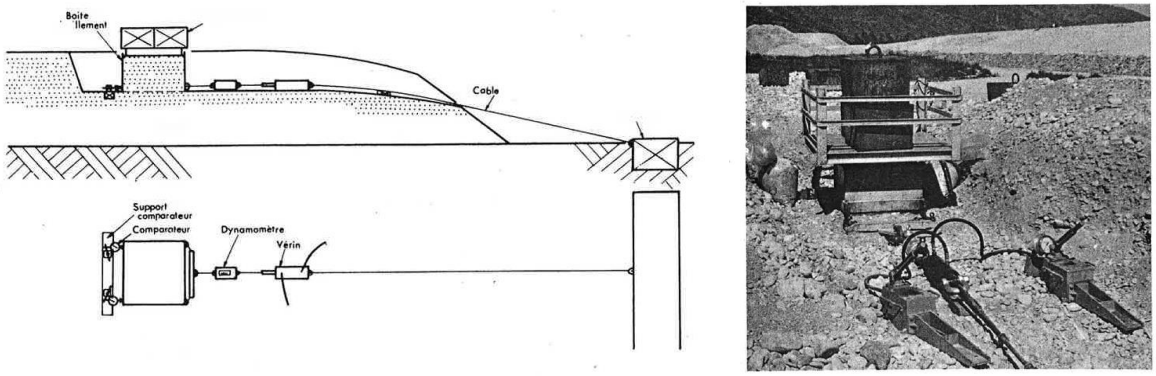

Figure 2.8 Direct shear box designed by Waldmann et al. (1971) as cited in Lareal (1975)

It was found that the dry density of the fluvial alluviums varies between 21.5 and 22.5 kN/m^3 and the horizontal permeability was estimated at 10^{-2} m/s (Kerisel et al., 1972; Lareal, 1975).

The experimental tests carried out on the experimental site of the Lyon metro are summarized in Table 2.6.

Table 2.6 Geotechnical characteristics of the alluviums at Part-Dieu

Author	Site location	Results
Lareal, 1975	Site in Part-Dieu	$28° < \phi < 35°$ c = 12 kPa *These results correspond to soils with a maximum depth of 5.5m*
	Site 1 in Gervans	$\phi = 34°$ c = 19.6 kPa
	Site 2 in Gervans	$\phi = 22°$ c = 24.5 kPa
	Site 3 in Gervans	$\phi = 33°$ c = 25.8 kPa
Kastner, 1982	Site in Saxe-Gambetta	Peak resistance: $\phi_{avg} = 33°$ c_{avg} = 24.5 kPa Resistance at 50 mm of displacement: $\phi = 29°$ c = 10 kPa *The pseudo-cohesion value obtained (20-25 kPa) is due to grain entanglement*
Bourdeau et al., 1989	Several locations in Lyon	*$28° < \phi < 33.6°$ 5 kPa < c < 28 kPa* *These results correspond to tests with normal stress between 50 and 160 kPa.*

The high compactness of the alluviums gives it dilatancy properties. The stress-displacement curves thus presented a remarkable peak found in all the tests. It has been also shown that the soil presented a lower shear resistance for low dry density and a higher water content. A non-zero value of the cohesion may be due to grain entanglement known in French as “enchevêtrement des grains” and capillary forces due to the observed moisture content (Lareal, 1975).

The alluviums’ shear behavior characterized by their cohesion and dilatancy was also seen in the 27 tests carried out by Bourdeau (1997).

Besides, empirical equations were determined for the alluviums relating the friction angle and the cohesion to the displacement in the shear box. One of these equations uses the peak cohesion and friction angle as follows:

$$C_{peak}(kPa) = 49 - 1.08\,\phi_{peak}\,(°) \qquad \text{Eq. 2.6}$$

On the other hand, a finite element numerical analysis was performed by Kastner (1982) using the software Rosalie. The elastic plastic constitutive model characterized by a hardening developed by Monnet and Gielly (1979) was employed to describe the behavior of the alluviums using a young modulus of 73 MPa, a cohesion of 24.5 kPa, a friction angle of 33° and an intergranular friction angle of 25°. The main advantage of this method is that it uses only 4 parameters. However, the calculation at that time was too long and expensive.

Pull-out tests were conducted on a portion of a diaphragm wall completely cast in the alluviums in Part-Dieu (Kerisel and Lareal, 1971; Lareal, 1975). The deformation modulus was estimated by Lareal (1975) as follows:

$$E\,(MPa) = 12 + 37z\,(m) \qquad \text{Eq. 2.7}$$

The ultimate unit skin friction was estimated at 60 kPa for a displacement of 40 mm. It was found that 50% of this value was mobilized by a displacement of 4.5 mm only.

3-1-2- Bugey power station

The only feedback on the molasse goes back to the construction of the ICEDA treatment and storage facility at Bugey, 30 km east of Lyon. It was noticed that in this location, the molasse is weathered in the upper 5 meters (Mattsson et al., 2013) and unlike the subsoil in Part-Dieu, there is a clay layer between the alluviums and the molasse. Despite the fact that the rigid inclusions were not embedded in the molasse and thus the load tests performed do not give much information about the behavior of this layer, some of the observations are presented hereafter.

- Characterization of the alluviums

The alluviums at Bugey's location seem to have a bulk unit weight of around 21 kN/m^3 and a saturated unit weight of 22.5 kN/m^3. Consolidated drained triaxial tests with a confining pressure of 50 to 500 kPa were carried out on samples with maximum grain size of 10 mm. In addition, pressuremeter tests were carried out as well as plate load tests in order to determine the deformation moduli. Due to many reasons related to the disturbance of samples in the triaxial tests and the inevitable slackening of the bottom of the excavation in the plate load test, the modulus was in general underestimated (Table 2.7). On the other hand, an instrumentation was performed and was calibrated with a numerical model showing a higher value (300 MPa). For all these reasons, an average value of 160 MPa was found suitable at that time.

Besides, Crosshole and Downhole seismic tests were performed on the alluviums showing that the average vertical velocity is only 10% lower than that of direct horizontal paths. Therefore, there does not seem to be any particular anisotropy in the alluviums.

➢ Characterization of the molasse

On another note, the molasse presented a 5-m layer of weathered material over a deeper layer of good quality. Laboratory tests on molasse samples showed a unit weight of 20.7 kN/m^3 and a dry unit weight of 17.5 kN/m^3. Identically, Crosshole and Downhole seismic tests did not show any global anisotropy in molasse layers.

Results for both soil layers are summarized in Table 2.7.

Table 2.7 Geotechnical characteristics of the alluviums and the molasse at Bugey's location

	Test	Results
Alluviums	Consolidated drained triaxial test	Mechanical resistance parameters: $\phi' = 42°$, c' = 0 kPa Young's modulus: E_y = 90 MPa
	Pressuremeter test	E_M = 46 MPa, E_y = 160 MPa P_l* = 4.6 MPa
	Plate load test	E_y = 80 MPa
Molasse	Consolidated drained triaxial test	Altered molasse (first 5 meters): $\phi' = 32°$, c' = 50 kPa Good molasse (at higher depth): $\phi' = 32°$, c' = 140 kPa
		The existence of cohesion even for low confining pressures is explained by the high compactness and the strong over-consolidation of the soil.
	Pressuremeter test	For weathered molasse: E_M = 14.3 MPa P_l* = 1.7 MPa For deep molasse: E_M = 172.8 MPa P_l* = 7.3 MPa
		Results from previous campaigns show the following values: E_M = 145 MPa (first loading) E_{MR} = 1430 MPa (reloading)
		The selected values are E_y = 340 MPa for undisturbed molasse and E_y = 100 MPa for the altered layers

3-1-3- Site investigations made by Antea Group (2010, 2014)

During the last two decades, the soil of Part-Dieu was investigated for several construction projects in the same area. Particularly, during the construction of the two towers "Oxygène" and "INCITY" in 2007 and 2014, several core drillings and pressiometric boring were performed. Based on the findings from the experimental tests carried out, a soil profile characterized by two separate layers of alluviums and molasse was established. Results from pressuremeter tests are shown in Table 2.8.

Table 2.8 Parameters from pressuremeter tests performed on the alluviums and the molasse

Project	Alluviums		Molasse	
	E_M (MPa)	**Pl* (MPa)**	**E_M (MPa)**	**Pl* (MPa)**
Oxygène	67	6.9	80	7
Incity	46	3.5	208	6.9

It was noticed that the values are scattered. It can be either due to the variability of the mechanical characteristics of the layers or to test conditions. In order to be more precise about these parameters, it was better for the tests to be in the exact location of Silex^2. Therefore, some additional drillings were performed back in 2010 and 2014. These tests allowed separating the alluviums layer into three sub-layers because of the difference in the geotechnical characteristics. The levels of the subsurface layers encountered together with their description are summarized in Table 2.9 and Figure 2.9.

Table 2.9 Subsoil layers encountered in Silex^2 location in a drilling performed in 2014

Soil layer	Top level (m NGF)	Average thickness (m)	Description
Embankment	168	3.5	Sands and gravels up to 5 cm in diameter
Alluviums 1	164.5	6.75	Sand, gravels and sandy gravels of medium to good compactness with a diameter between 30 and 100 mm
Alluviums 2	157.75	4	Sandy lenses of low compactness
Alluviums 3	153.75	5.75	Sand, gravels and sandy gravels of medium to good compactness with a diameter between 30 and 100 mm
Molasse	148	> 10	Silty sand soil that present greasy indurated clayey layers

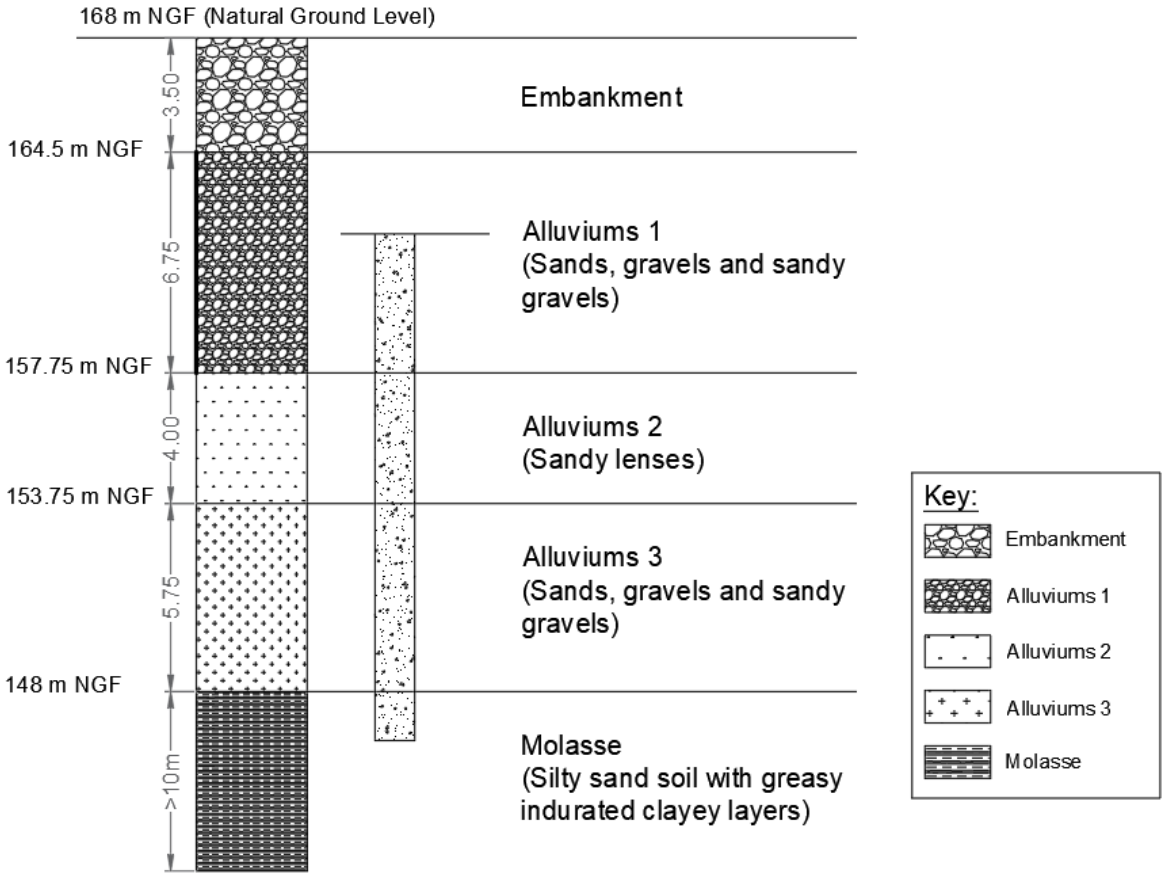

Figure 2.9 Soil profile at the location of Silex^2

The pressuremeter results undertaken for the alluviums and the molasse layers in the same investigation campaign are shown in Table 2.10.

Table 2.10 Geotechnical characteristics of the soil layers

Soil layer	Number of tests	Pressuremeter modulus E_M (MPa)		Limit pressure p_l* (MPa)	
Embankment	4	4.3*	2.5**	0.4*	0.2**
Alluviums 1	25	62*	34**	4.5*	3.9**
Alluviums 2	9	8*	3.7**	1.4*	0.6**
Alluviums 3	26	67*	38**	4.7*	3.8**
Molasse	21	95*	56**	4.8*	4.6**
** Harmonic value*	*** value at 5% fractile*				

Numerous classification methods for the soils exist in the world. They are based on sieve analysis results as well as Atterberg limits which are generally measured within the fine particles or more particularly the soil measuring less than 0.4 mm. The methods include:

- Unified Soil Classification System (USCS)
- Soil Classification System developed by the American Association of State Highway and Transportation Officials (AASHTO)
- GTR classification system (Guide des terrassement routiers)
- Fascicule 62 – Titre V
- Classification des Laboratoires des Ponts et Chaussées (LPC) which is an adapted version of the USCS.

The following analysis is based on Magnan (1997). Sieve analysis tests were carried out on 11 different samples. However, Atterberg limits were not measured and additionally, according to the standard NF EN ISO 17892-4 (2018), no sedimentation test is required if a sample contains 10% or less of particles measuring less than 0.063 mm. The results are shown in

and Figure 2.10.

Table 2.11 Soil classification according to LPC, Fascicule 62 and GTR systems

Soil layer	D_{max} (mm)	LPC (USCS)	Fascicule 62	GTR
Alluviums 1	50/80	Gm (GP)	Clean gravels	D2/D3
Alluviums 2	20/50	Sm – SL (SP – SM) / Sm (SP)	Transition sands / Clean sands	-
Alluviums 3	31.5/80	Sm – SL (SP – SM)	Transition sands	D3
Molasse	20/31.5	Sm – SA (SP – SC) or Sm – SL (SP – SM) / SL (SM) or SA (SC)	Transition sands / Silty or Clayey sands	B5/D2

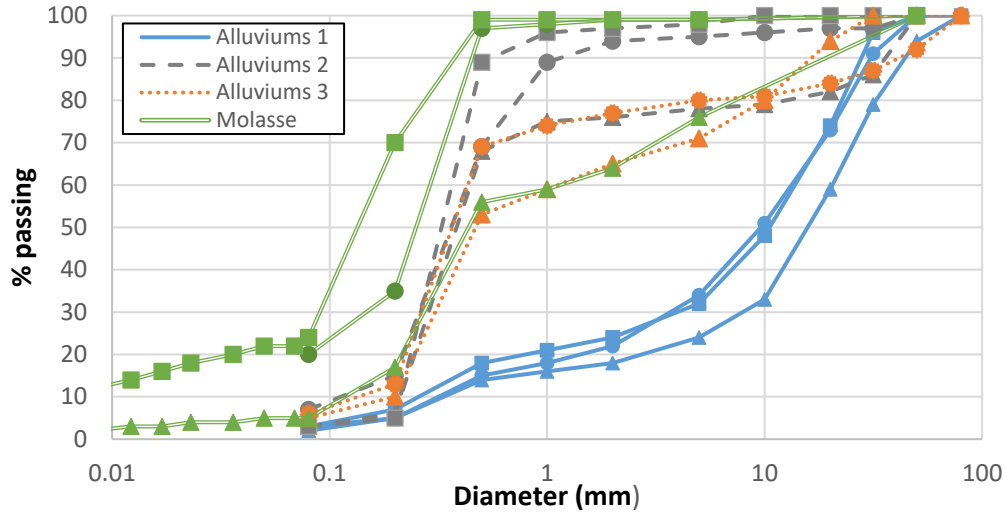

Figure 2.10 Sieve analysis results for alluviums and molasse samples

3-2- Hydrogeological hypotheses

Due to its proximity to the Rhône and Saône rivers, the city of Lyon is characterized by a very shallow ground water table. The different water levels are presented in Table 2.12.

Table 2.12 Different characteristics levels of the water table in Lyon

Characteristic levels of the water table	Description	Elevation (m NGF)
Quasi-permanent level	Level likely to be exceeded during the half of the reference time	162.5
Frequent high level	Level likely to be exceeded for 1% of the reference time	163.1
Frequent low level	Level likely to be exceeded for 1% of the reference time	161.9
Characteristic level	50-year return period level	164.4
10-year level	10-year return period level	163.9

The basement was considered floodable from a level of 164.4 m NGF. As previously shown in Table 2.2, the level of the piles head is below that of the water table, if a quasi-permanent level is to be assumed. Therefore, the contractor has opted for lowering, by 1.3 m approximately, the water table level using 6 pumps installed at different locations. During the piles execution, the water table was at 161.3 m NGF while according to a piezometric measurement right before and after the pumping, it was at 162.5 m NGF approximately. In the numerical analysis of the thesis, the frequent low level 161.9 m NGF was used.

The presence of water in superficial layers of alluviums made the design and the construction more challenging and this needed a good understanding of the behavior of both alluviums and molasse in presence of water by a good evaluation of their permeability. There are two underground water tables in Part-Dieu: one in the alluviums and a deeper one in the molasse. They are characterized in the following paragraph.

3-2-1- Characteristics of the alluvial water table

In his study on both alluviums and molasse, Kastner (1974) estimated the horizontal permeability of the alluviums at 10^{-2} m/s, while the vertical component was lower because of some layers of sandy lenses. On the other hand, measurements taken by Antea Group in 2014 showed a value of 4.6×10^{-3} m/s. It can be concluded that the alluviums are highly permeable.

The general flow of the water table is from Northeast to Southwest direction. The local flow is from east to west with a low gradient of about 1‰. Because of the huge number of diaphragm walls and underground structures existing in Part-Dieu and anchored in deep layers, such as the walls for Metro Line B and the shopping mall and the underground parkings to the east and northwest of the Part-Dieu station, the flow of the underground water table is subject to major changes. These walls anchored in the molasse in several locations form an obstacle to the alluvial groundwater flow.

3-2-2- Characteristics of the molasse water table

Similarly, the water table of the molasse flows in the same direction and with the same gradient. Unlike the alluvial water table, it is slightly influenced by the underground structures.

Its vertical permeability is relatively low compared to its horizontal permeability and to the permeability of the alluviums as well. Besides, it was noticed that this permeability decreases for higher depths where the soil becomes siltier.

Table 2.13 shows the permeability values measured in Part-Dieu and in other locations. It was recommended to measure the permeability of the molasse in the laboratory using oedometer apparatus. Several tests were conducted and they gave values between $5 \times 10^{-6} – 10^{-5}$ m/s, showing a relatively permeable soil.

Table 2.13 Permeability values of the molasse in different locations in Lyon

Reference	Location	Permeability
Kastner, 1974	Part-Dieu sites	LeFranc tests: $K_h = 1 – 2 \times 10^{-4}$ m/s (0 – 3 m) $K_h = 5 – 7 \times 10^{-5}$ m/s (3 – 15 m) Laboratory tests: $K_v = 0.75 – 1.5 \times 10^{-5}$ m/s (0 – 3 m) $K_v = 0.75 – 1.5 \times 10^{-5}$ m/s (3 – 15 m) Micromoulinet test: $K_v = 2.4 – 3 \times 10^{-5}$ m/s (3 – 15 m)
Tests performed at Antea Group in 2014	Nouvelles Archives départementales	$K_{v, avg} = 4 \times 10^{-6}$ m/s
	Centre Leon Bérard	$K_{v, avg} = 7.5 \times 10^{-5}$ m/s
	Piscine de Bron	$K_{v, avg} = 2.5 \times 10^{-5}$ m/s
	Tour Oxygene	$K_{v, avg} = 5 – 8 \times 10^{-5}$ m/s
Tests performed at the INSA in 2019	Silex[2] site	$K_{v, avg} = 5 \times 10^{-6} – 10^{-5}$ m/s

Based on all these results, the permeability of the molasse varies between 5×10^{-6} and 8×10^{-5} m/s. It is considered as relatively permeable.

3-2-3- Pore water pressure generation

Driven piles, in general, are more subject to a high generation of pore pressure at the pile tip due to the resistance of the soil against its penetration. This was shown by different authors for various types of piles and soils (Seed and Reese, 1955, 1957; Bjerrum and Johannessen, 1960; Lambe and Horn, 1964; Burns and Mayne, 1999; Wang et al., 2020). On the other hand, pile drilling may also result in the generation of a pore water pressure. This can lead in general to volumetric strains or a reduction of bearing capacity of soils (Ahlund and Ögren, 2016). The amount of strains developed varies in a non-liquefiable soil and a liquefiable one depending on its density (Nagase and Ishihara, 1988).

When a load is applied on a dry soil, the grains tend to move closer due to the induced compression. However, in a saturated soil, the soil cannot compress since the voids are filled with incompressible water resulting in an increase of the pore water pressure. This behavior varies from highly permeable soils (sands) to highly impermeable soils (clays). In the first case, the water can flow through the particles decreasing its pressure and allowing the consolidation of the soil. The flow of water in the soil is called seepage which can be upward or downward (or lateral) and results in the decrease or the increase of the effective stress respectively. In impermeable soils, the excess pore water cannot dissipate easily and this causes the water to be trapped in the soil increasing its pressure.

The permeability, also known as the hydraulic conductivity, is then the parameter that allows to evaluate the time needed to dissipate the excess pore pressure. It depends on the grain size distribution, the void ratio, the fluid viscosity and the soil saturation. Table 2.14 shows typical values for different types of saturated soils.

Table 2.14 Typical values for permeability for different saturated soils (Ahlund and Ögren, 2016)

Soil type	Hydraulic conductivity K (m/sec)
Clean gravel	$1 – 10^{-2}$
Course sand	$10^{-2} – 10^{-3}$
Fine sand	$10^{-4} – 10^{-5}$
Silty clay	$10^{-5} – 10^{-7}$
Clay	$< 10^{-8}$

4- Geotechnical instrumentation of Silex^2

The evaluation of the pile performance is not only based on the ultimate capacity (Chan and Lee, 1990; Chan, 2004) but also on the ultimate shaft and base loads together with the pile and soil stiffnesses (Fleming, 1996). In addition, displacement analysis is nowadays required in any pile design. This starts by plotting the pile load-settlement curve. To do so, and since the soil is not homogenized underneath the tower, load transfer curves at different depths are needed as seen in the LTM in Chapter 1. These cusrves are determined from previous experiences shown in the literature or in a specific site, they may be determined from instrumented piles (Bersan et al., 2018). This section presents the geotechnical instrumentation conducted in this project with the aim of analyzing the piles' performance.

4-1- Instrumentation selection in Silex^2

4-1-1- How to set up an instrumentation plan

"The purpose of geotechnical instrumentation is to assist with answering specific questions about ground/structure interaction. If there are no questions, there should be no instrumentation" (Dunnicliff and Powderham, 2001).

Before starting any geotechnical instrumentation project, it is essential to list the objectives of the project, the parameters to be measured with the expected values and how these parameters will help assessing the structure/soil performance and finally the best places to install the sensors (Eberhardt and Stead, 2011).

Dunnicliff (1988) presented an approach to plan any monitoring program. The main steps are:

- Definition of the project conditions
- Definition of the geotechnical questions that need to be answered
- Definition of the purpose of the instrumentation
- Selection of the parameters to be monitored
- Prediction of the magnitudes of change
- Selection of the instruments
- Choice of the instrument locations
- Setting up the installation plan
- Planning a regular calibration and maintenance
- Selection of data acquisition systems
- Planning the data collection, the processing, the interpretation and the reporting

The number and type of sensors used in a project strongly depend on the objective of the instrumentation, i.e., the desired parameters. For example, in order to be able to measure the load displacement or the load transfer, axial load cells, axial displacement instruments and strain gages are required. Besides, a pore pressure transducer and Osterberg cells can be used to measure the pore pressure change and the pile tip load respectively (Bica et al., 2014).

Different sensors may measure identical or related parameters, in order to check the consistency of the measurements. This is called "redundancy" in metrology and it is split into time and spatial redundancy. The former includes the acquisition frequency that should be sufficient to be able to detect incorrect

measurements and at the same time, should not weigh down the program. Briançon et al. (2016) suggested 12 to 24 measurements to be used per day in geotechnical engineering applications. Spatial redundancy comprises the installation of several sensors of the same type. This increases the reliability of the measurements, reduces the risk of incorrect measurements and limits the risk of losing information.

Generally, sensors that are easy to be installed, and simple to manipulate are preferred. A good choice of the types and numbers of selected sensors is necessary. At the same time, the person in charge of taking the measurements must have a good knowledge in geotechnical and a good understanding of the operating mode of the sensors. In addition, he must have precision, motivation, patience, perseverance and critical thinking. Besides, the instrumentation plan should be compatible with the initially listed objectives, capable of catching the desired resolution and durable to ensure long-term performances (Reese, 1969).

4-1-2- Application to Silex^2

In order to produce pile load settlement curves and to understand their behavior, sensors capable of measuring the stress and the deformation should be installed. Besides, the settlement of the soil under the tower is a very important parameter and should be measured as well.

Sensors need to have the following specifications:

- To be easy to be installed and simple to manipulate
- To be adequate for concrete
- To withstand temperature variation during concrete pouring, knowing that the expected ranges of temperature are between 20 - 25°C in the lab and (-5) - 60°C on site. This covers also the temperature in the first hours after pouring, before reaching an approximate constant value of 20°C.
- To have a lifespan of at least 10 years for long-term measurements

Based on the above, five types of sensors were selected for installation in Silex^2, according to the available instruments in the market, the parameters needed, the budget and the previous experience in the field.

Therefore, electrical resistance strain gages (ERSG), vibrating wire strain gages (VWSG) and fiber optic sensors (FOS) were used to measure piles deformation. Concrete pressure cells (CPC) were installed on the head of the piles to consider the applied stress. Finally, a fiberglass rod extensometer was set up in the soil to quantify its settlement at different altitudes.

All the used instruments, except optical fibers, are analog. Meaning they provide an electrical quantity as an output (voltage, current, resistance, etc.) as opposed to numerical or logical sensors.

On the other hand, the piles to be instrumented were chosen in a way to provide a wider range of information. Since the foundation plan is nearly symmetric, instrumenting only six piles (17A/B, 18A/B and 20 A/B), shown in red in Figure 2.4, was sufficient to deduce the deformations and stresses for the others.

In each pile, the strain gages were placed at 3 different depths in order to be able to catch the load transfer along the pile. Three concrete pressure cells were distributed in a symmetric way on the head of the pile in order to cover the whole section.

The used instruments are detailed in the following section.

4-2- Instrument identification system

An identification system was developed to show the location and the type of instrument installed in the corresponding pile. It has the following format: A-B-C-D-E according to Table 2.15.

Table 2.15 Identification system for all types of sensors

Sensor type	A	B	C	D	E
	Sensor type *(VWSG, ERSG, CPC, POT, FOS)*	**Pile number *(17A/B, 18A/B and 20 A/B)***	**Sensor number**	**Position in the pile**	**Position in the soil**
VWSG	x	x	x	x	
ERSG	x	x	x	x	
CPC	x	x	x		
POT	x				x
FOS	x	x	x		

For example:

- POT-2m is a potentiometer that measures the displacement of the soil at 2-m depth.
- VWSG-18A-12-Level1 is a vibrating wire strain gage (#12) located at the "level 1" in the pile 18A.

The levels at which the deformation sensors were installed are: Level 1 (11.2 m), Level 2 (4.25 m) and Level 3 (0.65 m), the distances being measured from the bottom of the reinforcing cage.

4-3- Instrumentation of pile foundations

4-3-1- Measurement of pile deformation

With a view to evaluate the skin friction mobilized along the pile, three types of sensors were used as indirect systems. This means that the load is calculated from the deformation measured using i) vibrating-wire strain gages, ii) electrical resistance strain gages and iii) strain optical fibers.

4-3-1-1- Vibrating Wire Strain Gages (VWSG)

Andre Coyne, a French consultant engineer, was the first to evaluate the strain by measuring the frequency of a wire in 1931, before vibrating-wire strain gage were made commercially available in Europe. The first models were installed in 1932 in Bromme Dam in France (Bordes and Debreuille, 1985). Ever since, a big variety of this type of sensors has been expanded in the whole world.

A vibrating-wire strain gage measures the deformation based on the variation of the natural frequency of a tensioned wire when it is compressed or extended. An electromagnetic coil positioned next to the wire can detect this change. The different components of the VWSG are shown in Figure 2.11.

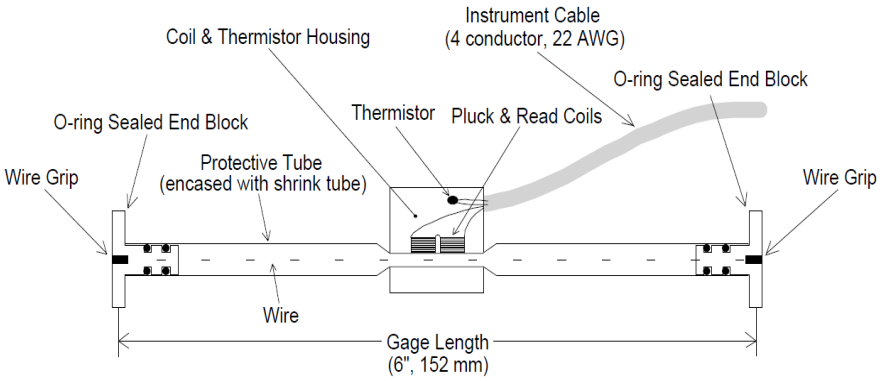

Figure 2.11 A typical model of vibrating wire strain gages (Hayes and Simmonds, 2002)

Measuring the strain through frequency variation is advantageous since voltage drops - caused by weather changes, corrosion or moisture - do not affect the frequency output (Hayes and Simmonds, 2002). The VWSGs were chosen because of their i) small size, ii) moisture resistance, iii) long term stability under static loading (McRae and Simmonds, 1991) and iv) possibility of using long cables without significant loss of accuracy (Paikowsky and Hajduk, 2004; Bica et al., 2014).

However, difficulties may be encountered when dealing with VWSGs especially to measure stresses due to residual load effects that are generally difficult to be detected in bored piles (Fellenius, 2002), but this aspect is not covered in this project where only relative deformation is measured. In addition, these sensors are unable to monitor rapidly changing parameters (Hayes and Simmonds, 2002). This inconvenient does not cause any major problem because the load is applied slowly.

Fourteen arc-weldable vibrating-wire strain gages of the model provided by SISGEO and shown in Figure 2.12 were installed in five of the instrumented piles following the schedule shown later in Table 2.18. Their typical frequency range is 520 – 1 020 Hz. Therefore, they can measure a strain value in the range 2 500 με (± 1 500 με). VWSGs have also a built-in thermistor that can measure the temperature of the structure where they are installed.

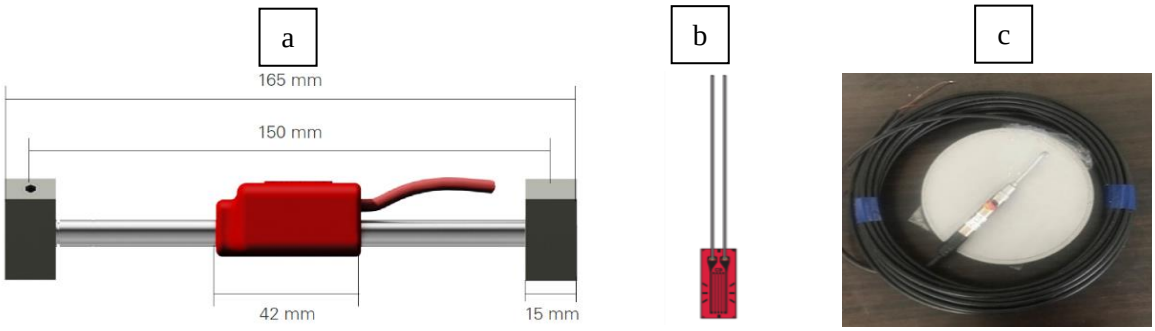

Figure 2.12 Different sensors used in Silex[2]: (a) VWSG, (b) ERSG and (c) CPC

The formula relating the deformation with the frequency was first expressed by Hawkes and Bailey (1973) as follows:

$$\mu\varepsilon\ (\mu m/m) = \frac{4L^2\rho\, f^2}{Eg} = f^2\, G \qquad \text{Eq. 2.8}$$

Where G is the gage factor, f the natural frequency, L the length of the vibrating wire, ρ the density of the wire material, E the modulus of elasticity of the wire and g the acceleration due to gravity.

Particularly, the strain gages used in this project have a gage factor of 4.043 (obtained from the compliance certificate) and the vendor suggests the following equation to calculate the total deformation using this factor:

$$\mu\varepsilon = (f^2 \times 10^{-3})\ G \qquad \text{Eq. 2.9}$$

Thus, since the wire is initially under tension, the relative measured deformation can be expressed as:

$$\Delta\mu\varepsilon = L - L_0 = (f^2 - f_0^2)\ G \qquad \text{Eq. 2.10}$$

It is important to know that the temperature change in the concrete can cause a strain change. Some strain gages, are thermally matched to the structural member. In that case, stress changes are calculated immediately from the change in the strain gage reading without any temperature corrections. For other types of gages, measured strains result from both temperature and stress variations and it should be calculated as their summation. The steel used for the vibrating wire and the concrete have a thermal expansion coefficient of CF_1 = 12.2 με/°C and CF_2 =10.5 με/°C respectively. The Eq. 2.11 calculates the total strain in the concrete corrected from thermal effects on the gage between two different moments defined by the indices "0" and "e". This equation includes the effects of the load variations together with the temperature change in the concrete given by the two parameters T_0 and T_e. The thermal strain may be expressed by the Eq. 2.12 and it can be deducted from the total strain as in Eq. 2.13 in a way to obtain the concrete's strain given from load variations only.

$$\mu\varepsilon_{total} = (L_e - L_0) + [(T_e - T_0)\ CF_1] \qquad \text{Eq. 2.11}$$

$$\mu\varepsilon_{thermal} = (T_e - T_0)\ CF_2 \qquad \text{Eq. 2.12}$$

$$\mu\varepsilon_{load} = (L_e - L_0) + [(T_e - T_0)(CF_1 - CF_2)] \qquad \text{Eq. 2.13}$$

4-3-1-2- Electrical Resistance Strain Gages (ERSG)

Electrical resistance strain gages (ERSG) were chosen to provide redundancy in case of failure of VWSG. These sensors have a resistance that changes when subject to strain, i.e., to a change in length.

The variation of resistance and length are also related by the means of a gage factor and are expressed as follows:

$$\frac{\Delta R}{R} = \frac{\Delta L}{L} G \qquad \text{Eq. 2.14}$$

In general, the variation of resistance is measured using a Wheatstone bridge circuit, shown in Figure 2.13 that consists of four different resistances. R_1 and R_2 are fixed resistances, R_4 is a variable one and R_3 is the resistance that corresponds to the strain gage. The equation that defines the initial relation between these resistances is:

$$\frac{R_1}{R_2} = \frac{R_3}{R_4} \qquad \text{Eq. 2.15}$$

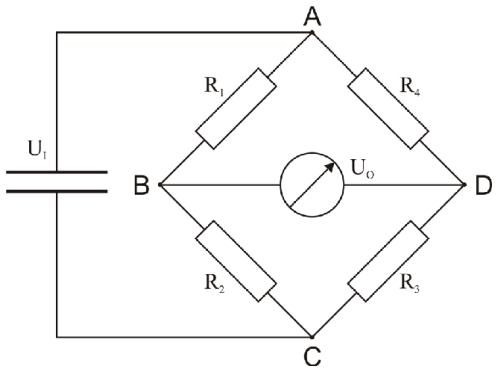

Figure 2.13 A classical Wheatstone bridge circuit

In the literature, many models of quarter, half or full bridges are available and they differ by their application, the number of wires and of active gages used). Table 2.16 shows in details all possible models with their use and limitations.

It was stated that the quarter bridge with two lead wires is the simplest but since the resistances of the wires are in series with the active gage, this makes it harder to differentiate the mechanical strain from the one caused by temperature change (Dunnicliff, 1988). In order to eliminate the effect of the temperature change in the wires, the quarter bridge with three lead wires (of resistance r) shown in Figure 2.14 was chosen. However, this configuration does not eliminate the influence of the temperature change in the gage since it is not compensated as in a half or full bridge. This temperature effect should be considered in the analysis.

The chosen circuit has four arms: two of them are inside the Datataker ($R = R_3 = R_4 = 350\ \Omega$), the active gage ($R_1 = 120\ \Omega$), which is installed in the pile and a dummy resistance that must be of equal value.

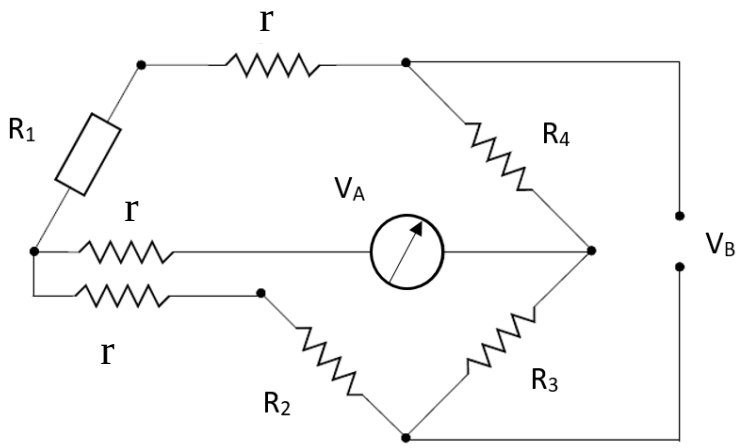

Figure 2.14 Quarter bridge circuit configuration used for the electrical resistance strain gages

Table 2.16 Possible configurations of Wheatstone bridge with their advantages and limitations (Dunnicliff, 1988)

Type	Advantages	Limitations
Full bridge (with dummy gages)	No temperature effects	Expensive
Full bridge (with both gages active)	No temperature effects	Expensive
Half bridge (with both gages active)	No temperature effects	Not suitable for biaxial stress fields/ Bridge is not always possible to achieve
Half bridge (with a dummy gage)	No temperature effects	The dummy gage should stay unstressed in the same temperature condition as the active gage
Quarter bridge (two-wire)	Easy to be installed and cheap	Sensitive to temperature change at gage and cables. Not suitable for geotechnical field usage because strain due to temperature cannot be differentiated from mechanical strain
Quarter bridge (three-wire)	No errors caused by temperature variation at cables	Sensitive to temperature change at gage

Based on the above, the initial equilibrium is:

$$\frac{R_1 + r}{R_2 + r} = \frac{R_3}{R_4} \qquad \text{Eq. 2.16}$$

Any strain change induces a variation of ΔR to the gage and Δr to the wires.

The following formula can be used:

$$\frac{V_A}{V_B} = \frac{\Delta R}{4((R + 2r) + 1/2\ \Delta R)} \qquad \text{Eq. 2.17}$$

But since r is small compared to R, this equation may be expressed as:

$$\frac{V_A}{V_B} = \frac{\Delta R}{4(R + 1/2\,\Delta R)} \qquad \text{Eq. 2.18}$$

What makes the use of electrical strain gages advantageous is that they are small and easy to be installed although they are not stable for long term and are generally more sensitive to humidity (Bica et al., 2014).

However, a model provided by KYOWA, shown in Figure 2.12, was found moisture proof and has excellent flexibility and thus thirty-six strain gages of this type were used in total as detailed later in Table 2.19. The strain gages have a resistance R_1 = 120 Ω and a gage factor 2.1 ± 1.0 %. In order to ensure an initial equilibrium, the dummy resistance R_2 had to be equal to 120 Ω as well.

When connected to a data logging system, a reading in ppm is provided for this type of bridges. The deformation can be estimated as follows:

$$\mu\varepsilon = \left(\frac{2}{Gage\ factor}\right) * Reading\ (ppm) \qquad \text{Eq. 2.19}$$

For this particular type of strain gages, the thermal output may be calculated using the actual temperature as follows:

$$Thermal\ strain\ \left(\frac{\mu m}{m}\right) = -29.51 + 2.56T\ - 0.0609T^2 + 0.3438\,.\,10^{-3}T^3 - 0.4794\,.\,10^{-6}T^4 \qquad \text{Eq. 2.20}$$

Both types of strain gages (mechanical VWSG and electrical ERSG) were distributed at three different depths. The exact position of the sensors with respect to the pile is shown in Figure 2.16.

4-3-1-3- Fiber optic sensors (FOS)

The previously described sensors are categorized as conventional instrumentation. For many decades, this type of instrumentation was convenient due to its limited cost compared to other types of instrumentation especially when it includes fiber optic sensors (FOS). However, it has various shortcomings. The number of sensors that can be installed in a pile, for example, is limited due to the cost, the cabling congestion and the limited number of ports in the used data acquisition systems (Bersan et al., 2018).

Since the pile-soil interaction is of interest in this thesis, fiber optic sensors were installed along the reinforcing cage of the piles in order to get a continuous distribution of the strain and consequently the mobilized shear stress. Six sensors provided by Dimione, the French distributor of LUNA products, were used. They were interrogated by the OdiSI 6100 which comprises an interrogator unit, a stand-off cable of 50 m and different remote modules that can be used for standard (10 m) and extended length (50 m) (Figure 2.15). The precision of this type of FOS is up to 1 με. The sampling resolution was set at 2.6 mm with a measurement rate equal to 10 Hz.

Figure 2.15 ODiSI 6 100 interrogator unit with the stand-off cable and the remote module

The six sensors were installed along the six instrumented piles in order to get the deformation profile. In some locations where the FOS is 20 m long, a jumper cable was used to bring the optical connector to the electrical cabinet located in the EDF tower (shown in Figure 2.4). Table 2.17 presents their lengths and positions.

Table 2.17 Locations and dimensions of the Optical Fibers

FOS Number	Length (m)	Extension Length (m)	Location
1	50	-	Pile 20B
2	30	20	Pile 20A
3/4	30	20	Pile 17B/17A
5/6	30	20	Pile 18B/18A

- Thermal compensation of strain measurements using FOSs

Identically to the classical strain gages, the deformation (με) in the FOS is calculated as the ratio of the change in length (μm) to the original length (m). However, the strains measured using the interrogator ODisI 6 100 are influenced by the change in temperature. This effect can be safely ignored if the variation generates a low thermal strain compared to the strain being measured. Otherwise, a temperature compensation is needed especially in the first few meters of the pile where the temperature variation is important and might generate high thermal strains. Kania et al. (2020) showed that the strain profile in an axially loaded pile underwent a great variation after making the thermal correction. Experiments are generally carried out using a strain and a temperature fiber optic sensor in a way to decouple both strain measurements. According to Kania et al. (2020), the mechanical strain after temperature compensation may be calculated as follows:

$$\varepsilon_m^z = \Delta\nu_s^z \, k_\varepsilon - (0.95 \, \Delta\nu_T^z \, k_\varepsilon + \Delta\nu_T^z \, k_T \, \alpha_L) \qquad \text{Eq. 2.21}$$

Where $\Delta\nu_s^z$ is the spectral shift in the strain cable at depth z which is influenced by the change in both temperature and strain, $\Delta\nu_T^z$ is the spectral shift in the temperature cable due to the change in temperature only. The spectral shift is measured in GHz.

k_ε and k_T are the strain and temperature conversion factors that are specific to each fiber and are expressed in με/GHz and °C/GHz and α_L is the thermal expansion coefficient of the fiber. The strain and temperature coefficients of a fiber are determined by applying on it a known mechanical strain or temperature and measuring the spectral shift. The calibration coefficient (GHz/με) is calculated by plotting the strain as function of the recorded spectral shift.

On the other hand, when exposed to a high temperature, the FOS and the pile in which it is installed experience the same thermal expansion. This comes from the fact that it is less stiff than the concrete or the steel of the pile (Luna Innovations Incorporated, 2013). Therefore, the thermal expansion coefficient to be used in Eq. 2.21 is equal to the coefficient of the monitored structure, i.e., of the pile in this case.

In Silex[2], the temperature was measured using the thermistor of the VWSGs and therefore the thermal and mechanical strains can be immediately calculated by using Eq. 2.22 and Eq. 2.23.

$$\varepsilon_m^z = \varepsilon_r^z - \varepsilon_{th}^z \qquad \text{Eq. 2.22}$$

$$\varepsilon_{th}^z = \Delta\nu_T^z \, k_T \, \alpha_L = \Delta T \, \alpha_L = \Delta T \, \alpha_p \qquad \text{Eq. 2.23}$$

Where ε_r^z is the measured strain and α_p is the thermal expansion coefficient of the pile calculated in terms of α_s of the steel and α_c of the concrete as follows:

$$\alpha_p \, A_b = \alpha_c \, A_c + \alpha_s \, A_s \qquad \text{Eq. 2.24}$$

A_c and A_s are the cross-sectional areas of the concrete and the steel. The thermal expansion coefficient of the pile is 10.9 με/°C using 11 and 10.5 με/°C for the steel bars and the concrete respectively.

4-3-2- Measurement of the stress at the head of the piles

Concrete pressure cells (CPC) are sensors that allow to measure the stress transferred from superstructure to the piles head. This instrument consists of two rigid disks filled with oil. The hydraulic pressure is thus converted to an electrical signal (4 - 20 mA), while a zero-value indicating the breakdown of the sensor. The stiffness of this pressure pad should be similar to that of the material where it is embedded to prevent arching effects. Therefore, this type of cells is not suitable for soil applications. It is recommended by GLOTZL that the minimum distance between two adjacent cells should be at least half a cell diameter to prevent the effect that each can make on the other. The cell must be also in complete contact with the surrounding material, i.e., the concrete. The lengths of the cables do not affect current sensors of this type as the current is very insensitive to electromagnetic disturbances and in our case, two wires are sufficient.

Based on the above, eighteen CPCs, provided by GLOTZL, were installed on the head of each of the instrumented piles, three sensors for each pile. A typical model of the CPC is shown in Figure 2.12.

Fourteen instruments have a measuring range 0 – 5 MPa which is enough for the construction phases, based on the load transfer shown earlier in this chapter. The rest can measure up to 15 MPa and are suitable for operation phases. These are installed on the top of 20 A/B and 18 A/B.

The distribution of all the sensors among the piles and their positions are detailed in Figure 2.16 and 2.17 and Table 2.18 to 2.20.

Table 2.18 List of the VWSGs installed in the instrumented piles

Pile	Sensor number	Pile	Sensor number	Pile	Sensor number
20B	VWSG-20B-1-Level1	**20A**	VWSG-20A-7-Level3	**18A**	VWSG-18A-10-Level1
20B	VWSG-20B-2-Level1	**17B**	VWSG-17B-8-Level1	**18A**	VWSG-18A-11-Level1
20B	VWSG-20B-3-Level2	**17A**	VWSG-17A-9-Level3	**18A**	VWSG-18A-12-Level2
20B	VWSG-20B-4-Level2			**18A**	VWSG-18A-13-Level2
20B	VWSG-20B-5-Level3			**18A**	VWSG-18A-14-Level3
				18A	VWSG-18A-15-Level3

Table 2.19 List of the ERSGs installed in the instrumented piles

Pile	Sensor number	Pile	Sensor number	Pile	Sensor number
20B	ERSG-20B-1-Level1	**17B**	ERSG-17B-13-Level1	**18B**	ERSG-18B-31-Level1
20B	ERSG-20B-2-Level1	**17B**	ERSG-17B-14-Level1	**18B**	ERSG-18B-32-Level1
20B	ERSG-20B-3-Level2	**17B**	ERSG-17B-15-Level2	**18B**	ERSG-18B-33-Level2
20B	ERSG-20B-4-Level2	**17B**	ERSG-17B-16-Level2	**18B**	ERSG-18B-34-Level2
20B	ERSG-20B-5-Level3	**17B**	ERSG-17B-17-Level3	**18B**	ERSG-18B-35-Level3
20B	ERSG-20B-6-Level3	**17B**	ERSG-17B-18-Level3	**18B**	ERSG-18B-36-Level3
20A	ERSG-20A-7-Level1	**17A**	ERSG-17A-19-Level1	**18A**	ERSG-18A-25-Level1
20A	ERSG-20A-8-Level1	**17A**	ERSG-17A-20-Level1	**18A**	ERSG-18A-26-Level1
20A	ERSG-20A-9-Level2	**17A**	ERSG-17A-21-Level2	**18A**	ERSG-18A-27-Level2
20A	ERSG-20A-10-Level2	**17A**	ERSG-17A-22-Level2	**18A**	ERSG-18A-28-Level2
20A	ERSG-20A-11-Level3	**17A**	ERSG-17A-23-Level3	**18A**	ERSG-18A-29-Level3
20A	ERSG-20A-12-Level3	**17A**	ERSG-17A-24-Level3	**18A**	ERSG-18A-30-Level3

Table 2.20 List of the CPCs installed on the top of each instrumented pile

Pile	Sensor number	Pile	Sensor number	Pile	Sensor number
20B	CPC-20B-1*	**17B**	CPC-17B-7	**18A**	CPC-18A-13
20B	CPC-20B-2	**17B**	CPC-17B-8	**18A**	CPC-18A-14
20B	CPC-20B-3	**17B**	CPC-17B-9	**18A**	CPC-18A-15*
20A	CPC-20A-4	**17A**	CPC-17A-10	**18B**	CPC-18B-16
20A	CPC-20A-5	**17A**	CPC-17A-11	**18B**	CPC-18B-17
20A	CPC-20A-6*	**17A**	CPC-17A-12	**18B**	CPC-18B-18*

** These sensors have a measuring range of 0 – 15 000 kPa*

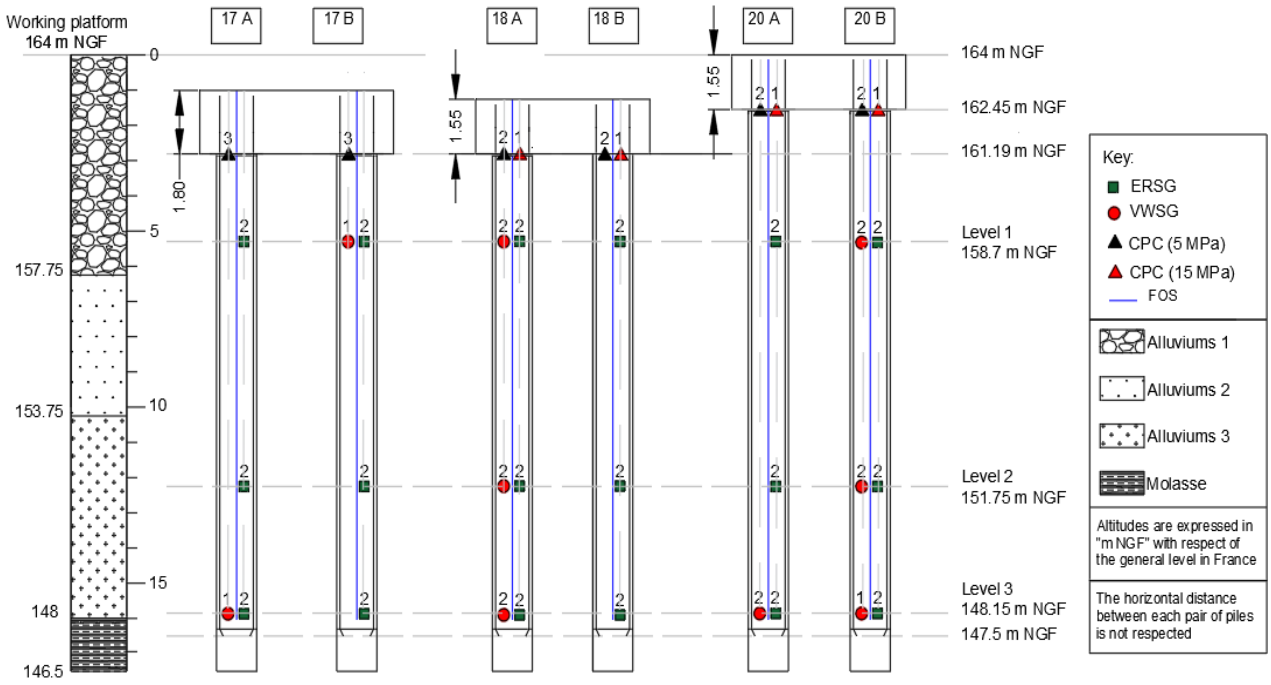

Figure 2.16 General soil profile and pile instrumentation layout

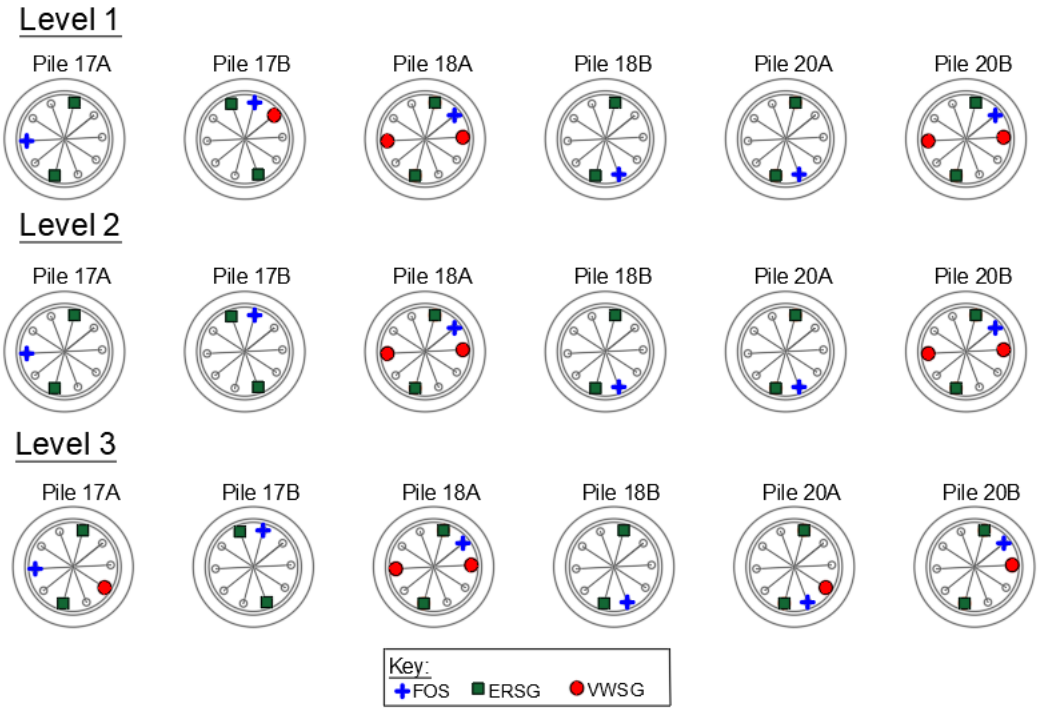

Figure 2.17 Instruments positions in the piles at three different levels

4-4- Measurement of the soil's displacement

The soil displacement was measured using a fiberglass rod extensometer, supplied by GLOTZL. It consists of six anchors installed at different depths (2, 8, 14, 20, 27 and 35 m measured from its top) as shown in Figure 2.18, six rods and a reference head. It can detect the relative movement between an anchor point and the measuring head. This displacement, detected in both the alluviums and the molasse layers is transferred by means of the fiberglass rods. Since access to the reference head is difficult, displacement sensors, called potentiometers (POT), are installed inside. They have an internal resistance strip whose values vary with the displacement. Accordingly, six of these sensors, measuring up to 60 mm of maximum displacement and provided by GLOTZL were used.

This range was chosen based on a retro-analysis done with the tower "Oxygène" built in 2007 in the same neighborhood and which showed that the settlement of the soil beneath Silex[2] was estimated at 15 mm , with an additional 10 mm due to long term considerations. This analysis was based on the given the pressuremeter moduli E_M of the soil layers.

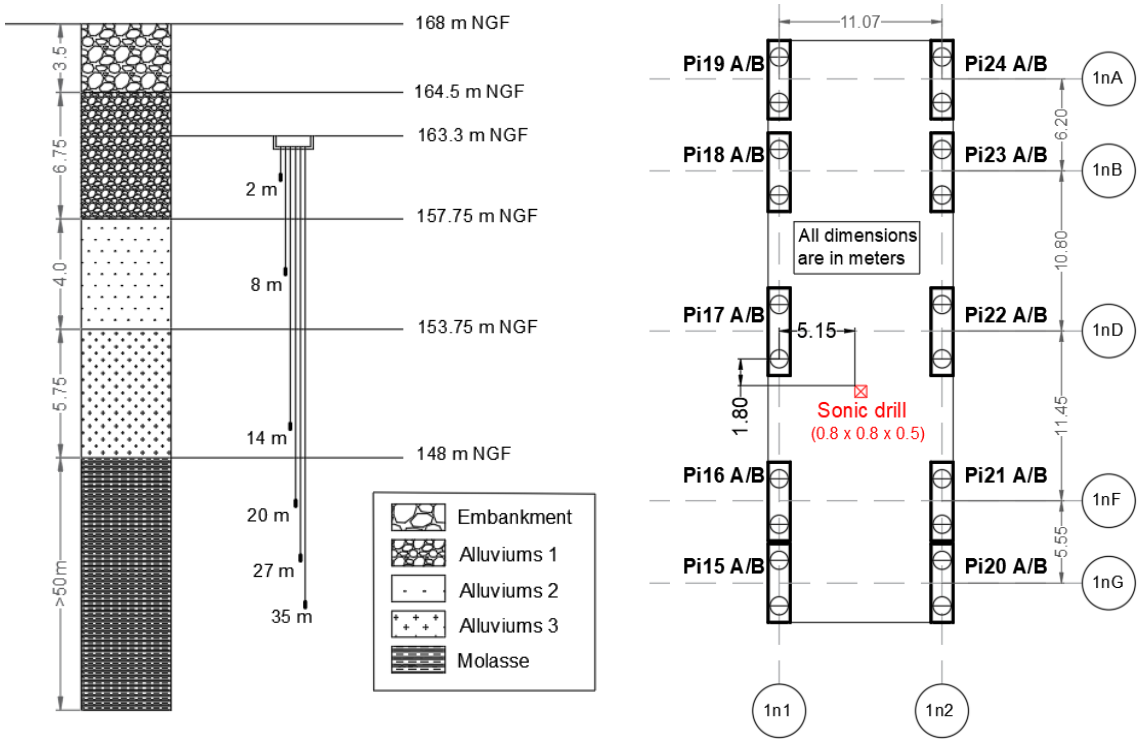

Figure 2.18 Position of the fiberglass rod extensometer in the soil

The extensometer and the displacement sensors are shown in Figure 2.19.

The instrumentation schedule is summarized in Table 2.21, presenting for each type of sensors, among others many information in relation with the supplier, model, geometrical and metrological characteristics.

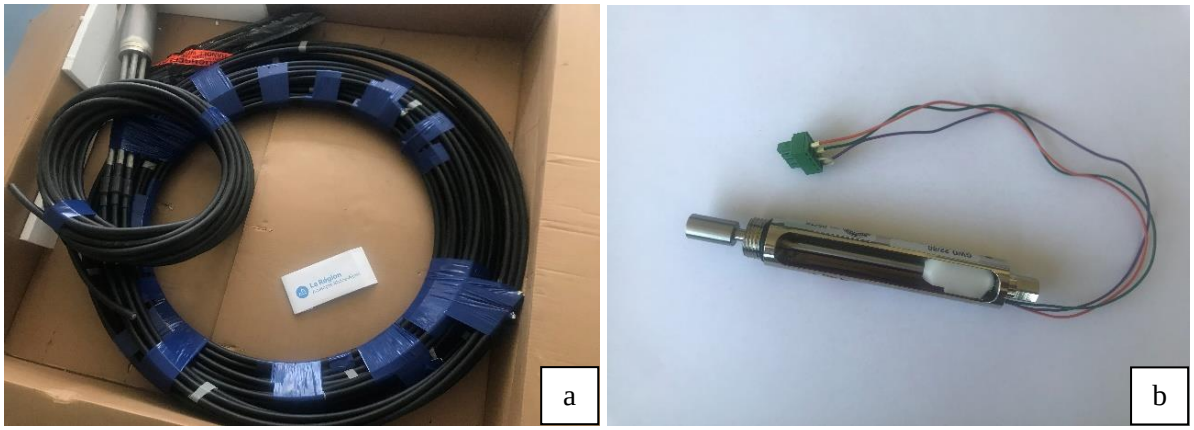

Figure 2.19 (a) Fiberglass rod extensometer and (b) one of its potentiometers

Table 2.21 Summary of electrical instruments with their characteristics by type

	Concrete pressure cell (CPC)		**Vibrating wire strain gage (VWSG)**	**Electrical resistance strain gage (ERSG)**	**Potentiometer (POT)**
Supplier	GLOTZL	GLOTZL	SISGEO	KYOWA	GLOTZL
Model	E Φ 30 AI 50	E Φ 30 AI 150	0VK4000VS00	KFGS-5-120-C1-11	GWLO 22/60
Quantity	14	4	14	36	6
Physical Parameter	Stress		Deformation	Deformation	Displacement
Measured parameter	Current (mA)		Frequency (Hz)	Resistance (Ω)	Resistance (Ω)
Diameter/ Length	ϕ 300 mm		150 mm	5 mm	-
Measuring range	0 – 5 000 kPa	0 – 15 000 kPa	2 500 με (±1500 με) 520 – 1020 Hz	-	0 – 60 mm
Operating Temperature	-25°C – 80°C	5°C – 60°C	-20 °C – 80°C	-	-30°C – 70°C
Calibration factor	0.32 mA/bar	0.10667 mA/bar	-	-	-
Resolution	< à ± 1% f.s.		< 1με	-	< à ± 1% f.s.
Other	Overload protection: 20% Initialization time: 6 s		Coil resistance: 150 Ω Max length: 1000 m	Resistance: 119.8 Ω ±0.2%	Resistance 4.7 kΩ

4-5- Installation procedure

The instruments in the project were installed according to the following procedure:

- Laboratory and in-situ preparation before the installation of the reinforcing cage (Figure 2.20)
  - All sensors were checked in the laboratory to check their calibration and ensure they are working properly
  - To install vibrating wire strain gages, mounting blocks were welded on site on the steel bars using a mounting jig as a reference. Gages were then fixed on them to allow their compression or tension. As recommended by the vendor, once the strain gage installed, it should be screwed to give a value of 2500 $\mu\varepsilon \pm 10\%$.
  - The electrical resistance strain gages were previously glued on a 1-m length steel bar in the laboratory. A special coating was applied to protect them from moisture before they were finally scotch-taped. These bars were then welded on the reinforcing cage on site.
  - The optical fibers were taped on the steel bars along the pile
  - Colored tags with codes indicating the number of the sensor and the corresponding pile were attached to the cables to facilitate their identification on site

The electrical cables, together with the optical fibers, were fastened to the steel cage using plastic cable fasteners or adhesive tapes. A steel tube served as a channel to take them out of the cage (Figure 2.21-a/b). They were put inside plastic bag and fixed either in the middle at the steel tube or on the periphery to protect them from any damage that may be caused by the installation (Figure 2.21-c/d).

- Installation of the reinforcing cage
  - As shown earlier in this chapter, CFA piles were used in this project. Thus, a drill of 1.22 m diameter was executed in the soil using a proper machine that suits the type of the soil (Figure 2.22).
  - After pumping down a workable concrete into the drill, the equipped reinforcing cage was lifted using a crane and then introduced in the concrete. It took many days before it was possible to continue the following steps of the installation (Figure 2.23).

Figure 2.20 Installed examples of (a) VWSGs, (b) ERSGs and (c) Optical fibers

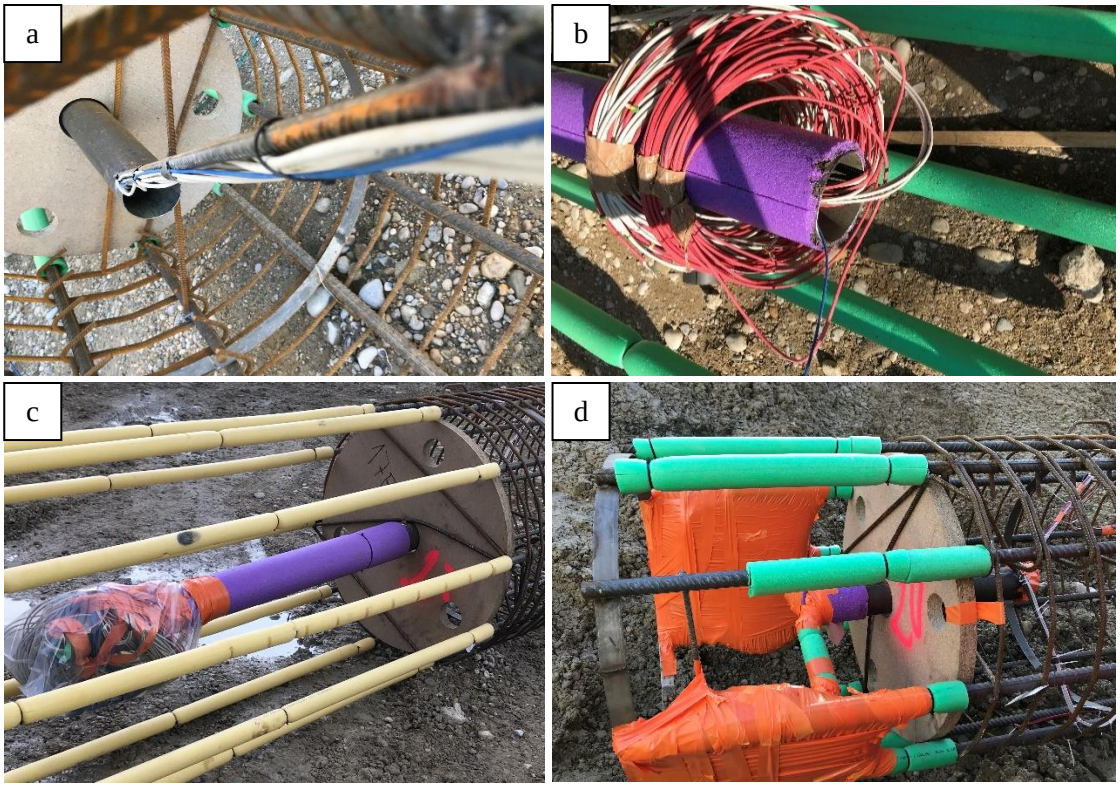

Figure 2.21 Cable arrangements at the pile's head

Figure 2.22 The drilling machine used to execute the piles

Figure 2.23 Installation of the reinforcing cage in the wet concrete using a vibrator

- Pile breaking and installation of the CPCs

After piles breaking, the tube that had the cables was shattered and the cables of the instruments were pulled outside the piles' heads through ducts in the transfer structure and then in the concrete slab. A thin layer of Tufnol sealing mortar was applied on the top of the pile to install the CPC horizontally (Figure 2.24).

- Installation of the fiberglass rod extensometer

Following the sonic drilling, rods and anchors were placed in a geotextile hose and were installed in a way to have the last one reaching 35-m depth. The head of the extensometer being fixed with a rope on the drilling machine for few hours, a specific grout for stiff clayey soil was used to fill the drill hole with the following composition: 15% cement, 80% Kaolin and 5% Bentonite (NF P 94-156, 1995). The installed six displacement sensors were finally connected to an 18-wire cable until the electric cabinet (Figure 2.25).

- Finalization of the installation

All the cables and optical fibers were brought out of the transfer structure and were then pulled in the concrete slab through ducts, until an electrical cabinet, located in the basement of the nearby EDF tower, which is equipped with the data logging systems that will be presented hereafter (Figure 2.26 and 2.27).

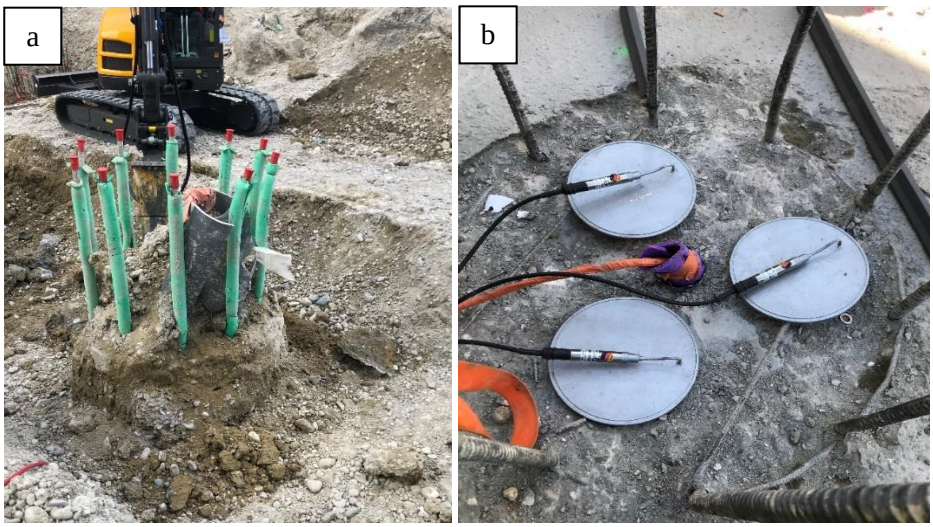

Figure 2.24 (a) Pile head breaking using the hydraulic hammer and (b) installation of the CPCs

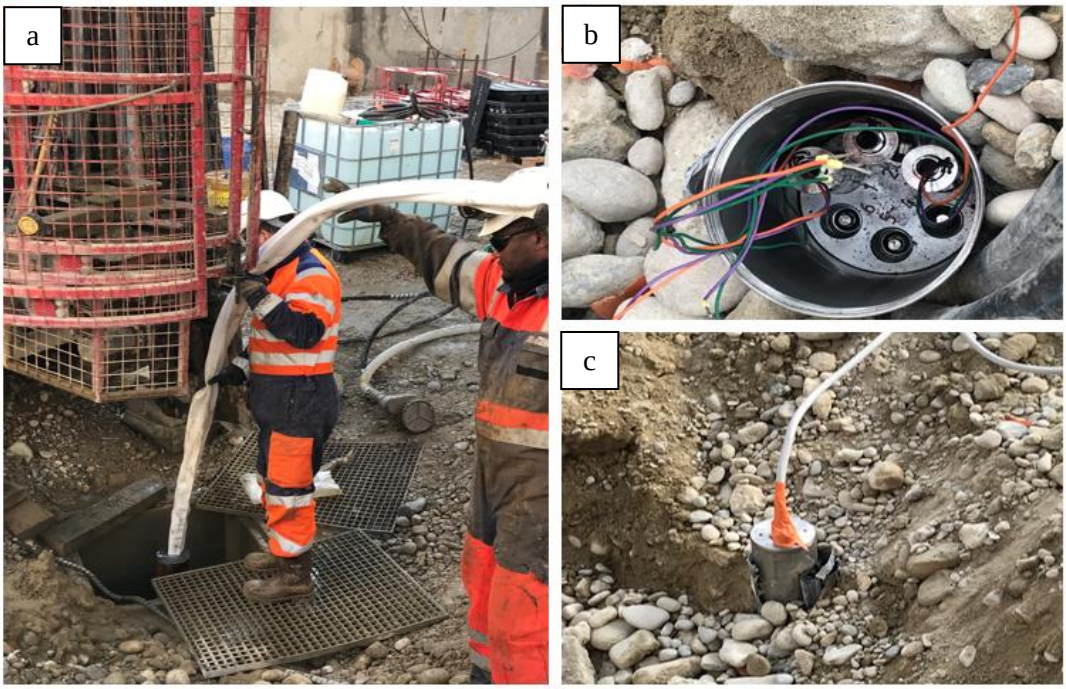

Figure 2.25 (a) Introduction of the fiberglass rod extensometer in the sonic drill and (b, c) installation of the potentiometers with the 18-wire cable

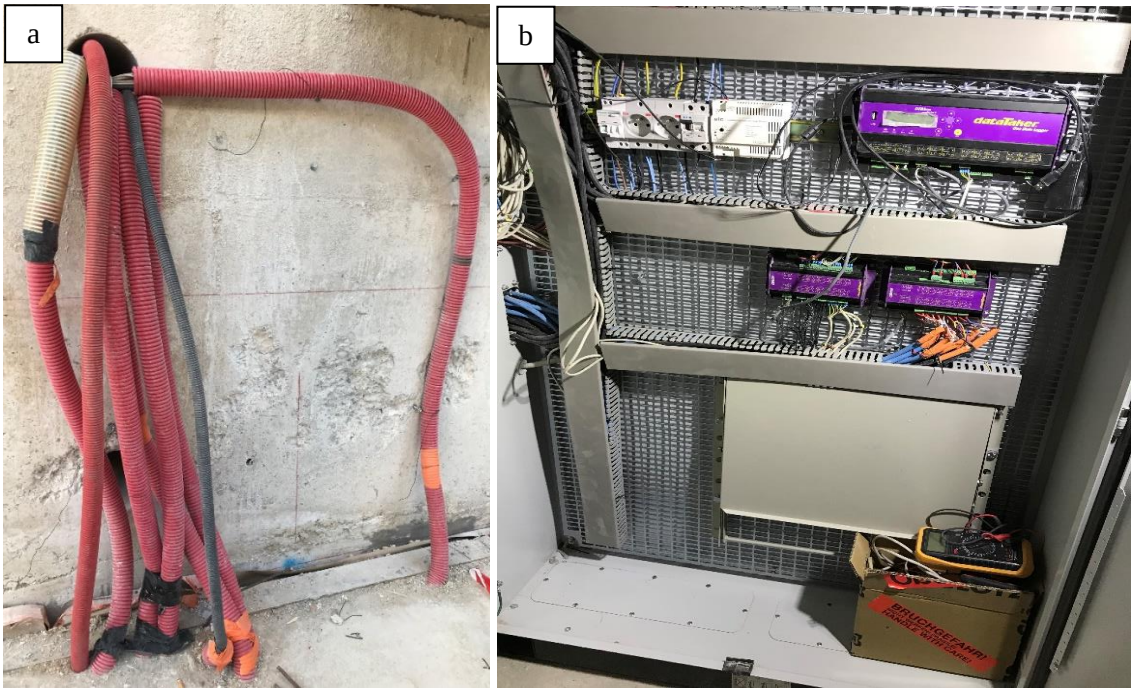

Figure 2.26 (a) Introduction of the ducts into the dedicated room in EDF tower and (b) the electrical cabinet equipped with the data logging machines

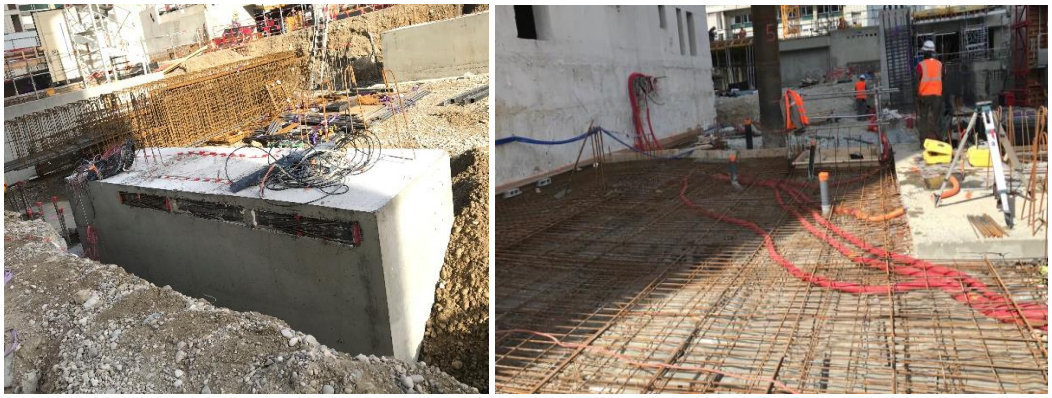

Figure 2.27 The instruments cables prepared on site and pulled in ducts until the EDF tower

4-6- Data acquisition systems

In addition to instrument calibration and installation, data collection, processing and interpretation are also of high importance. Two different data logging systems were installed in the electrical cabinet and were used in Silex[2] as presented in Figure 2.28.

- Measurements for CPCs, VWSGs, ERSGs and potentiometers were retrieved using a data logger "Datataker DT85GLM3-4". It has 16 analog channels and was connected to three additional channel expansion modules (CEM) with 20 additional channels each.

- As previously explained, optical fibers were connected to an Optical Distributed Sensor Interrogator (LUNA ODiSI 6100) which is configured to measure Rayleigh High Definition Fiber Optic Sensors.

A measurement was taken right after the installation of the sensors to ensure they were working properly. The “zero readings” were taken directly after the casting of the slab since we are not interested in the residual loads accumulated during the installation. Here are why all results will be analyzed based on relative measurements for both loads and deformations.

The frequency of readings generally depends on the construction activities. It should be moderate to avoid missing events or overloading the data processing (Dunnicliff, 1988). During the first stages of construction, readings had to be taken every two hours. After the values had stabilized, two measurements per day were enough (Briançon et al., 2016).

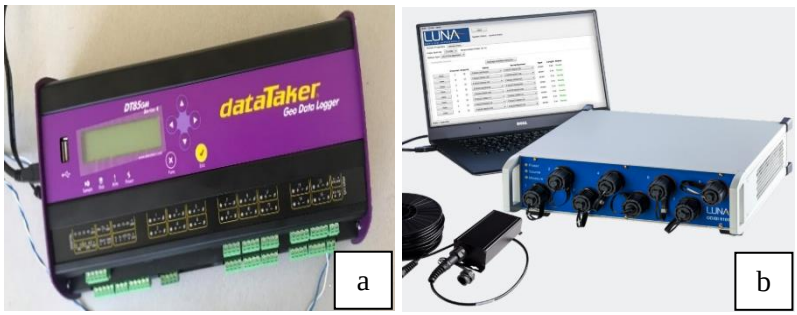

Figure 2.28 Data Logging Systems: (a) Datataker and (b) optical machine

5- Numerical modeling using Flac3D

In order to have a deeper insight into the behavior of the pile embedded in the alluviums and the molasse, a numerical modeling with the finite difference method was adopted. It enabled a realistic selection of parameters and constitutive laws by comparing the numerical results with instrumentation measurements. In the following section, we present the numerical tool, the retained geometrical hypotheses and the developed models as a prelude to the results that will be presented in Chapter 3 and 4.

5-1- Presentation of the numerical method used in Flac3D®

5-1-1- Finite Difference Method (FDM)

As seen in Chapter 1, the FEM is the predominant method for most of the geotechnical studies and this shows in the large number of software that uses it. However, the finite difference method (FDM) is also a good means for solving a variety of soil mechanics problems especially for large-deformation simulations. This technique consists in replacing the derivatives by differential equations. The flaws that were always attributed to the FDM were related to the way it was formulated, but with the new non-conventional formulations used in FLAC3D for example, this technique offers many advantages allowing the modeling of complex behaviors and mechanisms, with a reasonable run time (Jimenez, 2019).

5-1-2- Presentation of FLAC3D®

FLAC3D® (Fast Lagrangian Analysis of Continua in 3 Dimensions) is a numerical modeling software for engineering mechanics computation that uses a non-traditional method based on explicit Lagrangian formulation. It is good for non-linear materials, those subject to large deformations and it can also be used to model structures from any shape, not necessarily rectangular elements. For this reason, in the latest decades, it has started to be widely used in many domains especially in geotechnical fields (Rayhani and El Naggar, 2008; Ghee and Guo, 2011; Wu et al., 2011; Xie et al., 2013; Kwon et al., 2013; Wu et al., 2016; Jimenez, 2019).

FLAC3D® has many developed options such as dynamic, thermal and creep analysis modules and it provides the possibility to implement user-defined constitutive models, using FISH (mainly for 2D) or C++ programming. The second method is more efficient in terms of computation time and it was used and validated by many researchers (Souley et al., 2003; Jenck, 2005).

The seventh version of FLAC3D® has been used in this thesis. It has 21 built-in material constitutive laws that can be applied to the materials allowing them to yield and flow, with a grid that can deform and move. It has been enhanced to facilitate the modeling procedure through a built-in text editor and the "building blocks" and "Extrusion" panes that allow to easily construct 3D models from 2D sections, using AutoCAD® drawing files for example.

The numerical computation in FLAC3D® is based on the following three properties:

- Finite difference method that uses differential equations and thus replace every derivative with an algebraic expression. Since no matrices are formed, the equations are given at every single step. As a result, even a large calculation can be made without excessive memory requirements.

- Lagrangian Elements method, which allows the mesh to deform with the material as opposed to Eulerian formulation. This is a good advantage when working in large-strain mode.

- Explicit method, which allows solving static problems using dynamic approaches (Jenck, 2005). The solution requires a number of steps to arrive at an equilibrium (or steady-flow). Nonlinearity can be solved as well as linearity. The main disadvantage of this method is that it requires small time steps to ensure the convergence of the model. One of the advantages of this method above all, is the unnecessary use of iterations in order to calculate the stress state, even for nonlinear constitutive laws.

The differences between explicit and implicit methods are described by Billaux and Cundall (1993).

For each cycle, equations of motion are used to calculate the new velocities and displacements from the stresses (at time t). Velocities allow the determination of the deformation rate after a time step (Δt) and using the constitutive law, new deformations and stresses (at t+Δt) are then calculated (Eq. 2.25 to 2.27). This is the incremental algorithm presented in Figure 2.29 and used to formulate all the constitutive laws available in FLAC3D in addition to the user-defined ones. The fundamental principle of the explicit method is that when a calculation is done in any block of the shown sequence, the variables used from the previous block remain constant and are not directly updated, especially for short time steps. However, one of the inconvenients of this method is the big number of cycles needed due to small steps Δt when working with linear problems and small deformations in FLAC3D (Jenck, 2005).

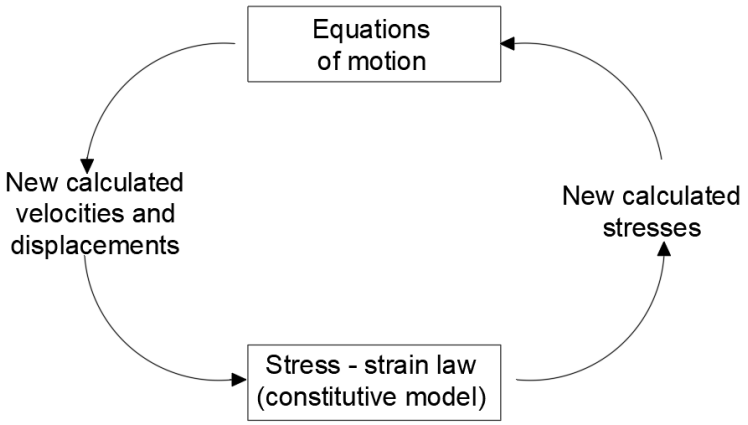

Figure 2.29 General calculation sequence in FLAC3D (Billaux and Cundall, 1993)

In FLAC3D, tension and extension are taken positive. The equation of motion in a Lagrangian reference is given by:

$$\sigma_{ij,j} + \rho b_i = \rho \frac{dv_i}{dt} \qquad \text{Eq. 2.25}$$

Where ρ is the mass density, [b] the body force per unit mass, [v] the velocity.

The deformation rate ξ_{ij} is then calculated allowing to determine the new stresses σ_{ij} later by adopting any constitutive law that may use an additional parameter k.

$$\xi_{ij} = \frac{1}{2}\left(v_{i,j} + v_{j,i}\right) \qquad \text{Eq. 2.26}$$

$$\sigma_{ij} = H_{ij}(\sigma_{ij}, \xi_{ij}, k) \qquad \text{Eq. 2.27}$$

In the previous equations, partial derivatives are calculated with respect to the current position vector [x].

5-1-3- Numerical formulation and some other definitions

The numerical formulation in FLAC3D is based on three approaches: finite volume, discrete model and dynamic solution. In other terms, the Newton's law is transformed into discrete forms at the nodes. The system can then be solved using explicit finite difference method.

Therefore, the grid is generated using simple zones formed by tetrahedral elements shown in Figure 2.30 which are characterized by constant strain rate and on which the velocity variations in space are considered, based on Eq. 2.26. The vertices of these elements are the nodes of the defined mesh which are referred to as gridpoints. In a way to overcome some numerical problems, a mixed discretization is recommended. An 8-noded zone in FLAC3D can be discretized into 5 tetrahedra according to the two different overlays shown in Figure 2.31. The calculation of nodal forces is carried out using one overlay or a combination of both. The latter is advantageous in case of symmetry loading. It ensures symmetric zone response since the nodal forces are calculated by averaging of the two overlays (Itasca, 2019).

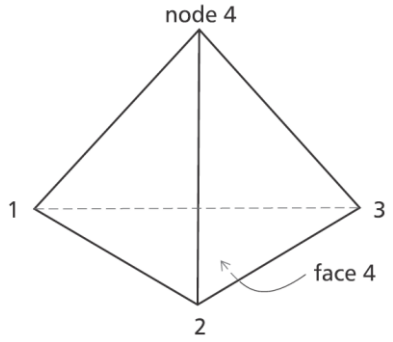

Figure 2.30 Example of the tetrahedron used in FLAC3D formulation

5-1-3-1- Definition of the convergence criteria in FLAC3D

At the end of each phase (initial state, construction, excavation, load application…), the system must reach equilibrium or in other words, a static solution in all the elements. In FLAC3D, the equilibrium state is reached depending on one of the following criteria: maximum out-of-balance force, local force ratio,

average force ratio, maximum force ratio and convergence. The software checks for each of the elements the imbalance according to the threshold set by the user. These criteria are explained in Table 2.22.

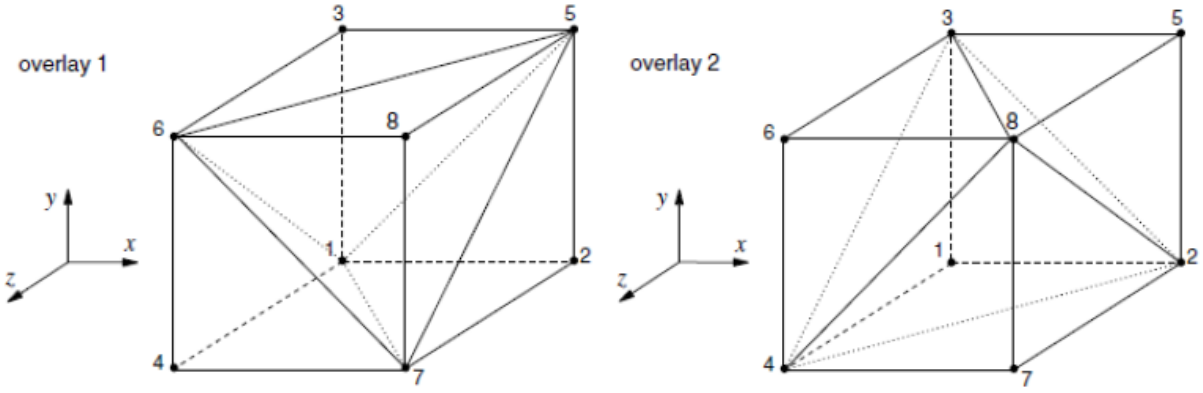

Figure 2.31 Two overlays of an 8-node zone with 5 tetrahedra

Table 2.22 Definition of the convergence criteria used in FLAC3D

Criterion	Definition as extracted from Itasca (2019)	Discussion
Maximum Out-of-Balance Force	"Maximum absolute value of the force remaining after all forces are summed together. If the force is zero, the gridpoint can be thought of as being converged, or at equilibrium."	Unitless value. The target value varies from a model to another.
Average force ratio	"It is the sum of all out-of-balance force components at every gridpoint divided by the sum of all total forces applied at a gridpoint". The default target value is 10^{-5}.	Fast method but insufficient sometimes especially for localized convergence problems.
Maximum force ratio	"It is the maximum out-of-balance force divided by the average total force acting on all gridpoints".	
Convergence	"The convergence value for a gridpoint or node is defined as the ratio of the current mechanical force ratio to the target force ratio of the gridpoint". The system is converged when a value of 1 is reached. The target local force is 10^{-4} by default.	Slow but too precise

By default, the criterion employed by FLAC3D is the average force ratio of 10^{-5}. However, in some cases, such as in intermediate stages of a model that have negligible effects on the final state, a value of 10^{-3} is sufficient. In general, it is recommended to use a maximum local ratio of 10^{-4} for regular engineering problems (Itasca, 2019).

More practically, two important things should be verified in order to check if the model has reached equilibrium in a certain phase:

- Check whether the displacement and velocity are changing or no in a particular location

- Check the contour plots of the convergence /or force ratio (depending on the chosen criterion) so that the zones characterized by slow convergence can be located

5-1-3-2- Large-strain / Small-strain modes

FLAC3D offers the possibility to work in large or small-strain modes. The former involves large displacements and deformations and the node coordinates after each step. However, the latter is better used for small displacements and displacement gradients where the node coordinates are not updated. This is the mode used in FLAC3D by default and it will be used in the following since we are dealing with small strains in piles problems.

5-1-3-3- Fluid mode

In FLAC3D, it is possible to model the fluid-mechanical interaction in two ways:

- Without a fluid flow: In this mode, the pore pressure or simply the water table level are assigned at gridpoints. No flow is allowed in this case by considering a constant water table level or a hydrostatic pore pressure. This model provides a faster solution and is sufficient in case of drained materials. In this calculation mode, failure is controlled by the effective-stress state but pore pressures do not change (Itasca, 2019).
- With a fluid flow: The water table level and the pore-pressure are allowed to change resulting in a transient-flow. Additional properties must be assigned to the materials (permeability, fluid modulus, Biot coefficient…). The behavior of the soil can be drained or undrained depending on the assigned parameters. Using this mode, it becomes possible to model the pore water pressure generated due to any external load.

In this thesis, we will limit ourselves to the case without fluid flow since the generated pore water pressure resulting from the construction of a drilled shaft is negligible as seen in Section 3-2-1.

5-1-4- Constitutive laws in FLAC3D

Available constitutive laws in FLAC3D can be categorized into three groups: null (used for excavated zones), elastic (linear or transverse isotropic material) and plastic laws (MC, PH, Cam Clay…). Each constitutive model has a list of possible failure states that can explain the current plasticity state of zones. Failure can occur in shear, tension, volume or shear joint. A suffix "-n" or "-p" may be attributed to express an actual or past failure respectively. It should be noted that in case of Mohr-Coulomb, for example, past shear plastic flows are possible and they can be due to stress redistribution in yielding elements, after which the new stresses do not satisfy anymore the yield criterion. The latest version of FLAC3D has now a wide variety of constitutive models that are implemented are ready to be used. Of these models, three were used in this thesis.

- Constitutive model used for the concrete elements: linear elastic
- Constitutive model used for the soil elements: Mohr-Coulomb and the plastic hardening models

5-1-5- Interfaces in FLAC3D

Interfaces are used in FLAC3D to represent a joint, fault, a contact between a foundation and the soil or fixed non-deformable boundary at any position in the space. They are used generally so that slip and/or separation can be allowed.

The interface is one-sided and consists of no thickness joint triangular elements, that are attached to the zones' surface faces, also called target faces, through the interface nodes. The opposite faces are called host faces. The interface is created by separating all zone faces found at the desired location (plane) before placing the new elements and nodes at one side.

Based on the actual stress state, the absolute normal penetration and the relative shear sliding are calculated for each interface node during each timestep. The normal and shear forces of the interface nodes at a calculation time (t+Δt), describing the elastic interface response, may be calculated based on the constitutive model, using the following equations.

$$F_n^{t+\Delta t} = k_n u_n A + \sigma_n A \qquad \text{Eq. 2.28}$$

$$F_{si}^{t+\Delta t} = F_{si}^{t} + k_s \, \Delta u_{si}^{t+(1/2)\Delta t} \, A + \sigma_{si} A \qquad \text{Eq. 2.29}$$

Where u_n is the absolute normal penetration of the interface node into the target face, A is the representative area associated with the interface node, σ_n is the additional normal stress due to interface stress initialization, Δu_{si} is the incremental relative shear displacements vector and σ_{si} is the additional shear stress vector due to the interface stress initialization.

These forces are generated at the interface nodes that are in contact with zone surface faces. They are then equally distributed to both the target and the host faces in opposite directions.

Three behaviors or contact states are possible (Itasca, 2019):

- Bonded interface where the interface remains elastic if stresses remain below the bond strengths (shear and tensile bond strengths)
- Slip while bonded interface where the interface can slip without separation (intact bond).
- Coulomb sliding interface where the bond is broken. The behavior is governed by the friction angle, the cohesion and the stiffness.
- Separation

By default, the interfaces are assigned a linear elastic-perfectly plastic model, based on Coulomb sliding and/or tensile and shear bonding. The slip and separation that may occur at the soil-pile interface can be modeled in FLAC3D (Maheshwari and Watanabe, 2006). The default behavior of an interface node is shown in Figure 2.32.

Based on the above, interface elements have the following properties: cohesion (c_{int}), friction (ϕ_{int}) and dilation (ψ_{int}) angles, normal (k_n) and shear (k_s) stiffnesses, and tensile (Ts) and shear (S_s) bond strengths.

The shear force is limited using Coulomb criterion as follows:

$$F_{smax} = c_{int} A + \tan \phi_{int} \, (F_n - pA) \qquad \text{Eq. 2.30}$$

Where p is the pore pressure interpolated from the target face.

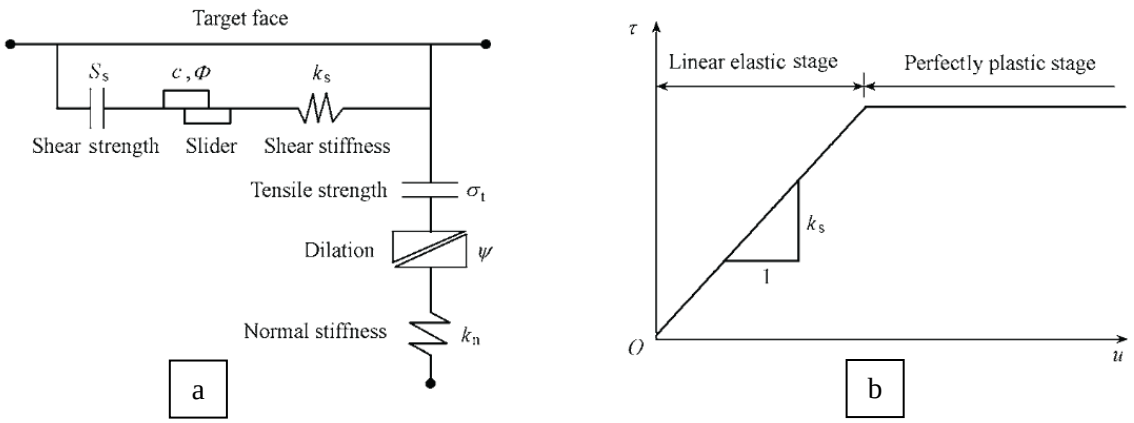

Figure 2.32 (a) Computation theory of interface element and (b) linear elastic perfectly plastic behavior (Wu et al., 2011)

F_n and F_{si} are then compared respectively with the normal tensile strength T_s and the maximum shear strength F_{smax}.

- If $F_n < T_s$ and $F_{si} < F_{smax}$: elastic range / slip while bonded state
- If $F_n < T_s$ and $F_{si} \geq F_{smax}$: Coulomb sliding state. In this case, the interface forces need to be corrected according to Eq. 2.31 and Eq. 2.32, if the interface has dilation characteristics or Eq. 2.31 only otherwise.

$$|F_s| = F_{smax} \quad \text{Eq. 2.31}$$

$$F_n = F_n + \frac{|\text{Fs}|_0 - F_{smax}}{Ak_s} \tan\psi_{int}\ k_n \quad \text{Eq. 2.32}$$

Where $|\text{Fs}|_0$ is the shear force before the correction.

- If $F_n \geq T_s$: separated state

As a rule of thumb, it is recommended by Itasca for the normal and shear stiffness to be ten times the maximum equivalent stiffness of the stiffest neighboring zone, following the following equation:

$$k_n = k_s = 10 \max\left[\frac{K + \frac{4}{3}G}{\Delta z_{min}}\right] \quad \text{Eq. 2.33}$$

Where Δz_{min} is the smallest width of an adjoining zone in the normal direction (Figure 2.33).

The maximum is calculated over all the zones adjacent to the interface that can have different materials.

However, a long computation time can be directly related to high values of k_n and k_s since FLAC3D does "mass scaling" based on stiffnesses (Itasca, 2019). Thus, adjustments are made possible in some cases, while ensuring that the normal penetration and detachment on the pile-soil interface are avoided (Rayhani and El Naggar, 2008).

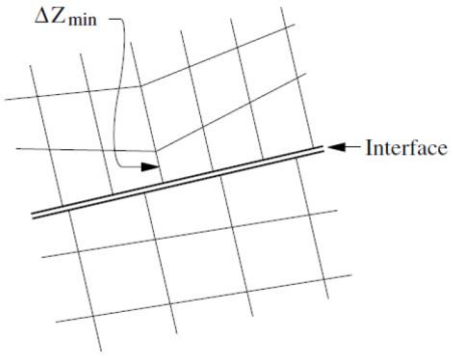

Figure 2.33 Definition of Δz_{min} used in the calculation of the interface stiffness

Moreover, more advanced interface models showing nonlinear behaviors can be implemented identically to the soil constitutive models. Wu et al. (2011) for example, have improved the existing model by replacing the linear elastic part by a hyperbolic elastic one and by modifying the plastic model in order to represent a non-linear strain-softening behavior. However, these models need to be calibrated using some experimental tests that were impossible to be carried out in this project so we will stick to the default model.

5-2- Numerical modeling in Silex^2 - General hypotheses

Many models with different geometries were performed in FLAC3D in this study. They will be introduced in the current section but the results will be shown later in Chapter 3.

Two computers served alternately for FLAC3D calculations.

- Intel ® Core ™ i7-7920HQ CPU: The computation of a single pile analysis took between 2 hours and 5 hours depending whether the soil was dry or saturated.
- Intel ® Core ™ i9-9900 CPU: Used for larger models with two or more piles. The pile groups models took between 6 and 12 hours while the global models took between 4 and 7 days depending on the mesh and the defined characteristics.

5-2-1- Modeling of isolated piles

The model including a single pile is the first and the simplest model executed in FLAC3D. It was used to gain insight on the behavior of the piles embedded in Lyon's subsoil layers and to perform various sensitivity analyses. The diameter of the pile was 1.22 m where its length was initially 16 m but based on latest version of the documents provided by the company, it was estimated at 15.5 m. The dimensions and the position of the piles are shown in Figure 2.34.

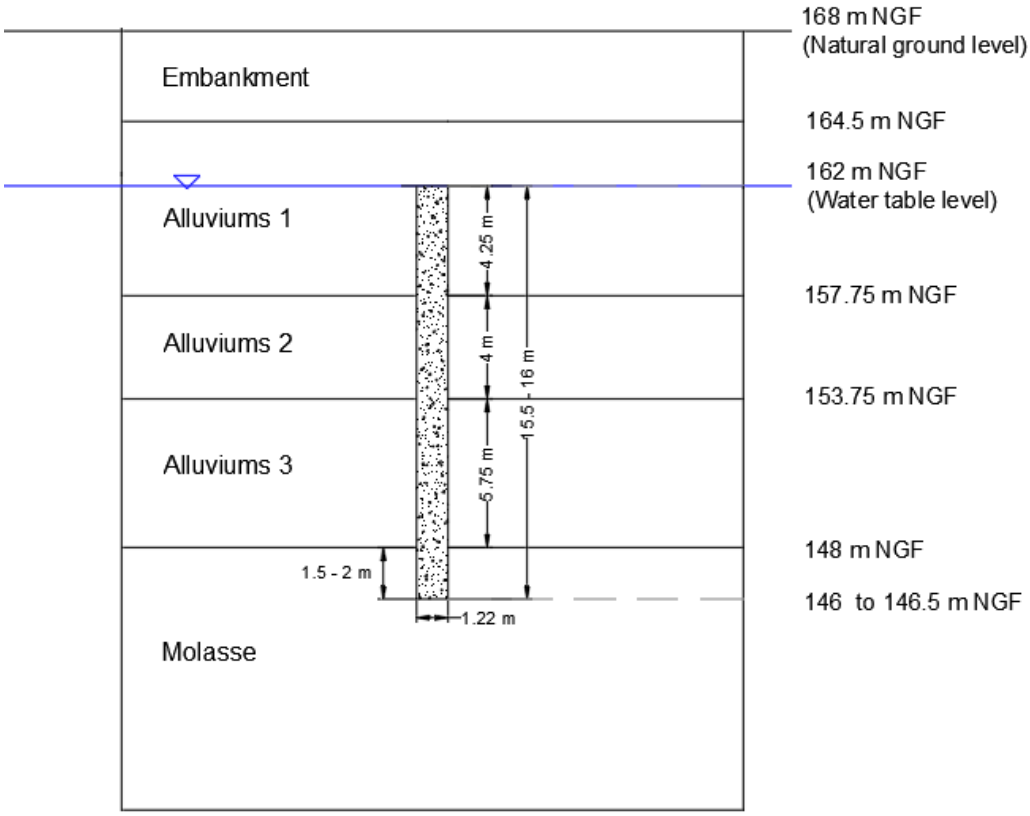

Figure 2.34 Soil profile and pile dimensions

5-2-1-1- Geometry and boundary conditions of the model

Real and artificial boundaries conditions exist. The former refers, for example, to the horizontal limit of the model, to the natural ground level… Artificial boundaries, such as symmetry planes, do not exist in reality but are introduced to reduce the number of zones and thus reduce the calculation time.

In the single pile model shown in Figure 2.36, a semi-infinite boundary condition is applied. Due to the symmetry, and since only vertical loads are considered with no buckling, a model with quarter pile is enough. This step reduced the computation time without affecting the results. The origin of the coordinate axes of the model are located in the center of the upper part of the pile, and the orientation of the z-axis along the pile axis is ascending. As for the applied conditions on the boundaries, zero horizontal displacements are allowed on all lateral sides including the symmetry planes and vertical displacements are restrained on the lower boundary.

Horizontal and vertical limits of the single pile models were defined in a way to avoid boundary effects based on many previous experiences with FEM and FDM analyses. Here are some previous findings:

- Guo and Randolph (1997): In order to minimize the boundary effects, the depth should exceed 4L and the lateral boundary should be the maximum of 2.5 L and 75r, where L and r are the length and the radius of the pile respectively. This study was performed using FLAC.

- Neves et al. (2001): The lateral boundary should be 30 times the diameter from the axis of symmetry (center of the pile) and the lower boundary is at a distance L from the tip of the pile.
- Karthigeyan et al. (2006) and Fakharian et al. (2008): The horizontal dimension of a quarter model should be equal to 20 times the pile diameter while the depth should exceed L+20D (Figure 2.35).

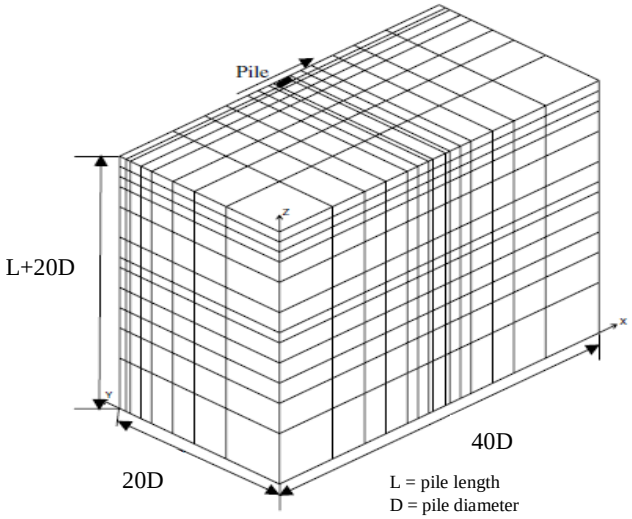

Figure 2.35 Typical geometry and mesh for 3D finite element analyses of isolated piles (Karthigeyan et al., 2006)

In the previous references, it was shown that the minimum dimensions of the models depend on many factors such as the load type, the dimensions of the piles and the soil characteristics. Therefore, a parametric study was made for Silex^2 project to validate theses dimensions as it will be shown in this paragraph. For a better presentation, it should be mentioned that the three dimensions of the single pile model will be designated as W1 x W2 x H based on Figure 2.36.

First, the horizontal dimensions (W1 and W2) and the corresponding mesh was varied. The following models were tested:

- 15 x 15 x 50
- 20 x 20 x 50
- 25 x 25 x 50
- 30 x 30 x 50
- 40 x 40 x 50

In order to choose the best model, the vertical displacement at the boundaries was checked. It can be seen in Figure 2.37 that when a load of 10 000 kN was applied at the head of the pile, the settlement difference between the 25 x 25 x 50 and the 40 x 40 x 50 models was less than 0.2 mm. Additionally, it was shown that the load settlement curves were superimposed. Therefore, the model 25 x 25 x 50 was chosen as a first step.

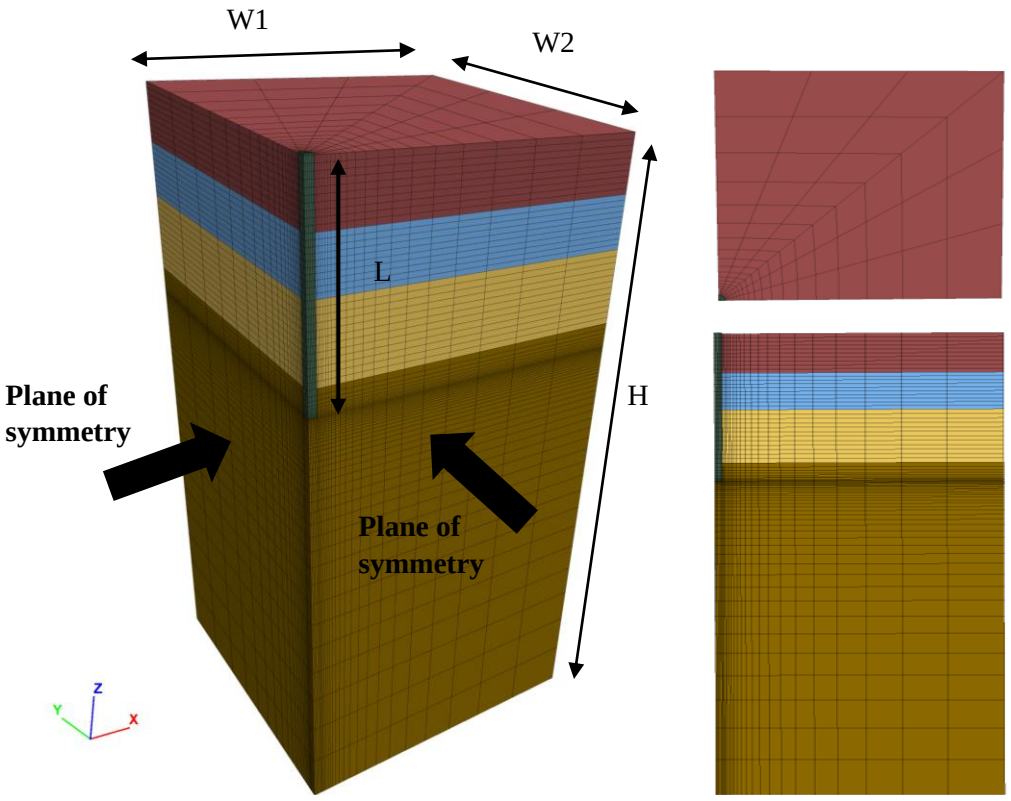

Figure 2.36 Different views of the model: Plan, sectional and 3-dimensional views

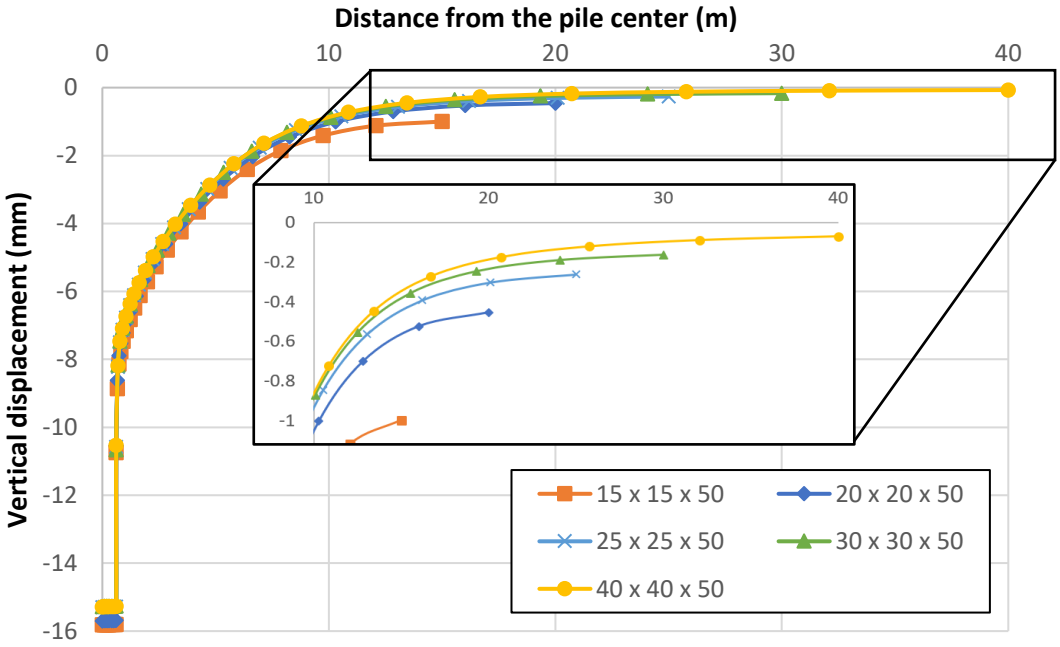

Figure 2.37 Variation of the vertical displacement of the soil for different models

The vertical dimension H of the model was also checked as follows:

- 25 x 25 x 50
- 25 x 25 x 60
- 25 x 25 x 70

Figure 2.38 shows that the difference between the three models is negligible (less than 0.5 mm) for the same applied load. A vertical dimension of 50 m is considered sufficient and by combining these two sections, the model 25 x 25 x 50 will be used for all single pile models.

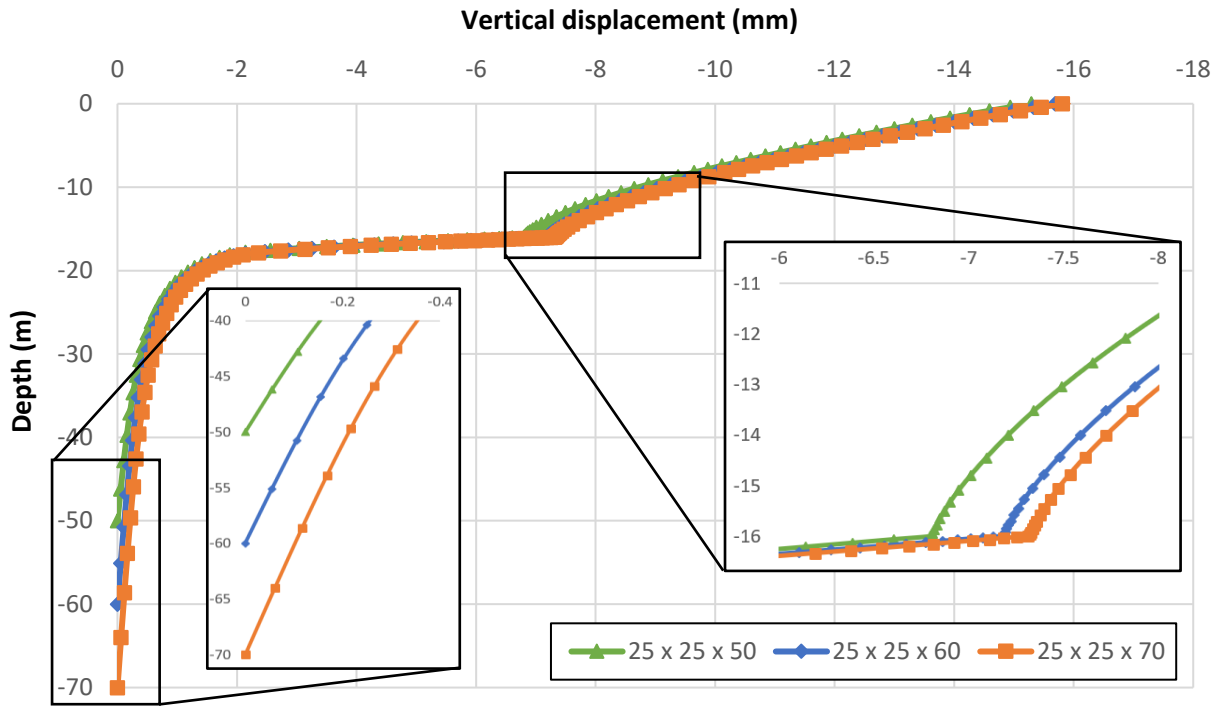

Figure 2.38 Variation of the vertical displacement of the soil with depth for different models

5-2-1-1- Mesh of the soil-pile domain

The overall model is composed of "8-noded brick" elements. The mesh, shown in Figure 2.39, is fine in the whole model, except around the interfaces at the wall and the tip of the pile, where it is more refined in order to capture the pile behavior at that level due to high stress gradient. The limit of this refined zone is considered at a distance equal to half of the diameter of the pile.

Several trials were performed and the best mesh was chosen when the displacements were not changing anymore along the boundary. The minimum aspect ratio (width/height) is 0.2 near the pile shaft and 1 directly near the pile tip. It increases to reach around 10 near the horizontal boundaries of the mesh. A more refined mesh is not recommended since it would require longer analysis time without making any substantial changes.

For the 25 x 25 x 50 model, the used mesh had 11961 zones in total (1 161 zones for the pile and 10 800 for the soil layers). The zone faces at the soil-pile interface were separated creating two separate gridpoints at each level. Besides, separate interfaces were used for pile wall and pile tip (Figure 2.40). The 558 interface elements have the same vertical dimension as the surrounding soil. The number of nodes and elements is shown in Table 2.23 and Figure 2.40, assuming that a common node between two interfaces is always counted with the one below.

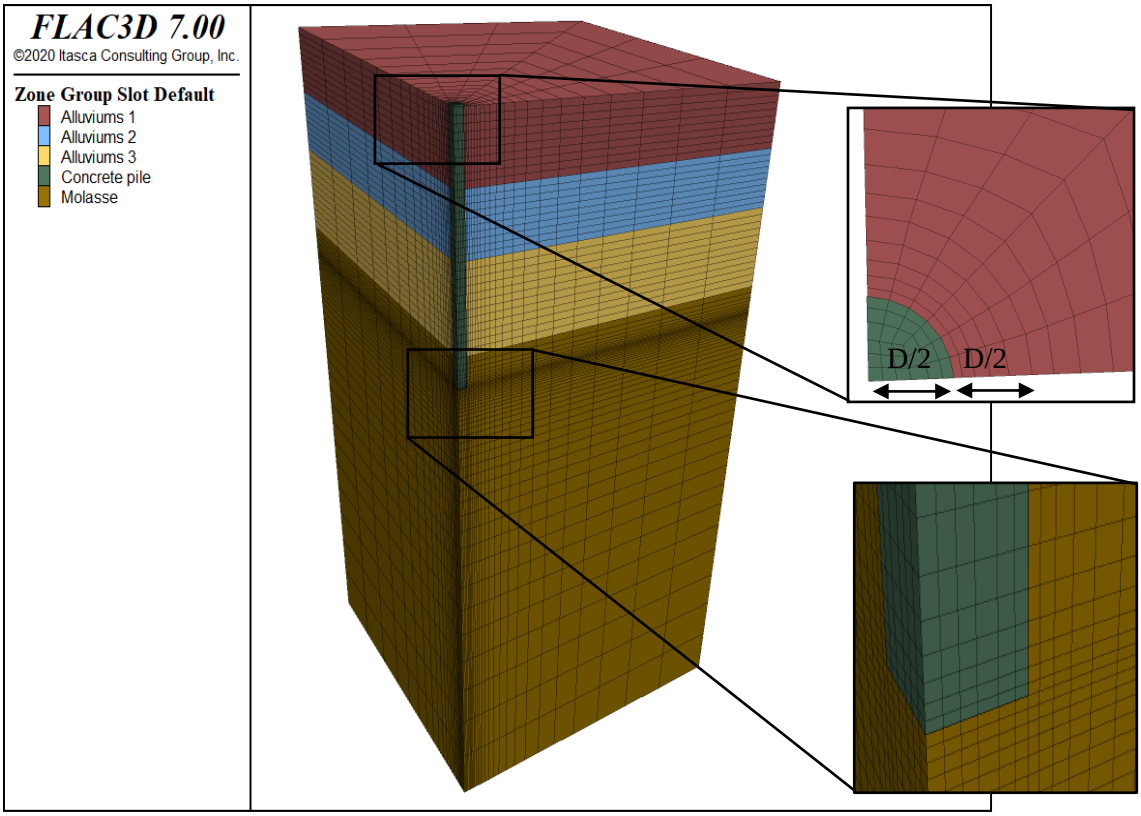

Figure 2.39 Details of the mesh in FLAC3D - model 25 x 25 x 50

Table 2.23 Number of elements and nodes constituting the interfaces

Interface	Side (4 layers)	Base	Total
Nodes	294	37	331
Elements	504	54	558

It should be noted that in the final circulated design documents, the length of the piles changed from the one assumed initially and the average pile length became 15.5 m. Therefore, the pile length used in the different studies presented in Chapter 3 varies and it will be specified accordingly.

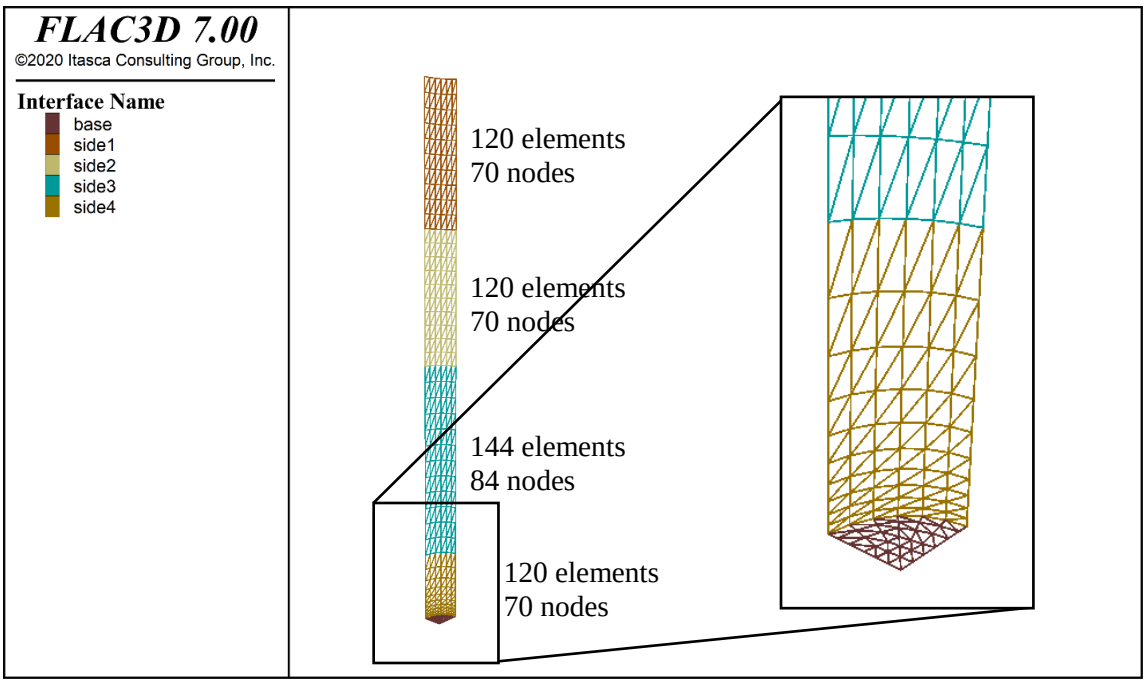

Figure 2.40 Details of the mesh in the interfaces together with the number of elements and nodes in each of them

5-2-2- Modeling of pile groups

As described in Section 2-3-1 of this Chapter, Silex[2] is founded on 10 pairs of pile foundations, each connected with a reinforced concrete transfer structure (Figure 2.4). It was thus very important to model the pile group behavior when subject to axial loads. The term "isolated" pile groups or "Group I" will be used to designate the models with two piles only, which will be presented first.

On the other hand, other models describing the interaction of the nearby piles on a specific pile group will also be studied. They will be designated by Group II.

Table 2.24 presents a summary of the characteristics of the pile groups used in FLAC3D.

Table 2.24 Characteristics of the pile groups

Pile No (A/B)	Pile tip (m NGF)	Pile head (m NGF)	Pile length (m)	TS level (m NGF)	TS height (m)	center-to-center spacing (m)
17, 22	146.5	162	15.5	163.8	1.8	3.66
15, 16, 18, 19 20, 21, 23, 24	146.5	162	15.5	163.55	1.55	3.06

5-2-2-1- “Isolated” pile groups (Group I)

According to the NF P 94-262 (2012), the bearing capacity of a pile group should be evaluated when the center-to-center distance “d” is less than 3 times the pile diameter. Based on Table 2.24, the spacing between the piles 17A/B which are studied in this section is either 3.66 m, which is exactly equal to 3D.

Due to the symmetry of the pile-soil domain, half of the model is sufficient. In order to choose the horizontal and vertical limits that prevent the occurrence of boundary effects, a parametric study was performed and load settlement curves were compared as well as the vertical displacement along the borders.

The model 50 x 25 x 50 was finally adopted as shown in Figure 2.41. It should be noted that in this study, the transfer structure is not modeled for a good comparison with the single pile model. The model had 61 966 zones in total (57 150 for the soil and 4 816 for the piles).

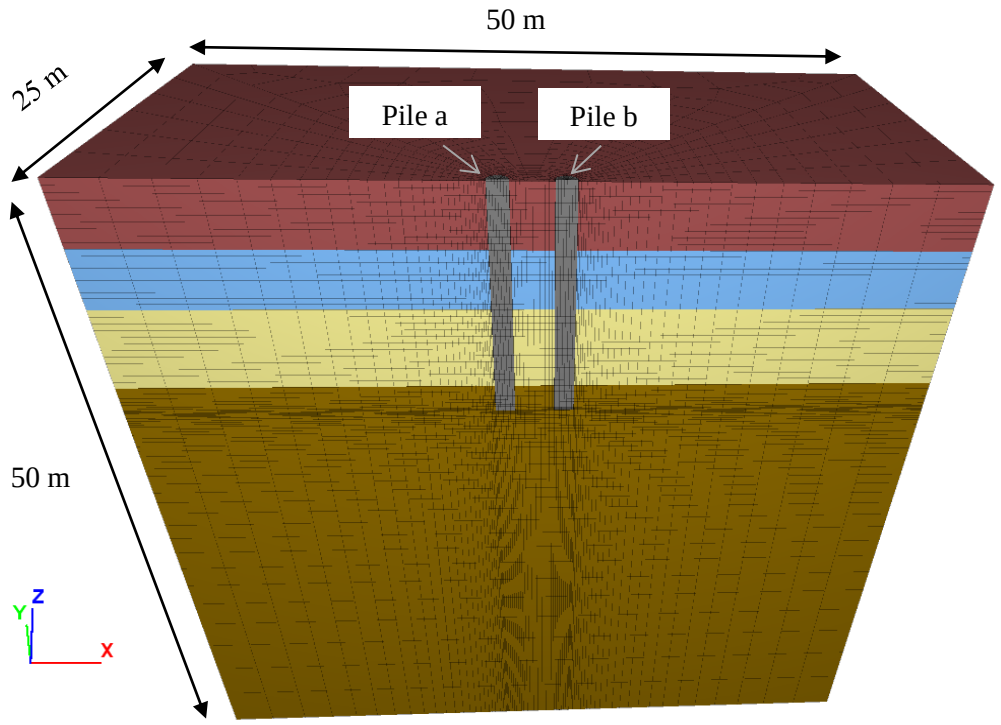

Figure 2.41 Typical model of “isolated” pile groups

5-2-2-2- Pile groups in interaction with each other (Group II)

In order to be able to examine the influence induced on a pile group by the others groups, a new model was designed.

The pile group 17A/B was also studied. For the sake of simplicity in this case, artificial boundaries that represent the symmetry axes between the pile groups had to be set in the midspan of each two groups delineating three boundaries of the model even though the pile groups 17, 18 and 19 does not have exactly the same center-to-center spacing. In addition, a distance of minimum 40 m was considered at the left side of the model in order to minimize boundary effects from this side. A plan view showing these axes together

with the FLAC3D model of the pile group 17A/B are presented in Figure 2.42. This model had 99 000 zones in total (94 184 for the soil and 4 816 for the piles).

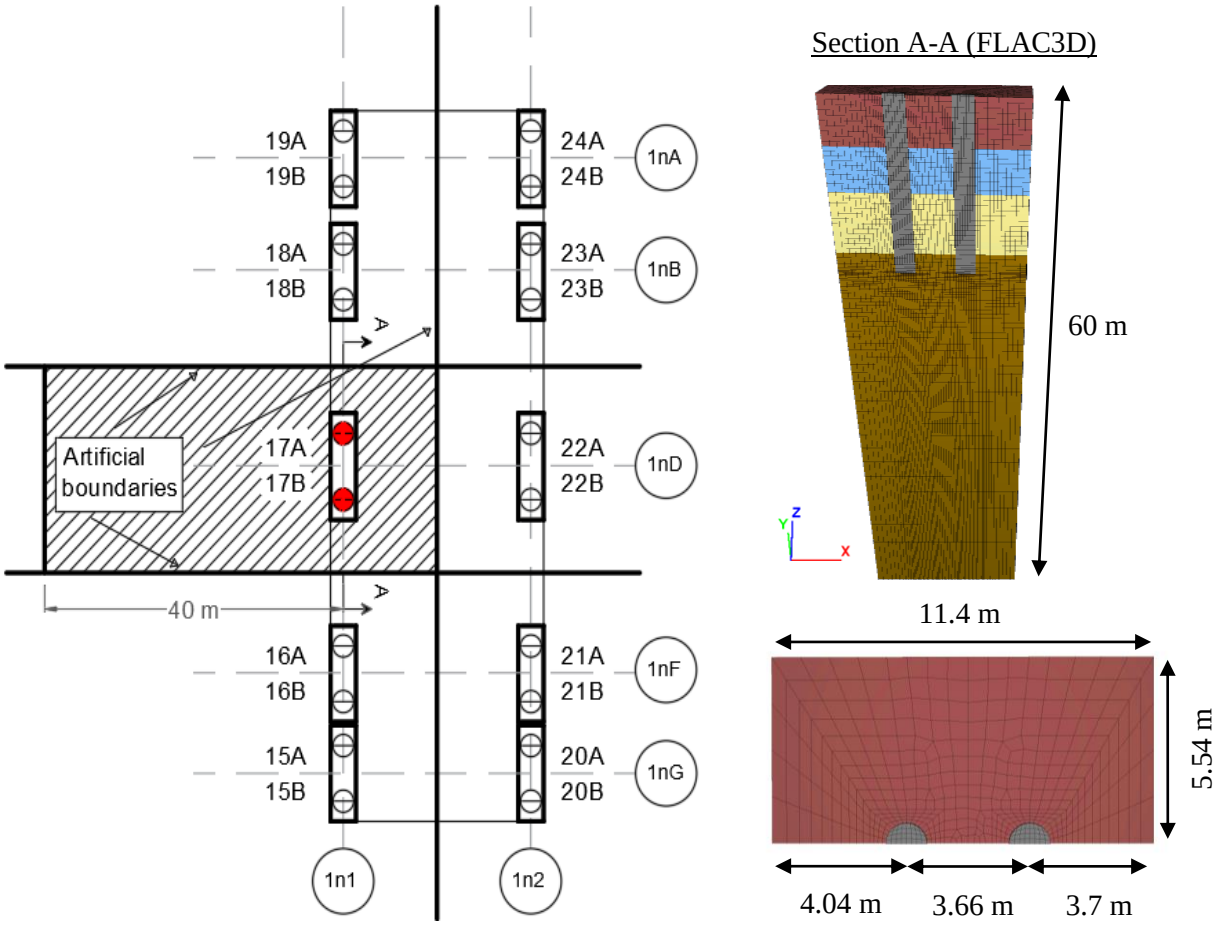

Figure 2.42 Geometric characteristics of Group II model for the piles 17A/B

5-2-3- Global model

In order to assess the global behavior of the foundations, it was important to model all the piles according to the real geometry. However, due to time limitations, some simplifying hypotheses were taken:

- The site was considered isolated, i.e., without any interaction with the neighboring structures. No boundary effects were considered at the borders.
- Only a quarter of the model was considered even though it was not perfectly symmetric and the existing structures that surround Silex^2 were different from each side
- The piles were considered as equally loaded. A load of 10 000 kN was applied on the head of each of the piles as a first step and the vertical displacement was assessed accordingly.

An example of this model is shown in Figure 2.43. It comprises 225 882 elements.

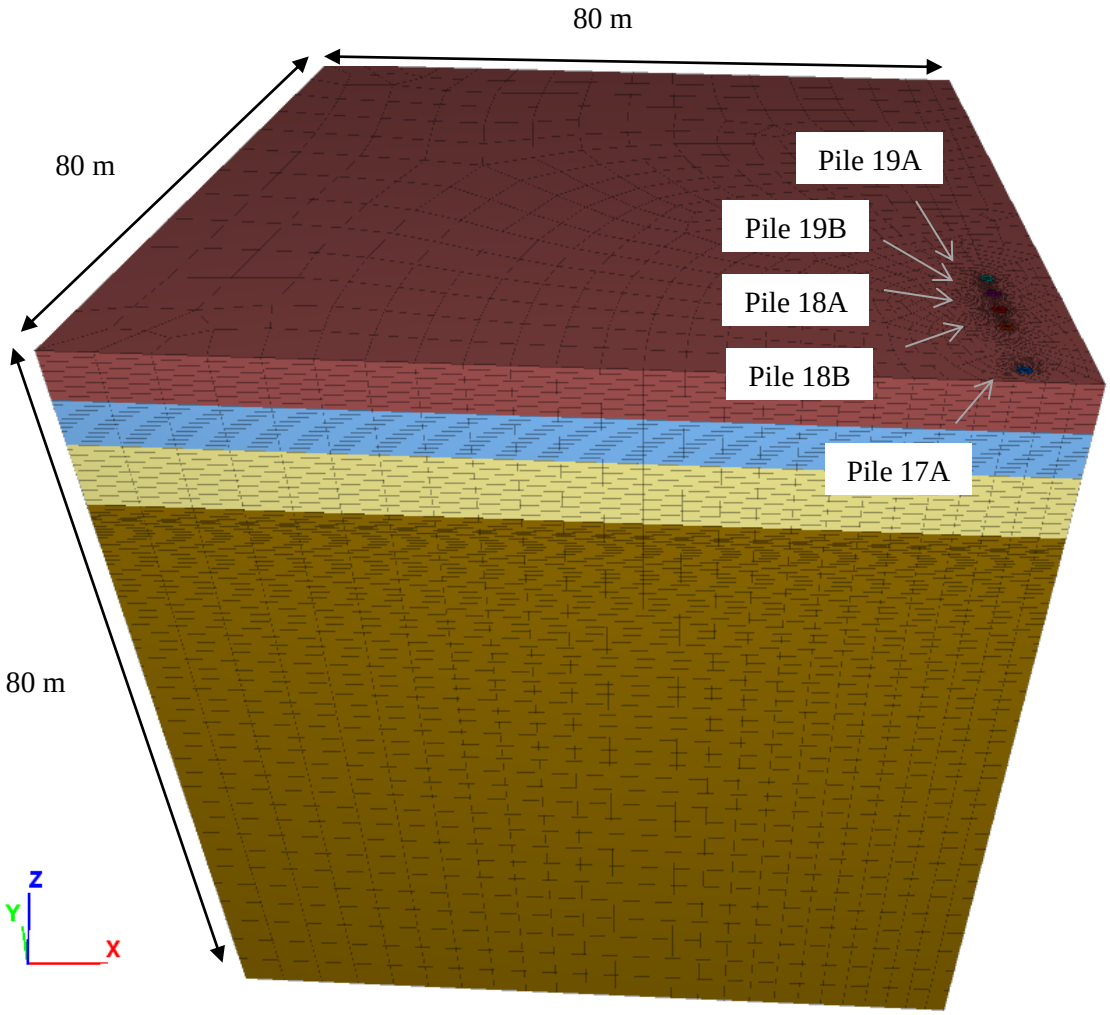

Figure 2.43 Typical example of a global model

6- Conclusion

This chapter was intended to present in details the tower Silex[2] and its foundations in particular. It gave also a global review on the soil formation in Lyon: the fluvial alluviums that consists of sands and gravel of compacity and the molasse which is a sandy layer of particular characteristics.

The instrumentation carried out was also presented, allowing on one hand, the measurement of the deformation in the piles and the stress at their head. On the other hand, a fiber glass extensometer was installed to estimate the settlement of the soil. FLAC3D the numerical tool used was presented as well.

Chapter 3: Results of the numerical models and comparison with analytical methods

1- Introduction

In this chapter, the four different models described in Chapter 2 are examined. In sum, there are few references in the literature that studied the behavior of axially loaded piles using FLAC3D. The few existing references do not describe in a clear manner the influence of each parameters they used in their models. Firstly, sensitivity analysis was performed in the isolated pile model. Then a comparison was made with the pile group models before the global model was studied.

On the other hand, two analytical methods (load transfer method and elastic theory) were applied on this particular project and were compared with the numerical approach.

It should be noted that the order in which these studies are presented in this chapter might be different from the order in which they were practically performed, which may explain why some conclusions were not considered in all the subsequent analyses. However, all findings were included in the global model and in the concluding analysis in chapter 4.

2- Results of the numerical modeling with FLAC3D

2-1- Analysis of the isolated pile models

Isolated piles are the first and simplest models performed in FLAC3D in this thesis. Despite the fact that a pile load test could not be done on site, these numerical models were still useful for a better understanding of the behavior of the pile with respect to its surrounding soil layers.

2-1-1- General calculation hypotheses

2-1-1-1- Calculation phases

The calculations phases were as follows:

- Phase 0: Initialization of the in-situ stresses after assigning the constitutive models and the characteristics of the soil layers and the soil-pile interface only. In this phase, the pile is assigned the same parameters of the adjacent soil. Horizontal stresses are calculated using K_0 procedure as in Eq. 3.1. An equilibrium is then reached and displacements are set to zero.

$$\sigma'_h = K_0\,\sigma'_v \;\; ; \quad K_0 = 1 - sin\phi \text{ (Jaky, 1944)} \qquad \text{Eq. 3.1}$$

- Phase 1: Installation of the pile by modifying the constitutive model to linear elastic isotropic model and its parameters to the corresponding ones. The pile was assumed to be “wished in place” which means that the effect caused by its construction on the stress conditions of the soil is neglected. After phase 1, an equilibrium is reached and displacements are also set to zero.

- Phase 2: The vertical load is applied on the head of the pile in small load steps. Iterations were performed within each load step, to satisfy the equilibrium as shown in Section 2-1-1-3.

2-1-1-2- Load application method

The load application on the head of the pile can be modeled in two ways:

- By applying a vertical displacement velocity V for a given number of steps N which gives an axial displacement D according to the equation N = D/V. The velocity should be kept small to minimize inertial forces and to prevent the shocks in the system.
- By applying a vertical stress at the head of the pile, by small increments.

Both methods were tested and compared by using different velocities (5×10^{-7}, 1×10^{-7} and 5×10^{-8} m/step) or different load increments (200 steps of 50 kN or 100 steps of 100 kN for example for a total of 10 000 kN). The computation time and the results varied from one case to another.

Besides, in order to solve the problem of long computations resulting from small velocities, an option called "servo mechanism" was used which varies the velocity automatically depending on the convergence of the system and thus makes the simulation faster.

On the other hand, it turned out that load application was faster in terms of calculation time and easier since the applied load can be directly controlled. Therefore, in the coming models, the load was applied on the head of the piles by steps of 25 kN each.

2-1-1-3- Choice of the convergence criteria

The method that should be used varies from one case to another and depends on the geometry of the model, the load application and the impact of the current calculation phase on the final state of the model. Among the convergence criteria available in FLAC3D and detailed in chapter 2, two methods with various target limits were tested:

- The average force ratio with either a limit of 10^{-4} or 10^{-5}
- The criterion "Convergence = 1" which implies that the equilibrium is reached for a convergence value lower than 1 and which is equivalent to a local force ratio equal to 10^{-4}. According to Itasca (2019), this corresponds to an average force ratio equal to 10^{-5} for a moderately complex model.

After comparing these methods, it was decided that an average force ratio of 10^{-4} is to be used for initial state, material properties assignments, and intermediate construction phases (e.g., soil excavation) since a more reduced ratio does not improve the calculation. On the other hand, for all load application phases, an average force ratio of 10^{-5} was found better.

2-1-2- Sensitivity analysis

Several factors can affect the behavior of deep foundations. Amongst them is the presence of the water table, the pile's Young modulus, the soil parameters, but also the parameters assigned to the soil-pile interface. This section is intended to provide highlights on the influence of these parameters on the piles in the project. The soil parameters initially used by "Eiffage Construction Confluences" in their Plaxis3D design will serve as a starting point for this analysis. They are summarized in Table 3.1.

Table 3.1 Soil parameters based on an internal document provided by the company

	γ (kN/m^3)	E (MPa)	c (kPa)	ϕ (°)	ψ (°)
Alluviums 1	20	135	50	35	5
Alluviums 2		20			
Alluviums 3		150			
Molasse		300			

In this table, the deformation modulus was deduced from the harmonic mean of all the pressuremeter moduli measured in the soil layers using Eq. 1.134. The diameter and the length of the piles in this section are 1.22 m and 16 m unless otherwise stated. The boundary dimensions of the model are 25 m x 25 m x 50 m based on the results shown in the previous chapter and a Mohr-Coulomb constitutive model is used for the soil.

It should be also noted that the maximum dead load applied on the head of the piles during the construction of the steel structure is around 3 000 kN (Table 4.5 and 4.6 of Chapter 4). Therefore, this study will be limited to this load range.

2-1-2-1- Influence of the water table level

The site location is characterized by a very shallow ground water table estimated at 161.9 m NGF which means that the piles are almost totally submerged in the water. The following study was made in order to understand the effect of the water table on the behavior of the pile and the soil layers. Thus, in this section, the ground water table is modeled without allowing any flow since the load is applied slowly on the piles and no pore water pressure is supposed to be generated. Different examples with a water table level varying from the top to the bottom of the pile were modeled. In these models, saturated soil layers were assumed beneath the water table and the parameters were kept constant.

The analysis showed that for a load up to 5 000 kN, the piles behavior was not greatly affected by the presence and the location of the water table. In fact, the pile settlement slightly increased with the rise in water table level from 3.73 mm for a totally dry soil to 4.06 mm when the water is near the head of the piles.

On the other hand, the piles in Silex^2 are likely to match the case with a shallow water table located at z = 0 m. The results are presented in Figure 3.1 and Figure 3.2 and are summarized in Table 3.2.

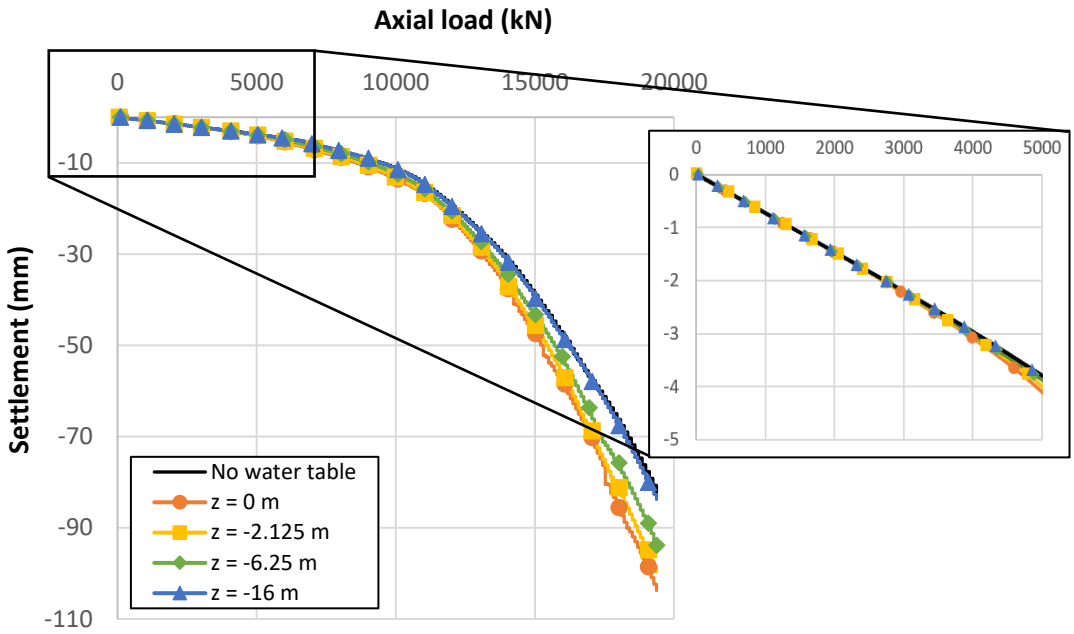

Figure 3.1 Pile load settlement curves for different ground water levels

Table 3.2 Pile's head settlements for different cases and different load values

Dry soil (No water table)		Water table at z = 0 m		Water table at z = -2.125 m		Water table at z = -6.25 m		Water table at z = -16 m	
Load (kN)	**Disp. (mm)**	**Disp. (mm)**	**Increase (%)**	**Disp. (mm)**	**Increase (%)**	**Disp. (mm)**	**Increase (%)**	**Disp. (mm)**	**Increase (%)**
2 000	1.42	1.43	0.7	1.42	0	1.43	0.7	1.43	0.7
3 000	2.18	2.18	0	2.16	-0.92	2.15	-1.38	2.14	-1.83
5 000	3.73	4.06	8.85	3.95	5.9	3.83	2.68	3.75	0.54
10 000	11.2	13.47	20.27	13.13	17.23	12.34	10.18	11.29	0.8

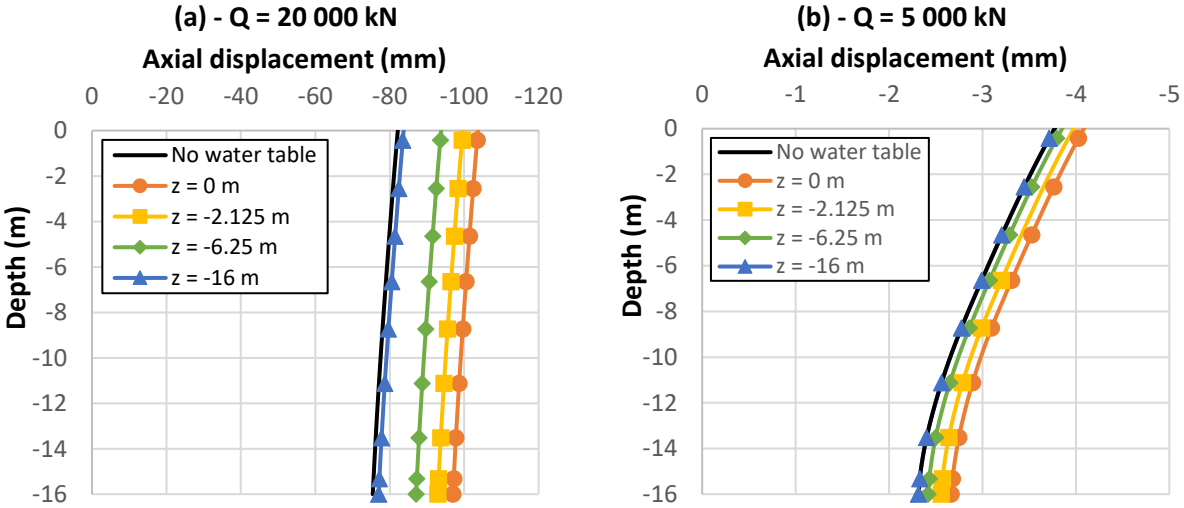

Figure 3.2 Variation of the pile's axial displacement with respect to the depth

It can be seen that the effect of the water table is relatively negligible which agrees well with the high permeability of the soil. Therefore, in the following isolated pile models, the water table will not be considered. However, its influence will be checked later for other geometries in order to verify this hypothesis.

2-1-2-2- Influence of the soil-pile interface parameters

The creation of the interface in FLAC3D allows not only the modeling of the slip and separation that may occur between the structure and the soil but it is also a way to determine the normal and shear stresses at the interface. This is the main reason why an interface should be added.

By default, the behavior of an interface element in FLAC3D is governed by the Mohr-Coulomb failure criterion. It has four main parameters: the cohesion c_{int}, the friction angle ϕ_{int}, the shear stiffness k_s and the normal stiffness k_n.

These stiffnesses are in general calculated using the parameters of the stiffer material i.e., the concrete in the case of a pile-soil interface, based on Eq. 3.2. Therefore, for a range of Young modulus of the concrete equal to (15.7 – 34.5 GPa) and since Δz_{min} in the actual FLAC3D model is equal to 0.07 m, k_n and k_s of the interface were estimated in the range (2.5 – 5.5) x 10^9 kPa/m according to this equation.

$$k_n = k_s = 10\, max\left[\frac{K + \frac{4}{3}G}{\Delta z_{min}}\right] \qquad \text{Eq. 3.2}$$

On the other hand, the cohesion and the friction angle were estimated differently. In the literature, several options are possible:

- Assign to the interface the same cohesion and the friction angle as the soil. This case resembles the case with no interface and the failure occurs when the soil elements surrounding the pile reach the ultimate unit skin friction.
- Assign to the interface parameters that make it stiffer or weaker than the soil since experience showed unrealistic behavior of the pile especially at the tip when the soil parameters are assigned. As an example, the angle ϕ_{int} which may also be referred to as δ' as defined in Eq. 1.132 can vary between 0 and ϕ_{soil} depending on the roughness of the interface and consequently the interface will have reduced strength parameters. In this regard, one can take for example the values $c_{int} = 0$ and $\phi_{int} = 2/3\ \phi_{soil}$ according to the Eurocode 7 (2005). On the other hand, many authors suggested to use the ultimate skin friction q_s of the soil as a cohesion and a zero-friction angle so that the effect of the normal stress could be neglected. The ultimate skin friction q_s may be estimated according to the pressure limit of the soil measured in a pressuremeter test (NF P 94-262, 2012).

In the case of Silex^2 piles, when the cohesion and the friction angle of the soil were estimated at 50 kPa and 35° respectively (Table 3.1), it was shown that in the majority of the above-mentioned cases led to an interface which is weaker than the adjacent soil resulting in a full mobilization of the shaft friction. The only exception to this is the case where the interface was assigned the same parameters as the soil.

The determination of the interface parameters requires experimental tests (Wu et al., 2016). However, since this was not possible in this thesis and since few studies exist that use pile-soil interface in FLAC3D, a

sensitivity analysis was performed in order to evaluate and analyze the influence of each parameter on the behavior of an axially loaded single pile. The soil parameters were chosen so that the interface resistance can be reached and they were considered to be constant (Table 3.1) while each interface parameter was changed at a time.

2-1-2-2-1- Variation of the normal and shear stiffness

The relative soil-pile movement is controlled by the normal and shear stiffness of the interface (Rayhani and El Naggar, 2008). In the following subsection, the cohesion and the friction angle of the interface are considered invariant, whereas the normal and the shear stiffnesses were modified alternatively. The mobilized unit skin friction τ is plotted against the pile-soil relative displacement s_i, which in FLAC3D corresponds to the vertical component of the relative shear displacement vector of the interface nodes. The (τ – s_i) curves at two different depths (in Alluviums 1 and 3) for several values of shear and normal stiffnesses are shown in Figure 3.3 and Figure 3.4 respectively.

- Variation of the shear stiffness k_s

In this study, k_n was fixed at 10^9 kPa/m and k_s was varied from 10^6 to 10^9 kPa/m. It can be seen that for all cases, the ultimate skin friction was the same while the slope of the elastic part increased with the value of the shear stiffness. When the stiffness became greater than 10^7 kPa/m, the curves were very close.

- Variation of the normal stiffness

In this study, k_s was then fixed at 10^6 kPa/m. By varying k_n from 10^4 to 10^9 kPa/m, the slope of the curves was the same but the ultimate skin friction varied from one case to another. Since the normal stress is in a direct relation with the normal stiffness, the ultimate skin friction is straightly affected based on Eq. 3.3.

$$q_s = c_{int} + \sigma_n * \tan \phi_{int} \qquad \text{Eq. 3.3}$$

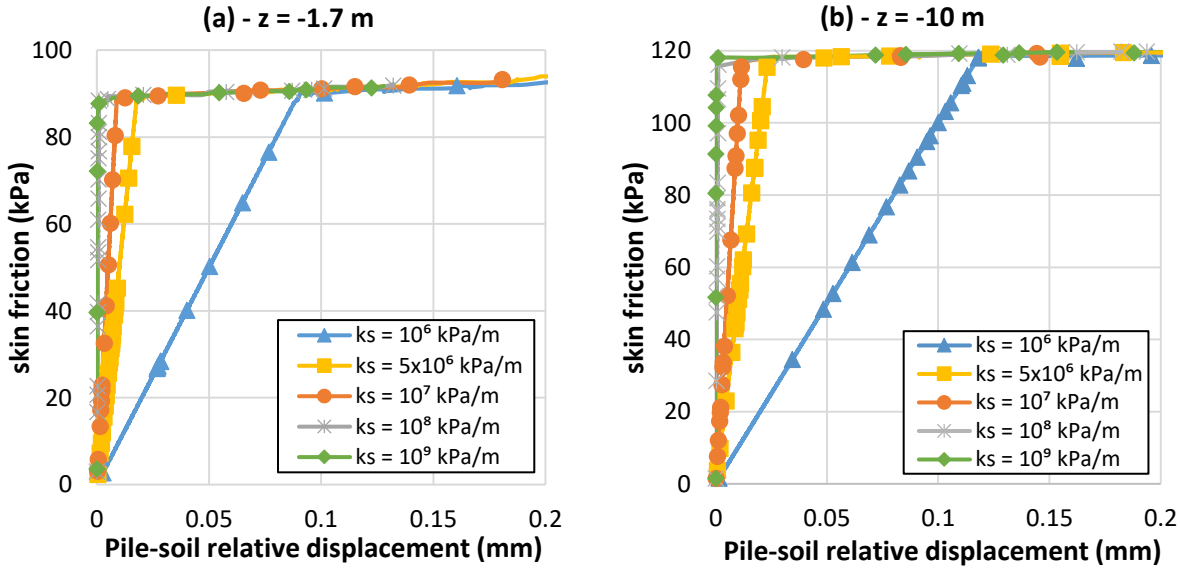

Figure 3.3 Load transfer curves (τ – s_i) for different values of shear stiffness

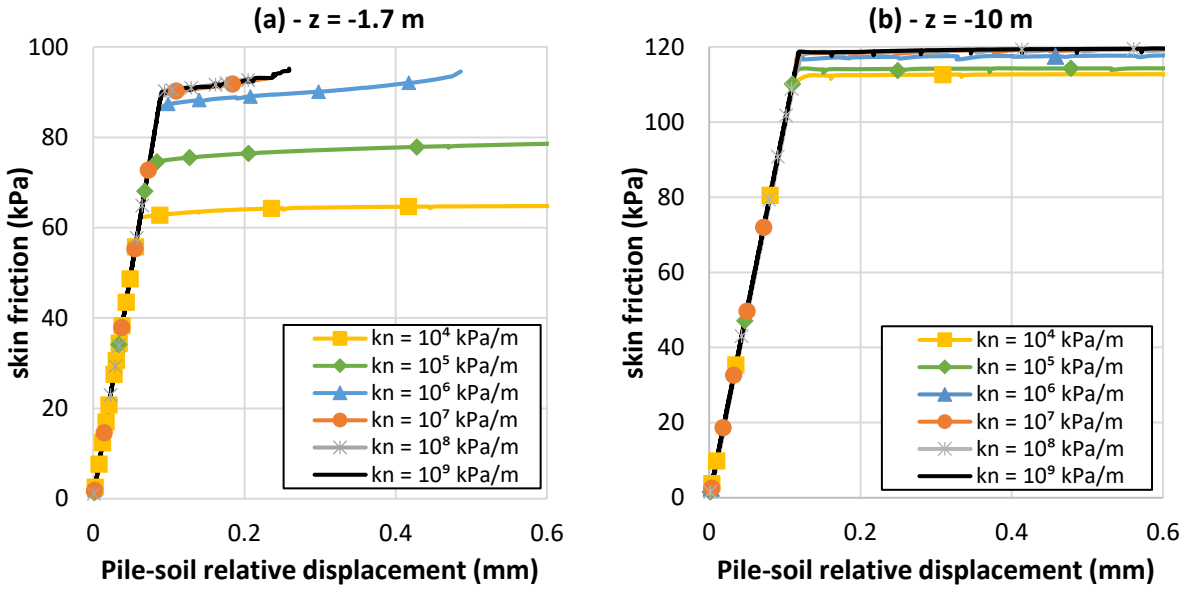

Figure 3.4 Load transfer curves ($\tau - s_i$) for different values of normal stiffness

The load settlement curves were also compared for different values of stiffness (Figure 3.5). They showed that by using k_n and k_s that are greater than 10^7 kPa/m and 10^6 kPa/m respectively, the curves were about the same. These findings are in close agreements with the results of the previous ($\tau - s_i$) curves.

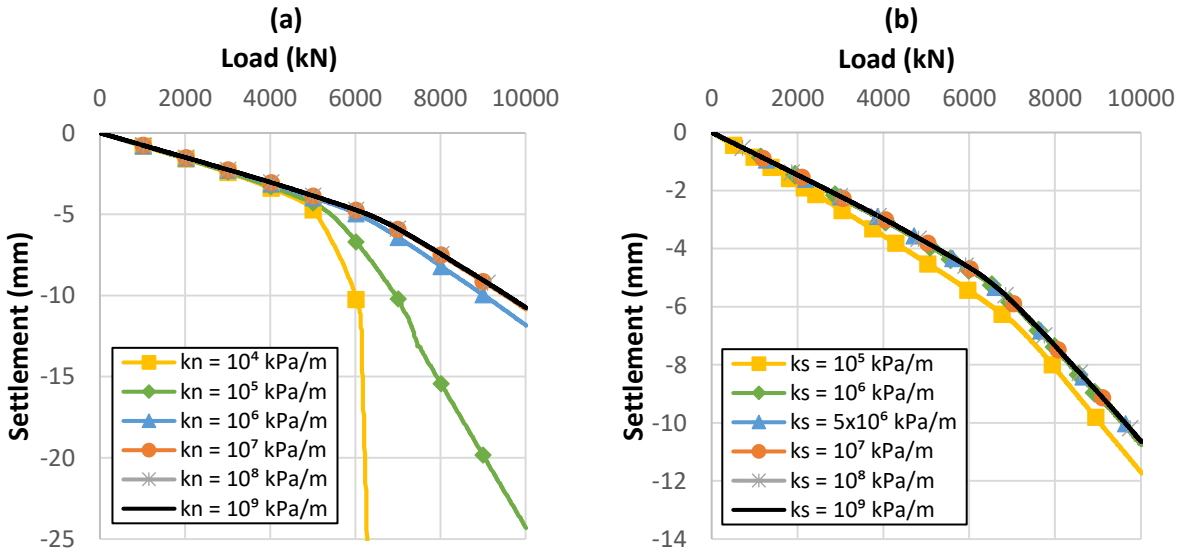

Figure 3.5 Pile load settlement curves for different normal and shear stiffnesses

On the other hand, it is recommended to keep the normal stiffness larger or equal to the shear stiffness in order to avoid interpenetration between the concrete and the soil at the interface level (Xie et al., 2013). In other words, the normal displacement of the interface, should not exceed 10% of the adjacent zone size

which corresponds to a value of 6 and 7 mm at the shaft and the tip of the pile respectively (Itasca, 2019). It is calculated as follows:

$$u_n = \frac{\sigma_n}{k_n} \qquad \text{Eq. 3.4}$$

In this context, the normal displacement of the interface is shown in Figure 3.6 for different stiffness values. It can be noticed from these plots that when $k_n < k_s$, an interpenetration occurred which is revealed by a high normal displacement (16 mm) while this value decreased for the other cases: 5 mm when the stiffnesses were equal and 0.3 mm for $k_n > k_s$.

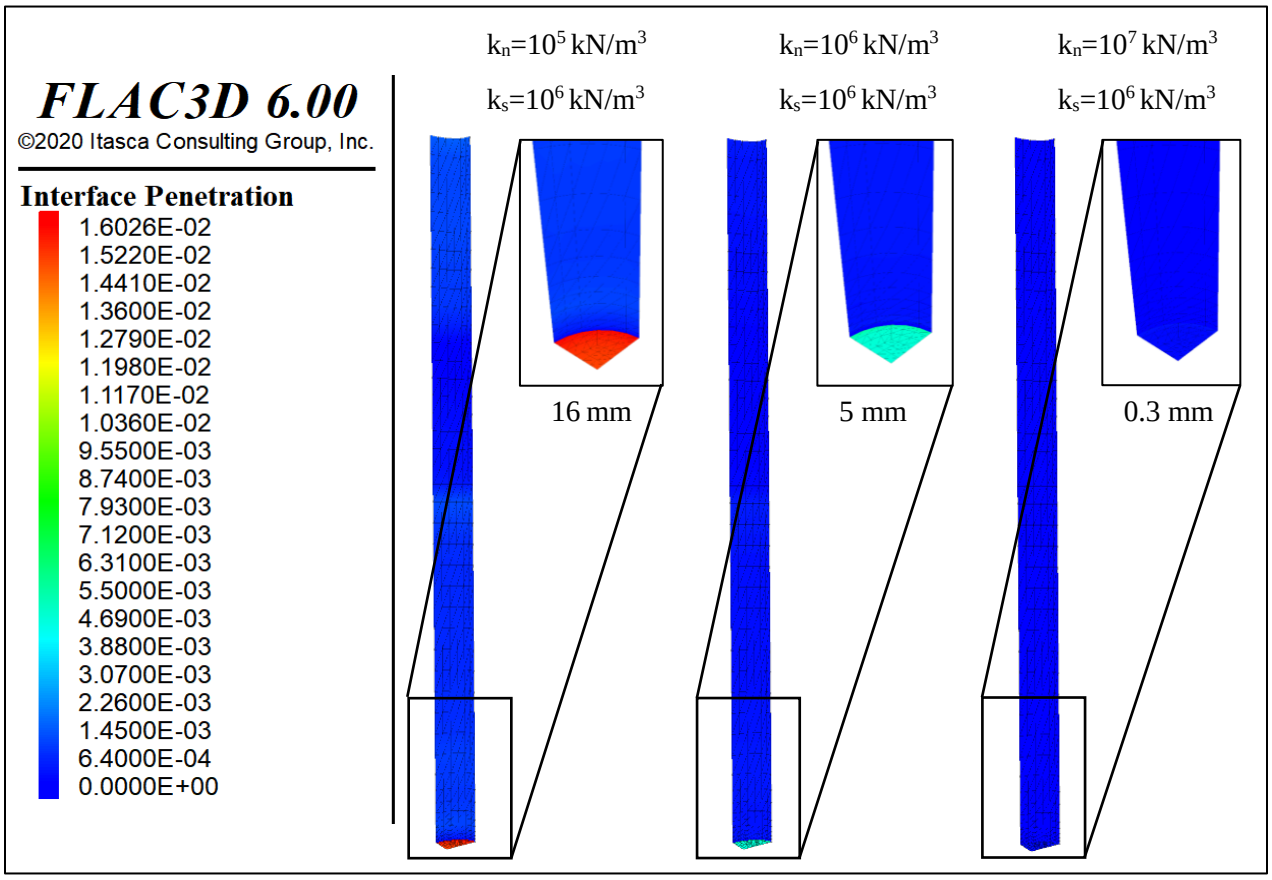

Figure 3.6 Interface penetration for different normal stiffnesses

Finally, it was shown in other FLAC3D studies that when a large contrast in material stiffnesses exists, the model takes too long to converge. It was advised by Itasca to reduce these values while ensuring that this does not affect the results. Thereupon, a value equal to $5x10^8$ kPa/m was used for both stiffnesses in the following section.

2-1-2-2-2- Variation of the cohesion and the friction angle

It was shown that for a high normal stress, the variation of the friction angle has a greater impact than the cohesion (Wu et al., 2016). In this section, the normal and shear stiffness were equal to $5x10^8$ kPa/m while the cohesion and the friction angle have been changed. In order to observe the influence of the interface, the soil parameters were chosen in a way to ensure that the interface's ultimate resistance can be reached. In other words, the cohesion and the friction angle of the soil were fixed at 50 kPa and 35°. For the sake of simplicity, one soil layer was defined along the pile. A load of 10 000 kN was applied on the head of the pile.

Two sets of studies were performed by varying the cohesion and the friction angle of the interface elements:

- Set 1: the friction angle was null while the cohesion has been varied from 0 to 40 kPa.
- Set 2: the cohesion was 20 kPa while the friction angle has been varied from 0 to 35°.

Figure 3.7 illustrates the mobilized shear stress calculated at a certain depth in the soil against the pile-soil relative displacement in both studies.

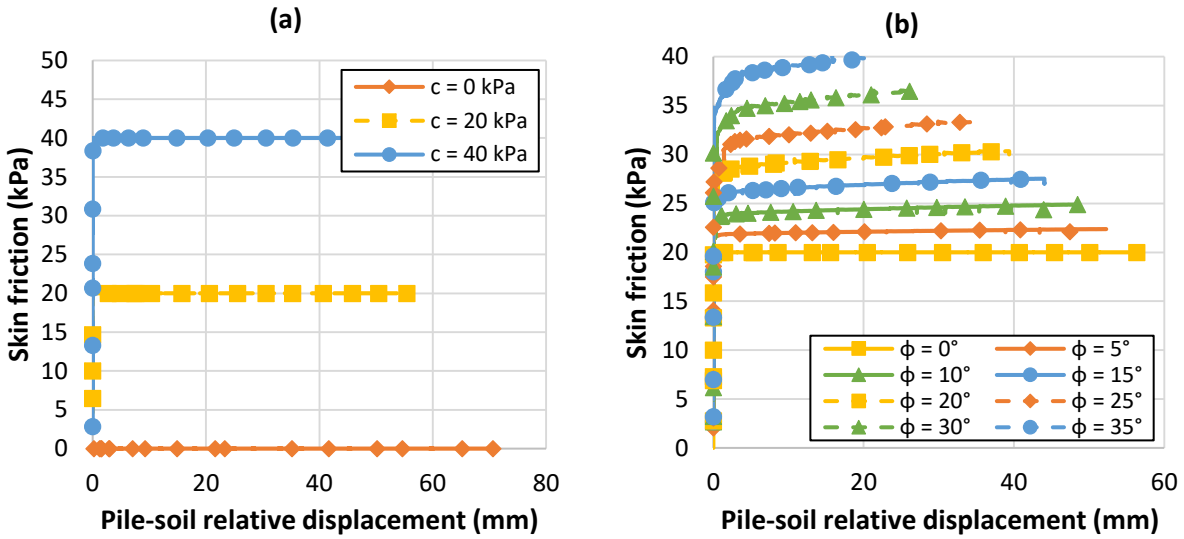

Figure 3.7 Load transfer curves (τ – s_i) for different cohesion and friction angle values

It can be noticed that the ultimate skin friction increases with the cohesion and the friction angle.

Figure 3.7 shows clearly that the variation of the mobilized shear stress follows the Mohr Coulomb failure criterion according to Eq. 3.3. However, the relation between φ_{int} and τ is not linear because of the normal stress in the same equation.

On the other hand, graphs showing the vertical displacement and the load transferred along the pile with respect to the depth for different cases of cohesion and friction angles (c_{int}, ϕ_{int}) are presented in Figure 3.8 and 3.9. These curves were plotted for an applied load equal to 5 000 kN.

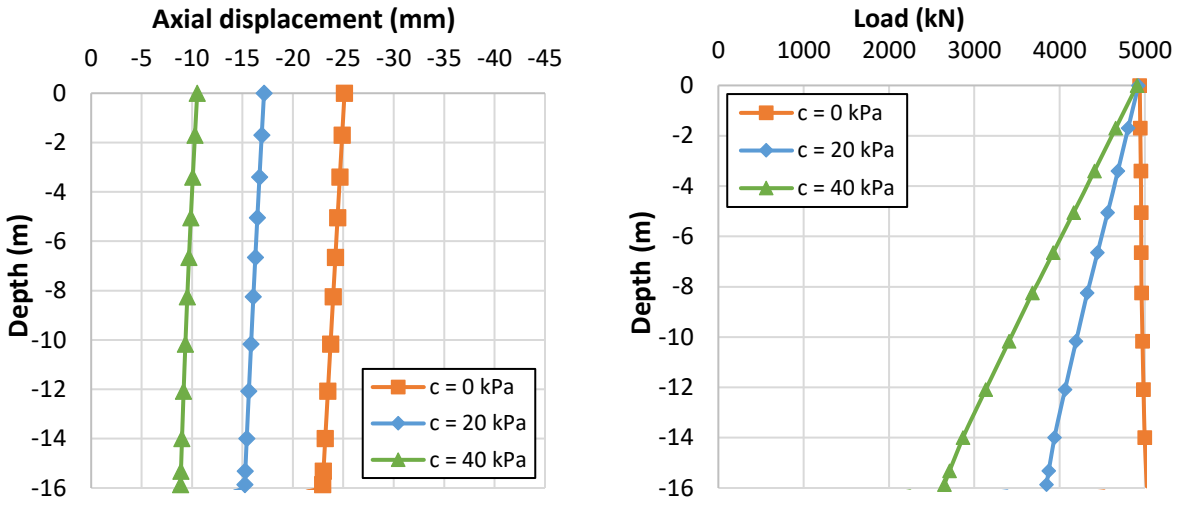

Figure 3.8 Load and displacement profiles along the pile for $\phi_{int} = 0°$

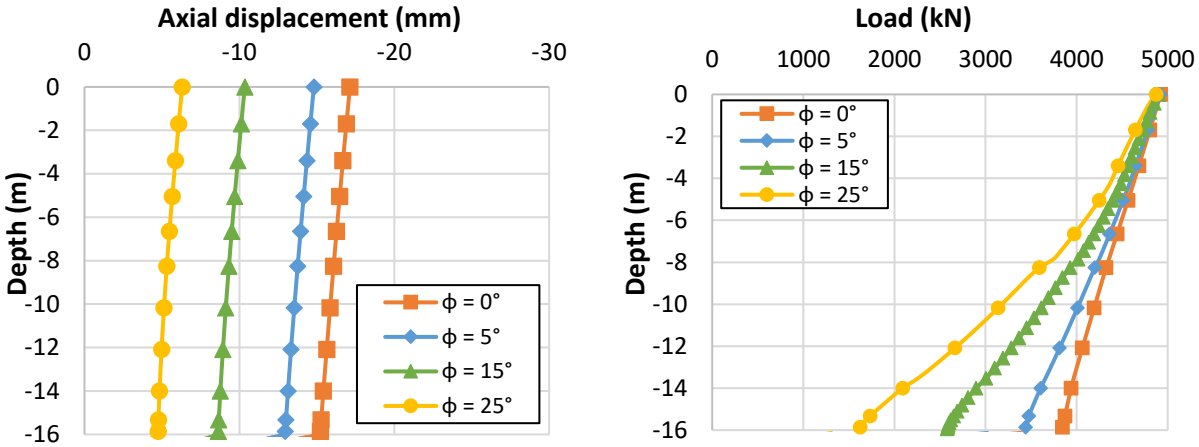

Figure 3.9 Load and displacement profiles along the pile for $c_{int} = 20$ kPa

The axial displacement along the pile is lower when the interface is stiffer, i.e., for greater values of cohesion and friction angle. This is caused by the increase of the skin friction along the shaft of the pile and consequently the decrease of the load at its base, assuming that the total load is invariant. It can be also seen that when the cohesion and the friction angle of the interface had a zero value, the skin friction is zero and the applied load was completely carried by the pile's tip.

In addition to the previous models where the cohesion and the friction angle were varied, another case without interface was also performed. For a better comparison of this model with the others, it was suggested to give the interface the same friction angle as the soil (35°) and to vary the cohesion. Results are shown in Figure 3.10.

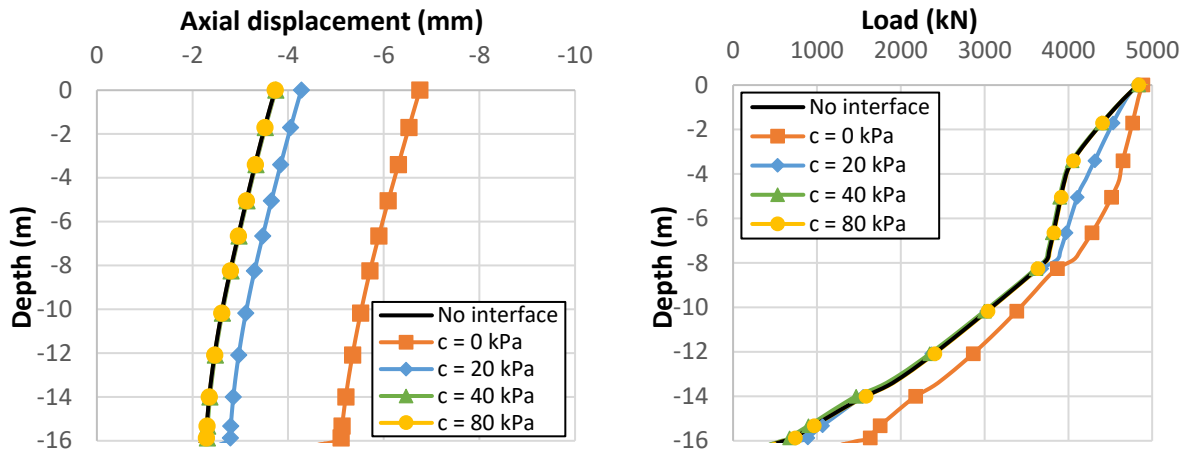

Figure 3.10 Load and displacement profiles along the pile for ϕ_{int} = 35°

The example when the interface was not modeled appeared to give similar results to the case where the interface had the same properties as the adjacent soil, i.e., c = 50 kPa and ϕ = 35°. In this case, the failure occurs in the soil. These findings validate the previous results of Wu et al. (2016) and Xie et al. (2013). Therefore, provided that the interface has the same parameters of the soil, the difference between the models with or without interface is negligible. Some researchers suggested not to model it in order to reduce the computation time (Jenck, 2005; Jimenez, 2019).

2-1-2-3- Influence of the soil parameters

The behavior of the piles depends largely on the soil parameters which remain unknown in Silex[2] or have been roughly estimated in previous projects. A sensitivity analysis was performed with the purpose of testing a wide range of soil properties. This analysis was undertaken on a single pile subject to 5 000 kN which is the maximum possible applied load on site. Firstly, it was shown that for this load the influence of the soil density was negligible. Two different unit weights were tested which are 18 kN/m^3 and 20 kN/m^3 and the settlement obtained was 3.73 and 3.76 mm respectively.

In the following section, the influence of the Young modulus, the cohesion, the angles of friction and of dilatancy of the soils was examined. The Young modulus assigned to the concrete in all these models was 34.5 GPa based on Section 2-3-2 of Chapter 2.

2-1-2-3-1- Influence of Young's modulus of the "alluviums 2" layer

The location and the thickness of the alluviums 2 layer varies from a location to another in Part-Dieu. Thus, it was necessary to understand and evaluate the effect of the absence, or the presence of this layer and in the second case, the influence of its parameters as well on the behavior of the piles, especially the modulus. In this section, the interface is assumed to have the same parameters as the soil so that they can reach the ultimate skin friction capacity together.

The modulus has been varied from 20 to 150 MPa (Table 3.3) and the results are shown in Figure 3.11 and 3.12 and Table 3.4 for Q = 5 000 kN. It should be noted that the load values in the profiles are displayed after subtracting the initial load along the pile measured prior to its loading and thus they are the result of the pure loading activity.

Table 3.3 Soil parameters used – Influence of the modulus of alluviums 2

Soil layer	Soil parameters				Interface parameters	
	E (MPa)	c (kPa)	ϕ (°)	ψ (°)	c_{int} (kPa)	Φ_{int} (°)
Alluviums 1	135	50	35	5	50	35
Alluviums 2	**Varies**					
Alluviums 3	150					
Molasse	300					

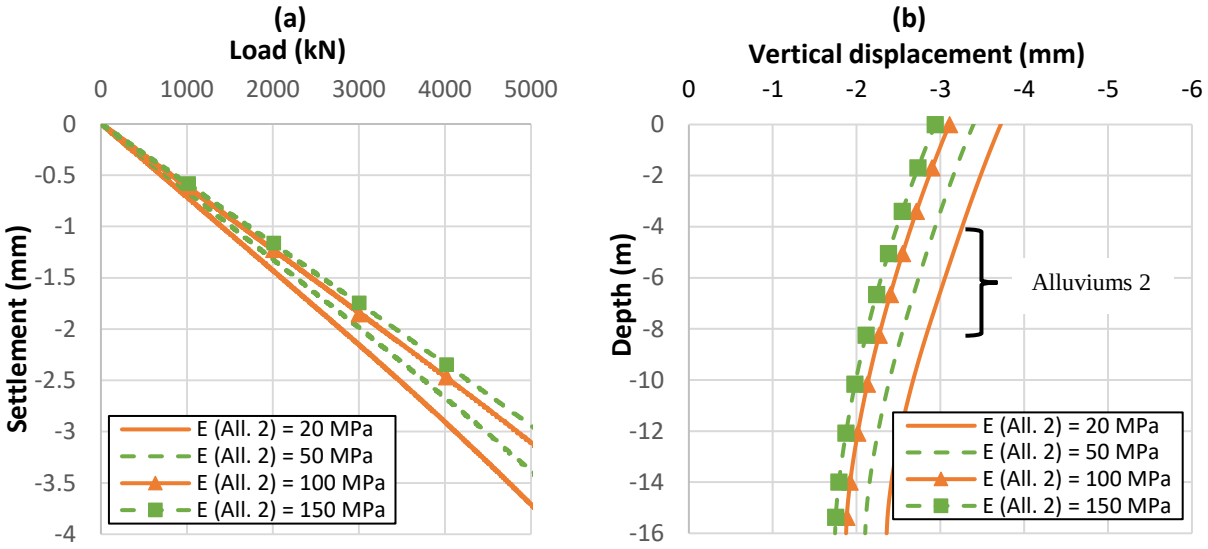

Figure 3.11 (a) Pile load settlement curves and (b) displacement profile for different moduli

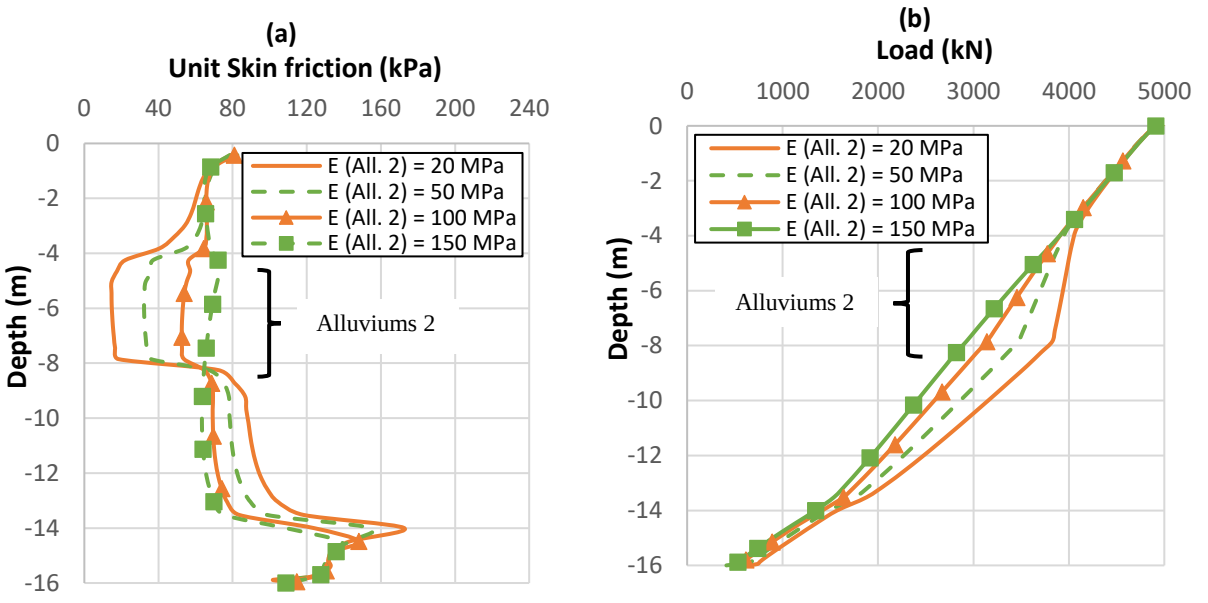

Figure 3.12 (a) Unit skin friction profile and (b) load profile for different moduli

Table 3.4 Summary of the pile settlement, the skin friction and the tip force for Q = 5 000 kN for different moduli

	Q_s (kN)	Q_b (kN)	Head displacement (mm)	Tip displacement (mm)
E = 20 MPa	4 358	642	-3.73	-2.36
E = 50 MPa	4 450	550	-3.41	-2.1
E = 100 MPa	4 539	461	-3.12	-1.87
E = 150 MPa	4 589	411	-2.95	-1.74

The model with the lowest modulus (20 MPa) generates the lowest mobilized unit skin friction in the pile section between -4.25 and -8.25 m and consequently the lowest skin friction force and the highest axial displacement.

On the contrary, in the model with 150 MPa, the skin friction seems homogeneous along the pile shaft since the moduli of all the layers are close. The load at the tip in this case is lower which causes lower pile settlements for identical properties at the tip of the pile. This case may represent the real behavior of the piles in case the alluviums 2 layer was not present in this location.

2-1-2-3-2- Influence of Young's modulus of the "molasse" layer

The molasse layer, which starts at 148 m NGF in average, was a critical point in this thesis since it was not well characterized in previous projects. Besides, the embedment of the piles in this layer was not properly defined and the bottom of the reinforcing cage was limited to 147.5 m NGF so that no instruments could be installed at higher depths.

Therefore, in this study, the modulus of the molasse was varied from 100 to 400 MPa while keeping the other parameters constant (Table 3.5). The interface elements were assigned the same parameters as the soil. The results of the comparative tests are shown in Figure 3.13 and 3.14 and Table 3.6 for Q = 5 000 kN.

Table 3.5 Soil parameters used – Influence of the modulus of the molasse

Soil layer	**Soil parameters**				**Interface parameters**	
	E (MPa)	**c (kPa)**	**ϕ (°)**	**ψ (°)**	**c_{int} (kPa)**	**ϕ_{int} (°)**
Alluviums 1	135	50	35	5	50	35
Alluviums 2	20					
Alluviums 3	150					
Molasse	**Varies**					

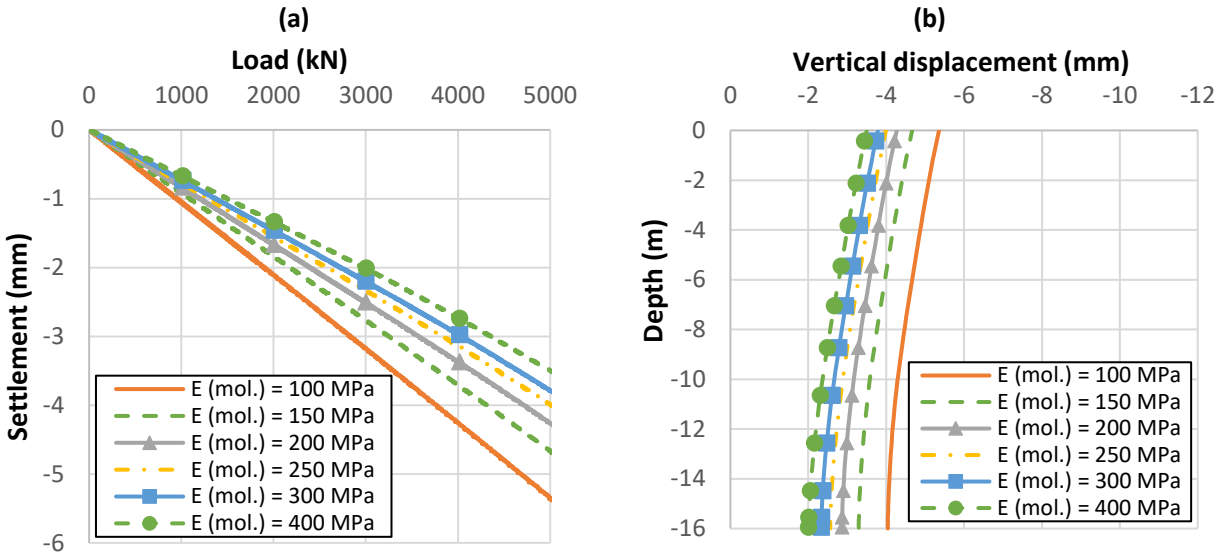

Figure 3.13 (a) Pile load settlement curves and (b) displacement profile for different moduli

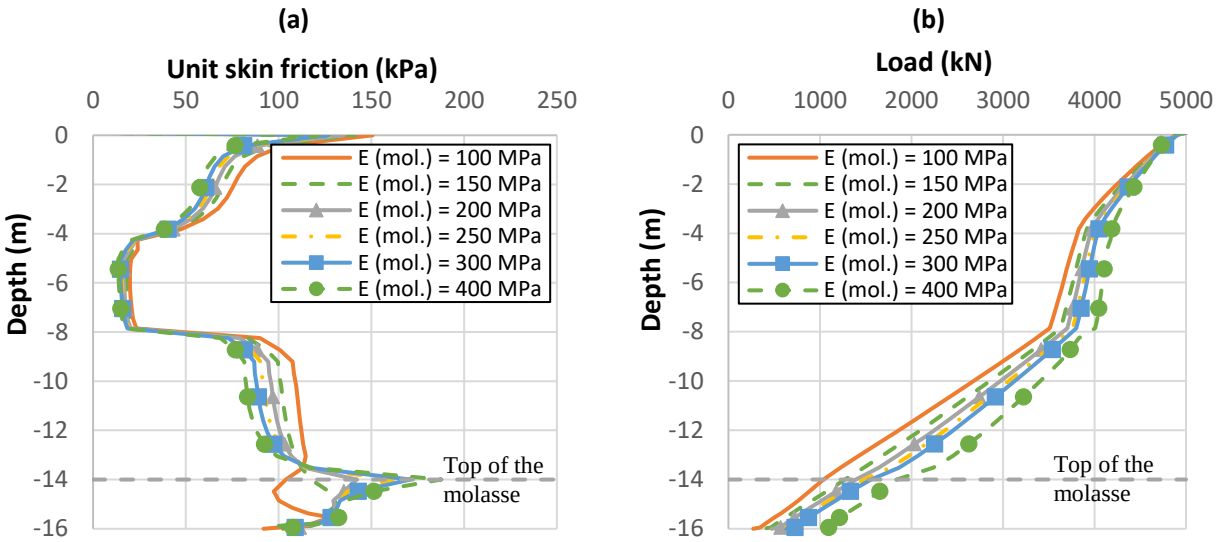

Figure 3.14 (a) Unit skin friction profile and (b) load profile for different moduli

Table 3.6 Summary of the pile settlement, the skin friction and the tip force for Q = 5 000 kN for different moduli

	Q_s (kN)	Q_b (kN)	Head displacement (mm)	Tip displacement (mm)
E = 100 MPa	4 729	271	-5.37	-4
E = 150 MPa	4 628	372	-4.7	-3.3
E = 200 MPa	4 528	472	-4.3	-2.9
E = 250 MPa	4 442	558	-4	-2.56
E = 300 MPa	4 368	632	-3.8	-2.3
E = 400 MPa	4 000	1000	-3.5	-2

As the embedment of the pile in the molasse is estimated at 2 m in this section, the behavior observed in the previous figures is driven simultaneously by the mobilized skin friction and the end-bearing pressure that are both affected by the Young modulus of the molasse. The graphs show that a larger value of the modulus increases the mobilized skin friction at the pile's shaft only in the molasse layer while it decreases in the upper part. The total mobilized load at the pile's shaft is however lower (Table 3.6).

It can be noticed by examining Figure 3.14, that the end-bearing effect takes precedence over the skin friction, which in any case is limited to 2 m only at its best. This is caused by a variation of the modulus under the tip of the pile. It was noticed that the variation of the load transferred to the pile's tip is more pronounced than in the previous section and that it increases with the modulus of the molasse. Despite the high load at the tip, the displacement is lower because of the effect of the modulus at this level.

It can be deduced from the two previous sections that the modulus of the molasse has a more significant effect. The modulus of the soil is a critical parameter in the analysis of the pile's behavior, the reason why several methods exist in the literature that estimate this parameter from experimental, analytical or numerical results.

2-1-2-3-3- Influence of the friction angle of the soil

There are few studies that characterize the strength of the alluviums and the molasse in Part-Dieu. Shear box tests were performed on the upper layer of the alluviums and few triaxial tests were carried out on the molasse (Section 3-1 of Chapter 2). However, since these are not enough, it was necessary to understand the influence of the strength parameters of the soil on the behavior of the pile.

In this paragraph, the friction angle has been varied from 15° to 35° while the other parameters were fixed as shown in Table 3.7. The interface was assigned the same parameters as the adjacent soil.

Table 3.7 Soil parameters used – Influence of the friction angle

Soil layer	**Soil parameters**				**Interface parameters**	
	E (MPa)	**c (kPa)**	**ϕ (°)**	**ψ (°)**	**c_{int} (kPa)**	**ϕ_{int} (°)**
Alluviums 1	135	50	**Varies**	0	50	**Varies**
Alluviums 2	20					
Alluviums 3	150					
Molasse	300					

The results are shown in Table 3.8 and Figure 3.15 and 3.16. The lowest value (15°) was eliminated from this study since it generated an unrealistic pile's behavior with an exaggerated pile settlement.

Table 3.8 Pile settlements for different values of friction angle

Load (kN)	Settlement (mm)			
	ϕ = 20°	ϕ = 25°	ϕ = 30°	ϕ = 35°
1 000	-0.71	-0.71	-0.71	-0.71
2 000	-1.44	-1.44	-1.43	-1.43
3 000	-2.21	-2.16	-2.15	-2.15
4 000	-3.1	-3.00	-2.94	-2.91
5 000	-4.63	-4.01	-3.79	-3.73

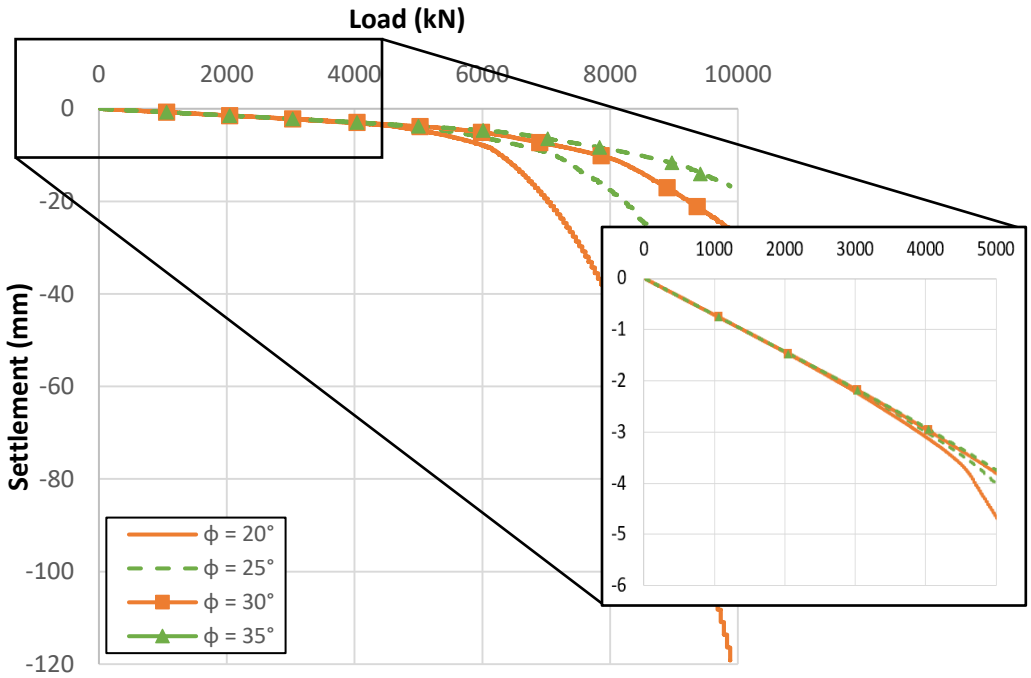

Figure 3.15 Pile load settlement curves for different values of friction angle

Identically to the section 2-1-2-2 (pile interface), it can be noticed that when the friction angle increased, the shaft friction increased and consequently the load at the pile's tip decreased resulting in a lower axial settlement. It was also shown that with a lower friction angle, the soil next to the pile yields more and for a lower applied load.

The model where ϕ = 20° represents the lowest mobilized total load at the pile shaft. The interface elements in this case reached the ultimate value defined by the Mohr-Coulomb criterion and thus a sliding occurs.

However, it was noticed that the three values (25°, 30° and 35°) gave close results for a load going up to 5 000 kN. The skin friction and the pile's axial deformation are not affected by this variation as seen in Figure 3.16.

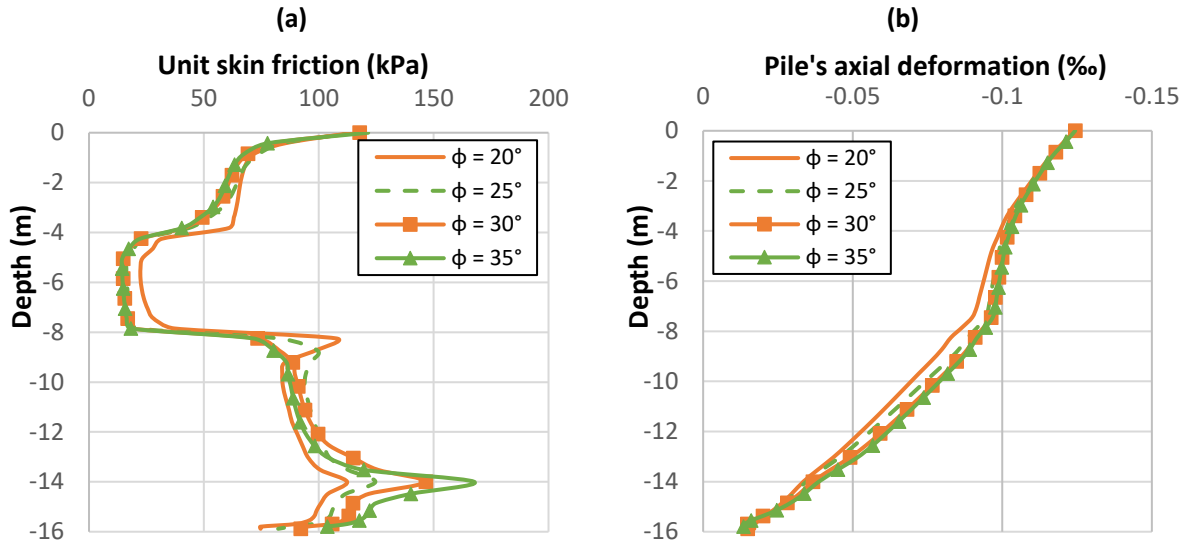

Figure 3.16 (a) Unit skin friction and (b) pile's deformation for different moduli at 5 000 kN

2-1-2-3-4- Influence of the cohesion of the soil

For the same reasons mentioned above, the influence of the cohesion was studied in this section. Therefore, it was varied from 10 to 50 kPa while the other parameters were fixed as shown in Table 3.9. The interface was assigned the same parameters as the adjacent soil.

The results are shown in Table 3.11 and Figure 3.17 and 3.20

Table 3.9 Soil parameters used – Influence of the cohesion

Soil layer	Soil parameters				Interface parameters	
	E (MPa)	c (kPa)	ϕ (°)	ψ (°)	c_{int} (kPa)	ϕ_{int} (°)
Alluviums 1	135	**Varies**	35	0	**Varies**	35
Alluviums 2	20					
Alluviums 3	150					
Molasse	300					

The effect of the variation of the cohesion is similar to that of the friction angle. It can be seen in the following figures and table that the settlement of the pile decreases when the cohesion increases. This effect is more pronounced when the load exceeds a certain limit, i.e., 4 000 kN in this example. This marks the point where the shear stress at some interface elements becomes fully mobilized.

In this study, if a load of 3 000 kN should be considered, the influence of the cohesion and the friction angle on the skin friction and the pile's deformation may be absolutely neglected (Figure 3.20).

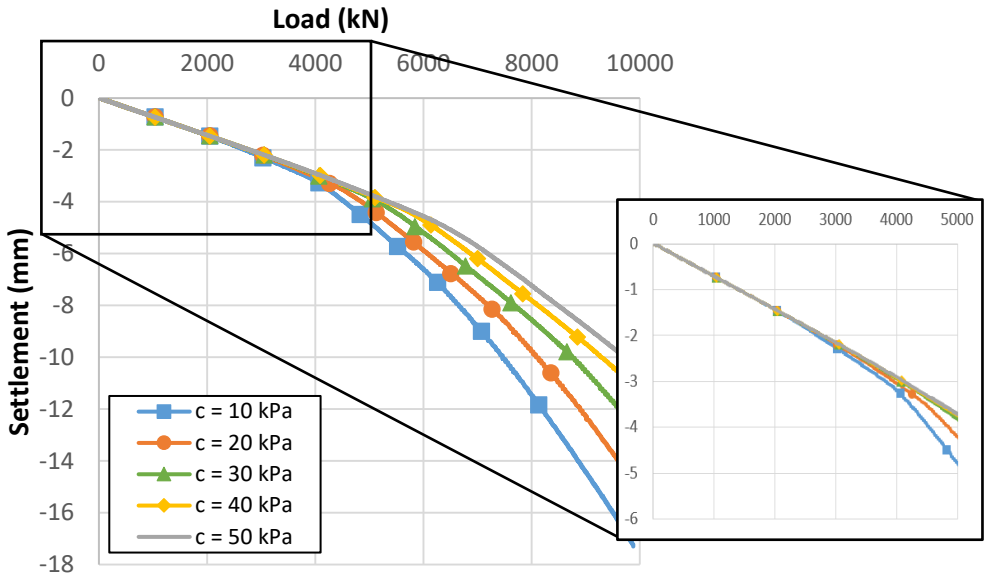

Figure 3.17 Pile load settlement curves for different values of cohesion

Table 3.10 Pile settlement for different values of cohesion

Load (kN)	Settlement (mm)				
	c = 10 kPa	c = 20 kPa	c = 30 kPa	c = 40 kPa	c = 50 kPa
1 000	-0.71	-0.71	-0.71	-0.71	-0.7
2 000	-1.44	-1.43	-1.43	-1.43	-1.43
3 000	-2.25	-2.17	-2.15	-2.15	-2.15
4 000	-3.20	-3.04	-2.94	-2.92	-2.91
5 000	-4.76	-4.19	-3.81	-3.73	-3.70

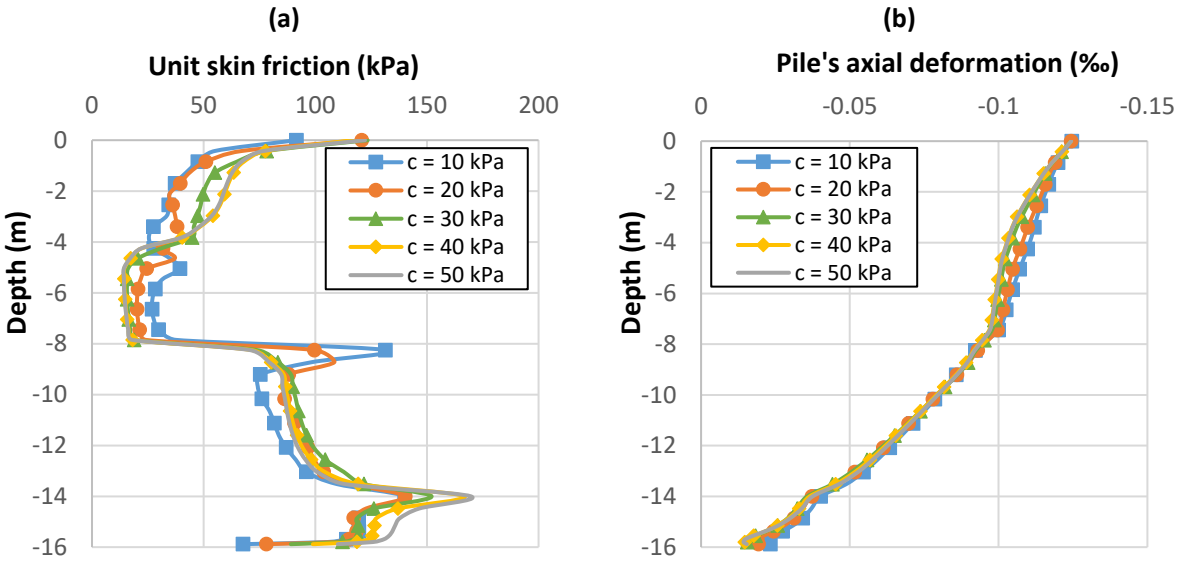

Figure 3.18 Unit skin friction (a) and pile's deformation (b) for different moduli at 5 000 kN

2-1-2-3-5- Influence of the dilatancy angle of the soil

It was shown by many researchers that the dilatancy angle is in close relation with the friction angle of the soil. As an example, it could be determined for sands as follows (Bolton, 1986):

$$\begin{cases} \psi = \phi - 30° & for\ \phi > 30° \\ \psi = 0 & for\ \phi \leq 30° \end{cases} \qquad \text{Eq. 3.5}$$

In this case, for a friction angle equal to 35°, the dilation angle is ψ = 5°.

The dilatancy angle has been varied while the soil layers had a friction angle of 35° and its influence on the pile's behavior was checked. Unfortunately, the relation shown in Eq. 3.5 could not be adopted in these examples because by varying the friction angle, the effect of the dilatancy angle could not be isolated and verified.

The results are presented in Table 3.11. They showed that for a load up to 5 000 kN, where the soil remains in the elastic domain, the variation of this angle has a minimal impact on the pile's settlement.

Table 3.11 Pile settlement for different values of angle of dilatancy

Load (kN)	**Settlement (mm)**				
	ψ = 0°	**ψ = 5°**	**ψ =10°**	**ψ = 15°**	**ψ =20°**
1 000	-0.71	-0.71	-0.71	-0.71	-0.71
2 000	-1.43	-1.43	-1.43	-1.43	-1.43
3 000	-2.14	-2.14	-2.15	-2.15	-2.16
4 000	-2.91	-2.91	-2.90	-2.90	-2.89
5 000	-3.74	-3.71	-3.69	-3.67	-3.66

2-1-2-4- Influence of Young modulus of the pile

A linear elastic constitutive law was assigned to the piles. According to the results of the concrete crushing tests presented in details in Chapter 2, the experimental secant elastic modulus was around 34.5 GPa. However, if the creep of the concrete was to be considered, the modulus should be reduced in a fictitious way up to a value 15.7 GPa in order to be able to evaluate the induced deformation. Therefore, an analysis was carried out to study the influence of the concrete modulus on the behavior of the pile.

In this study, the pile length was 15.5 m, according to the latest revisions of the design documents. This length will be conserved in the following sections.

Figure 3.19 and Table 3.12 show that the pile settlement decreases as the concrete's Young modulus increases. For an applied load equal to 5 000 kN, it drops by 17% when the modulus varies from 10 to 15 GPa and by 38% when it varies from 10 to 35 GPa. This becomes negligible for a value greater than 25 GPa (by comparing the case of 25 GPa to 35 GPa for example).

The axial deformation of the pile which is calculated as the shortening or the expansion of the pile over its original length, also increases when this modulus decreases. This study can help evaluating the permanent deformations caused by the creep.

Table 3.12 Pile settlement for different deformation moduli

Load (kN)	Settlement (mm)					
	E_p = 10 GPa	E_p = 15 GPa	E_p = 20 GPa	E_p = 25 GPa	E_p = 30 GPa	E_p = 35 GPa
1 000	-1.15	-0.96	-0.87	-0.8	-0.76	-0.72
2 000	-2.33	-1.96	-1.75	-1.62	-1.53	-1.47
3 000	-3.5	-2.94	-2.63	-2.43	-2.3	-2.2
4 000	-4.72	-3.96	-3.55	-3.3	-3.12	-3
5 000	-5.99	-5	-4.49	-4.18	-3.96	-3.81
10 000	-15.77	-13.67	-12.6	-12.71	-12.23	-11.22

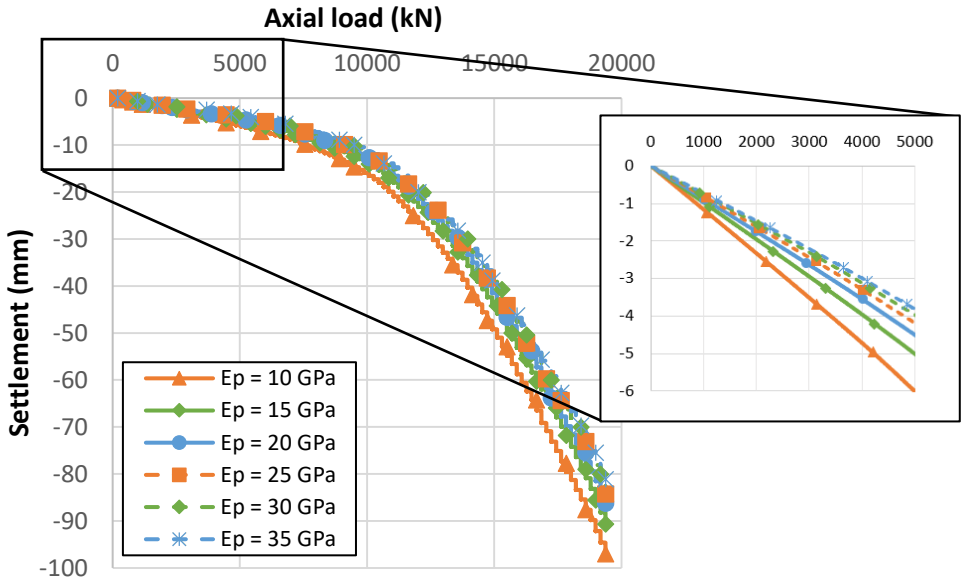

Figure 3.19 Pile load settlement curves for different elastic moduli

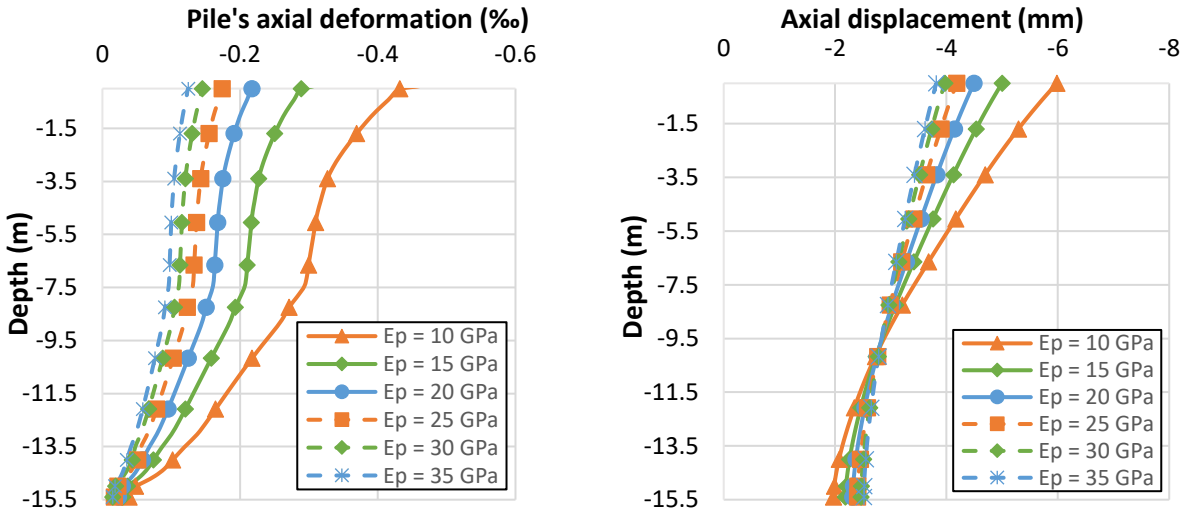

Figure 3.20 Pile's axial displacement and deformation when subject to a load of 5 000 kN

2-1-2-5- Influence of the constitutive law – Comparison between MC and PH models

The major difficulty that may be encountered while modeling geotechnical problems regards the choice of the constitutive law that describes the best the behavior of the structure and the soil. Parallel to this, there is also the choice of the parameters which remains a critical point in the numerical modeling, especially when a high number of parameters is required. The elastic perfectly plastic model with a Mohr Coulomb criterion is the simplest and is sufficient in most cases. However, more advanced models may be employed such as the Plastic Hardening model.

In this section, these two models were tested using the parameters in Table 3.1 or in Table 3.13. The objective of this analysis was to compare the results obtained using the two constitutive models without judging the correctness of the parameters.

The parameters of the PH model were extracted from a previous study performed on a similar project in the same neighborhood. p_{ref} was assumed to be equal to 100 kPa. The first approach considers a E_{50}^{ref} modulus equal to the Young modulus of the layers used in Mohr-Coulomb. The interface elements were assigned a cohesion equal to the ultimate unit skin friction "q_s" and a zero friction.

Table 3.13 Soil parameters used in the PH model

	$E_{50}^{ref} = E_{oed}^{ref}$ (MPa)	E_{ur}^{ref} (MPa)	m	R_f	ν_{ur}	c kPa)	ϕ (°)	ψ (°)	K_{nc}	OCR
Alluviums 1	135	405	0.6	0.9	0.2	50	35	5	0.5	1
Alluviums 2	20	60								
Alluviums 3	150	450								
Molasse	300	900								

The load settlement curves in the two modes are presented in Figure 3.21. It can be seen that the settlement in the PH model was lower than that in Mohr-Coulomb. This is due to the high stiffness of the soil.

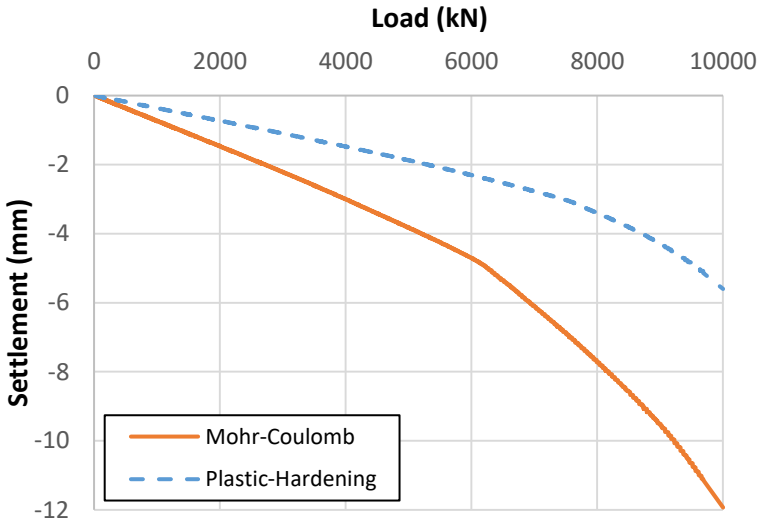

Figure 3.21 Pile load settlement curves in Mohr-Coulomb and Plastic Hardening models

Based on an estimation suggested by Frank et al. (2019), the settlement of a single pile under 70% of its creep resistance load would be estimated at 0.006 times its diameter D, for bored piles. It will be shown later in Section 3-2-2 that this load corresponds to 7 978.5 kN. For a 1.22-m diameter pile, the settlement should be around 7.32 mm. It is shown in Figure 3.21 that the PH models gave settlement that are too small with respect to this hypothesis, which may be caused by an overestimation of the moduli.

In general, in order to verify the accuracy of a constitutive law and determine its parameters, we need to perform experimental tests. The main problem remains actually in the fact that the moduli used in PH models were hard to be determined in this thesis since no triaxial or oedometer tests could be performed on the alluviums and since there is no clear relation between the moduli of PH compared to the ones used in MC. The available equations in the literature are based on experimental tests performed on particular soils and cannot be thus generalized. However, some tests were performed on molasse samples giving some parameters that will be shown in Chapter 4.

Therefore, it was suggested to perform a model that uses MC for the alluviums and PH for the molasse using the same previous parameters. This will be designated as “Combined MC - PH”. This is shown in Figure 3.22.

This model increases the settlement compared with the first PH model, since the moduli of the alluviums do not depend anymore on the pressure and are consequently lower. The new load settlement curve is located between the two initial ones. It represents better the real case.

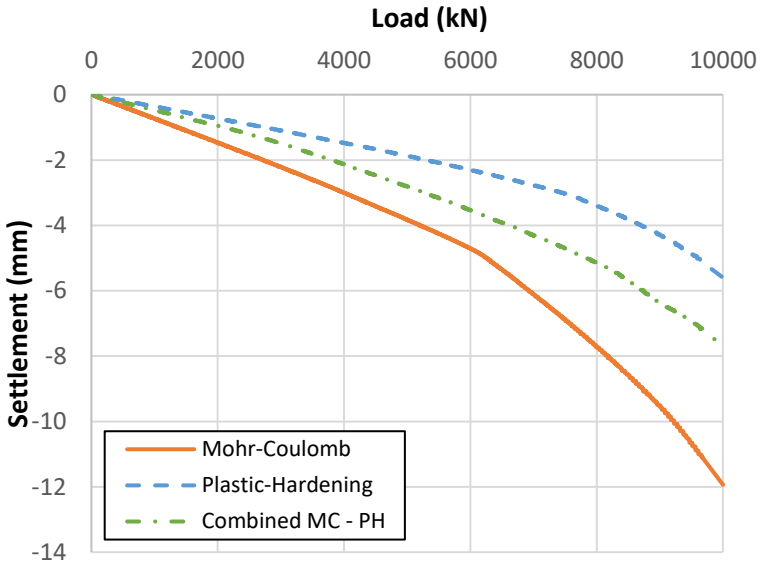

Figure 3.22 Pile load settlement curves in different models

2-1-2-6- Summary and Conclusions

In the previous section, a sensitivity analysis was performed on a single pile model in FLAC3D. The influence of different types of parameters on the pile's behavior was tested. In summary, these were the main findings that correspond to the load range assumed in this project only (Table 3.14).

Table 3.14 Summary of the models tested in the sensitivity analysis

Section	Tested parameter	Main findings
2-1-2-1	Water table level	It has no great influence over the behavior of the pile
2-1-2-2	Soil-pile interface parameters	○ The normal and shear stiffnesses have no role on the load settlement curves provided that they are higher than 10^7 kPa/m and 10^6 kPa/m respectively. The first condition was also imposed in order to avoid interpenetration between the pile and the soil ○ The influence of the cohesion and the friction angle was found important when the skin friction is fully mobilized (for a load which is higher than the load range in this project). When these parameters were increased, the ultimate skin friction increased too while the pile settlement showed lower values.
2-1-2-3-1	Young modulus of the alluviums 2 layer	When the modulus of this layer was increased, the mobilized skin friction increased and the settlement decreased. The case with high modulus can be likened to that without this layer at all.
2-1-2-3-2	Young modulus of the molasse layer	Since the pile is embedded in the molasse, both the skin friction and the end-bearing pressure are affected by the variation of the modulus but the latter takes precedence over the former. Therefore, when the modulus of the molasse increased, the load at the pile's tip increased but the settlement decreased.
2-1-2-3-3 **2-1-2-3-4**	Strength parameters of the soil (c and ϕ)	When the cohesion and the friction angle were increased, the skin friction increased and consequently the load at the pile's tip decreases resulting in a lower axial settlement. However, this effect is minor for small load values.
2-1-2-3-5	Dilatancy angle of the soil	For a small load, where the soil remains in the elastic domain, the variation of this angle has a minimal impact on the pile settlement.
2-1-2-4	Elastic modulus of the pile	The pile settlement decreased when the Young modulus of the concrete was increased.
2-1-2-5	Constitutive law	It affects a lot the behavior of the piles. However, it all depends on the chosen parameters

It can be concluded that the main factors that affect the pile's behavior in Silex^2 are the parameters of the interface, the Young modulus of the soil and the pile, as well as the assigned constitutive law.

In the following section, a comparison will be made with pile group models using the parameters defined initially in Table 3.1.

2-2- Analysis of pile groups

Since the piles in Silex[2] are grouped in pairs, it was necessary to study the group effect that may occur when the piles are being loaded. Therefore, two different approaches were suggested, studied and discussed.

- Isolated pile groups (designated in the following as Group I)
- Pile groups in interaction with each other (designated in the following as Group II)

Both were introduced in Chapter 2 and the results of the numerical analysis will be shown hereafter. It should be noted that in this section the length of the piles is 15.5 m.

2-2-1- Isolated pile groups (Group I)

2-2-1-1- Comparison with single pile model

The geometry of this model was shown in details in the section 5-2-2-1 of Chapter 2. In order to be able to compare later this model with results from analytical methods, the hypothesis of equally loaded piles was chosen. Thus, a load of 10 000 kN was applied on each of the piles. Two cases were studied for a pile's Young modulus equal to 34.5 GPa and 15.7 GPa.

The load settlement curve obtained for the pile "a" of the group was compared to the one from the single pile model in Figure 3.23. The displacement contours from FLAC3D are presented in Figure 3.24.

Table 3.15 summarizes the settlement calculated in both cases. Although the center-to-center distance between the piles is equal to 3 times the pile diameter, this analysis showed that the settlement of the pile group "S_G" is 27.5% higher than the settlement of a single pile when 5 000 kN was applied for the case of E_p = 34.5 GPa. This value decreases to 21.8 % when the modulus is lower (E_p = 15.7 GPa).

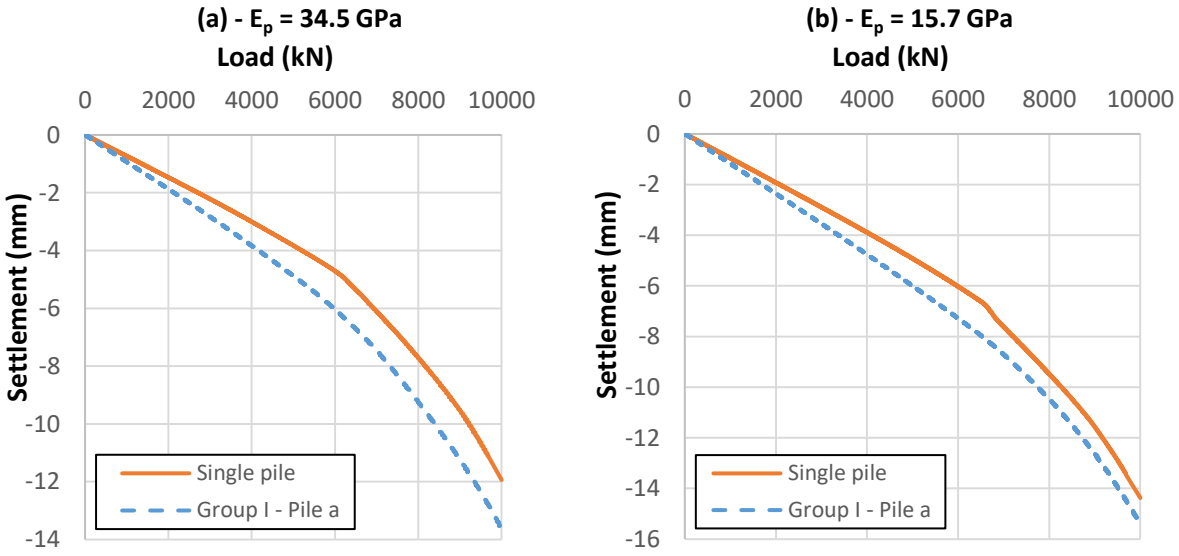

Figure 3.23 Load settlement curves of a single pile and pile "a" of Group I

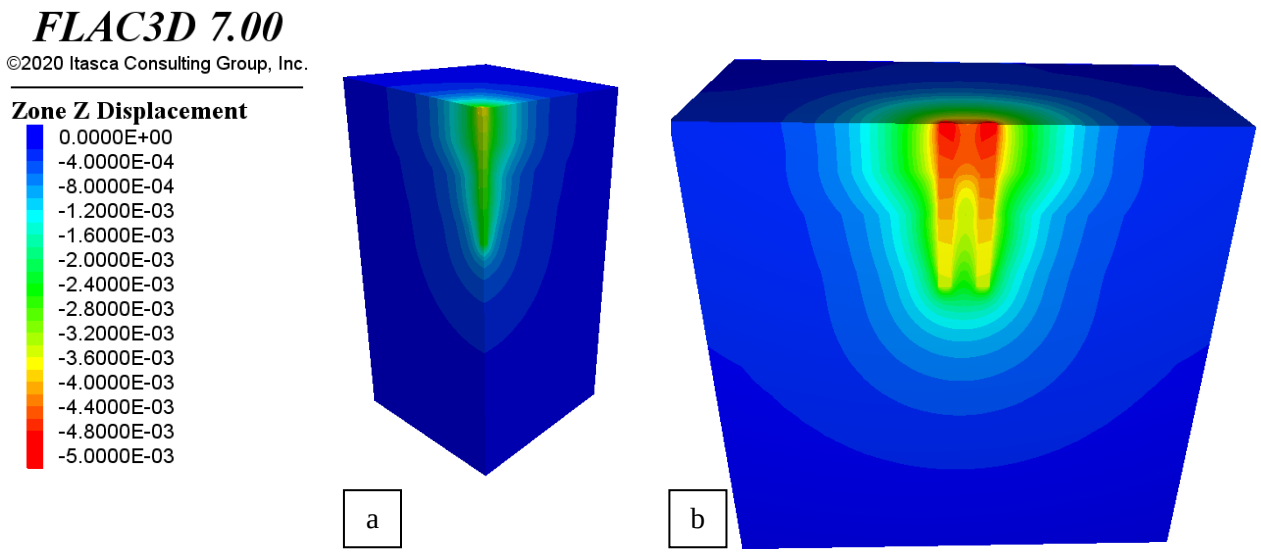

Figure 3.24 Displacement contours of the single pile (a) and Group I (b) for E_p = 34.5 GPa and Q = 5 000 kN

Table 3.15 Comparison between the settlement of a single pile and the pile "a" of the Group I

Load (kN)	E_p = 34.5 GPa				E_p = 15.7 GPa			
	S (mm) single pile	S_G (mm) Group I	Increase (%)	S_G/ S	S (mm) single pile	S_G (mm) Group I	Increase (%)	S_G/ S
1 000	-0.73	-0.93	27.4	1.27	-0.95	-1.16	22.1	1.22
2 000	-1.47	-1.88	27.9	1.28	-1.91	-2.35	23	1.23
3 000	-2.21	-2.82	27.6	1.28	-2.5	-3.55	42	1.42
4 000	-3.01	-3.83	27.2	1.27	-3.89	-4.73	21.6	1.22
5 000	-3.82	-4.87	27.5	1.27	-4.91	-5.98	21.8	1.22
10 000	-11.94	-13.64	14.3	1.14	-14.37	-15.42	7.3	1.07

2-2-1-2- Influence of the water table

The influence of the water table on the pile group was checked in this paragraph by modeling a water table starting from the top of the pile (z = 0).

Results are shown in Figure 3.25 and Table 3.16.

When a water table was added to the model, the pile settlement increased by 13.5% for an applied load equal to 10 000 kN. It can be noticed, however, that for a load lower than 5 000 kN, the influence of the water table can be neglected.

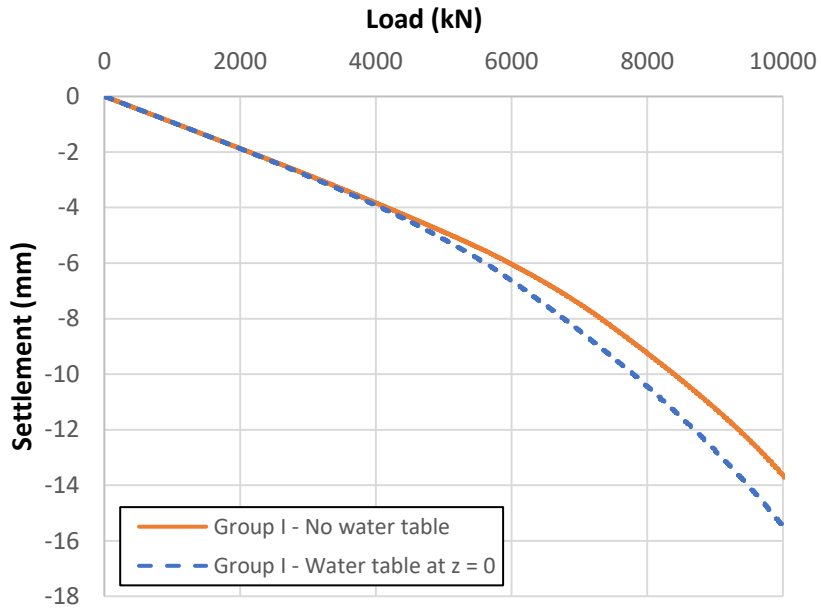

Figure 3.25 Pile load settlement curves of Group I for the cases with and without water table

Table 3.16 Pile settlement values with and without water table

Load (kN)	Group I - No water table	Group I - water table	
	Disp. (mm)	Disp. (mm)	Variation (%)
1 000	-0.93	-0.92	-1.1
2 000	-1.88	-1.87	-0.5
3 000	-2.82	-2.87	1.8
4 000	-3.83	-3.9	1.8
5 000	-4.87	-5.12	5.1
10 000	-13.6	-15.43	13.5

2-2-1-3- Effect of the concrete slab and the transfer structure

In the previous models, the load was directly applied on the head of the piles. However, in reality, the load is transferred to the piles through the transfer structure (TS) which is also connected to a concrete slab. In this section, the effect of the concrete slab and the transfer structure were studied in order to evaluate the load that may be dissipated in the soil underneath them.

Different models were compared with different hypotheses. It should be noted that a linear elastic constitutive model was assigned to all the concrete elements. We started by modeling the TS without the concrete slab. Many variations were tested by ensuring or not the contact of this structure with the soil. Then, once the slab has been modeled, it was noticed that by placing a concrete structure which has the same length and width of the model, which are here equal to 50 and 25 m, the amount of load transferred to the slab was exaggerated and the results turned to be erroneous. Therefore, it was suggested to reduce the dimensions of the slab on the top of the model so that they match the real case.

The different cases can be summarized as follows:

- Model 3.1: The TS was only modeled as a load application support without any contact with the soil. The slab was not modeled.
- Model 3.2: The TS was laying on the soil. The slab was not modeled.
- Model 3.3: The TS and the slab were modeled, being both in contact with the soil.
- Model 3.4: The TS and the slab were modeled, being both in contact with the soil. The slab had reduced dimensions: 11.4 x 5.54 m (Figure 3.26).

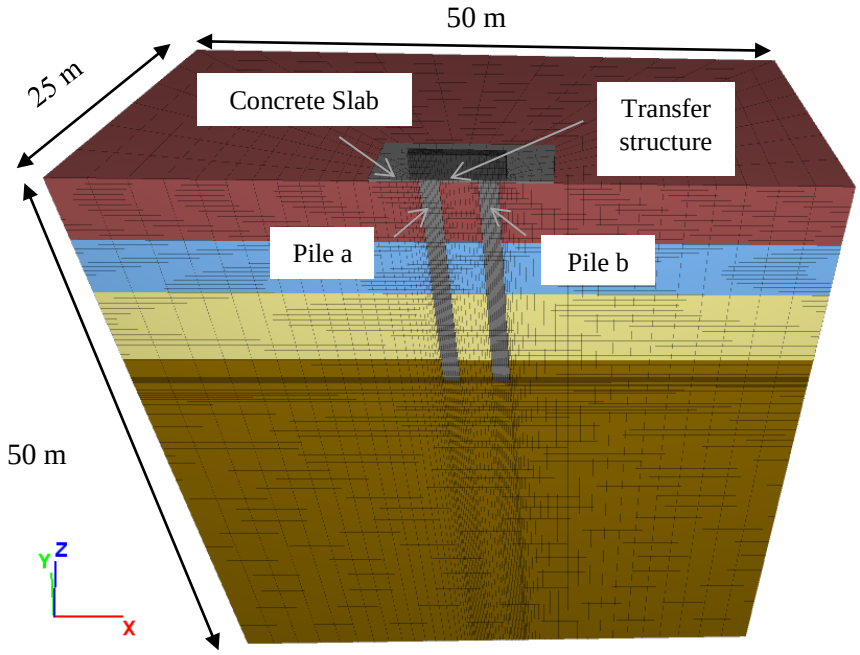

Figure 3.26 3-dimensional view of Model 3.4

For a better comparison between these models, a load was applied on the TS and the calculation was stopped when the load at the piles' head became equal to 10 000 kN. Results are shown in details in Table 3.17 and Figure 3.27.

It was shown that the load settlement curve of the model 3-1 was in close agreement with the model without any TS (Table 3.15). That is because the load applied on the TS was fully transferred to the piles and it was transferred equally. The total applied load needed to reach the 10 000 kN was around 20 000 kN.

However, the models 3.2, 3.3 and 3.4 perform differently. Since the TS was in direct contact with the soil, it was shown that the load was partially transferred to it. This load was assumed to be sustained by bearing pressure on the TS. An increase of the vertical displacement of the piles and the soil was observed in these cases, and in particular in the upper layer of the soil (Alluviums 1).

In the models where the slab is represented (Model 3.3 and 3.4), the initial load at the piles head (before loading) was higher than in Model 3.1 and 3.2 since the load of the slab was partially transferred to the

piles. Additionally, once the vertical load was applied on the TS in Model 3.3, it was noticed that only 70% of it was transferred to the piles, while the rest was being dissipated in the soil and the slab that have higher stiffness than the soil, compared to Model 3.1 for example. The load needed to obtain 10 000 kN on each of the piles was 28 696 kN, which is equivalent to an increase of 43%.

On the contrary, Model 3.4 was performed as an enhancement of Model 3.3 by reducing the dimensions of the slab and thus making the model closer to the reality. This model showed that the total load should be increased by 33% in order to be able to provide the needed load numerically. Besides, the settlement increased by 14.7% from 13.6 (in Model 3.1) to 15.6 mm (in Model 3.2) due to the load transferred to the soil.

Model 3.4 represents the best the scenario in Silex[2], since there is no reason for the slab or the transfer structure to lose the contact with the soil below. Therefore, Table 3.18 sums up the settlement of the pile for each load and the amount of total load that should be applied on the top of the transfer structure.

Table 3.17 Results of the different models used to study the influence of the concrete slab and the transfer structure

	Pile settlement (mm)	Axial load on the piles (kN)	Total applied load (kN)	Load transferred to the soil below the TS (kN)	Load transferred to the surrounding soil and/or slab (kN)
Model 3.1	13.6	10 000	20 393	310	≈ 0
Model 3.2	14.9	10 000	22 860	1 485	1 375
Model 3.3	16.98	10 000	28 696	696	8 000
Model 3.4	15.6	10 000	26 596	643	5 953

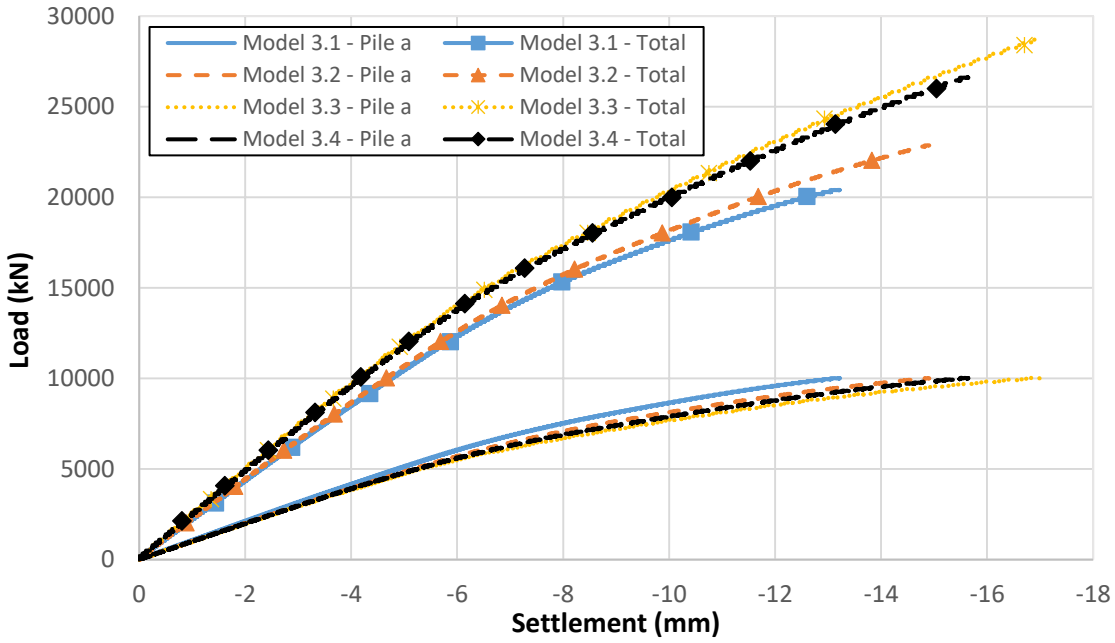

Figure 3.27 Pile load settlement for the different models used to study the influence of the concrete slab and the transfer structure

Table 3.18 Pile settlement and load applied for Model 3.4

Load (kN)	Model 3.4	
	Settlement (mm)	Total applied load (kN)
1 000	-0.99	2 588
2 000	-1.99	4 989
3 000	-3.00	7 391
4 000	-4.05	9 794
5 000	-5.23	12 270
10 000	-15.49	26 591

2-2-2- Pile groups in interaction with each other (Group II)

2-2-2-1- Comparison with previous models

The geometry of this model was shown in details in the section 5-2-2-2 of Chapter 2. Identically to the previous section, the piles were equally loaded and the transfer structure was not modeled for a better comparison with single pile models.

As shown in Figure 3.28 and Table 3.19, the settlement of the pile group II is 123.8% higher than the settlement of a single pile when 5 000 kN was applied for the case of E_p = 34.5 GPa. This value decreases to 101.4% when the modulus is lower (E_p = 15.7 GPa). It can be noticed that the settlement values of Group II are substantially higher than those of Group I. This is caused by the strong effect of the nearby piles on the Group 17A/B in spite of the relatively high distance between them as shown in the foundation plan.

It is certain that the observed effect varies from a pile group to another. For example, it is expected that the group 18A/B will be more influenced by the surrounding piles due to the close spacing with the piles 19A/B but since the final objective is to study the global model, too little attention was paid on each of the cases separately.

Table 3.19 Comparison between the settlement of a single pile and the pile "a" of the Group II for E_p = 34.5 GPa and E_p = 15.7 GPa

Load (kN)	E_p = 34.5 GPa				E_p = 15.7 GPa			
	S (mm) single pile	S_G (mm) Group II	Increase (%)	S_G/ S	S (mm) single pile	S_G (mm) Group II	Increase (%)	S_G/ S
1 000	-0.73	-1.67	128.8	2.29	-0.95	-1.93	103.2	2.03
2 000	-1.47	-3.33	126.5	2.27	-1.91	-3.9	104.2	2.04
3 000	-2.21	-5.01	126.7	2.27	-2.5	-5.84	133.6	2.34
4 000	-3.01	-6.79	125.6	2.26	-3.89	-7.85	101.8	2.02
5 000	-3.82	-8.55	123.8	2.24	-4.91	-9.89	101.4	2.01
10 000	-11.94	-20.61	72.7	1.73	-14.37	-22.89	59.3	1.59

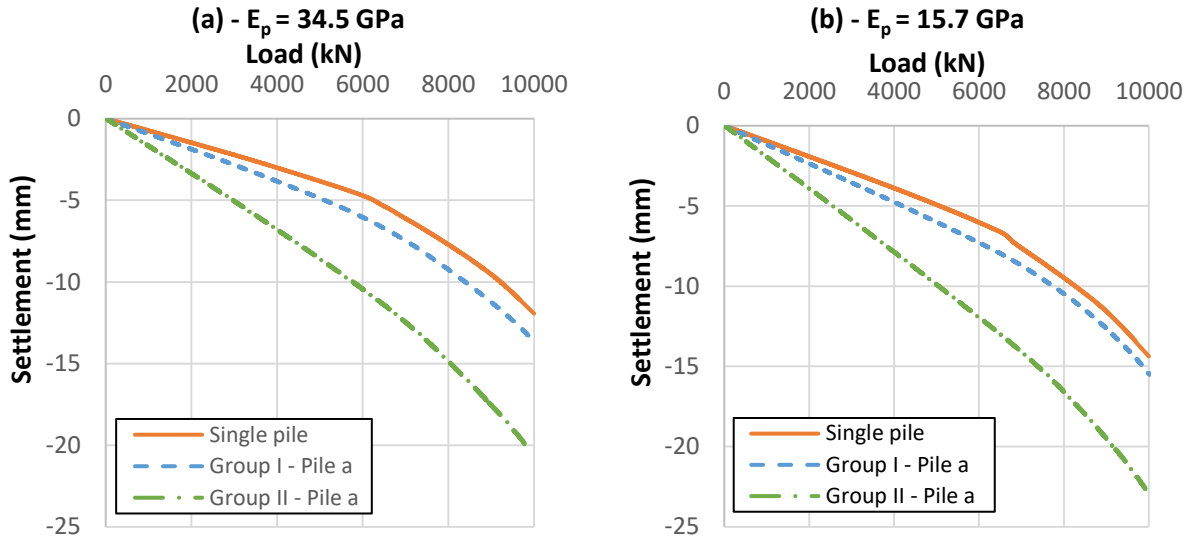

Figure 3.28 Pile load settlement curves of a single pile and pile "a" of the groups I and II

2-2-2-2- Influence of the water table

Identically to the previous sections that dealt with water table, this latter was modeled starting from the top of the pile, i.e., for z = 0.

Results are shown in Figure 3.29 and Table 3.20.

When adding a water table to the model with the pile group II, the pile settlement increases by 8.7% for an applied load equal to 10 000 kN. It can be noticed, however, that for a load lower than 5 000 kN, the influence of the water table can be neglected similarly to the previous cases.

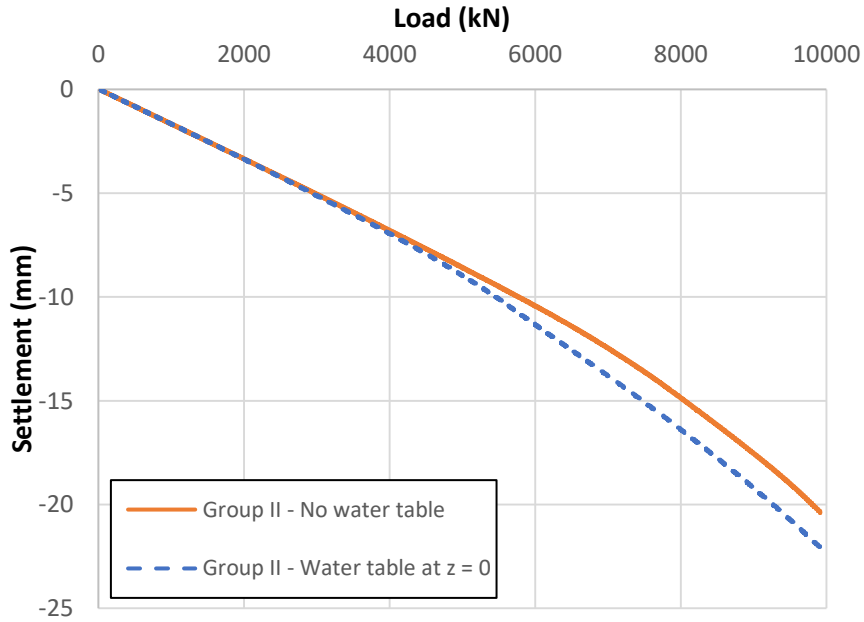

Figure 3.29 Load settlement curves for the cases with and without water table

Table 3.20 Pile settlement with and without water table

Load (kN)	Group II - No water table	Group II - water table	
	Disp. (mm)	Disp. (mm)	Increase (%)
1 000	-1.67	-1.66	-0.6
2 000	-3.33	-3.34	0.3
3 000	-5.01	-5.13	2.4
4 000	-6.79	-6.93	2.1
5 000	-8.55	-8.97	4.9
10 000	-20.61	-22.4	8.7

2-3- Analysis of the global model in FLAC3D

The main purpose of the global model was to be able to make an overall analysis of the pile-soil system, especially that the measurements obtained by the instrumentation reflect the real behavior of the piles and not their response when subject to a load individually. Several factors affect this behavior such as the geometry, the applied load, the influence by the nearby structures, the constitutive law and the presence or not of the water table. However, time and cost limitations forced us to make simplifying assumptions which we tried to reduce their effect on the final results. These hypotheses are as follows:

- The piles were assumed to have the same length and the same top and bottom levels
- Even though it was shown that the piles were loaded differently, it was decided as a first estimation to apply the same load on the top of each of the piles, e.g., 10 000 kN in the majority of the cases. The real applied load will be used in further stages.
- Nearby structures (EDF, Silex[1], RTE…) were not modeled in this project

Using the model shown in the paragraph 5-2-3 of Chapter 2, many studies were performed. Results will be shown in the following subsections.

2-3-1- Response of the piles to the applied load

As a first stage, 10 000 kN was applied on each of the piles and their response was observed. The selected pile's modulus was 34.5 GPa and the water table was not modeled in this section. Their effect will be analyzed later.

It was predicted that the response of each pile would be different since the distances between them are not equal. The displacement contours of Figure 3.30 and 3.31 show that the smallest settlement belongs to the piles 17A and 19A. This finding agrees well with the geometry of the model. In fact, in this model, the piles 17B, 18A and 18B are each surrounded by two other piles that are relatively close to them while the pile 19A is surrounded by only one. The pile 17A is a particular case since it is also affected by the pile 17B located on the other side of the symmetry axis, which is not shown here. However, the center-to-center distance between 17A and 18B is bigger than 7 m which explains the minor observed impact.

On the other hand, Figure 3.32 and Table 3.21 show that by assigning to the soil the parameters defined in Table 3.1, the settlement of the piles varies between 5.09 and 5.94 mm for an applied load equal to 3 000 kN and between 8.66 and 10.16 mm for a load equal to 5 000 kN.

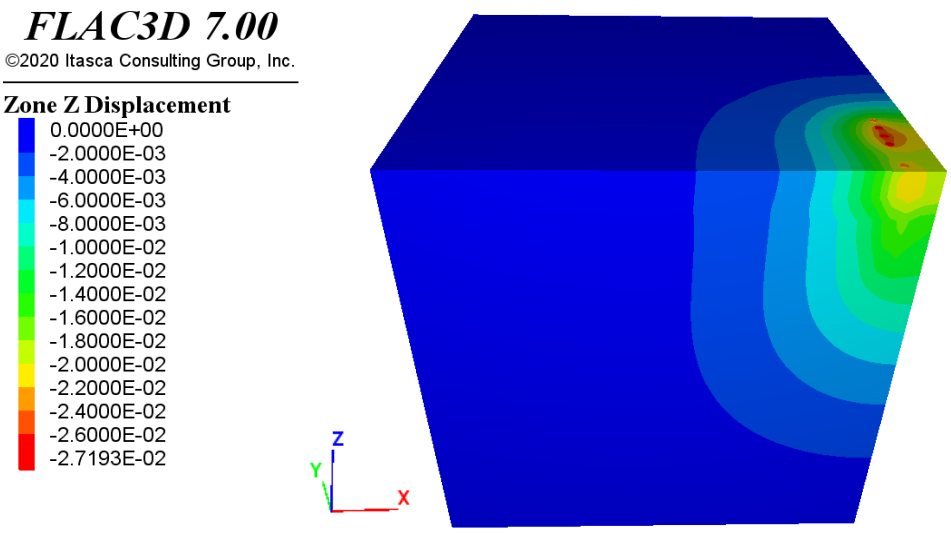

Figure 3.30 Displacement contours in FLAC3D at the end of the calculation

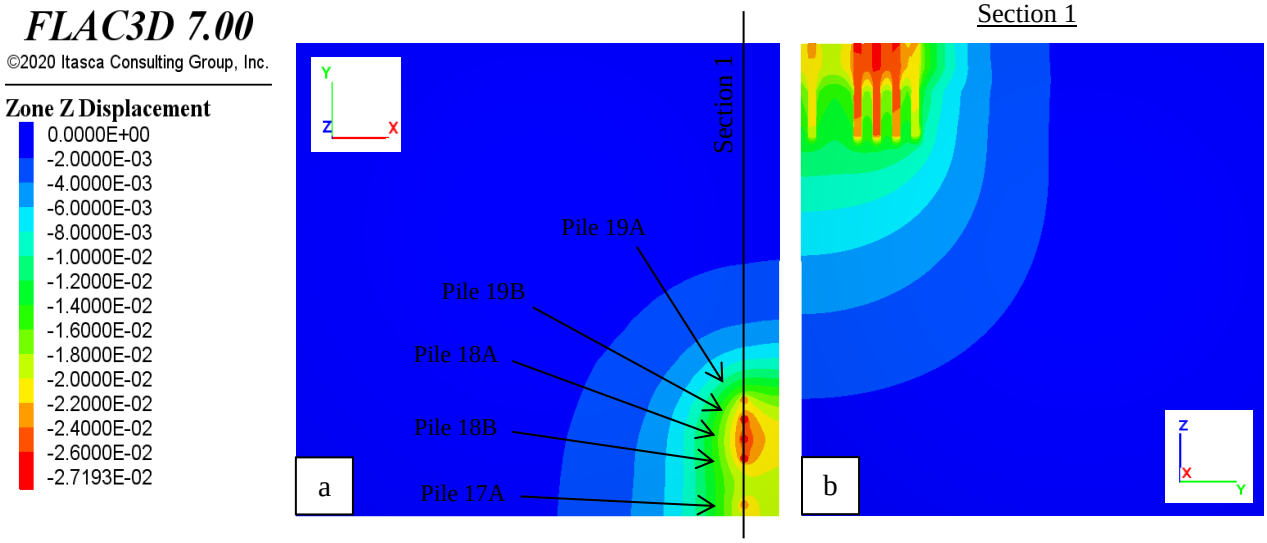

Figure 3.31 Displacement contours in the FLAC3D model at the end of the calculation: (a) Plan view and (b) along a vertical plane at the axis of the piles

Table 3.21 Settlements of all the piles

Load (kN)	Settlement (mm)				
	Pile 17A	**Pile 18B**	**Pile 18A**	**Pile 19B**	**Pile 19A**
1 000	-1.86	-1.91	-1.95	-1.87	-1.68
2 000	-3.71	-3.83	-3.91	-3.74	-3.36
3 000	-5.63	-5.82	-5.94	-5.69	-5.09
4 000	-7.52	-7.81	-7.98	-7.65	-6.82
5 000	-9.51	-9.93	-10.16	-9.73	-8.66
10 000	-22.53	-26.35	-26.97	-26.16	-22.39

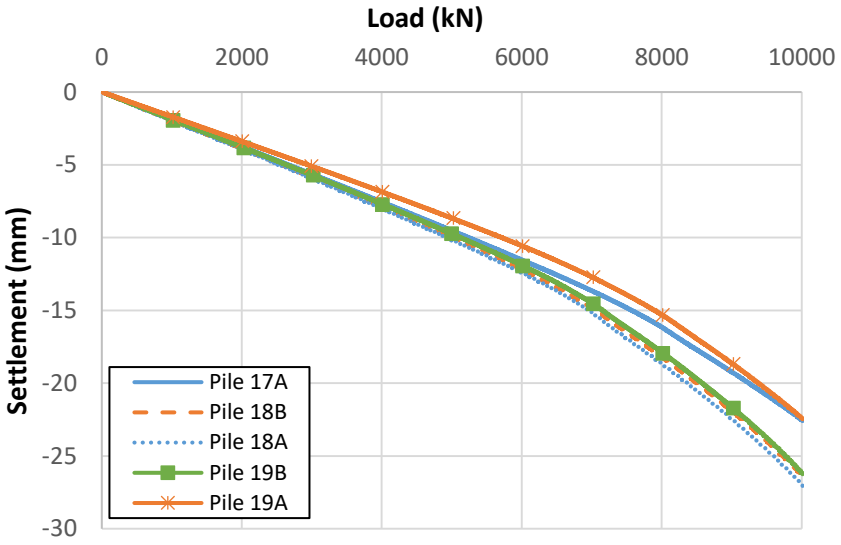

Figure 3.32 Pile load settlement curves of the different piles in the Global model

A comparison between this case and the previous models (single pile and pile groups) was also performed. The load settlement curves of the pile 17A are presented in Figure 3.40. This figure shows that the settlement values, as predicted by the global model, are higher than those determined from the other models, but they are closer to the Group II model where the symmetry axes were chosen so that all the surrounded piles could be modeled.

This study showed that the response differs from a pile to another. It is driven by the geometry of the model, especially the spacing between the piles. However, the real behavior may be different than the one observed here because in reality the piles are not equally loaded, are not all positioned at the same altitude and are connected via a transfer structure and a concrete slab. Some of these ideas will be discussed in Chapter 4.

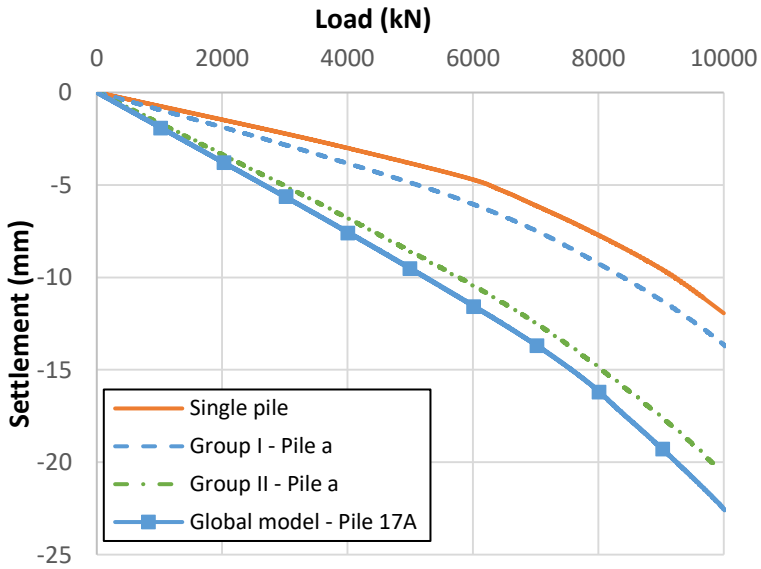

Figure 3.33 Pile load settlement curves for all the piles

2-3-2- Influence of the Young modulus of the pile

Based on results of the paragraph 2-1-2-4, it was envisioned that the modulus of the pile would affect the behavior of the global model. In this section, the two selected values for the analysis were 34.5 GPa and 15.7 GPa based on the experimental test shown earlier. For a better visualization, the load settlement curves of the piles 18A and 19A will only be shown, while verifying each time that they represent the lowest and the highest values among all the piles. This comparison is presented in Figure 3.34 and Table 3.22.

For a load equal to 5 000 kN, the comparison shows that:

- Pile 18A: The settlement went from 10.16 mm for 34.5 GPa to 11.47 mm for 15.7 GPa.
- Pile 19A: The settlement went from 8.66 mm for 34.5 GPa to 9.9 mm for 15.7 GPa.

Table 3.22 Pile settlement for E_p = 34.5 GPa and E_p = 15.7 GPa

Load (kN)	Settlement (mm)			
	E_p = 34.5 GPa		E_p = 15.7 GPa	
	Pile 18A	Pile 19A	Pile 18A	Pile 19A
1 000	-1.95	-1.68	-2.23	-1.93
2 000	-3.91	-3.36	-4.47	-3.87
3 000	-5.94	-5.09	-6.77	-5.87
4 000	-7.98	-6.82	-9.06	-7.84
5 000	-10.16	-8.66	-11.47	-9.9
10 000	-26.97	-22.39	-29.1	-24.44

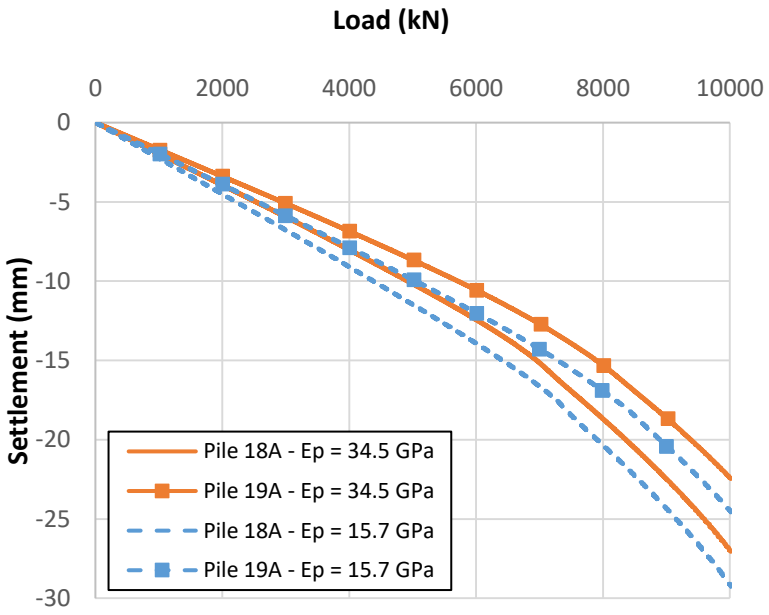

Figure 3.34 Load settlement curves for E_p = 34.5 GPa and E_p = 15.7 GPa

2-3-3- Influence of the water table

As could be seen in the single pile and pile group models, the water table had a minor impact on the behavior of the foundations when subject to a load which was lower than 5 000 kN. In order to validate this finding, it was necessary to test this idea in the global model as well. Therefore, new models showing the water table at the top of the piles (z = 0) were added to this study for both cases (E_p = 34.5 and 15.7 GPa).

Figure 3.35 shows that by modeling the water table, the settlement of the piles increased significantly for a load higher than 5 000 kN. However, this impact is so minor for lower loads especially if the real applied load in Silex[2] during the construction is considered.

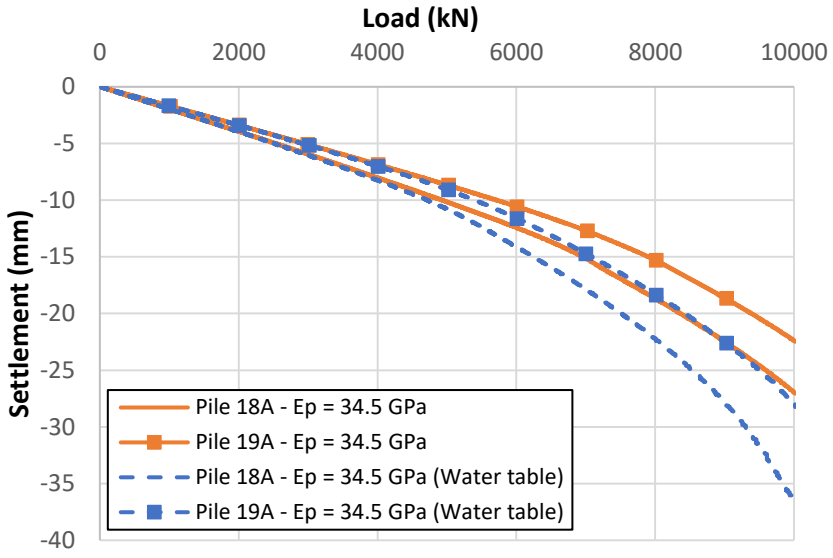

Figure 3.35 Load settlement curves of the piles 18B and 19B for different cases

The detailed values are shown in Table 3.23 and a particular comparison was made between the displacement contours obtained for Q = 5 000 kN in the case of E_p = 34.5 GPa (Figure 3.36).

It can be seen that:

- For E_p = 34.5 GPa: The settlement range of the group of piles went from (8.66 – 10.16 mm) to (9.08 – 10.79 mm) after adding the water table to the model
- For E_p = 15.7 GPa: The settlement range of the group of piles went from (9.9 – 11.47 mm) to (10.19 - 11.9 mm) after adding the water table to the model

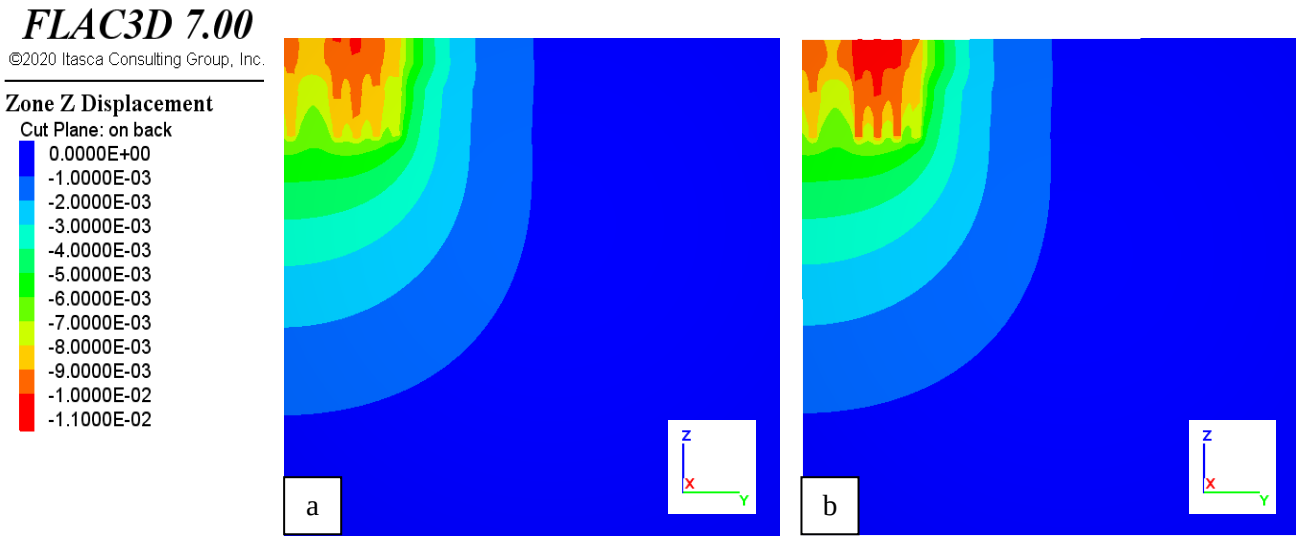

Figure 3.36 Displacement contours in the FLAC3D model along a vertical plane at the axis of the piles: (a) without water table and (b) with water table for Q = 5 000 kN

Table 3.23 Pile settlement for E_p = 34.5 GPa and E_p = 15.7 GPa without and with a water table

Load (kN)	Settlement (mm)							
	E_p = 34.5 GPa				E_p = 15.7 GPa			
	Without water table		With water table		Without water table		With water table	
	Pile 18A	Pile 19A	Pile 18A	Pile 19A	Pile 18A	Pile 19A	Pile 18A	Pile 19A
1 000	-1.95	-1.68	-1.95	-1.68	-2.23	-1.93	-2.23	-1.94
2 000	-3.91	-3.36	-3.93	-3.37	-4.47	-3.87	-4.48	-3.88
3 000	-5.94	-5.09	-6.03	-5.15	-6.77	-5.87	-6.83	-5.91
4 000	-7.98	-6.82	-8.21	-6.97	-9.06	-7.84	-9.22	-7.95
5 000	-10.16	-8.66	-10.79	-9.08	-11.47	-9.9	-11.9	-10.19
10 000	-26.97	-22.39	-36.52	-28.03	-29.1	-24.44	-38.98	-30.56

After having studied numerically the group effect that may occur in the foundations of Silex[2], some of the analytical methods were analyzed and compared, in order to see their efficiency, since they are in general faster and cheaper in terms of computation cost. These are presented in the following paragraph.

3- Comparison with analytical methods

In this paragraph, some of the analytical and empirical methods defined in chapter 1 will be used. In particular, the French standard will be employed to estimate the bearing capacity of the piles based on pressuremeter tests. On the other hand, for the settlement calculation, the load transfer method (LTM) as suggested by Frank and Zhao (1982) and the elastic theory (Poulos and Davis, 1980) will be also tested.

3-1- Analytical calculation of the bearing capacity of the piles

The bearing capacity of the piles was calculated analytically using the module "Taspie+" of Foxta, which is a software dedicated to foundation design. "Taspie+" employs the French standard (NF P 94-262, 2012) to also determine the ultimate shaft and base resistances together with the critical creep load and the allowable loads at different load combinations. This method uses the pressuremeter modulus "E_M" of the soil layers, the ultimate unit skin friction "q_s" and the limit pressure under pile base "q_b" both determined according to the standards. The soil layers were assigned the parameters shown in Table 3.24.

Table 3.24 Soil parameters implemented in Foxta based on pressuremeter tests and the French standards

Soil layer	Thickness (m)	E_M (MPa)	q_s (kPa)	q_b (kPa)
Alluviums 1	4.25	62*	170	N/A
Alluviums 2	4	8 *	61	N/A
Alluviums 3	5.75	67*	170	N/A
Molasse	1.5	95*	200	9200
* *Harmonic mean value*				

The resistance values of the piles in Silex[2] are estimated as follows:

- Ultimate pile resistance: R_c = 19 355.68 kN
- Ultimate skin friction resistance: R_s = 8 600.68 kN
- Ultimate tip resistance: R_b = 10 754.6 kN
- Critical creep resistance: $R_{c,cr}$ = 11 397.81 kN

On the other hand, the bearing capacity of a pile group should be evaluated when the center-to-center distance "d" is less than 3 times the diameter D of the pile. However, as for the settlement, it should be verified until a distance of 8D.

It is common in France, according to the standard (NF P 94-262, 2012), to apply a reduction of the shear resistance only, considering that the tip resistance is not highly affected. The ultimate bearing capacity of a pile group is then calculated based on the following equation:

$$R_{gu} = n_1 n_2 (R_b + \eta R_s) \qquad \text{Eq. 3.6}$$

Where n_1 and n_2 are non-zero values that represent the number of piles in each direction.

The group efficiency factor η is substituted in the French standard by the symbol C_e. It is calculated as follows:

$$\eta = 1 - C_d\left(2 - \left(\frac{1}{n_1} + \frac{1}{n_2}\right)\right) \quad \text{Eq. 3.7}$$

$$C_d = 1 - \frac{1}{4}\left(1 + \frac{d}{D}\right) \quad \text{Eq. 3.8}$$

In Silex^2, the spacing between the piles differs from a group to another. The results are summarized in Table 3.25. While the capacity of the groups 17A/B and 22A/B is equal to the sum of the capacities of each of the piles, it is not exactly the same for the other piles where the resistance decreased by 2.9%.

Table 3.25 Bearing capacity of the different piles in the groups

Pile No (A/B)	Spacing between piles d (m)	C_d	η	R_c (kN)	R_{gu} (kN)
15, 16, 18, 19, 20, 21, 23, 24	3.06	0.123	0.94	21 026.43	40 820.25
17, 22	3.66	0	1	21 026.43	42 052.86

3-2- Analytical methods for settlement calculation

3-2-1- Elastic theory (Poulos and Davis, 1980)

Analytical methods are the best in terms of reducing the computation time and the cost. However, their limitations were shown by several authors. Since the applied load in Silex^2 is not high, i.e., piles and soil layers may stay in the elastic domain, it was decided in this section to compare between the results obtained by FLAC3D and the elastic theory proposed by Poulos and Davis (1980) shown in details in Chapter 1. It should be noted that the pile length in this section is 15.5 m while the soil layer characteristics are the same as defined in Table 3.1. This method uses the elastic parameters only (E, ν).

3-2-1-1- Single pile analysis

Based on this method, two configurations are possible:

- A floating pile with the hypothesis that the stratum is the grey clay layer at 96 m NGF, 66 m away from the top of the pile, considering in other terms that the molasse is not that stiff (Figure 3.37-a).
- An end-bearing pile by considering that the molasse is the rigid stratum at the tip level of the pile. A 1.5-m layer of molasse still exists at the lower part of the pile (Figure 3.37-b).

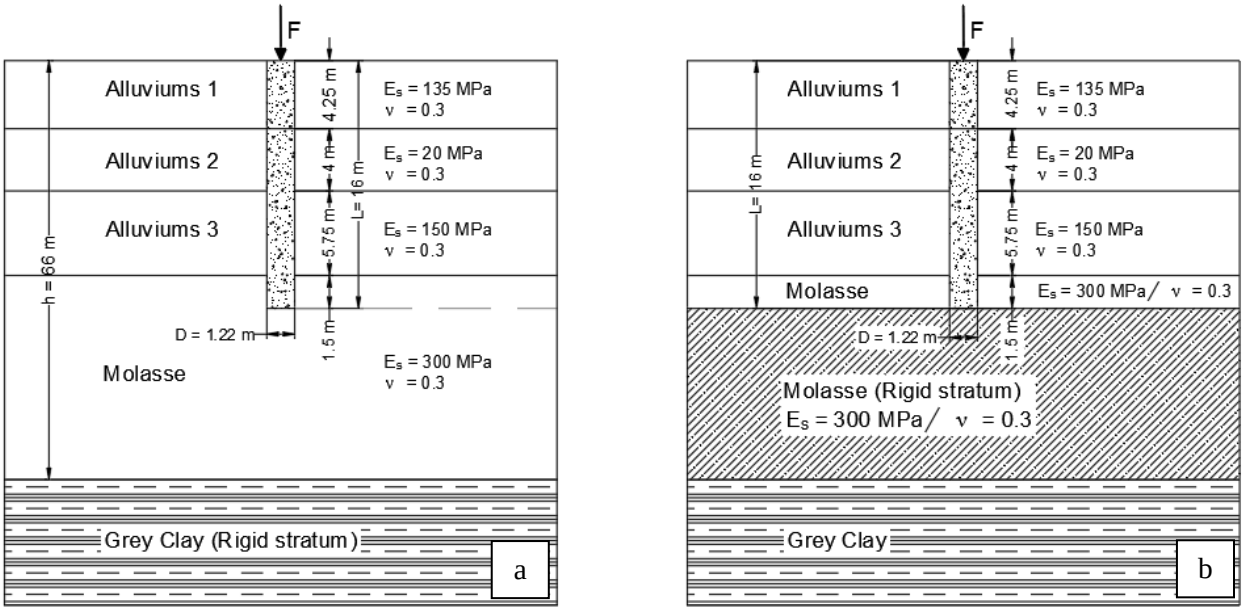

Figure 3.37 Example of (a) floating pile and (b) end-bearing pile (Poulos and Davis, 1980)

The corresponding equations of the settlement calculations are recalled hereafter:

$$S = \frac{FI}{E_s D} \qquad \text{Eq. 3.9}$$

$$I = \begin{cases} I_0 R_k R_h R_\upsilon & \text{floating pile} \\ I_0 R_k R_b R_\upsilon & \text{end-bearing pile} \end{cases} \qquad \text{Eq. 3.10}$$

The coefficients used in these equations were defined in Chapter 1.

For a non-homogeneous soil, it was suggested by the authors to use the weighted average modulus E_{av} instead of E_s in Eq. 3.9. Depending on the chosen configuration (Figure 3.37-a or Figure 3.37-b), E_{av} is either 259 or 123 MPa for the floating and the end-bearing pile respectively.

The pile settlement was then calculated using the parameters in Table 3.26 and the graphs from Figure 3.38 and 3.39.

Table 3.26 Correction factors used in the elastic theory analysis (E_p = 34.5 GPa)

	Floating pile ($E_s = E_{av}$ = 259 MPa)	**End-bearing pile ($E_s = E_{av}$ = 123 MPa)**
K'	133	280
I_0	0.12	0.12
R_K	1.4	1.18
R_v	0.95	0.942
R_h	0.92	-
R_b	-	0.8
I	**0.147**	**0.1067**

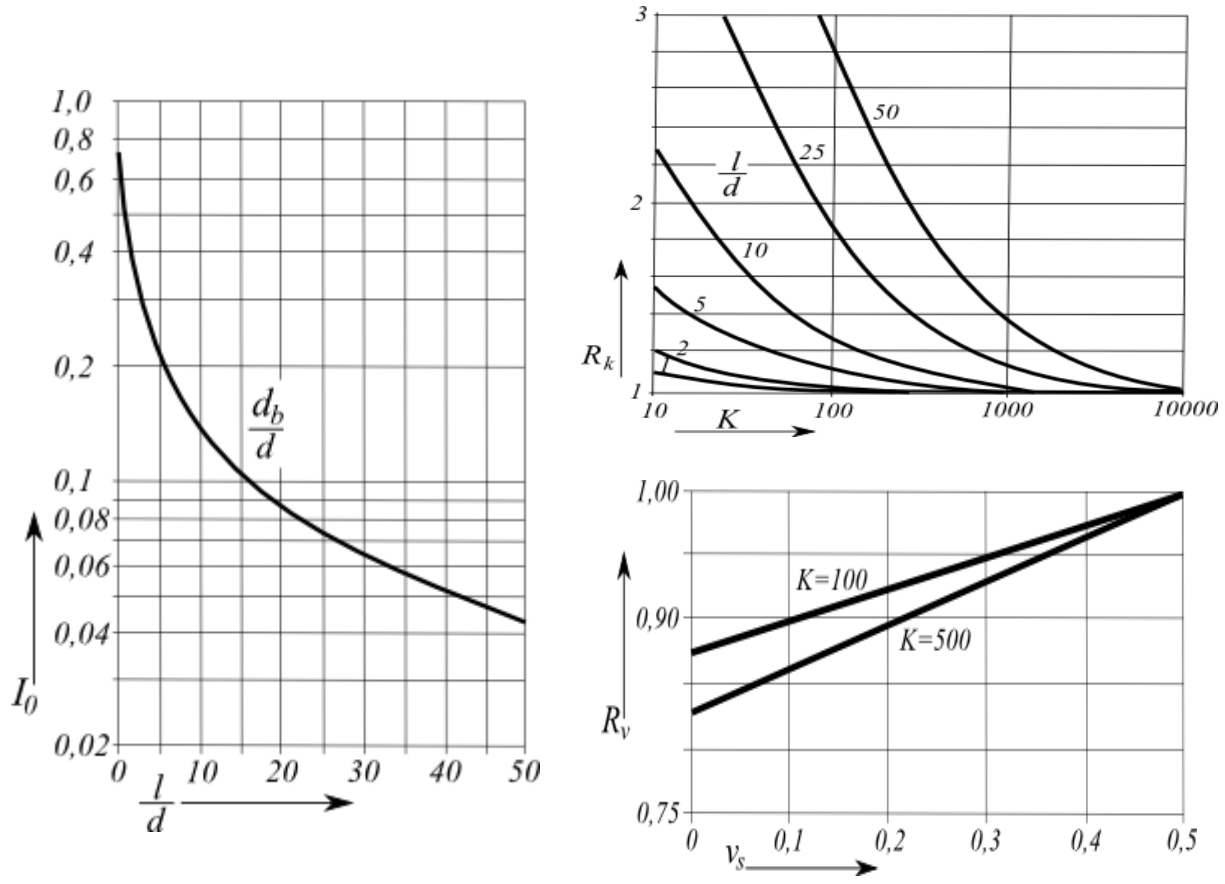

Figure 3.38 Settlement influence factor I_0 and correction factors for compressibility and Poisson's ratio (Poulos and Davis, 1980)

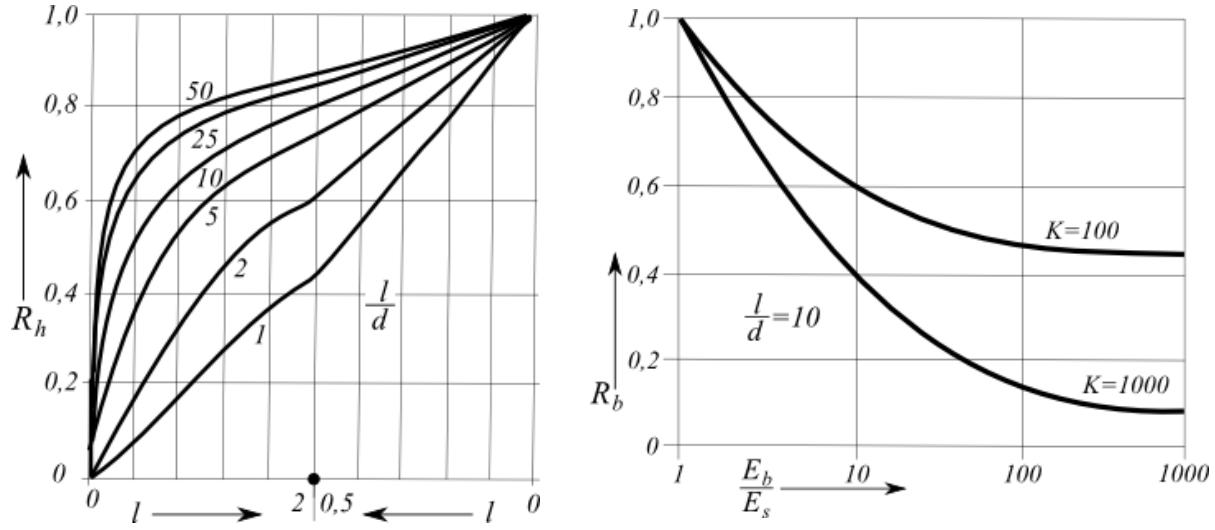

Figure 3.39 Depth and base modulus correction factors for settlement (Poulos and Davis, 1980)

Assuming a pile's modulus equal to 34.5 GPa, the pile settlement was related to the applied load using the following equations:

$$S(mm) = \begin{cases} 4.65 \times 10^{-4}\ F\ (kN) & Floating\ pile \\ 6.626\ \times\ 10^{-4}\ F\ (kN) & End - bearing\ pile \end{cases} \qquad \text{Eq. 3.11}$$

In order to compare these results with numerical ones, it was important first to understand and evaluate to role of the parameters used in both methods. The elastic theory requires Young's moduli and Poisson's ratios of the soil and the concrete only. However, in FLAC3D, additional parameters are needed such as the cohesion, the friction and the dilation angle as well as the soil-pile interface parameters, in case of a Mohr-Coulomb model.

In an attempt to reduce the number of parameters, an initial comparison was made between the cases with and without the interface being modeled. It was shown in Figure 3.40 that for a small load (< 5 000 kN), the interface has no influence on the pile load settlement curve.

The same observation can be made by comparing the linear elastic to Mohr-Coulomb models for the same load, which agrees well with the fact that the soil remains in the elastic domain in the case of Mohr-Coulomb model.

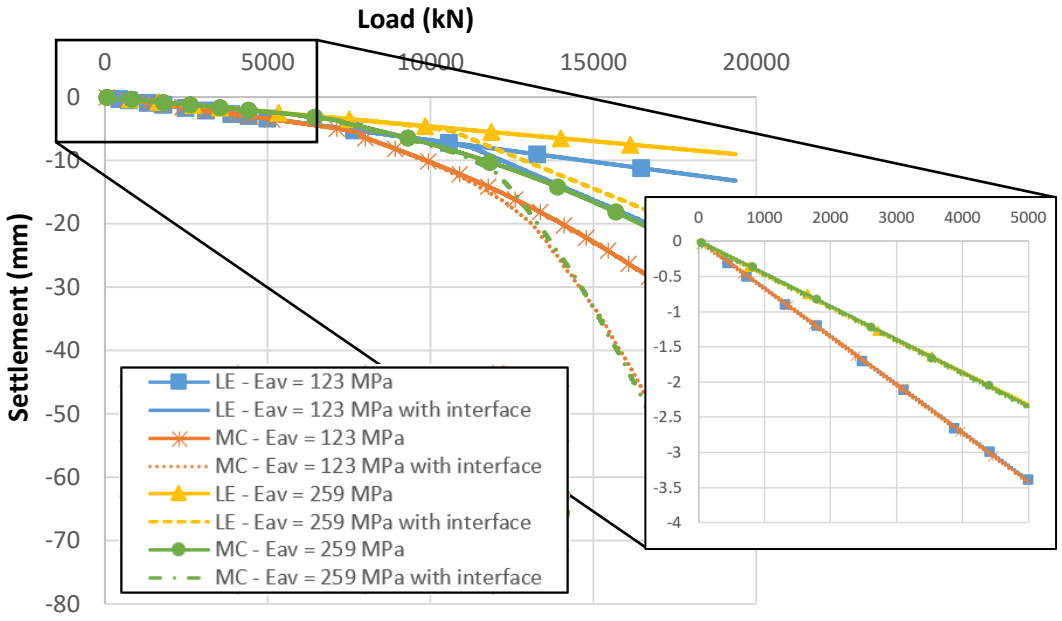

Figure 3.40 Load settlement curves in the models with/without interface

Now that the interface parameters can be neglected, the settlement calculated using the elastic theory (for both floating and end-bearing piles) was compared with the 6 models of FLAC3D presented in Table 3.27. In this study, the Young modulus of the concrete was chosen equal to 34.5 GPa.

Table 3.27 Six models performed in FLAC3D to be compared with the elastic theory

Model	Label	Constitutive law	Parameters
Model 3.5	LE – All layers	Linear elastic	Parameters defined in Table 3.28
Model 3.6	MC – All layers	Mohr-Coulomb	
Model 3.7	LE – E_{av} = 123 MPa	Linear elastic	Unified average modulus E_{av} = 123 MPa
Model 3.8	MC – E_{av} = 123 MPa	Mohr-Coulomb	
Model 3.9	LE – E_{av} = 259 MPa	Linear elastic	Unified average modulus E_{av} = 259 MPa
Model 3.10	MC – E_{av} = 259 MPa	Mohr-Coulomb	

Table 3.28 Soil characteristics used in the comparison

Soil layer	Model 3.5	Model 3.6 (Additional parameters)			
	E (MPa)	ν	c (kPa)	ϕ (°)	ψ (°)
Alluviums 1	135	0.3	50	35	5
Alluviums 2	20				
Alluviums 3	150				
Molasse	300				

As for the results, Figure 3.41, 3.42 and 3.43 show that there is a similarity between the load settlement curves obtained by the elastic theory and FLAC3D when the same unified average modulus is used. However, these curves vary significantly from the ones obtained by using different layers (Model 3.5 and 3.6).

By comparing FLAC3D curves, it can be deduced that the linear elastic part of the Mohr-Coulomb curve gives close results to the linear elastic model and consequently the cohesion and the friction angle do not play any role for a load that is less than 5 000 kN.

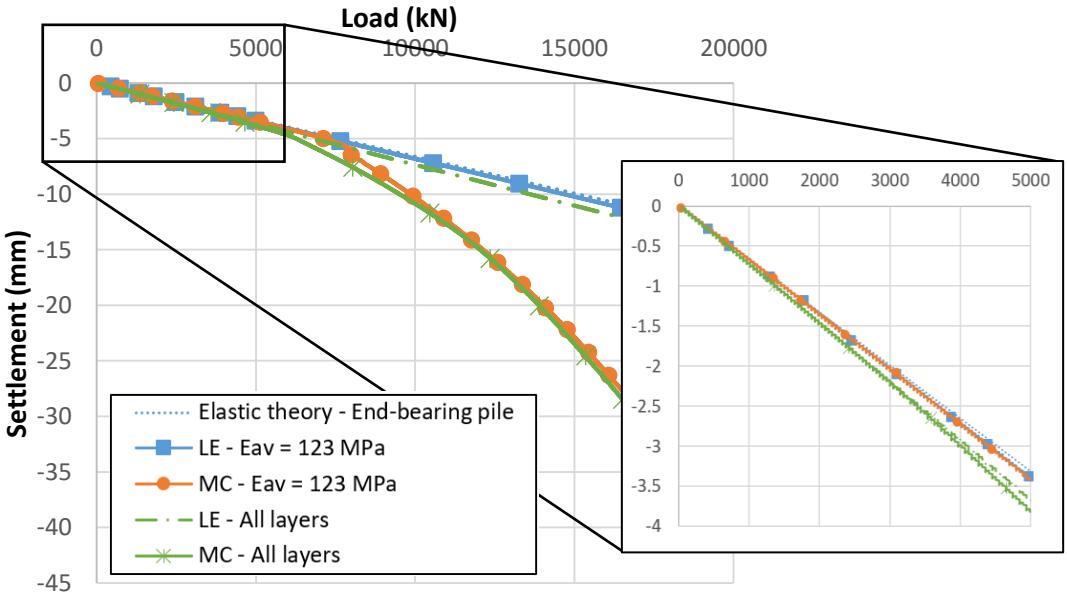

Figure 3.41 Load settlement curves obtained by considering an end-bearing pile

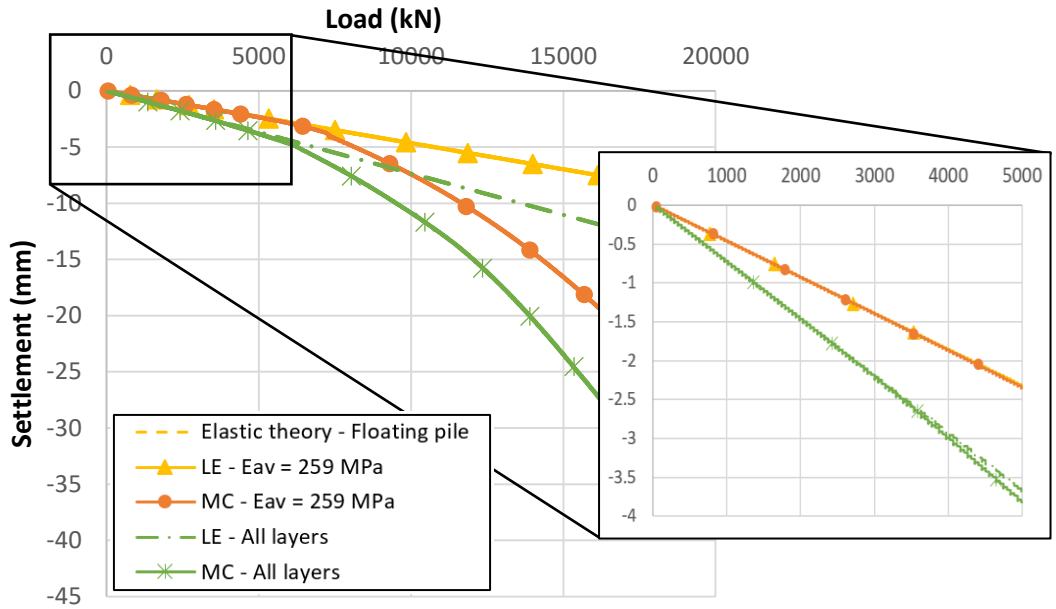

Figure 3.42 Load settlement curves obtained by considering a floating pile

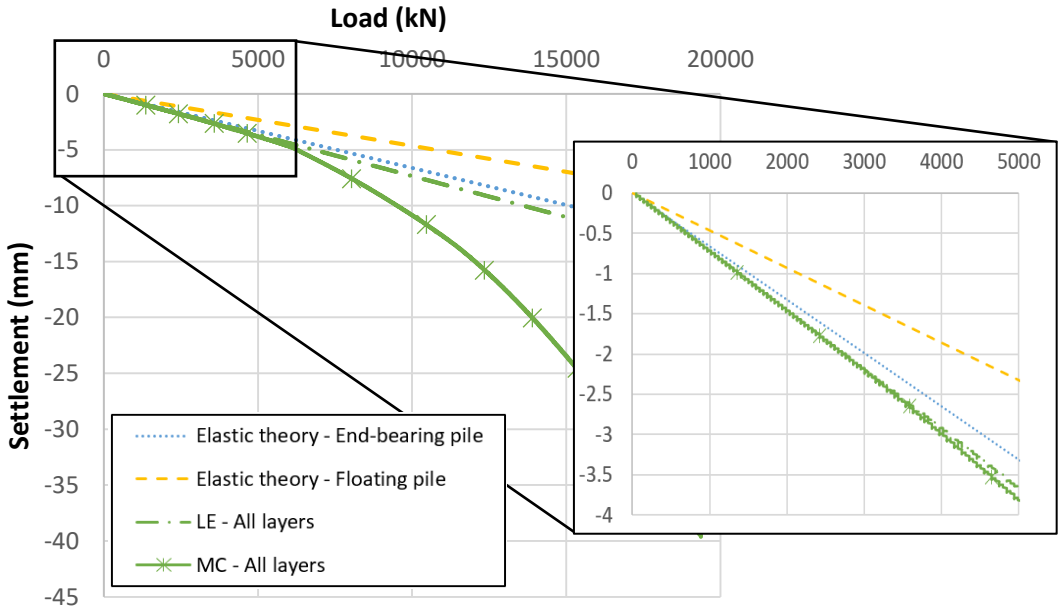

Figure 3.43 Load settlement curves obtained in both floating and end-bearing pile

On a closer view, based on Figure 3.44, Figure 3.45 and Table 3.29, the following observations were made:

- The equation used in the elastic theory to calculate the average modulus in the end-bearing pile (123 MPa) overestimates the modulus of the alluviums 2 layer and thus overestimates the mobilized skin friction and the relative pile-soil displacement in this pile section in particular. Consequently, this would lead to an overestimation of the overall mobilized shear stress along the pile. However,

by looking at the overall behavior of the pile in Model 3.6 and 3.8, it can be seen that the mobilized skin friction was then compensated in the alluviums 3 and the molasse layers. This can be explained by the fact that the same parameters were assigned to the molasse at the pile's tip.

- Identically to the previous case, the equation used to estimate the average modulus in a floating pile (259 MPa) overestimates the modulus of the alluviums 2 layer and thus overestimates the mobilized shear stress and the relative pile-soil displacement in this piles' section. However, it can be seen that the mobilized shear stress along the pile in Model 3.10 is much higher, leading to a lower end-bearing effort and thus to a bigger pile displacement.

Table 3.29 Pile settlement in different models

Load (kN)	Settlement (mm)				
	Elastic theory End-bearing pile	Elastic theory Floating pile	MC - 123 MPa	MC - 259 MPa	MC - All layers
1 000	-0.66	-0.465	-0.66	-0.48	-0.73
2 000	-1.33	-0.93	-1.35	-0.96	-1.47
3 000	-1.99	-1.395	-2.01	-1.41	-2.21
4 000	-2.65	-1.86	-2.71	-1.88	-3.01
5 000	-3.31	-2.325	-3.4	-2.36	-3.82

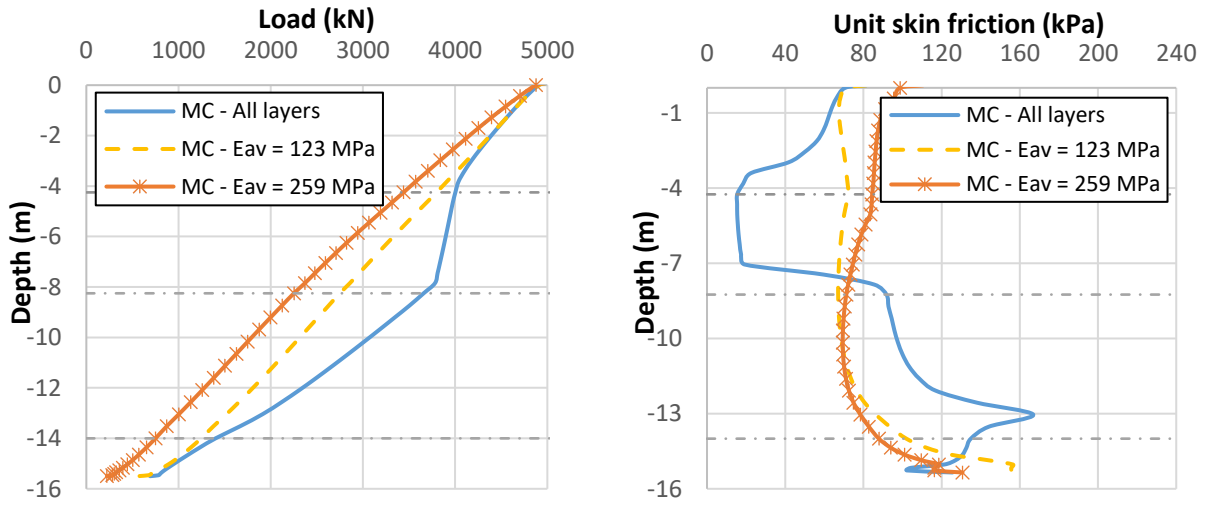

Figure 3.44 Load and unit skin friction profiles along the pile for different cases (The dashed lines indicate the limit of the layers)

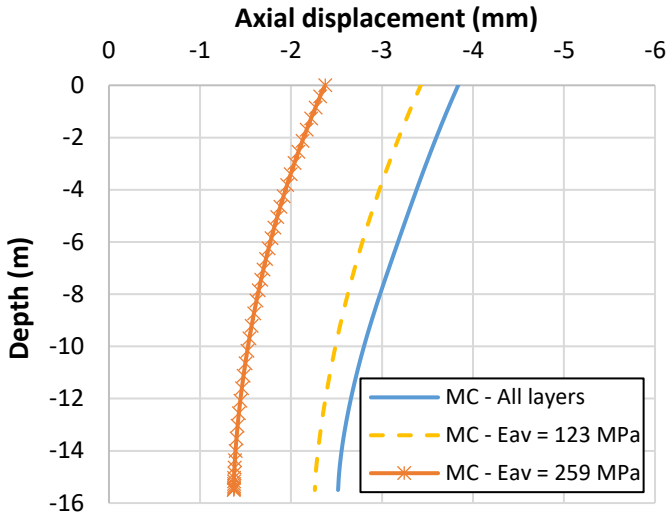

Figure 3.45 Pile displacement profiles along the pile for different cases

Figure 3.43 and Table 3.29 allow to consider that using these parameters, the pile behaves as an end-bearing pile in the elastic domain (<5 000 kN). However, we found that this comparison is not accurate. Firstly, this is due to the exaggerated value of the modulus along the pile's shaft in Model 3.8 which will obviously increase the skin friction and decrease the end-bearing pressure, reducing also the settlement compared to the other models. Secondly, the behavior of the end-bearing pile, as formulated in the elastic theory, is mainly driven by the modulus of the stratum which is identical to that of the model with four layers (300 MPa). In both cases the contrast between the stiffness of the stratum and the above layer is between 2 and 2.27. This will evidently give close results.

This is mainly caused by the neglect of the contrast between the four layers. In order to test the accuracy of these findings, a new model that has only two layers was tested. The three layers of alluviums are now merged into a single layer that has a Young modulus equal to 150 MPa. The same analysis was then done and by comparing the curves obtained from analytical and numerical methods, a very good agreement can be seen between the FLAC3D model including both layers and the elastic theory with end-bearing pile now that a suitable average modulus is used.

It can be concluded that both elastic methods underestimate the settlement in the case of Silex[2] due to the presence of the alluviums 2 layer which has a very low modulus compared to the others. The elastic theory method is best at predicting the behavior of a pile in the linear elastic state but only when the soil is homogenous or when the contrast between the layers is not high which is not really the case in this project.

On another note, it will be shown in this Chapter 4 of this thesis that the pile behaves as a floating pile especially that the measurements with the fiber optic sensors presented a negative skin friction in the upper section of the pile.

3-2-1-2- Pile groups analysis

Even though the elastic theory for single pile models did not show promising results for the previously cited reasons, we decided to pursue the study and upgrade it to pile group cases.

The elastic theory has been developed to calculate also the settlement of pile groups. The Eq. 1.65 and Eq. 1.66 defined in Chapter 1 can be solved using one of the following approaches:

- Equal loads with different settlements for a flexible cap
- Equal settlements for a rigid cap

3-2-1-2-1- Isolated pile groups

In this section, the analytical calculation of isolated pile groups will be shown. It should be restated that this case is far away from the reality but will be analyzed by way of indication only.

The two piles under a same cap were considered as equally loaded. It was also assumed that both piles will behave identically when subject to the same load, especially that they have the same geometry and a symmetry is considered in the model. Therefore, the settlements of all piles were considered to be equal to the settlement of the pile cap.

This corresponds to the case of a rigid cap not in contact with the soil and was compared to the "isolated pile group" numerical model performed in FLAC3D earlier. According to the paragraph 2-2-1-3, this matches well with the "Model 3.1" which, in turn, gave the same results as the model without any TS. This model was used in this comparison.

As an example, the pile group 17A/B was studied.

In the case of two piles, the pile group settlement may be defined as follows:

$$S_G = S(1 + \alpha_{12}) \qquad \text{Eq. 3.12}$$

Where S is the settlement of the single pile subject to the same load and α_{12} is the interaction factor between the two piles.

Identically to the method used for single piles, charts are available for different slenderness ratios for both floating and end-bearing piles. The calculations were done based on Poulos and Mattes (1971) by assuming first the case of end-bearing piles. Based on Section 3-2-1-1, the pile stiffness factor for this case study was K' = 280 and the dimensionless spacing was d/D = 3.

The chart in Figure 3.46 gives the interaction factor α_E based on values of K' and d/D for L/D =10 and ν_s = 0.5. It was shown that the effect of the Poisson's ratio is small compared to other parameters.

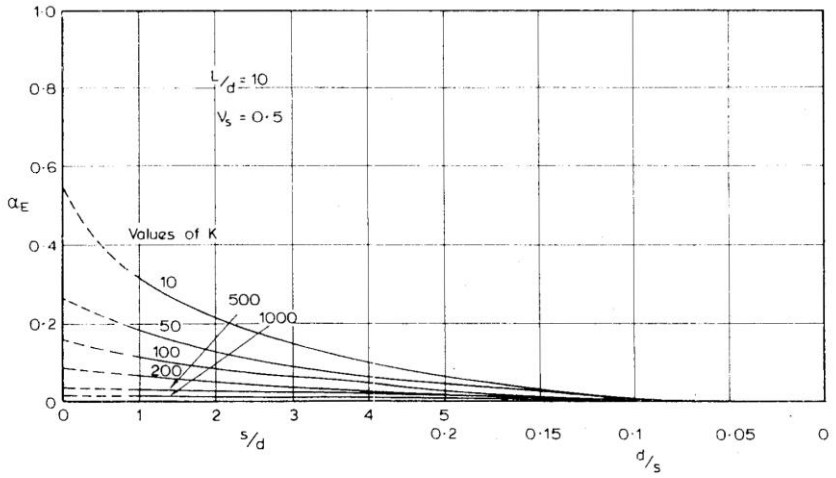

Figure 3.46 Interaction factors for end-bearing piles, L/D = 10 (Poulos and Davis, 1980)

However, if the stratum is compressible, the behavior of the pile group will lie between that of floating piles in a homogeneous soil and piles resting on a rigid base. Corrections should be made and the interaction factor is calculated as in Eq. 3.13.

$$\alpha = \alpha_F - F_E\,(\alpha_F - \alpha_E) \qquad \text{Eq. 3.13}$$

Where α_F is the interaction factor of the piles when considered as floating piles in a homogeneous soil and F_E is a factor that depends on some parameters. They can be both determined from Figure 3.47.

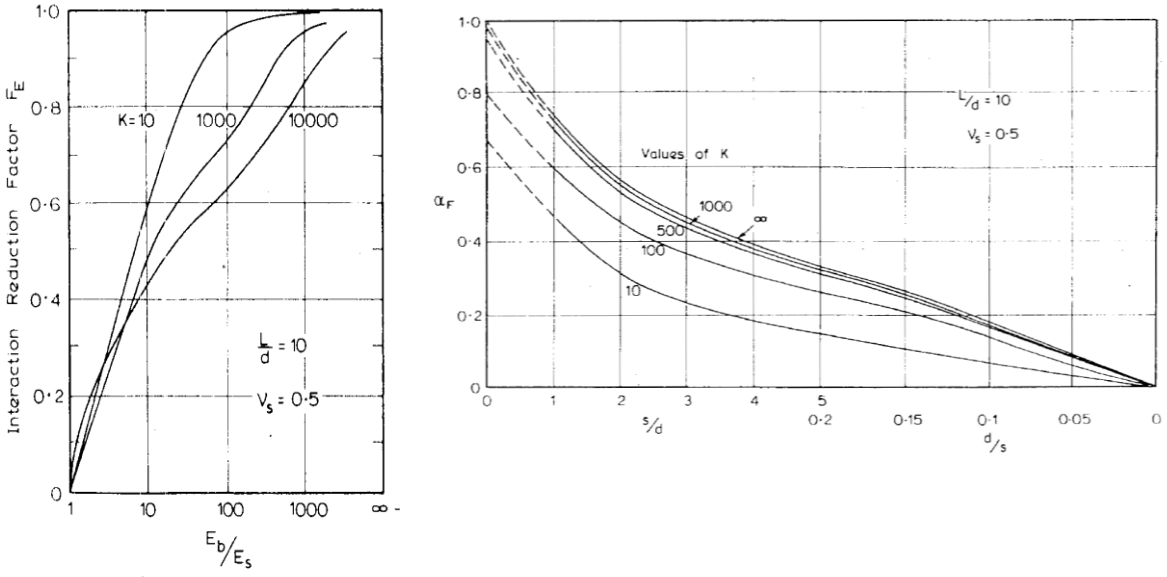

Figure 3.47 Interaction reduction factor F_E and interaction factor for floating pile, L/D = 10 (Poulos and Davis, 1980)

Based on these charts: $\alpha_E = 0.03$, $\alpha_F = 0.38$ and $F_E = 0.13$

The pile group settlement is:

$$S_G = S\,(1 + \alpha_{12}) = 1.33\,S \qquad \text{Eq. 3.14}$$

Table 3.30 and Figure 3.48 show a comparison between the single pile and pile group settlement for different applied loads. They were also contrasted with FLAC3D models.

Table 3.30 Pile settlement calculated based on elastic theory and FLAC3D models

Load (kN)	Elastic theory calculation			FLAC3D (Group I)		
	S (mm) (End-bearing pile)	S_G (mm)	S_G/ S	S (mm)	S_G (mm)	S_G/ S
1 000	-0.66	-0.88	1.33	-0.73	-0.93	1.27
2 000	-1.33	-1.76	1.33	-1.47	-1.88	1.28
3 000	-1.99	-2.65	1.33	-2.21	-2.82	1.28
4 000	-2.65	-3.52	1.33	-3.01	-3.83	1.27
5 000	-3.31	-4.39	1.33	-3.82	-4.87	1.27

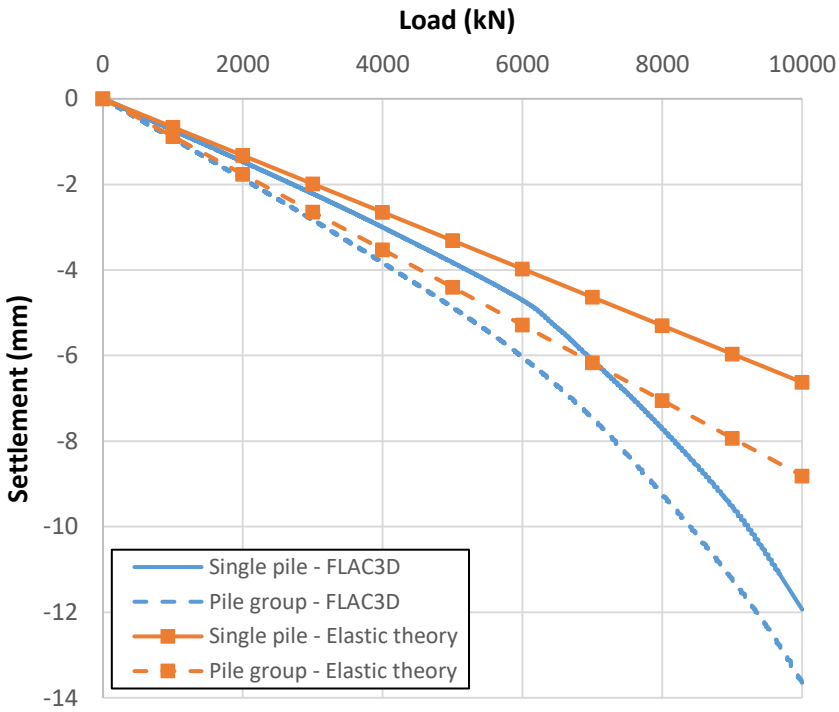

Figure 3.48 Load settlement curves from elastic theory and FLAC3D

It can be noticed that for up to 5 000 kN the difference between **S_G/ S** values in both methods is not high. However, we should keep in mind that the settlement of a single pile in the elastic theory (end-bearing pile case) was not that close to FLAC3D values as shown in the previous section.

3-2-1-2-2- General pile groups

In this section, all piles were considered to be connected by the means of a flexible raft foundation. Thus, the hypothesis of equal settlement could not be anymore assumed. Furthermore, in reality the loads applied on the top of each transfer structure are not equal according to the load transfer tables shown in Chapter 2. However, for the sake of simplicity, the piles will be considered as equally loaded. The same hypothesis applies to FLAC3D models that will be used as a reference.

The generalized formula for n piles is used, which can now be expressed as follows:

$$S_k = S\left(1 + \sum_{\substack{j=1 \\ j\neq k}}^{N} \alpha_{kj}\right) \qquad \text{Eq. 3.15}$$

Where S_k is the settlement of any pile in the group, α_{kj} is the interaction factor between the piles k and j and $\alpha_{kk} = 1$

Based on the position of the adjacent piles with respect to the pile k, the interaction factor α_{kj} should be determined from the graphs of the paragraph 3-2-1-2-1. It is shown that, when the center-to-center distance exceeds 9 times the diameter of the pile, this factor becomes zero and no influence is to be considered. Particularly in this example, the distance between the piles located on the same horizontal axis exceeds 11 m and thus they do not affect each other. This is in close agreement with the French standard that requires a minimum of 8D (= 9.76 m) in order to abstain settlement verification.

In Table 3.31 and 3.32, the interaction factor and the settlement of the 5 modeled piles will be presented. The rest can be estimated by symmetry.

The piles 17A and 19A presented the lowest settlement when subject to the same load, identically to the numerical method.

Quantitatively, Figure 3.49 shows that the settlement estimated analytically is lower than that predicted in FLAC3D. The group effect is thus underestimated using this method. For example, while three piles only play a major role in the settlement estimation of pile 17A according to the theory of elasticity, it was noticed in FLAC3D that three other piles are of high influence. Besides, the elastic theory for pile groups uses the values obtained for a single pile which were underestimated in this case as shown in 3-2-1-1.

Table 3.31 Interaction factors calculated for different piles

Pile No	**Affected by**	$\sum_{j=1}^{N} \alpha_{kj}$	S_k
17A	17B, 18A and 18B	0.48	1.48 S
18B	17A, 17B, 18A, 19A and 19B	0.84	1.84 S
18A	17A, 18B, 19A and 19B	0.96	1.96 S
19B	19A, 18A and 18B	0.91	1.91 S
19A	19B, 18A and 18B	0.64	1.64 S

Table 3.32 Pile settlement calculated analytically and then numerically (in parentheses)

Load (kN)	Single pile (End-bearing)	Settlement of the pile group				
	S (mm)	S_{17A} (mm)	S_{18B} (mm)	S_{18A} (mm)	S_{19B} (mm)	S_{19A} (mm)
1 000	-0.66 *(-0.73)*	-0.98 *(-1.86)*	-1.21 *(-1.91)*	-1.29 *(-1.95)*	-1.26 *(-1.87)*	-1.08 *(-1.68)*
2 000	-1.33 *(-1.47)*	-1.97 *(-3.71)*	-2.45 *(-3.83)*	-2.60 *(-3.91)*	-2.55 *(-3.74)*	-2.18 *(-3.36)*
3 000	-1.99 *(2.21)*	-2.95 *(-5.63)*	-3.66 *(-5.82)*	-3.90 *(-5.94)*	-3.81 *(-5.69)*	-3.26 *(-5.09)*
4 000	-2.65 *(-3.01)*	-3.93 *(-7.52)*	-4.88 *(-7.81)*	-5.19 *(-7.98)*	-5.07 *(-7.65)*	-4.34 *(-6.82)*
5 000	-3.31 *(-3.82)*	-4.90 *(-9.51)*	-6.09 *(-9.93)*	-6.48 *(-10.16)*	-6.34 *(-9.73)*	-5.42 *(-8.66)*

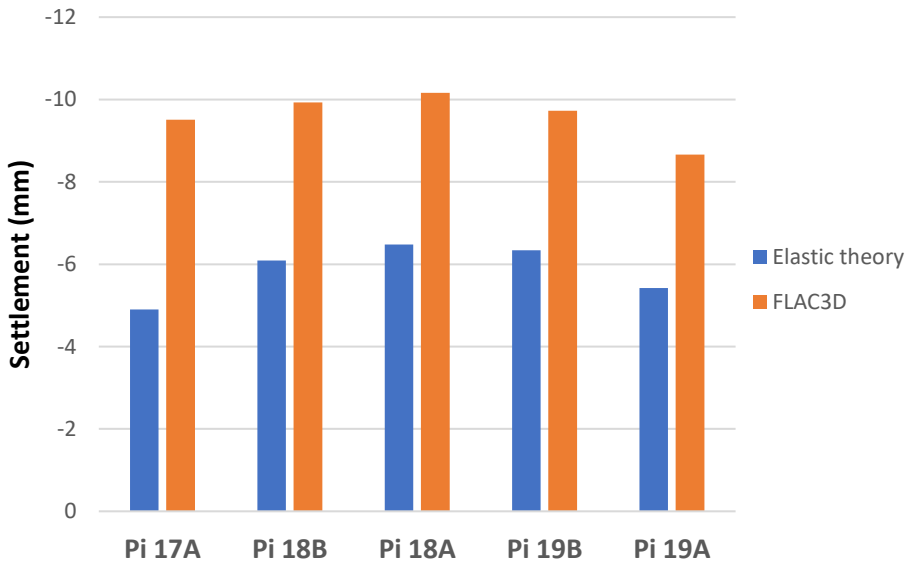

Figure 3.49 Settlement of the different piles at 5 000 kN using analytical and numerical methods

3-2-2- Load transfer method (Frank and Zhao, 1982)

Foxta software uses among others the load transfer method as described by Frank and Zhao (1982) to calculate the settlement of the piles. Therefore, the same model shown in Section 3-1 was also used here. The load transfer curves relative to each layer are presented in Figure 3.50.

The model layout and the final pile load settlement curve are shown in Figure 3.51.

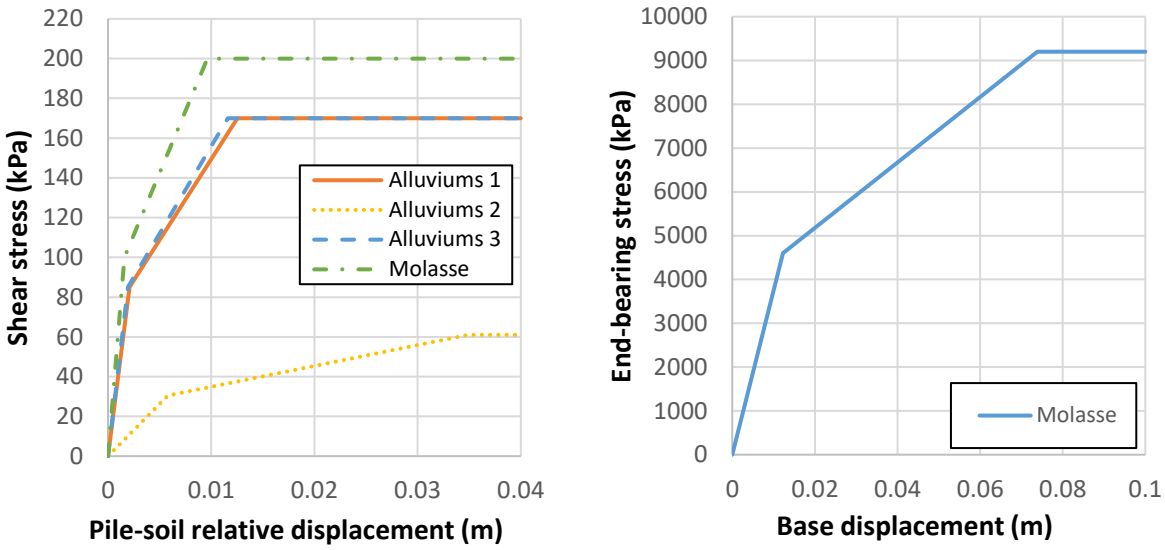

Figure 3.50 Load transfer curves for skin friction and tip resistance based on Frank and Zhao (1982)

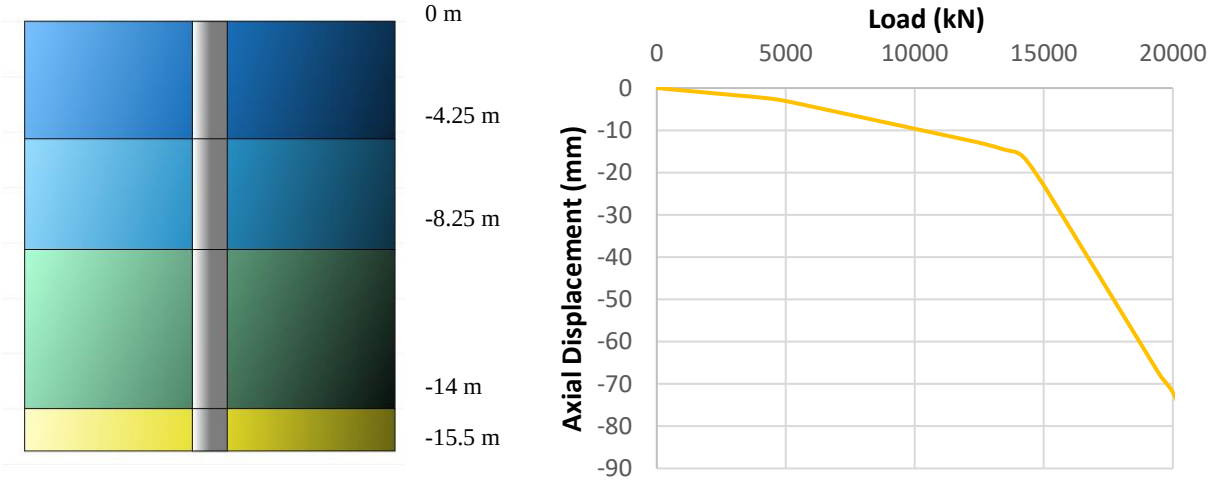

Figure 3.51 The isolated pile model and the load settlement curve in Foxta

The method suggested by Frank and Zhao (1982) gives realistic results for a load which is less than 70% of the creep resistance defined earlier which corresponds in this case to 7 978.47 kN (Hoang et al., 2018). At this load, the settlement should be around 0.006D = 7.32 mm (Frank et al., 2019). The actual settlement obtained from Foxta is around 7 mm which is so close to the expected value.

The objective of this study was to validate the choice of the deformation moduli that should be assigned to soil layers in FLAC3D based on the pressuremeter moduli measured during in-situ tests. It is known that the pressuremeter modulus is defined for a deformation range of 1% to 10% which is higher than the expected deformation measured in the case of geotechnical structures, which ranges between 0.1% and 1% as shown in Figure 1.18 (Atkinson and Sallfors, 1991; Hoang et al., 2018). It is then necessary to find a

formula that relates the experimental moduli to the deformation moduli and that can be used in the numerical analysis, in FLAC3D in this example.

Firstly, the deformation moduli were calculated based on Eq. 3.16 for a Poisson's ratio of 0.3. The parameters shown in Table 3.1 were used for the soil layers and the Young modulus of the concrete was 34.5 GPa.

$$E_y = \frac{(1+\nu)(1-2\nu)}{1-\nu}\frac{E_M}{\alpha} = 0.74\frac{E_M}{\alpha} \qquad \text{Eq. 3.16}$$

For a better comparison with Foxta, the interface elements were assigned a null friction angle and a cohesion that has the same value as q_s used in Foxta (Table 3.24).

The load settlement curves obtained in FLAC3D using the linear elastic and Mohr-Coulomb models were compared to the results of Foxta in Figure 3.52.

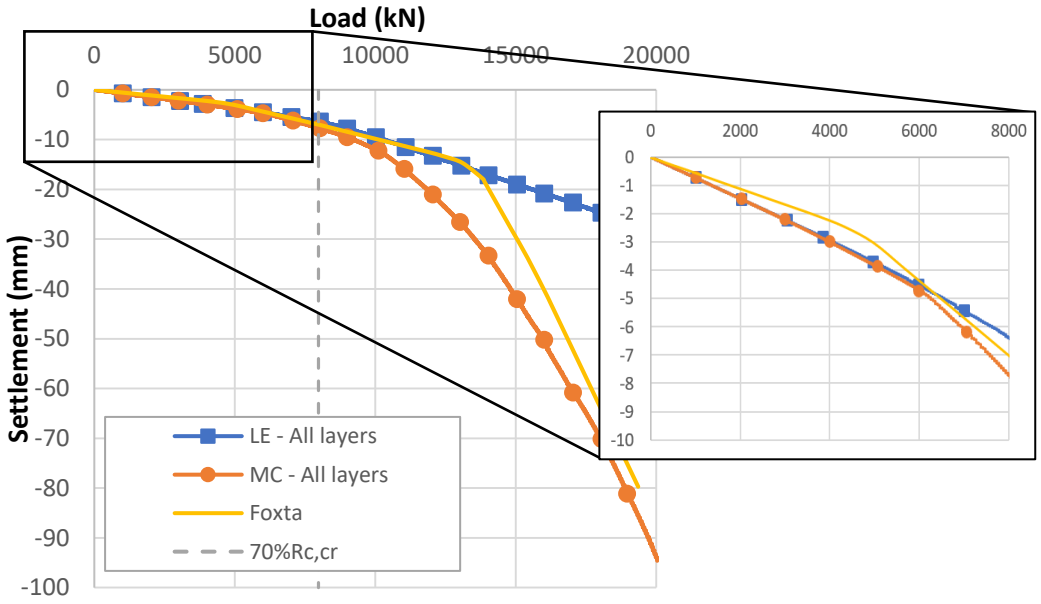

Figure 3.52 Pile load settlement curves in Foxta and FLAC3D using initial parameters

This analysis shows that the linear parts of the curves were not matching well. For Q < 6 000 kN, FLAC3D overestimated the settlement and consequently it appeared that the Young modulus in this load range was underevaluated.

Based on the sensitivity analysis performed in Section 2-1-2-3, the Young modulus assigned to the soil layers was found to be a key parameter in the estimation of the pile's behavior. It is clear that the moduli used previously do not give representative load-settlement curves and it should be increased.

As a means to enhance this type of analyses, Bohn (2015) suggested new equations to correlate the Young moduli with the pressuremeter ones. These are shown earlier in Chapter 1 (Eq. 1.135 and 1.131) for the

shaft and the tip. When applied on the alluviums and the molasse, these equations gave the new moduli shown in Table 3.33.

Table 3.33 Deformation moduli according to the method suggested by Bohn (2015)

	E_M	E (shaft)	E (tip)
Alluviums 1	62	245	-
Alluviums 2	8	32	-
Alluviums 3	67	264	-
Molasse	95	375	326

In accordance with these parameters, the new load settlement curves obtained in FLAC3D are shown in Figure 3.53.

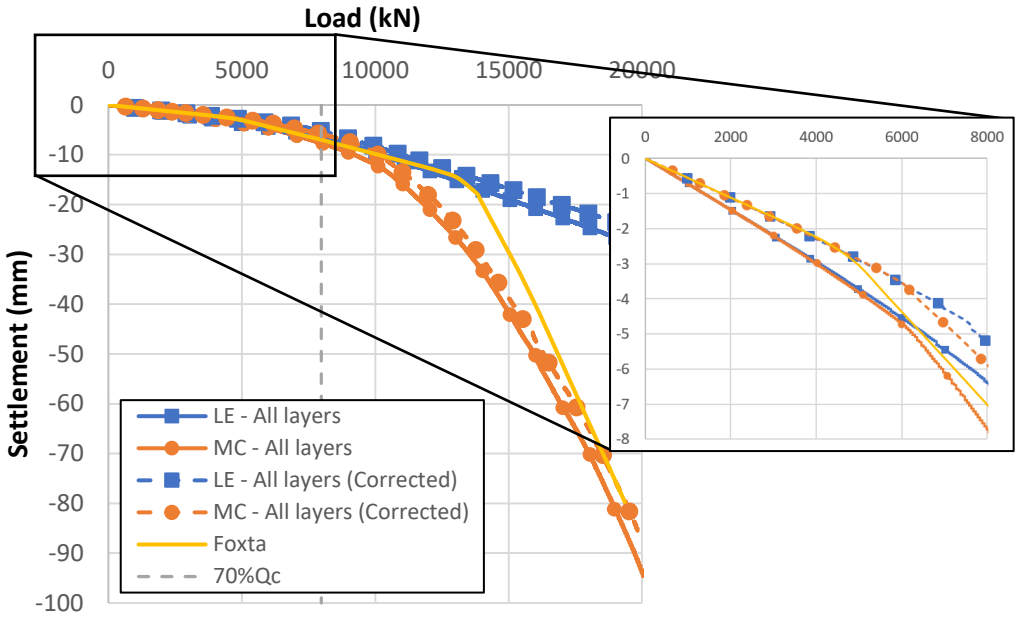

Figure 3.53 Load settlement curves in Foxta and FLAC3D using corrected parameters

The close view to the right of Figure 3.53 shows that the new moduli allowed to have new curves that have the same initial elastic part as in Foxta's curve. The results were thus in close agreement for Q < 5 000 kN.

In order to broaden the subject a bit more and understand the reason of the settlement variation in the range (5 000 – 8 000 kN), it should be remembered here that the parameters used in each method are different. While Foxta uses only the pressuremeter moduli and the ultimate unit skin friction "q_s" and the limit pressure under pile base "q_b", more parameters such as the cohesion and the friction angle should be added to the soil layers in a Mohr-Coulomb model in FLAC3D. In this context, if we take a look back at the sensitivity analysis performed earlier in this chapter, we can notice that the variation observed in Figure 3.53 could be also seen by modifying the cohesion and the friction angle of the soil. In fact, in this

section, as shown in Table 3.1, the cohesion and the friction angle were 50 kPa and 35° respectively which, in our opinion should be reduced.

With the aim of improving this analysis, a new model was tested where the three layers of alluviums were assigned a cohesion of 25 kPa which might be closer to the reality. The new corrected load settlement curve as shown in green in Figure 3.54 is closer to the Foxta curve in the same load range.

In addition, it is also known that the LTM gives a non-linear model (trilinear in this case), while FLAC3D uses an elastic perfectly plastic model which may explain the bigger elastic section in LTM curve. However, since our concern is for 0 – 5 000 kN only, these findings were satisfying for us as for now.

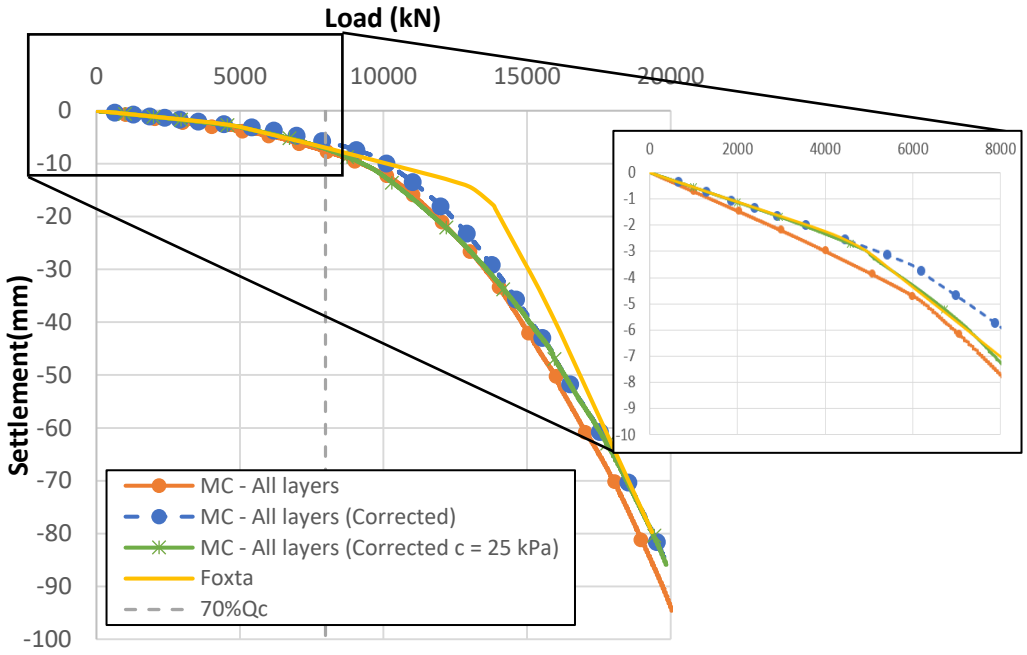

Figure 3.54 Load settlement curves in Foxta and FLAC3D using new corrected parameters

4- Conclusion

Our intent in this chapter was to provide a deeper understanding of the pile's behavior in FLAC3D. Therefore, four different geometrical models were studied for this purpose. Firstly, the single pile model's aim was to study the influence of each of the parameters used in the model on the response of the axially loaded piles. While some parameters such as the water table, the cohesion, the friction angle and the dilatancy angle played no role in the load range that corresponds to Silex^2 (0 – 5 000 kN), it turned out that others such as the Young modulus of the concrete, the Young modulus of the soil layers and the parameters of the interface were of high importance.

Secondly, two-pile groups were also analyzed in FLAC3D. Two geometries were tested and compared with single pile models. In all these models, the influence of the elastic modulus of the pile and the water table was also studied. However, in order to estimate the real behavior of the piles, a "Global model", which included all the piles in the project was performed.

On the other hand, two analytical methods (LTM and elastic theory) were compared with the numerical approach in FLAC3D. The theory of elasticity showed unfortunately poor results with respect to the settlement estimation due to the layering of the soil. However, FLAC3D's load settlement curves showed good agreement with the curves obtained from the load transfer method especially after making few corrections on the soil moduli.

It is necessary now to calibrate the numerical models with the experimental tests and the instrumentation that were performed. This will be discussed in Chapter 4.

Chapter 4: Results of the instrumentation and validations with the numerical models

1- Introduction

In the previous chapters, the experimental and numerical tools used in the thesis were presented. A sensitivity analysis was performed using FLAC3D in Chapter 3, showing the influence of each of the soil and concrete parameters on the behavior of the soil-pile system. However, it was necessary to do some laboratory tests with the goal of characterizing the soil which will be shown in this Chapter. Besides, the results of the instrumentation will be presented and will be confronted with the numerical model performed in FLAC3D validating thus the geotechnical parameters as well as the constitutive law chosen for the alluviums and the molasse.

2- Interpretation of laboratory tests and soil characterization

During the project execution, it was possible to identify the four layers of alluviums and molasse described earlier.

On one hand, by having a deep look at the piles monitoring records, the four layers and the few meters of embankments were observed. In fact, starting from the working platform which corresponds to 164 m NGF (a level that is higher than the actual level of the piles' head shown in Table 2.2), the maximum drill rate (250 m/h) and the minimum torque (100 bar) were reached for few meters between 6 and 10 m depth reflecting the low compactness of the alluviums 2 layer. The drill rate then slowed down after this depth in the alluviums 3 reaching the lowest value below 16 m in the molasse layer (≈ 148 m NGF). This validates the very high mechanical characteristics of this layer. However, the position and the thickness of the layers were not similar in all piles.

On the other hand, a sonic drill was executed in Silex^2 at the location defined in Figure 4.1. This advanced technique uses high-frequency energy generated inside the sonic head to advance a casing and a core barrel into soils or rocks. The 0.15 m casing prevents the failure of the soil and the core barrel allows the extraction of disturbed and undisturbed samples of 0.12 m diameter as shown in Figure 4.2. This drill was executed starting from the level 162.8 m NGF and up to 35 m depth and it served thus to install the fiberglass rod extensometer as detailed in Chapter 2.

The extracted samples in this location of the site showed a few meters of gravels on top of a layer of clean sand between 154.3 and 155.8 m NGF, regarded as the alluviums 2 layer. It is then followed by another thick layer of sandy gravels in which another sandy layer was observed between 151.3 and 152.3 m NGF. This can be explained by the soil disturbance due to the drilling.

Underneath the alluviums, the molasse was detected at 15.5 m depth, i.e., 147.3 m NGF.

The samples served to perform several laboratory tests by Antea Group and GEOMAS (sieve analysis, triaxial, oedometer, shear box tests…).

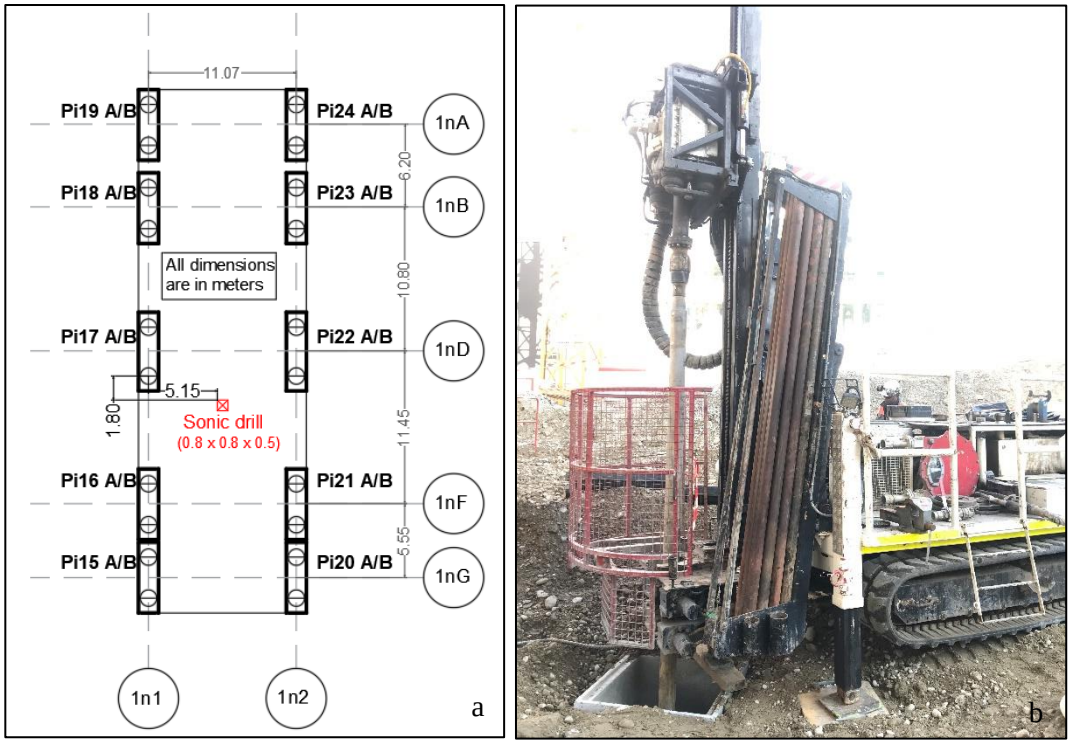

Figure 4.1 (a) Location of the sonic drill and (b) the drilling machine

Figure 4.2 Disturbed and undisturbed samples extracted from the sonic drill

The sieve analysis tests performed on the samples showed poorly graded gravels in alluviums 1 and 3 and poorly graded sand with silt or clay for the alluviums 2 and the molasse. While the maximum diameter ranged between 40 and 100 mm for the alluviums, it was much lower for the molasse and it varied according to the depth. D_{max} was found between 12 and 20 mm.

This paragraph shows the results of the recent experimental tests performed during 2018 – 2020 on the alluviums and the molasse. The samples on which the tests were performed were labelled using the depth from which they were extracted. For example, the sample S_1m_2m was retrieved between 1 and 2 m depth.

2-1- Characterization of the alluviums using shear box tests

The alluviums were not well characterized in the previous projects of the Part-Dieu area. Laboratory tests could not be performed in standard testing equipment because of the big diameter of the grains. This has led to an incorrect assessment of their behavior. Therefore, we tended to consider sometimes a zero cohesion while in other projects such as in Silex[2], the construction company suggested to use a cohesion equal to 50 kPa for design purposes. Consequently, using wrong parameters entails a wrong evaluation of the pile capacity and dimensions.

The main problem that prevented the characterization of the alluviums is that the standards set minimum dimensions for the equipment used in experimental tests (triaxial and shear box tests in particular). For example, the following equation applies for the shear box tests (NF P 94-071-1, 1994):

$$6D_{max} \leq h \leq L/2 \qquad \text{Eq. 4.1}$$

Where D_{max} is the maximum diameter of the grains in the sample and h and L are the height and the width of the shear box.

According to this equation, if the grains of the sample have a maximum diameter of 80 mm, then the shear box should have at least h = 480 mm and L = 960 mm. However, the dimensions of the shear box available in the laboratory at INSA Lyon are: 200 mm x 200 mm.

Therefore, in the literature many methods are proposed to "reconstruct" samples in the laboratory that have an admissible diameter with respect to the dimensions of the testing equipment. However, precautions should be taken since a variation of the soil characteristics (cohesion and friction angle for example) can be observed.

The following tests were performed as part of a "Projet d'Initiation à la Recherche et au Développement" done by one of the students at INSA Lyon. It was decided to use the reconstruction by analogy or similarity which was found convenient for the alluviums, especially that the percentage of fine particles is small. This method aims to reproduce the shape of the initial grading curve by imposing a maximum grain diameter that is admissible according to the standards.

The matrix was defined as the proportion of soil that has a maximum grain size of 2 mm while the inclusions had a bigger diameter.

A set of shear box tests was performed on alluviums extracted between 6 and 7 m. Since the admissible maximum diameter was 20 mm, several tests were performed on reconstructed samples with D_{max} = 20, 10, 5 and 2 mm.

The results are presented in Table 4.1 showing an increase in the shear strength with increasing inclusion percentage and decreasing L/D_{max}. This can cause us to overestimate the real cohesion and friction angle, knowing that the natural soil would have a lower L/D_{max} and a higher percentage of inclusions. This is in close agreement with the findings of some authors, who showed that even when the scale factor L/D_{max} meets the standards, the friction angle may be overestimated (Fry et al., 1989; Seif El Dine, 2007).

It was also shown that when the L/D_{max} increases, the friction angle decreases and then stabilizes after a certain value of L/D_{max} (Fry et al., 1989). In these experiments, the friction angle as shown in Table 4.1 and Figure 4.3, stabilizes at around 36°, which is close to the value assumed in the beginning of the thesis (35°).

Table 4.1 Values obtained from the shear box tests

	ϕ (°)	c (kPa)	L/D_{max}	Percentage of inclusions (%)
Test a (D_{max}= 20 mm)	45.6	24.7	10	69
Test b (D_{max}= 10 mm)	41.4	14.8	20	46
Test c (D_{max}= 5 mm)	38.5	12.3	40	12
Test d (D_{max}= 2 mm)	36.8	6.3	100	0

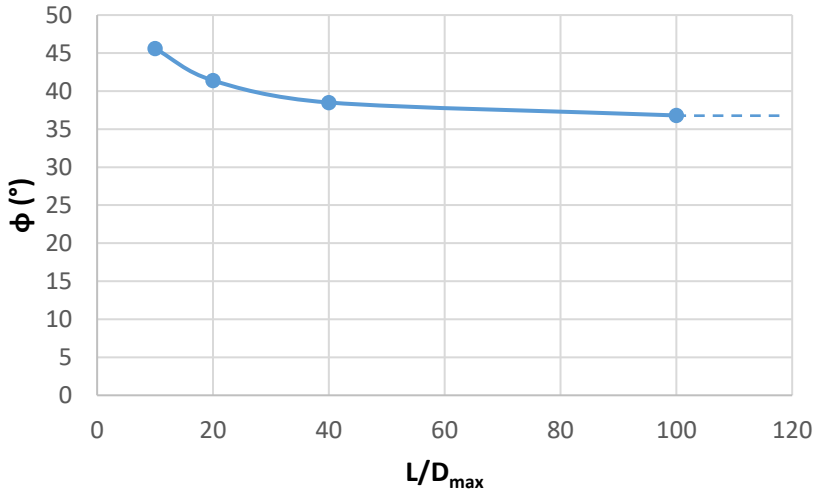

Figure 4.3 Variation of the friction angle with respect to the L/D_{max}

However, the cohesion of the sample is highly affected by the scale effect and its exact value was not well investigated. It is estimated in the range (5 - 25 kPa) in accordance with the literature, which is significantly lower than our initial hypothesis (50 kPa). Consequently, the influence of this parameter on the model's behavior should be reconsidered in this chapter.

This conclusion also works well for the three layers of alluviums.

2-2- Characterization of the molasse

The molasse is a layer of silty to gravelly sand. The silty character of this layer was determined via VBS tests that showed values in the range 0.23 - 0.4. Its natural water content varies between 18.6 and 21.6% and its dry density between 1.51 and 1.62 g/cm^3. It can be thus considered as medium dense sand.

Several experimental tests were performed on molasse layers as shown in Table 4.2 in order to represent the behavior of the soil in shear and compression conditions at the shaft and the tip of the piles.

Table 4.2 Tests performed by Antea Group or INSA

Sample number	Shear box tests	Triaxial tests (CU+u)	Triaxial tests (CD)	Oedometer tests
S_15m_16m			x	
S_16m_17m				x
S_18m_19m		x		
S_21m_22m	x			x
S_23m_24m	x	x		x

The two shear box tests performed on the molasse allowed to conclude the following parameters:

- S_21m_22m: c = 23 kPa; ϕ = 37°
- S_23m_24m: c = 39 kPa; ϕ = 33°

In the following sections, the triaxial and the oedometer tests were calibrated to determine the parameters of the molasse. FLAC3D was used to calibrate the oedometer tests, while the analysis of the triaxial tests was performed in the module SoilTest of Plaxis2D which is used to simulate soil tests without the need to create a finite element model.

It should be noted that the tests that did not show coherent results with the others were automatically eliminated. The calibration procedure will be detailed hereafter.

2-2-1- Calibration of triaxial (CU+u) tests

Triaxial tests should be performed in a way they can represent the best the site conditions in terms of effective pressure. The confining pressures σ_c are chosen to be equal to the mean pressure calculated in terms of effective stresses in triaxial conditions as follows:

$$\sigma_c = p' = \frac{\sigma_1 + 2\sigma_3}{3} \qquad \text{Eq. 4.2}$$

Therefore, for each value of p' corresponds a soil depth and that way, different moduli can be obtained.

The behavior of the soil in triaxial conditions can be described using MC or PH model for a more advanced representation (see Section 4-2-2 and 4-2-3 of Chapter 2). The latter is also an alternative to performing a big number of triaxial tests by using a stress-dependent stiffness as explained earlier in Chapter 1. The

parameters needed for a PH model are: c, ϕ, ψ, ν_{ur}, E_{50}^{ref}, E_{oed}^{ref}, E_{ur}^{ref} and m. They will be determined in the following.

Four CU+u tests were performed on each of the samples S_18m_19m and S_23m_24m with different confining pressures (100, 200, 400 and 800 kPa). After analyzing the stress-strain curves, the 800 kPa and the 400 kPa were eliminated for the first and the second sample respectively.

The friction angle and the cohesion are defined respectively as the slope and the y-intercept of the failure line from the Mohr-Coulomb failure criterion. They were estimated as follows:

- Cohesion: c = 25 kPa
- Friction angle: ϕ = 35°

Figure 4.4 and Figure 4.5 show the experimental and numerical stress-strain curves for the CU+u tests performed on both samples. The numerical curves obtained for the MC and PH models are drawn in discontinuous and continuous lines respectively.

Based on these curves, the undrained initial modulus was estimated at 255 MPa, which is used in general for deformations up to 10^{-5} (Combarieu, 2006). E_{50} was defined as the secant stiffness calculated at 50% of the ultimate deviator stress q_u in each case. Three different stiffnesses were determined for each sample. The reference stiffness E_{50}^{ref} corresponds for a p_{ref} = 100 kPa.

"CU+u" tests allow in general to have undrained parameters from which the drained values can be deduced.

The equation that can be used to calculate $\left(E_{50}^{ref}\right)'$ is:

$$E_u = E' \frac{1+\nu_u}{1+\nu'} \qquad \text{Eq. 4.3}$$

Where ν' = 0.3 and ν_u = 0.495.

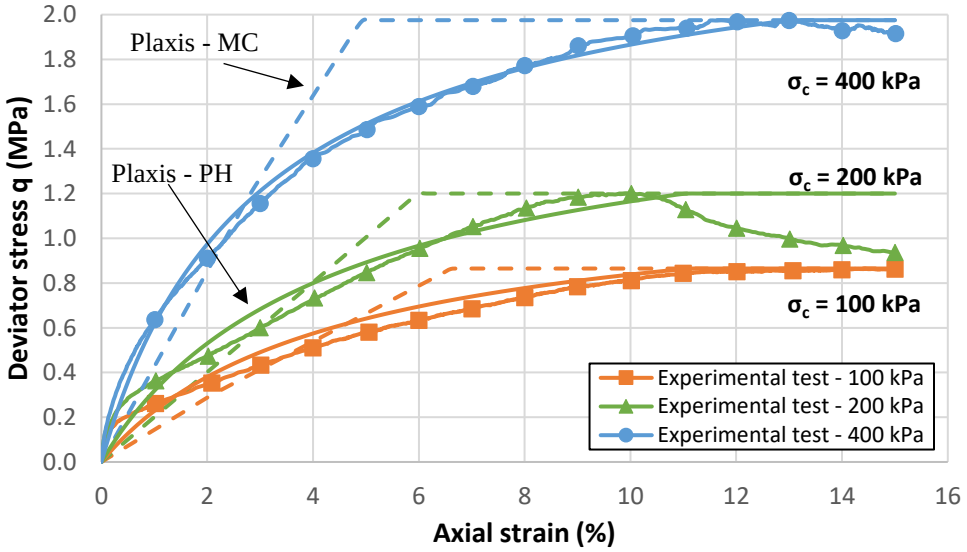

Figure 4.4 Experimental and numerical stress-strain curves of the CU+u tests carried out on the sample S_18m_19m

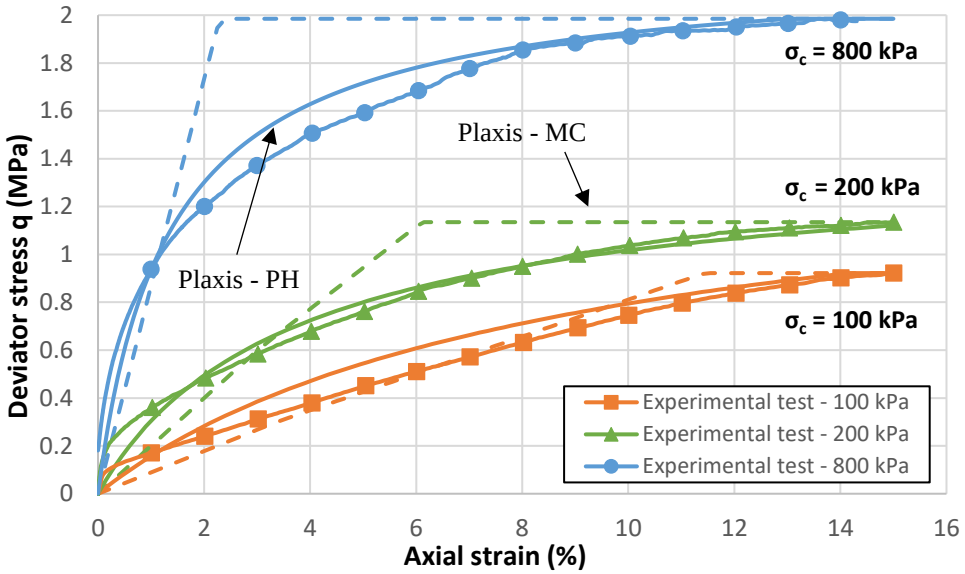

Figure 4.5 Experimental and numerical stress-strain curves of the CU+u tests carried out on the sample S_23m_24m

The failure ratio R_f which is the ratio of the ultimate deviatoric stress to the asymptotic stress (see Section 4-2-3 of Chapter 2) was also determined from the stress-strain curves.

The obtained values are summarized in Table 4.3.

Table 4.3 PH model parameters obtained from the different triaxial tests

Sample	Test	PH model			MC
		$(E_{50})_u$ (MPa)	$(E_{50})'$ (MPa)	R_f	E' (MPa)
S_18m_19m	Test 1 – 100 kPa	14.33	12.46	0.8	12.46
	Test 2 – 200 kPa	20	17.4	0.8	17.4
	Test 3 – 400 kPa	42.47	36.93	0.8	36.93
S_23m_24m	Test 1 – 100 kPa	8.87	7.71	0.6	7.71
	Test 2 – 200 kPa	19.89	17.29	0.8	17.29
	Test 3 – 800 kPa	86.26	75	0.9	75

The selected $(E_{50}^{ref})'$ and R_f values for the following sections are 12.46 MPa and 0.8 respectively.

2-2-2- Calibration of oedometer tests

Oedometer tests were also carried out on two molasse samples (S_21m_22m and S_23m_24m). Numerical tests were performed in FLAC3D resulting in the following calibrated parameters. The compressibility curves of one of the samples are shown in Figure 4.6.

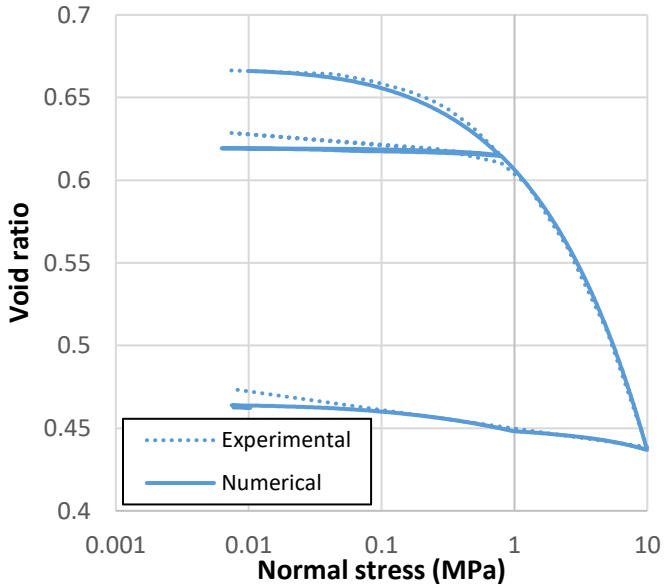

Figure 4.6 Experimental and numerical compressibility curves of the sample S_21m_22m

Based on the numerical curves obtained from FLAC3D:

- E_{oed}^{ref} = 17 MPa
- E_{ur}^{ref} = 250 MPa
- m = 0.5

Table 4.4 summarizes the different parameters obtained experimentally for the alluviums and the molasse.

Table 4.4 Parameters obtained from experimental tests

Parameter	**MC**			**PH**
	Alluviums 1	Alluviums 2	Alluviums 3	Molasse
c (kPa)	5-25	5-25	5-25	25
ϕ (°)	36	36	36	35
$\mathbf{E_{50}^{ref}}$ **(MPa)**	-	-	-	12.46
$\mathbf{E_{oed}^{ref}}$ **(MPa)**	-	-	-	17
$\mathbf{E_{ur}^{ref}}$ **(MPa)**	-	-	-	250
$\mathbf{R_f}$	-	-	-	0.8
m	-	-	-	0.5

3- Interpretation of the in-situ instrumentation

The instrumentation in Silex^2 was carried out between January and June 2019, but it was only in September 2019 that we started to visualize the results. The measurements were indeed analyzed based on the construction schedule of Silex^2. They will be summarized in this section.

3-1- Load application

The construction of Silex^2 lasted more than one year, due to the emergence of the COVID-19 pandemic in the world and in France in particular, which had caused two months of full lockdown followed by another two months of partial activities in all domains. Accordingly, the load was being applied gradually during the construction of the tower. It will be recalled that in the following the dates are given in the format: d/m/yy *(example: 3/9/20 corresponds to 3 September 2020).*

The zero value of all the electrical sensors corresponds to the beginning of the construction of the steel tower in September 2019. However, for the FOS, it corresponds to the 26/2/20 due to some technical problems. The analysis was then stopped on 3/9/20 since a drop in the measured deformations and stresses started to be observed which seemed to be uninterpretable.

Table 4.5 and Table 4.6 show the theoretical loads obtained from a numerical model provided by the company. The loads during this period consisted of the self-weight of the steel structure in addition to the weight of the concrete floor at each level and the facade of the building.

Note that the dates in these tables represent the pouring of the concrete floor in the mentioned level (and not the installation of the steel structure).

Table 4.5 Construction progress and evolution of the theoretical total loads at different stages

Level	Date (d/m/yy)	Load (kN)	Progress	Level	Date (d/m/yy)	Load (kN)	Progress
R+ 1	-	2 249.3	3.96%	**R+ 14**	-	30 130.8	52.99%
R+ 2	-	4 498.6	7.91%	**R+ 15**	29/5/20	32 240.2	56.70%
R+ 3	6/1/20	6 747.9	11.87%	**R+ 16**	-	34 382.9	60.47%
R+ 4		8 997.2	15.82%	**R+ 17**	12/6/20	36 565.6	64.31%
R+ 5	14/1/20	11 146.5	19.60%	**R+ 18**	-	38 748.2	68.15%
R+ 6	-	13 255.8	23.31%	**R+ 19**	26/6/20	40 930.9	71.98%
R+ 7	31/1/20	15 365.2	27.02%	**R+ 20**	3/7/20	43 113.6	75.82%
R+ 8	-	17 474.6	30.73%	**R+ 21**	-	45 296.3	79.66%
R+ 9	14/2/20	19 583.9	34.44%	**R+ 22**	31/7/20	47 609.2	83.73%
R+ 10	-	21 693.3	38.15%	**R+ 23**	-	49 922.1	87.80%
R+ 11	28/2/20	23 802.7	41.86%	**R+ 24**	14/8/20	52 235.1	91.86%
R+ 12	-	25 912.1	45.57%	**R+ 25**	-	54 548	95.93%
R+ 13	13/3/20	28 021.5	49.28%	**R+ 26**	-	56 861	100%

The installation of the steel structure ended on 1/10/20.

Table 4.6 Theoretical load applied at each pile at different construction stages

Pile No	Load per pile (kN)				
	14/1/20	29/5/20	31/7/20	3/9/20	1/10/20
	Level R+5	Level R+15	Level R+22	*(interpolated)*	Level R+26
Pi15	366.76	1 566.12	2 233.92	2 690	2 843.59
Pi16	412.84	1 533.76	2 139.13	2 525	2 650.99
Pi17	601.51	1 950.41	2 687.92	3 100	3 272.72
Pi18	440.45	1 560.64	2 176.60	2 550	2 703.55
Pi19	421.45	1 630.34	2 307.21	2 800	2 934.54
Pi20	383.32	1 551.17	2 226.00	2 690	2 849.89
Pi21	420.79	1 475.41	2 076.25	2 480	2 609.23
Pi22	586.84	1 800.53	2 502.29	2 950	3 103.21
Pi23	443.62	1 483.50	2 087.38	2 490	2 628.64
Pi24	420.95	1 548.23	2 211.47	2 680	2 834.15

As mentioned earlier, the analysis was performed on the measurements taken between September 2019 and September 2020. The progress of the construction during this period is shown in Figure 4.7.

Figure 4.7 Pictures of the construction site in September 2019 and September 2020 (at level R+25)

3-2- Measurement of the loads at the piles head

The concrete pressure cells were used to measure continuously the pressure at the piles' head. Since three sensors were installed for each pile, the averaged pressure was calculated allowing to determine the averaged load after multiplying by the section of the pile. The outliers were removed from the analysis.

Fifteen out of the eighteen sensors installed in the project showed good results, the others were either broken during the installation or not working properly.

The measurements were retrieved using the two following techniques and showed very close results:

- An automatic reading using the Data taker
- A manual reading using the Fluke multimeter

In the present study, only the measurements relative to the pile 17A were analyzed. The sensors installed in this pile, after assessing the losses will be recalled in the following figure. They include 2 CPCs, 6 ERSGs, 1 VWSG and 1 FOS (see Chapter 2 for more details).

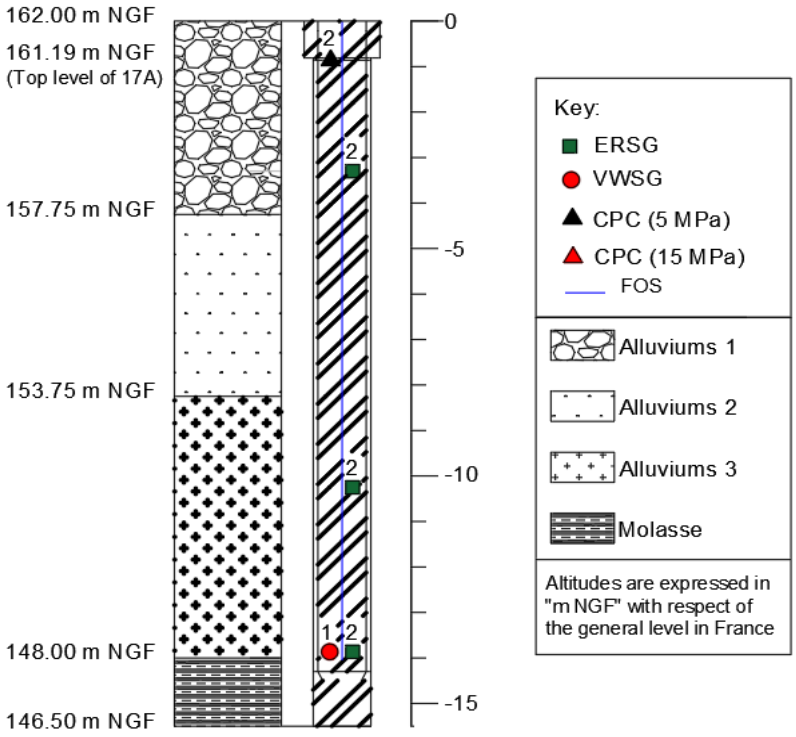

Figure 4.8 General soil profile and instrumentation layout of Pile17A

Figure 4.9 shows the evolution of the load over the time for the two sensors of Pile17A. The blue curves represent the calculated average in both reading methods separately. These were then compared to the theoretical load that was supposed to be applied on Pile17A during the same date. This comparison is shown in Figure 4.10 and Table 4.7, where it can be noticed that there is a slight discrepancy between the measured and the theoretical loads. In fact, the real measured load tends to be somehow lower than expected. This can have many causes such as an imperfection in the surface of the concrete which can lead to non-horizontal sensors. Besides, the CPCs are generally used between two media of different types, such as concrete and soil. Using them in this project between the pile and the TS may have caused some problems. In addition, this difference may be the result of the transfer of the load to the concrete slab and/or the soil underneath.

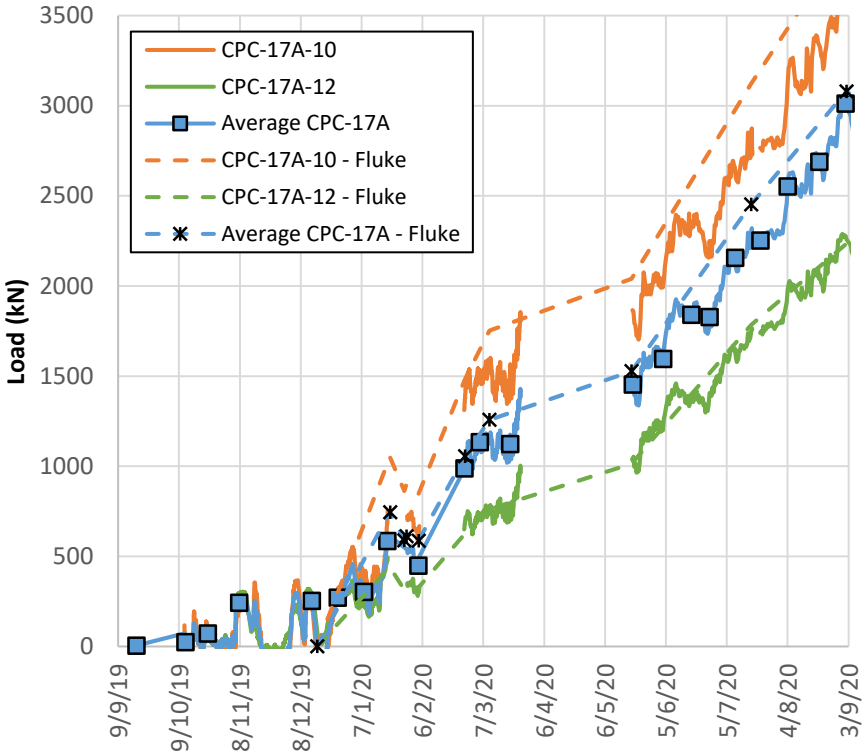

Figure 4.9 Evolution of the measured load on the head of Pile 17A

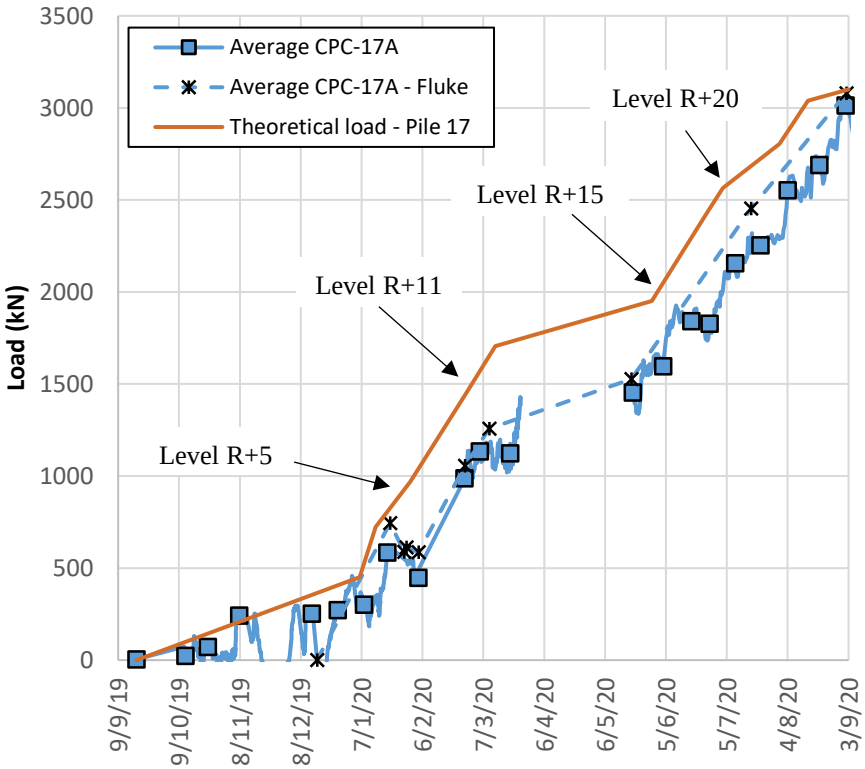

Figure 4.10 Comparison between the theoretical and the measured load on the head of Pile 17A

Table 4.7 Comparison between measured and theoretical loads for Pile 17A

Date	Measured average load (kN)	Theoretical load (kN)
14/1/20	320	724
26/2/20	1 011	1 460
29/5/20	1 590	1 950
3/7/20	2 035	2 565
3/9/20	2 960	3 100

3-3- Measurement of the pile deformation

As explained in Chapter 2, the deformation of the six piles (17A/B, 18A/B and 20A/B) was measured using three types of technologies to ensure redundancy. However, since the only working FOS is located in the pile 17A, it will be the main focus in the following analysis.

3-3-1- Pile deformation measurements

Since their installation, all the ERSGs and ten out of fourteen VWSGs showed a good functioning. However, some problems were encountered with the FOSs during the early construction phases and only one could withstand the harsh environment of the site. This FOS belongs to Pile17A and for technical reasons, the first measurement that could be taken was on 26/2/20 unlike the other sensors. Therefore, this measurement was considered as the tare value or the reference and consequently, the time frame of the measurements in this analysis will start from this new date.

It is important in any instrumentation to keep record of the position of each of the sensors with respect to a fix and known level during their installation. In this work for example, it was measured with respect to the bottom of the reinforcing cage, which was installed at 147.5 m NGF for all the piles. This allows to have a better comparison between the different sensors.

A comparison between the measurements of all the deformation sensors in the different instrumented piles is presented in Figure 4.11. In case of two sensors of the same type installed at the same level, their measurements were averaged after removing the outliers. A negative value reflects a pile shortening. For the sake of simplicity, a unified level for the piles' head was adopted at 162 m NGF in all the following figures. This matches the level chosen in the numerical models. The values are corrected using the temperature compensation shown in Section 3-3-2-2.

All the sensors showed the same deformation range. Some showed a negative skin friction while others did not. In fact, the measured deformation can vary depending on many factors:

- The resolution of the sensor in view of the total measured values
- A local change in the diameter of the pile
- A local change in the modulus of the concrete

The last two causes are governed by the following equation:

$$F(z) = E_p(z)A(z)\varepsilon(z) \qquad \text{Eq. 4.4}$$

Where E_p is moduli of the pile, $\varepsilon(z)$ is the deformation and A(z) is the cross-section of the pile.

No conclusion can be drawn from the measurements of the ERSGs and the VWSGs since they give single point values. This is one of the main reasons for the use of FOS in this project.

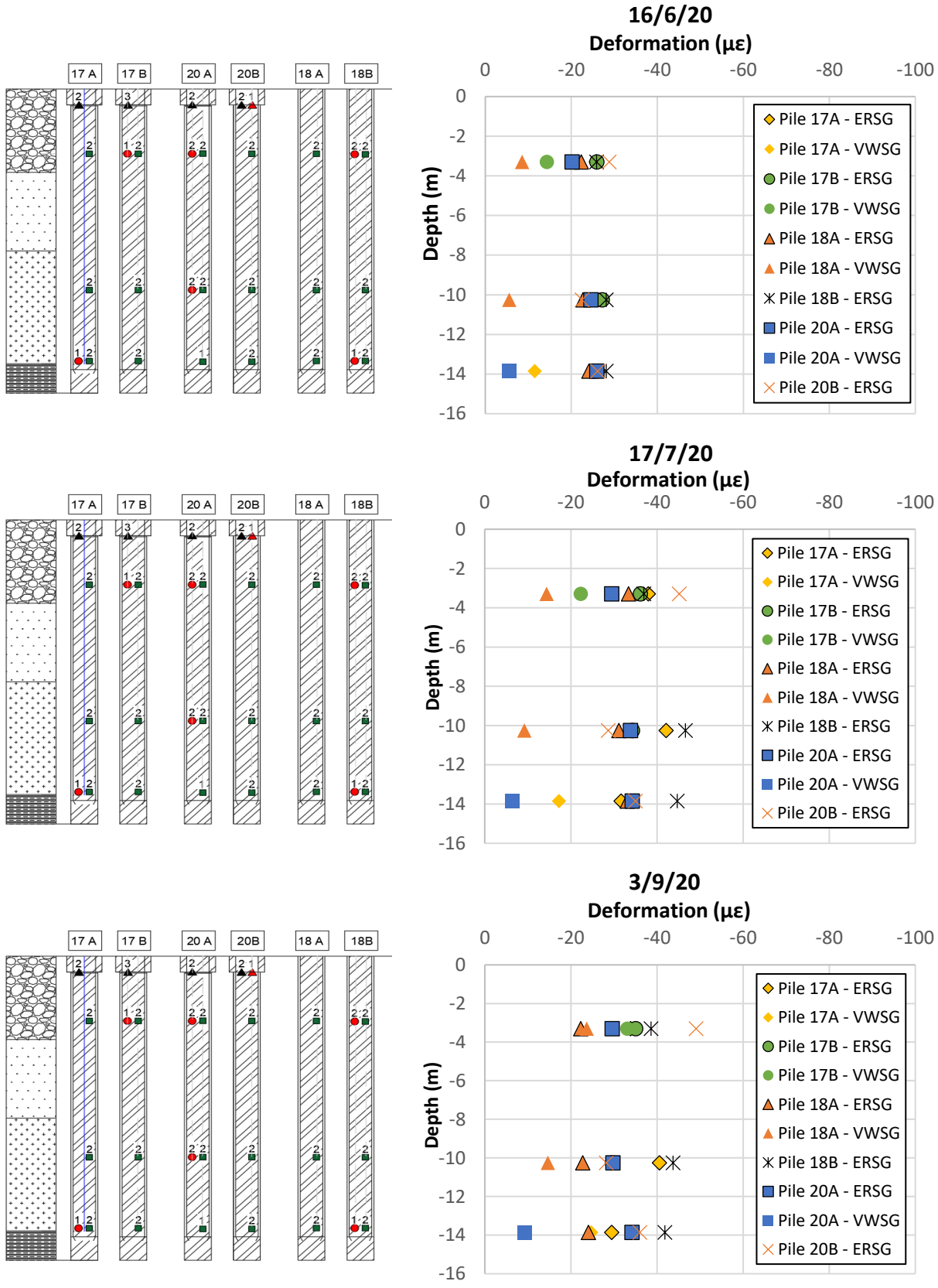

Figure 4.11 Deformation measured using different types of sensors in all piles

3-3-2- Analysis of Pile 17A

3-3-2-1- Deformation measurements

Figure 4.12 shows the pile deformation measured using the FOS at three different dates. It should be recalled that the head of Pile 17A is located at 161.19 m NGF, but in this figure, the origin of the axis is located at 162 m NGF, in order to facilitate the comparison with numerical results later.

At first glance, the following observations could be made:

- Between 4 and 11 m depth, the curves are quite smooth.
- The curve between 4 and 5.5 m shows a negative skin friction.
- The upper and lower parts misrepresent the behavior of the pile. The section above 4 m corresponds to the segment of the FOS that has been introduced in the steel tube and consequently it was not aligned with the reinforcing cage (Figure 2.21). The anomalies in the lower section of the curve may be caused by a deviation of the FOS from its original position during the installation of the reinforcing cage or to a variation in the pile's diameter. Therefore, the deformation profiles between 0 and 4 m depth and 11 and 14 m were removed later from the analysis.

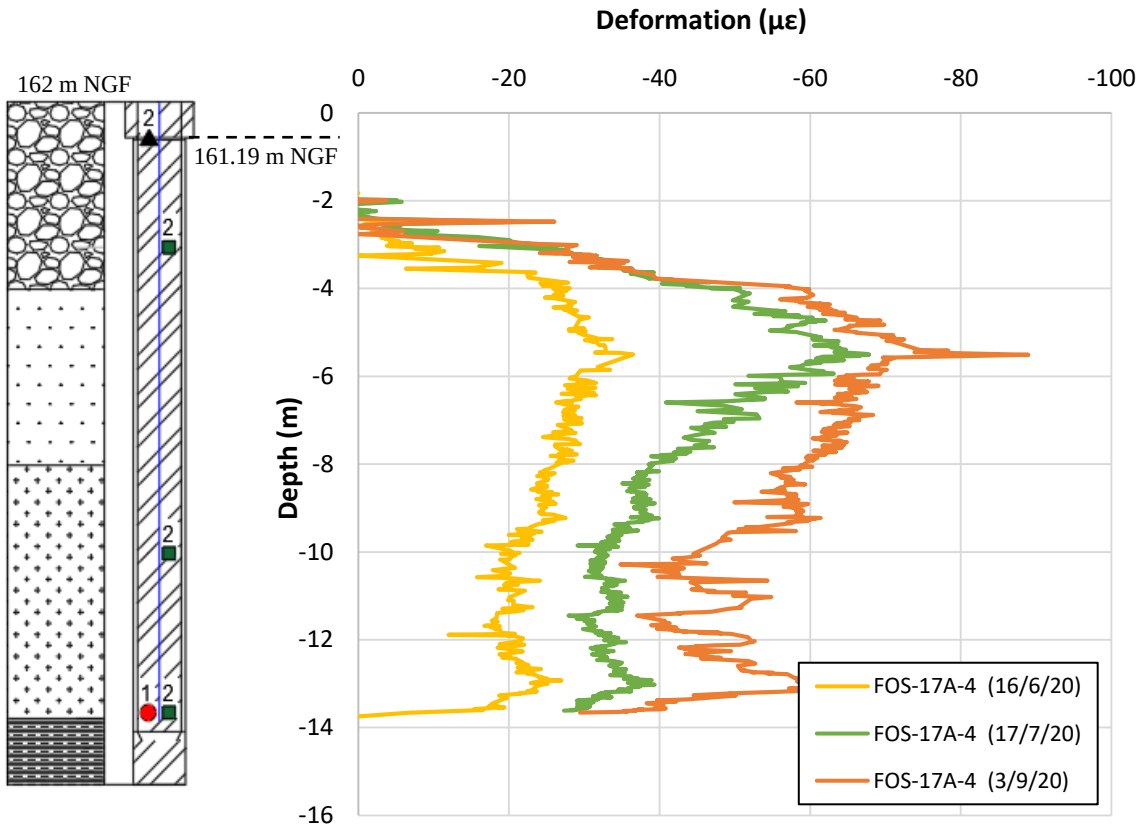

Figure 4.12 Strain distribution obtained from FOS-17A-4

Local strain reductions may be observed in FOS curves which were put down by several authors to the presence of stiffening rings in the reinforcing cage (Bersan et al., 2018; Kania et al, 2020). Besides, a change in the deformation can be also related to a variation in the pile's section. It is in general hard to differentiate between the contribution of the pile stiffness and of the soil friction on the measured strain and it is accentuated when the strain variation is incompatible with the properties of the soil.

The deformations measured by the six ERSGs and the single VWSG of Pile17A were also presented in comparison with the previous curves in Figure 4.13. The values measured by the ERSG were averaged at each level after removing the outliers.

It can be seen that the different sensors give values of the same order of magnitude, showing the good functioning of the sensors.

At the moment of writing, the maximum detected deformation between 26/2/20 and 3/9/20 was around 80 με at 5.5 m depth, which is considered relatively small but conform with the theoretical load and the one measured using the CPCs.

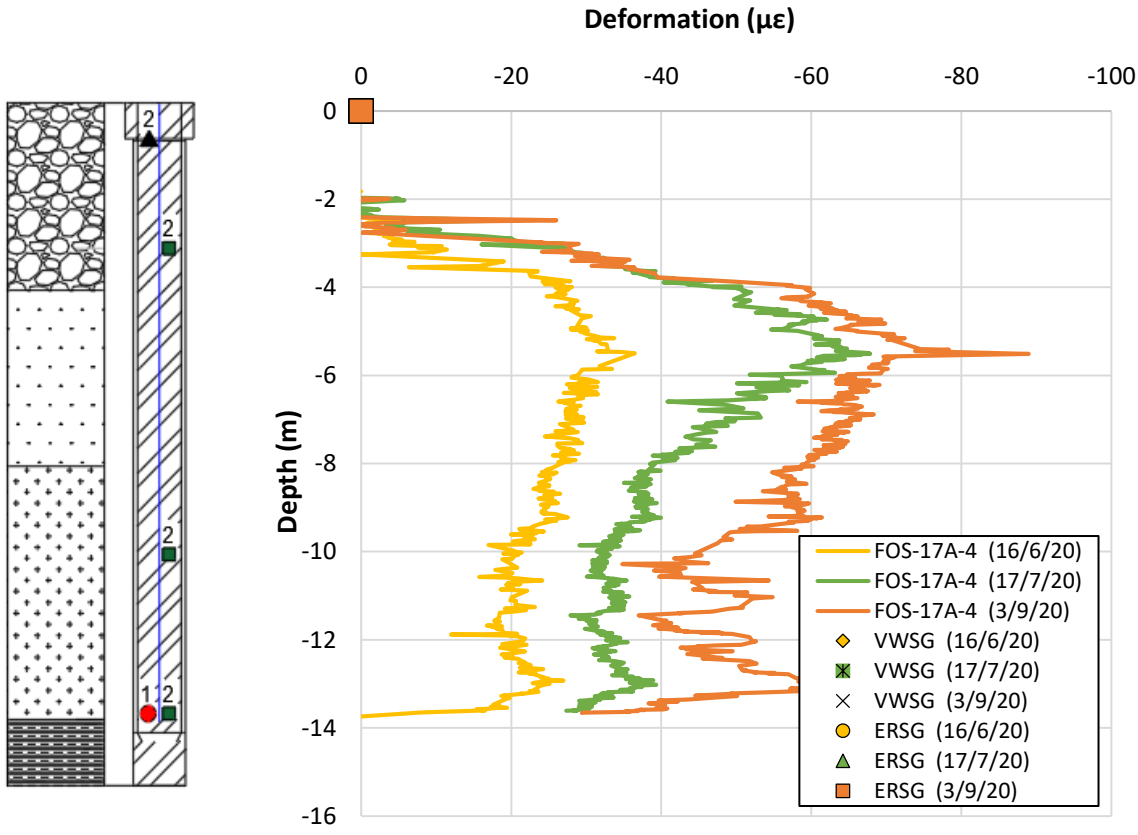

Figure 4.13 Strain measured by the ERSGs and the VWSGs in Pile 17A compared to FOS

On the other hand, all types of deformation sensors were judged to be sensitive to temperature variations. Knowing that at first stages of loading the deformation was found relatively small, a temperature compensation has been required.

3-3-2-2- Temperature compensation and corrected pile deformation measurements

The construction of the tower lasted for almost a year where the ambient temperature had in fact greatly varied. Therefore, a temperature compensation was suggested in order to evaluate the real mechanical deformation even though the deep-ground and consequently the concrete temperature were not expected to change a lot.

This was possible due to the temperature measured in the concrete using the built-in thermistors in the VWSGs, whose accuracy is ±0.5°C within 0 - 50 °C according to the datasheet provided by the supplier. The data collected from all the sensors all along the year are summarized in Figure 4.14. It shows that the temperature span was larger in the first few meters of the pile where $\Delta T = 4.8°C$. However, the sensors installed at higher depths showed a very small variation ($\Delta T = 1 – 2°C$ for z = -10.25 m and $\Delta T < 1°C$ for z = -13.85 m). This is very similar to the temperature variation observed in other projects (Kania et al., 2020).

It should be also noted that the temperature variation along the pile does not follow a unique sense and this can be due to the presence of the water table which may generate convection currents.

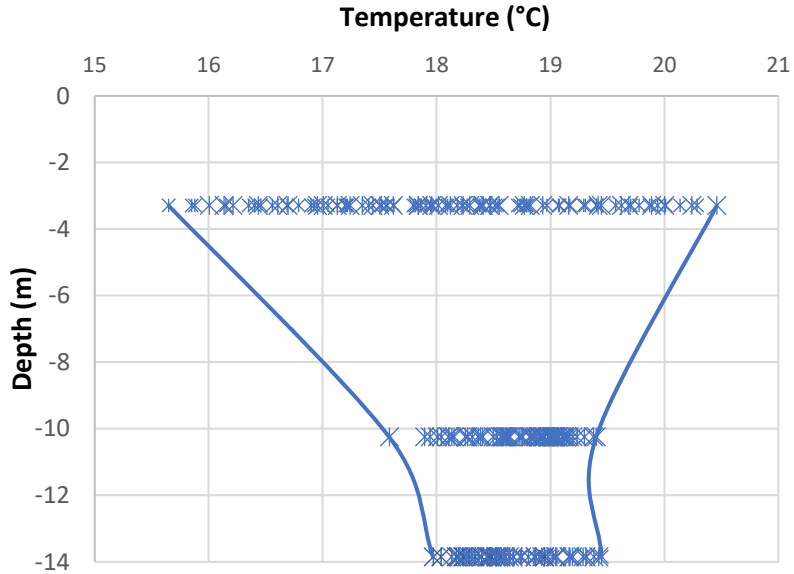

Figure 4.14 Concrete temperature at different depths measured by different gages

The temperature in Pile 17A was evaluated on 16/6/20, 17/7/20 and 3/9/20. The thermal strain and consequently the mechanical strain were calculated for each of the sensors using Eq. 2.13 and 2.20 shown in Chapter 2. For the VWSGs, the thermal strain is calculated based on the temperature variation with respect to the reference measurement (26/2/20), while in the ERSGs, it is estimated according to the actual temperature. The temperature variation can be considered as low to moderate, generating a low thermal strain. The obtained values are summarized in the following tables, knowing that a negative value reflects a temperature drop or a pile compression for the thermal or mechanical strains respectively.

Table 4.8 Thermal strains calculated for the electrical resistance strain gages

Strain gage number	16/6/20		17/7/20		3/9/20	
	Temp (°C)	Thermal strain (με)	Temp (°C)	Thermal strain (με)	Temp (°C)	Thermal strain (με)
ERSG-17A-19-Level1 ERSG-17A-20-Level1	17.3	-1.69	17.4	-1.62	18.3	-1.03
ERSG-17A-21-Level2 ERSG-17A-22-Level2	18.5	-0.88	18.3	-1.01	18	-1.19
ERSG-17A-23-Level3 ERSG-17A-24-Level3	18.8	-0.66	18.7	-0.73	18.5	-0.84

Table 4.9 Thermal strains calculated for the vibrating wire strain gage

Date	VWSG-17A-9-Level3	
	Temperature (°C)	Thermal strain (με)
26/2/20	18.9	0 (Reference)
16/6/20	18.8	-0.20
17/7/20	18.7	-0.37
3/9/20	18.5	-0.68

Table 4.10 Strain values before and after temperature compensation for the electrical sensors

Date	Strain (με)							
	VWSG-17A-9-Level3		ERSG-17A-19-Level1 ERSG-17A-20-Level1		ERSG-17A-21-Level2 ERSG-17A-22-Level2		ERSG-17A-23-Level3 ERSG-17A-24-Level3	
	Before	After	Before	After	Before	After	Before	After
16/6/20	-11.34	-11.54	-27.53	-25.85	-32.02	-31.13	-26.8	-26.12
17/7/20	-16.88	-17.25	-39.61	-38	-43.18	-42.17	-32.44	-31.7
3/9/20	-24.03	-24.71	-34.9	-33.87	-41.8	-40.61	-30.33	-29.48

On the other hand, the thermal input for the FOS measurements can be calculated using Eq. 4.5.

$$\varepsilon_{th}^{z} = \Delta T \, \alpha_p \qquad \text{Eq. 4.5}$$

Where α_p= 10.9 με/°C.

Since the temperature variation is measured at three depths only, it was interpolated along the pile in order to have a continuous variation. These values are then used to calculate the thermal strain so it can be compensated. The thermal input in this case varied along the pile from +12.4 με to – 10.2 με, which is a very high range compared to the measured deformation range (Figure 4.12).

Figure 4.15 shows the strain profile of the FOS before and after the temperature compensation. The deformation measured by the electrical sensors helped in correcting the FOS profile.

Besides, the strain at -14 m was determined using the VWSG measurements. The upper and lower parts of the curves and were substituted by new dashed lines that may represent a possible estimation of the strain in these depths. This was represented in Figure 4.16 which was later used in the comparison with the numerical models.

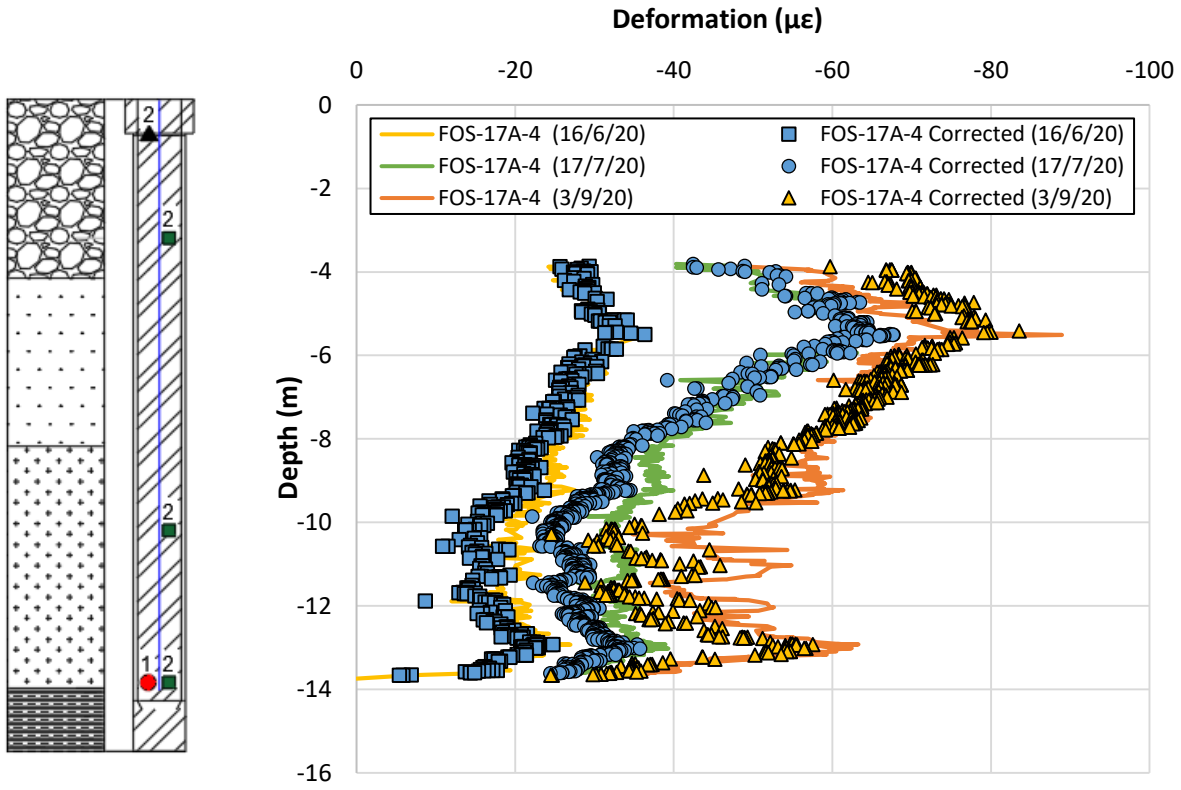

Figure 4.15 Strain distribution before and after temperature compensation

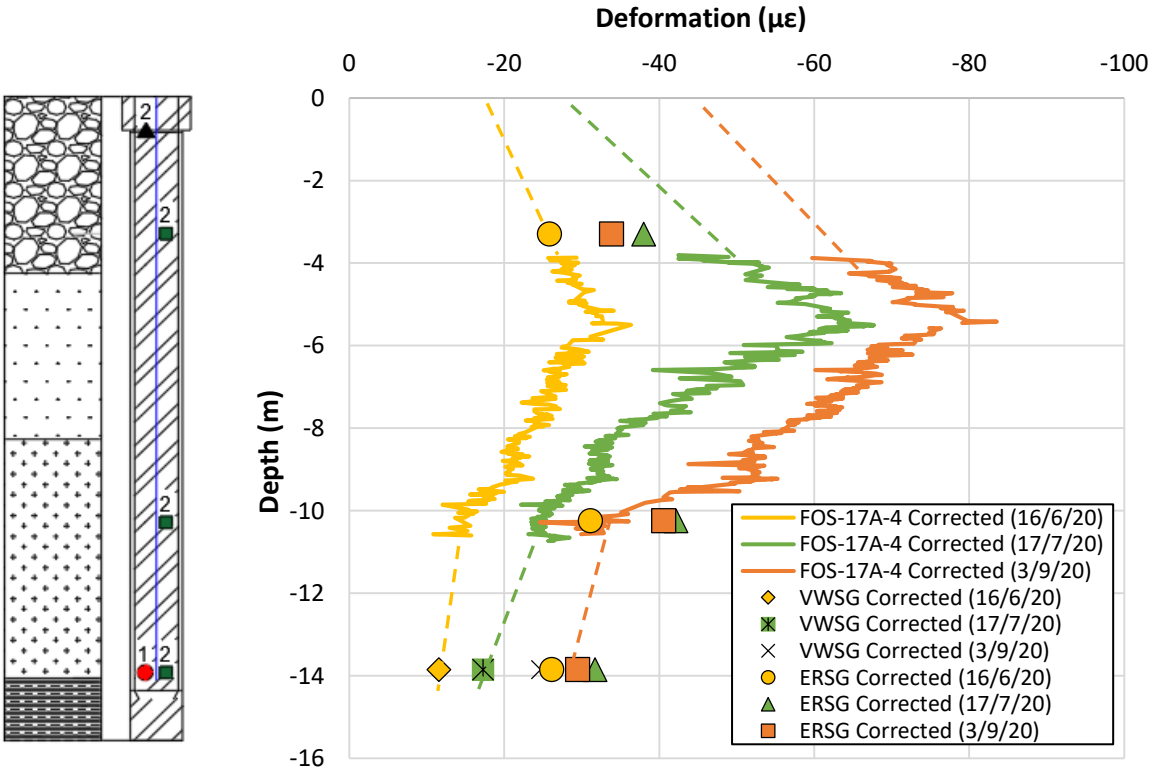

Figure 4.16 Compensated strain as calculated for all the sensors in Pile17A

3-3-2-3- Strain data interpretation

The load transfer curves, also known as resistance-displacement curves $(\tau - s)$ and $(\tau_b - s_b)$ for the pile shaft and tip respectively can be determined from an instrumented pile load test using a procedure described by Bersan et al. (2018). It starts by integrating the strain profile in order to determine the vertical displacement of the pile s(z). This method uses the displacement of the pile's head as measured by other sensors. Since this information was not available in this project, we will limit ourselves here to estimate the mobilized skin friction along the pile.

- The load distribution F(z) is calculated as follows:

$$F(z) = E_p(z)A(z)\varepsilon_m^z(z) \qquad \text{Eq. 4.6}$$

Where E_p is moduli of the pile, $\varepsilon_m^z(z)$ is the compensated strain and A(z) is the cross-section of the pile that may be subject to variations along the pile especially in bored piles, as explained in Chapter 1.

The tip resistance is calculated using this equation for a z = L.

- The mobilized skin friction τ at each depth z may be expressed using Eq. 4.7.

$$\frac{F(z)}{\Delta z} = \pi\, D\, \tau(z) \qquad \text{Eq. 4.7}$$

E_p is calculated as the weighted average of the moduli of concrete and steel as follows:

$$E_p A_b = E_c A_c + E_s A_s \qquad \text{Eq. 4.8}$$

Where the indices "c" and "s" designate the concrete and the steel respectively.

It was shown that given the low value of the steel ratio in the pile, it has almost no-influence on the Young's modulus of the pile. However, the concrete modulus may vary locally in bored piles due to air voids or moisture for example. It might slightly increase with depth or it may even vary with time. It was also shown that the modulus of the concrete may be subject to variations depending on the applied load. It is highest near the head of the pile and is negligible at its base where the stress is not high (Moayedi et al., 2019).

However, due to the lack of information, and as a first approximation, the Young modulus of the pile and the cross-sectional area were considered to be constant along the pile. The load profile shown in Figure 4.17 was calculated using the corrected deformation for a Young modulus of 34.5 GPa. It should be remembered that these values do not represent the total load that can be detected since the zero value corresponds to 26/2/20. Therefore, the theoretical load differences at the pile's head with respect to this date were added to the legend for reference.

In the part above 5.5 m, a negative skin friction was observed. The skin friction mobilized between 5.5 and 10.5 m depth after 26/2/20 were calculated based on the previous procedure and are summarized here in Table 4.11.

It can be noticed that the mobilized load Q_s at the pile shaft (5.5 – 10.5 m) between 26/2/20 and the three specified dates is 815, 1 670 and 1 969 kN respectively.

Table 4.11 Mobilized skin friction along Pile 17A

Depth (m)	16/6/20		17/7/20		3/9/20	
	Load (kN)	τ (kPa)	Load (kN)	τ (kPa)	Load (kN)	τ (kPa)
-5.5	1 395	78	2 692	245	3 290	122
-6	1 245	52	2 222	58	3 057	125
-6.5	1 144	13	2 110	102	2 817	47
-7	1 120	25	1 915	85	2 727	90
-7.5	1 072	50	1 751	181	2 555	83
-8	976	52	1 405	55	2 397	98
-8.5	877	26	1 300	22	2 210	74
-9	827	33	1 258	65	2 069	182
-9.5	765	52	1 133	46	1 720	82
-10	666	45	1 044	12	1 562	126
-10.5	580		1 022		1 321	
Qs = ΔQ	**815 kN**		**1 670 kN**		**1 969 kN**	
τ_{avg}	**43 kPa**		**87 kPa**		**103 kPa**	

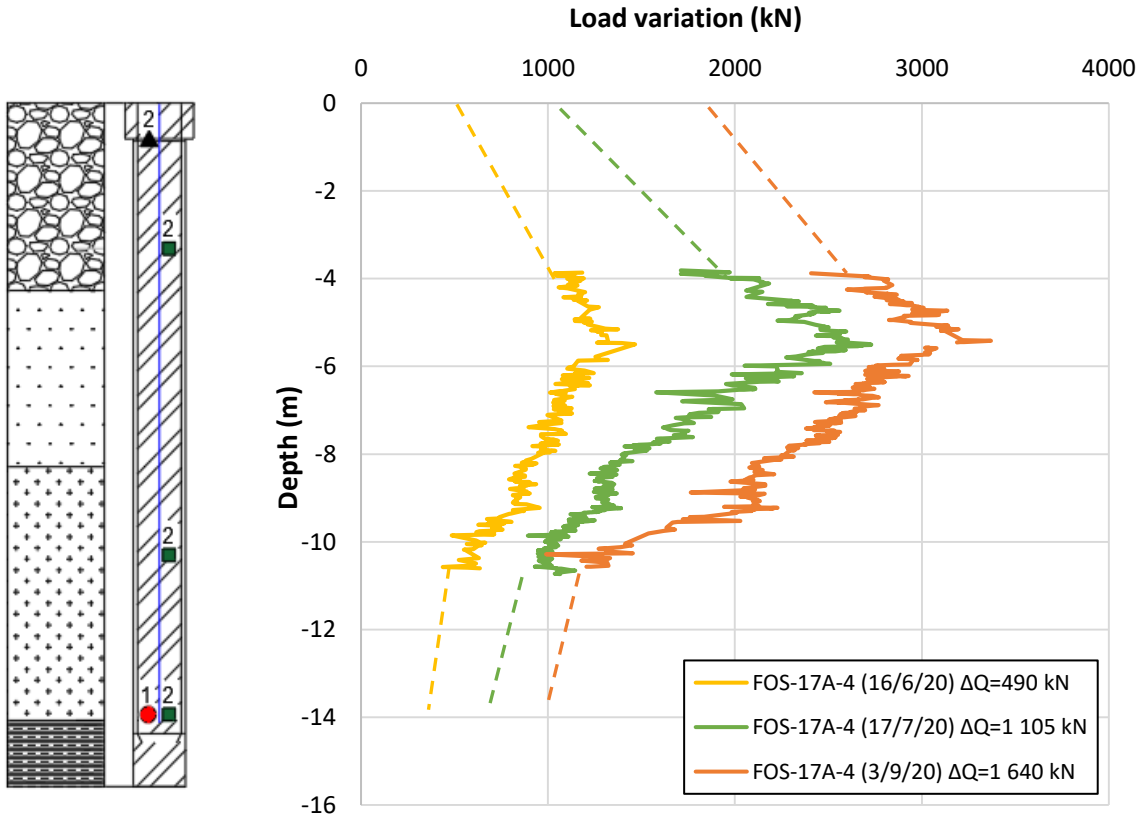

Figure 4.17 Load profile along the Pile 17A

3-4- Measurement of the soil settlement

The settlement of the soil was measured using the six displacement sensors that were connected to the fiberglass rod extensometer. Each of the sensors measured the displacement at a different depth (2, 8, 14, 20, 27 and 35 m) starting from 162.8 m NGF, the level of the manhole.

The measured settlements of the soil over the period extending from 18/9/19 to 1/10/20 are presented in Figure 4.18 and Figure 4.19. This period marks the beginning and the end of the steel structure installation and it also includes the concrete floor pouring and some facade works. The sensor installed at 35 m was considered as a reference point to the others the reason why it is not shown in Figure 4.18. It should be noted as well that the dates indicated in Figure 4.19 designate the floor pouring of the corresponding level.

The maximum settlement is of the order of 1.6 mm, measured above 8m depth. However, at higher depths, the settlement is less than 0.5 mm. This is predictable because of the small applied load. On the other hand, the settlement detected at 8 m should be lower than the one measured with a shallower sensor. The observed settlement difference between these two sensors is due to the sensor resolution (±0.6 mm). Besides, the profile shown in Figure 4.18 allows to validate the hypothesis of a negative skin friction especially that the settlement of the soil, despite its low value, is higher at shallow depths.

In this thesis, the pile's settlement was not measured in a direct way. Instead, a topographic survey of the site was carried out showing a vertical settlement of the tower of about 3 ± 1mm between September 2019 and July 2020. The expected maximum settlement was previously estimated by the company using a numerical model. They showed a value of 15 mm at "SLS Quasi-permanent", which goes beyond the current measurements.

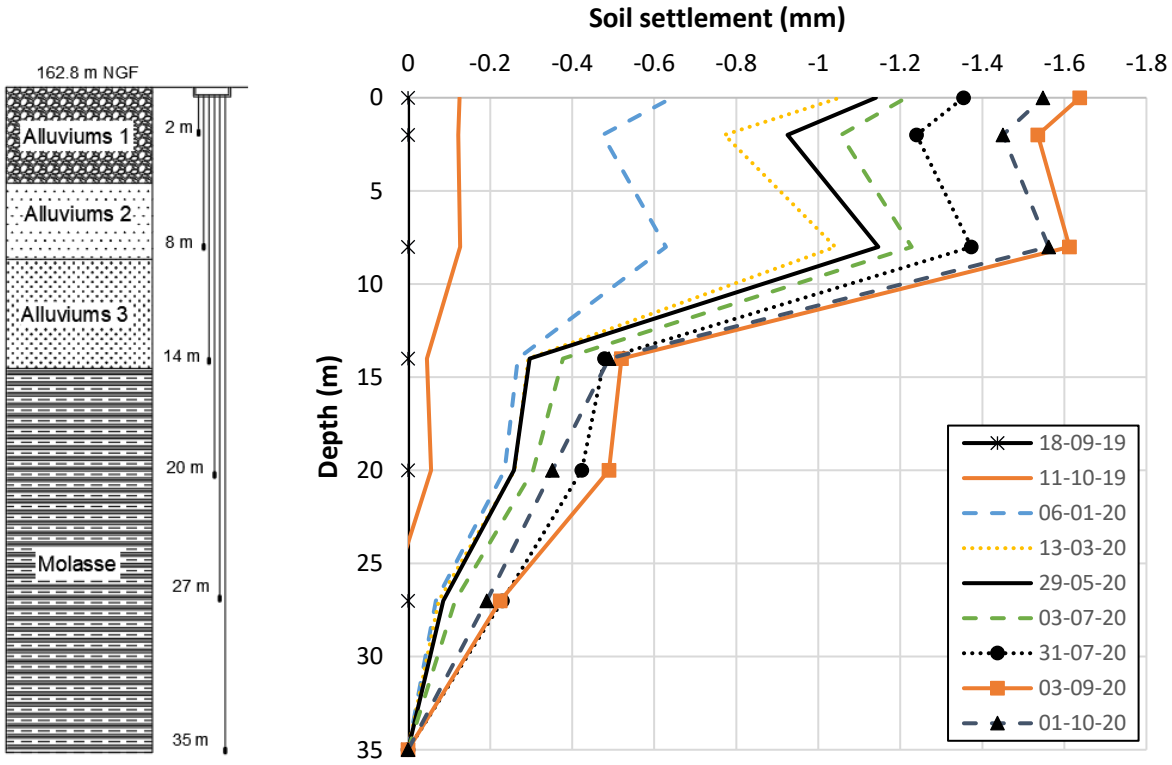

Figure 4.18 Measured soil settlement at different dates

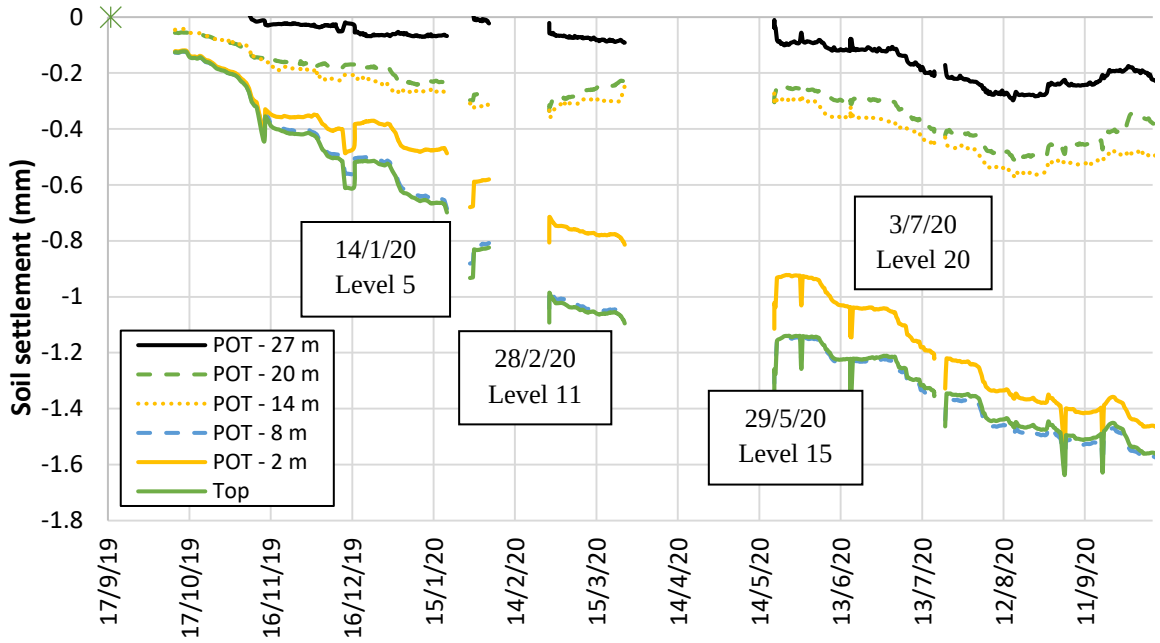

Figure 4.19 Measured soil settlement during the construction of the steel structure

4- Instrumentation performance and lessons learned

4-1- Instrumentation performance

Two aspects of the instrumentation performance are evaluated in this paragraph: the instruments durability and a comparison between the responses of two instruments of the same type against any variation. The former was assessed by making a comparison between the number of instruments installed and those remaining at the end of the project and the latter by studying the performance of all types of instruments with respect to the load variation.

In general, there is a high possibility to lose some sensors during any of the installation stages, especially when it is done in the field. However, 100% of the electrical sensors have survived during the casting of the piles, even though the CFA technique was used. All the FOSs, on the other hand, were severely damaged because the site personnel had to backfill on the top of the piles due to the lack of space. Therefore, the FOSs were either broken or pinched. Besides, during the construction of the transfer concrete structure, one optical fiber was cut and one sensor from each type (ERSG, VWSG and CPC) failed to survive due to a slippage of cables.

Unfortunately, by the time the optical fiber fusion splicer was provided, the transfer structure and a part of the concrete slab were already constructed without verifying the fiber optic cables and the connection with the jumper cables used to bring the optical connector to the electrical cabinet located in the EDF tower. Months later, a splicing of the fibers was performed and only one sensor out of the 6 installed could be saved: the one in Pile 17A.

Aside from having the cables broken accidentally on site, it was also expected to see some malfunctions during the data collection. The final assessment is summarized in Table 4.12.

Table 4.12 Final assessment of the sensors installed in the piles

Stage	VWSG	ERSG	FOS	CPC
Quantity (start of construction)	14	36	6	18
Quantity (end of construction)	10	36	1	15
Quantity (good performance)	9	33	1	15
Loss (%)	35 %	8%	83%	16.7%

This loss was relatively high but fortunately, the redundancy implemented in this project allowed ultimately to have enough measurements and thus relevant results.

On the other hand, all the types of sensors showed a good performance. The chosen frequency of readings was enough not to miss any event during construction of the tower. They were all able to detect the load variations, showing a compatibility between the measured load and deformation in the pile. Moreover, the displacement sensors installed along with the fiber glass extensometer had a measuring range a bit higher than the expected settlement.

4-2- Lessons learned from the instrumentation

This instrumentation has taught us that even if all precautions were taken during the installation of the sensors, errors might occur that can cause the damage of the sensors and thus lead to important problems, especially that the big number of people who intervene usually on site is uncontrolled.

On the other hand, environmental problems can cause unexpected damages to the sensors. The fiber optic connections, for example, could not survive the extreme temperature and pollution conditions of the construction site and therefore welding work was necessary to replace them. For future projects, these should be covered with a metallic tube during the construction. On the other hand, few comments can be made on the installation of these sensors. They have to be firmly attached to the reinforcing cage to avoid any deviation during the installation.

The cables that correspond to the electrical sensors were also cut and welded several times due to the tight space. Therefore, a minimized length should be provided for the time of the construction. These can be welded to extension cables later minimizing consequently the risk of losing sensors.

It is also noteworthy to mention the importance of the communication with the construction company, in order to avoid delays, or any change in the schedule.

5- Validation of the numerical models with respect to experimental results

In this section, the parameters calibrated from the laboratory tests in the previous sections were used with the aim to obtain the same behavior shown within the instrumentation. The numerical models presented in the following studies are based on the geometries presented in Chapter 2 (Section 5-2-1 for single pile models and Section 5-2-3 for the global models).

5-1- Analysis of single pile model

The lack of experimental tests for the alluviums made it difficult to calibrate a PH model and find the parameters in need. Therefore, an elastic perfectly plastic model with a Mohr-Coulomb failure criterion was adopted for the three layers of alluviums. The Young modulus was defined from the equations used in Chapter 3 (Table 3.1 and 3.33). Besides, the shear box tests performed on alluviums samples made us conclude the following values for the strength parameters:

- Friction angle: $\phi = 36°$
- Cohesion: c = 5 – 25 kPa which may vary from a layer of alluviums to another depending on the percentage of fine particles.

On the other hand, the triaxial and oedometer tests performed on the molasse layer allowed to calibrate a PH model that with the parameters presented in Table 4.4.

In this regard, several combinations of constitutive models and parameters for the alluviums and the molasse were tested. They are as follows (Table 4.13):

Table 4.13 Summary of the parameters used in the single pile analysis

Layer	Model 4.1	Model 4.2	Model 4.3	Model 4.4
Alluviums				
➢ **Law**	Elastic perfectly plastic model with a MC failure criterion			
➢ **Parameters**	Parameters of Table 3.1: • c = 50 kPa • $\phi = 35° / \psi = 5°$ • Young modulus: $\begin{cases} 135\ MPa & Alluv.1 \\ 20\ MPa & Alluv.2 \\ 150\ MPa & Alluv.3 \end{cases}$	• c (see note below) • $\phi = 36° / \psi = 5°$ • $E = \begin{cases} 245\ MPa & Alluv.1 \\ 32\ MPa & Alluv.2 \\ 264\ MPa & Alluv.3 \end{cases}$ Note: $\begin{cases} Model\ 4.2-a/4.3-a/4.4-a: & cohesion\ c = 5\ kPa \\ Model\ 4.2-b/4.3-b/4.4-b: & cohesion\ c = 25\ kPa \end{cases}$		
Molasse				
➢ **Law**	Elastic perfectly plastic model with a MC failure criterion	Elastic perfectly plastic model with a MC failure criterion	Plastic Hardening Model	Plastic Hardening Model
➢ **Parameters**	• c = 50 kPa • $\phi = 35° / \psi = 5°$ • E = 300 MPa	• c = 25 kPa • $\phi = 35° / \psi = 5°$ • E = 375 MPa *(shaft)* • E = 326 MPa *(tip)*	Parameters inspired from Model 4.2 (Table 4.14)	Parameters obtained from the experimental tests (Table 4.14)

Table 4.14 Parameters used for the molasse in Model 4.3 in Model 4.4

Parameters	Model 4.3 (a and b)	Model 4.4 (a and b)
c (kPa)	25	25
ϕ (°)	35	35
ψ (°)	5	5
$\mathbf{E_{50}^{ref}}$ **(MPa)**	375 (shaft) / 326 (tip)	12.46
$\mathbf{E_{oed}^{ref}}$ **(MPa)**	= E_{50}^{ref}*	17
$\mathbf{E_{ur}^{ref}}$ **(MPa)**	= $3E_{50}^{ref}$	250
$\mathbf{R_f}$	0.9*	0.8
m	0.5	0.5
$\mathbf{\nu_{ur}}$	0.2*	0.2*
Knc	0.43*	0.43*
OCR	1	4
** Default values in FLAC3D/ Plaxis2D*		

The load settlement curves of Pile 17A obtained from the previous models are shown in Figure 4.20 for a load that ranges between 0 – 5 000 kN, allowing to have the following conclusions:

- As expected, the models that used a PH for the molasse showed a lower settlement in the elastic range. This is caused by the used stress-dependent stiffness. The choice of E_{50}^{ref} is certainly important in this case and it shows by comparing Model 4.3 and 4.4. The former had a much lower settlement caused by the higher stiffness values.
- By comparing the "a" and "b" versions of each model, it can be deduced that the cohesion of the alluviums played an important role in the load settlement curves only after 3 000 kN.
  This effect was found accentuated beyond 5 000 kN, which is not our range of study. A lower cohesion in Model 4.3-a and Model 4.4-a, for example, generated a higher settlement than in the "b" version of the same models.
- The models 4.2-b, 4.4-a and 4.4-b gave curves that are close to the one obtained in Foxta using the load transfer method.

Although the instrumentation was not carried out in the framework of a pile load test, it was compared to the single pile models performed in FLAC3D assuming that it can give an idea about the behavior of the soil and the foundations.

This comparison was made on the basis of the measurements taken between 26/2/20 and 3/9/20. Here is a reminder of the main findings from the instrumentation of Pile17A:

- The applied load measured on the 26/2/20 was 1 011 kN
- The applied load measured on the 3/9/20 was 2 960 kN

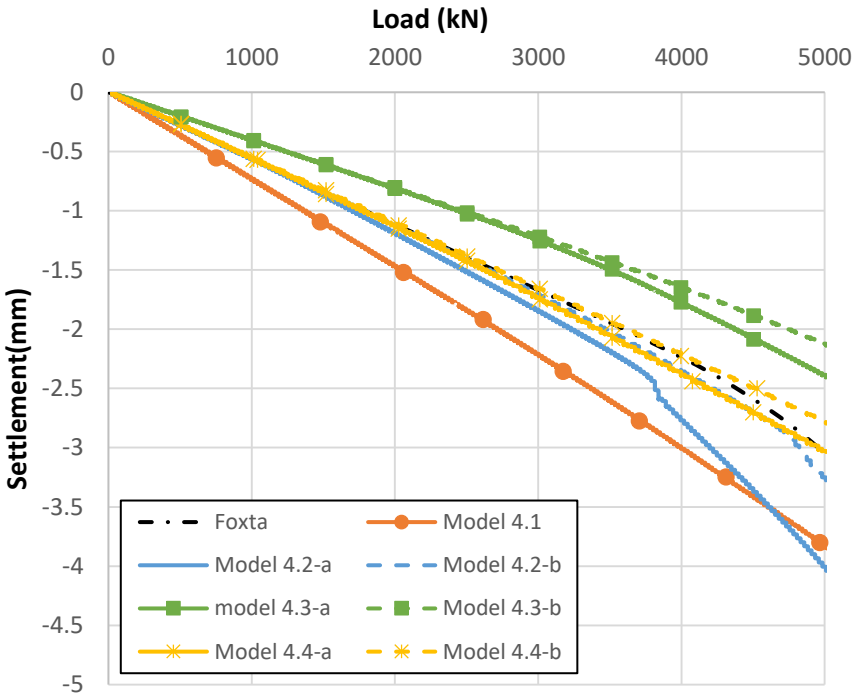

Figure 4.20 Load settlement curves of Pile 17A obtained for different constitutive laws and parameters

The same models detailed previously were used in this comparison. The strain distribution measured by the FOS between these two dates was compared to the strain estimated in FLAC3D models, using the same loads. It should be noted that in the numerical models, the deformation was estimated by considering the difference between the strain profile at 2 960 kN and the one at 1 011 kN in order to ensure a better comparison with the in-situ measurements.

The results are shown in Figure 4.21. The following observations could be done:

- All the curves in Figure 4.21 show approximately the same range of deformation given in micro-deformation "με". Therefore, the numerical model with the chosen constitutive law and parameters can be considered appropriate for the given load but can only be validated when higher loads will be applied on the head of the piles, which is not happening in the framework of this thesis.
- It should be also remembered that Model 4.1 employs the same parameters also used by the construction company during the design phase of the piles. These parameters are safe and thus the settlement and the deformation of the piles may be overestimated.
- This result validates the choice of the concrete's Young modulus chosen in FLAC3D. According to Figure 3.20, a lower modulus could have resulted in a higher deformation in the upper section of the pile in particular.
- At this small load, the cohesion and the friction angle do not strongly affect the response of the pile. Therefore, it is not yet possible to make a choice for the strength parameters of the alluviums and the molasse.
- The load mobilized at the shaft of the pile Q_s between -5.5 and -10.5 m varies from 300 to 550 kN from Model 4.1 to 4.4-b while in reality it reached 1 969 kN as shown in experimental results.

- The negative skin friction could not be observed in the numerical models. This was expected since the pile was considered to be isolated with no stress applied on the adjacent soil.
- It can be seen that the measured profiles do not respect the initial soil layers defined earlier and used in the numerical models. While it is true that the transition between the alluviums 3 and the molasse could not be seen due to the lack of instrumentation at this altitude, it was not shown neither between the other layers.
  For example, it can be noticed that the alluviums 2 which was supposed to have bad characteristics compared to the others is not shown in the profile of the FOS.
  This is despite the fact that this layer has been observed in the pile monitoring records between 6 and 10 m depth and in the samples extracted from the sonic drill as well.
- The difference between the numerical and the experimental curves may be caused by a wrong evaluation of the characteristics of the heterogeneous soil. In fact, the maximum unit skin friction assigned to the alluviums 2 in FLAC3D was 61 kPa (as shown in Figure 4.22) based on the standards and on other soil characteristics, while the actual mobilized skin friction was estimated in the range 47 – 182 kPa only between 26/2/20 and 3/9/20 according to Table 4.11.

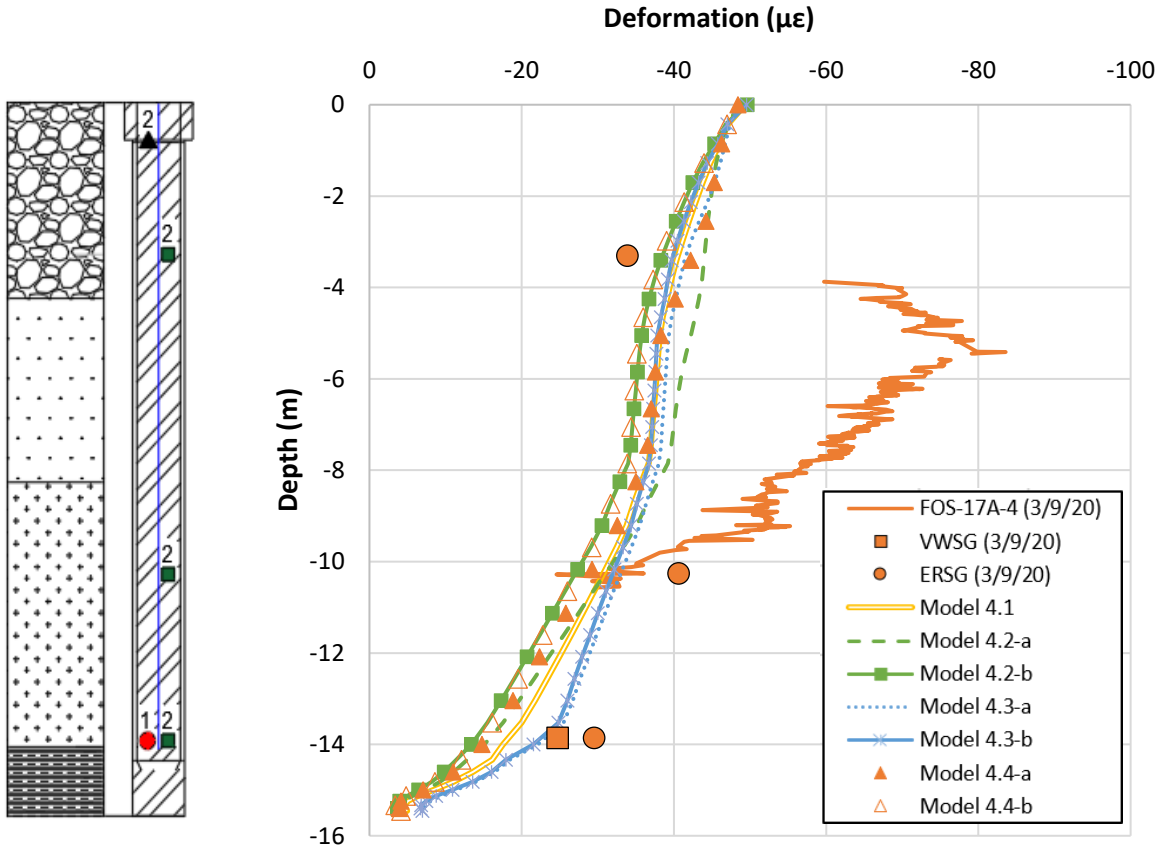

Figure 4.21 Comparison between the numerical and in-situ deformation curves

The load profile can be also estimated as in Eq. 4.6 by using a Young modulus of 34.5 GPa and a diameter of 1.22 m.

An envelope of the skin friction obtained in the previous seven FLAC3D models is presented in Figure 4.22 together with the skin friction calculated from the deformation measurement of the FOS.

It is noticed that the negative skin friction is not reflected at the top of the pile since the surrounding pile is not loaded. In addition, the overall mobilized skin friction is underestimated in the numerical models which means that the parameters are not well chosen.

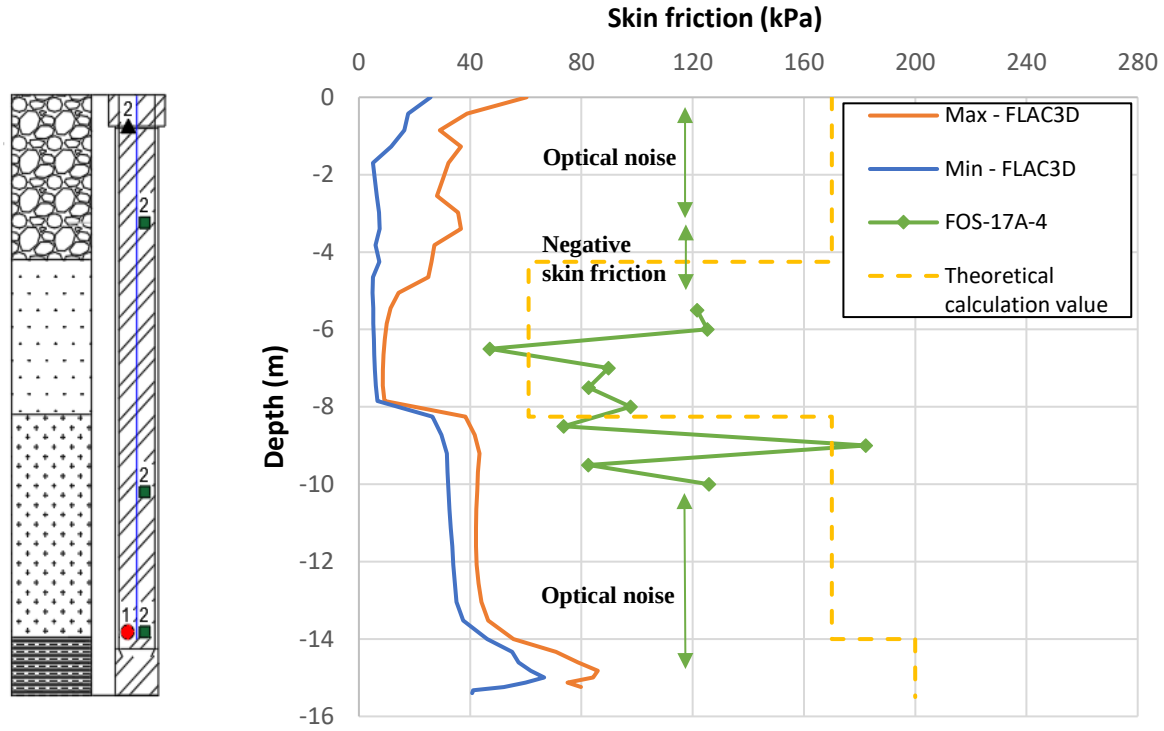

Figure 4.22 Mobilized skin friction as a function of depth between 26/2/20 and 3/9/20

In an attempt to improve these models, an additional stress was applied on the top of the soil adjacent to the pile in order to force a bigger displacement and thus create a negative skin friction. The main objective was to understand if this behavior can be due to a load transfer from the concrete slab and the transfer structure. Since there is no specific rule, several values were tried and a value of 30 kPa was found sufficient to modify the response of the pile by showing a negative skin friction in the upper 5.5 m and by reaching approximately the same deformation and soil settlement observed experimentally. The new deformation and skin friction profiles are presented in the following figures.

Figure 4.23 showed that the new models are in closer agreement with the real behavior of the pile. In particular, the models 4.2-a and 4.4-a can be associated together and it is the same for 4.2-b and 4.4-b. The deformation profile is modified and is now marked by a maximum value at 5.5 m depth. This value varies from 54 με in Models 4.2-b and 4.4-b to 66 με for Model 4.1 (in absolute terms).

The negative skin friction observed between 0 – 5.5 m is also shown in Figure 4.24. The mobilized skin friction load between 5.5 and 10.5 m also increased with respect of the previous models and reached 730 kN but it is still lower than the in-situ values shown in green.

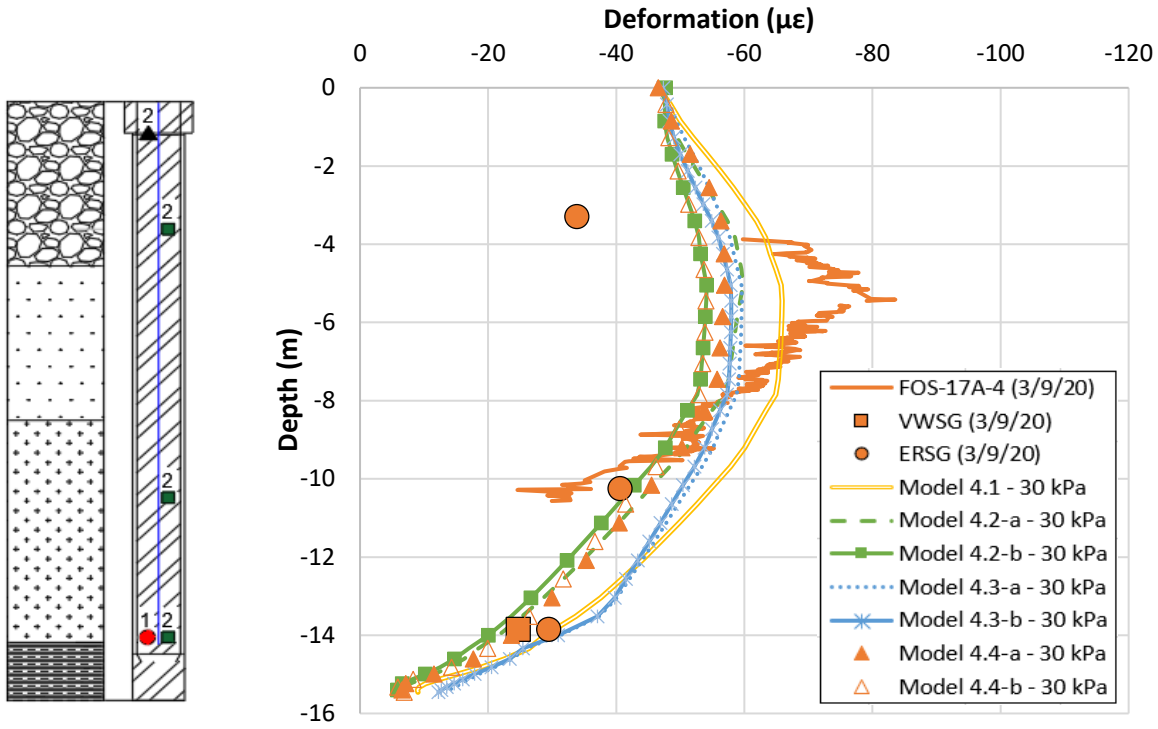

Figure 4.23 Comparison between the experimental and corrected numerical deformations

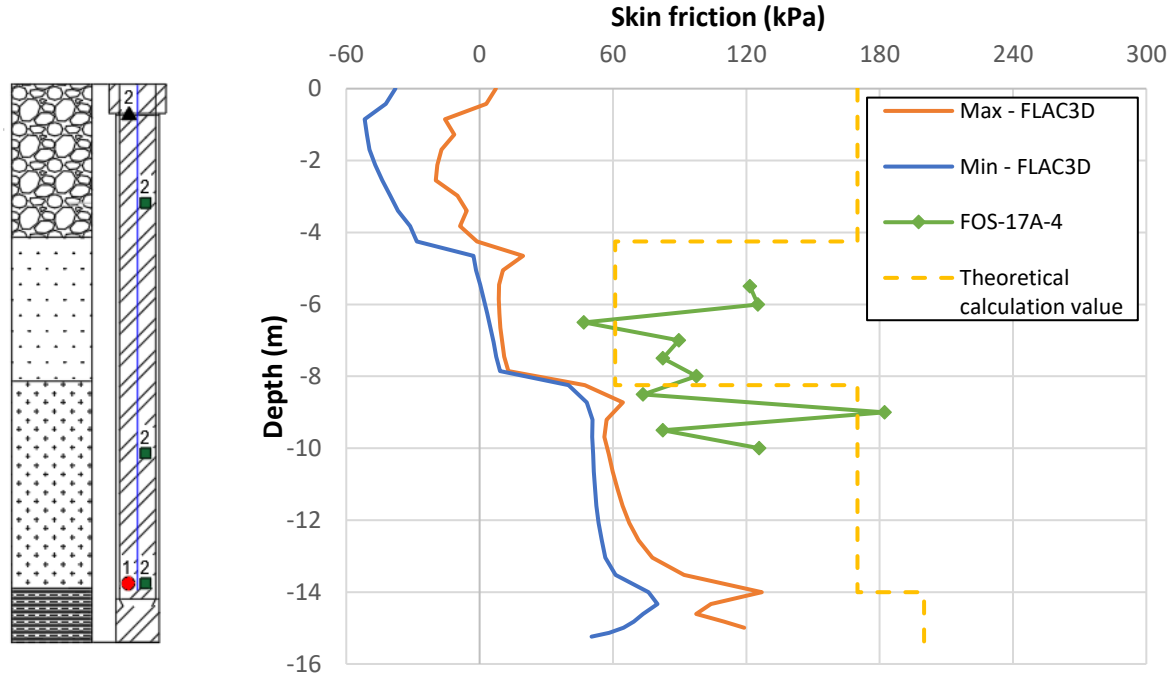

Figure 4.24 Corrected mobilized skin friction as a function of depth between 26/2/20 and 3/9/20 after applying a surface load on the soil

Figure 4.25 shows the settlement of the soil at the location of the fiberglass rod extensometer before and after applying the surface load on the top of the surrounding pile.

It can be seen that by performing this correction, the soil settlement increased significantly on the upper levels to match the in-situ settlement measured using the six displacement sensors. Note that the displacement sensors have a resolution of ±0.6 mm which can explain the observed differences.

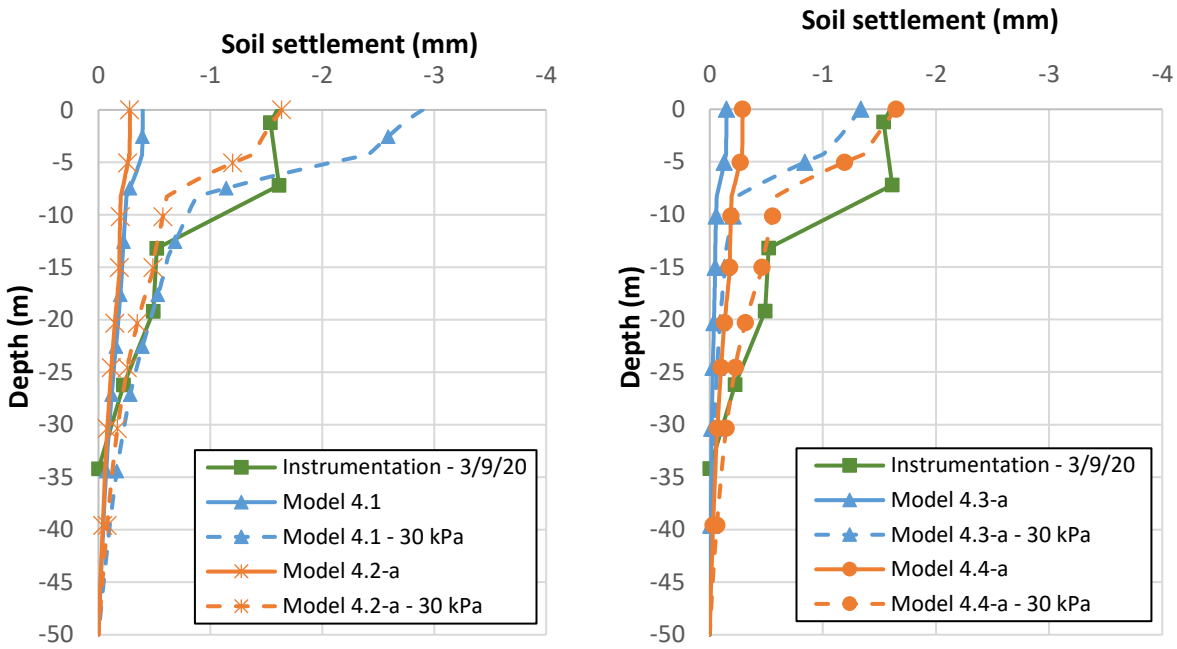

Figure 4.25 Numerical and in-situ soil settlement with respect to the depth

In conclusion, further investigations needed to be conducted in order to validate or eliminate any of the models. This will be done by implementing the same sets of parameters into the global model and by comparing with the in-situ instrumentation measurements. The results are shown later in paragraph 5-3.

5-2- The prediction of the foundations' behavior

In the early stages of the project, the soil parameters were compared to those obtained during the design of the nearby structures such as the "Oxygene" tower constructed in 2007. In "Oxygene", the settlement was estimated at 22 mm for "SLS Quasi-permanent" combination. By analogy with Silex[2], the settlement was estimated at 15 mm, with an additional 10 mm due to long term considerations by using the same parameters.

During the course of this thesis, a study was also performed in parallel by the construction company (ECC) in 2019 in order to predict the behavior of the foundation and the soil using the finite element software Plaxis3D. The Plastic Hardening model was assigned to all the soil layers using different parameters. Two possible configurations were assumed (k_{max} and k_{min}) using different stiffnesses of the foundations and different soil moduli. The results of this analysis were compared to those obtained from FLAC3D models

in this thesis. Therefore, the case with "k_{max}" was only considered in this comparison, which uses parameters that are similar to those defined in Table 3.1, but this time with a PH model (and not MC model). They are summarized as follows (Table 4.15):

Table 4.15 Parameters of the Plaxis3D model used by the construction company ECC

Soil layer	$E_{50}^{ref} = E_{oed}^{ref}$ (MPa)	E_{ur}^{ref} (MPa)	γ (kN/m³)	c (kPa)	ϕ (°)	ψ (°)
Alluviums 1	135	405	20	50	35	5
Alluviums 2	20	60				
Alluviums 3	150	450				
Molasse	300	900				

The comparison was drawn up on the basis of the loads calculated at different combinations of actions. In summary, the 3D model performed by the company showed the following global settlements:

- SLS QP: 8 – 11 mm
- SLS Char. Wind (South – North direction): 10.4 – 13.5 mm
- SLS Char. Wind (North – South direction): 10 – 14.51 mm

The loads and settlements values of the piles 17, 18 and 19 obtained by the construction company model performed in Plaxis3D are summarized in Table 4.16 for different load combinations, since they are the only piles involved in the global model in FLAC3D.

Table 4.16 Load and settlement at the piles' heads for different combination with k_{max} configuration (according to the construction company models)

Pile No	Coupled towers					
	SLS QP		SLS Char. Wind: South – North direction		SLS Char. Wind: North – South direction	
	Load (kN)	Settlement (mm)	Load (kN)	Settlement (mm)	Load (kN)	Settlement (mm)
Pi17	6 705.9	-	7 720.1	13.25	8 190.2	14.46
Pi18	5 528.4	-	6 397.0	12	6 988.9	13.4
Pi19	5 504.1	-	6 295.9	11.55	7 237.3	13.19

In the following, these settlement values will be confronted with FLAC3D results performed in this thesis.

The global models presented here and in the following paragraph had the same simplifying hypotheses presented in Chapter 3 except for the applied load. In fact, in these models, we tried to apply the actual load on each of the piles for a better representation of the reality. This led to a decrease in the settlement of all the piles due to the reduction of the applied load.

The transfer structure has not been modeled here since the loads were defined at the head of the piles without any indication about the one on the TS, and obviously, it cannot be equal to the sum of the loads in each

group as shown in the previous chapter. The water table was not modeled and the value of the Young modulus of the concrete was 34.5 GPa for short term settlements. Corrections can be made to consider other possible options.

Firstly, a "Global Model 1" was performed which has exactly the same parameters in the previous isolated pile study (Table 3.1). In Figure 4.26, the load settlement curve was compared with the curves of single pile and pile group models as shown in Chapter 3.

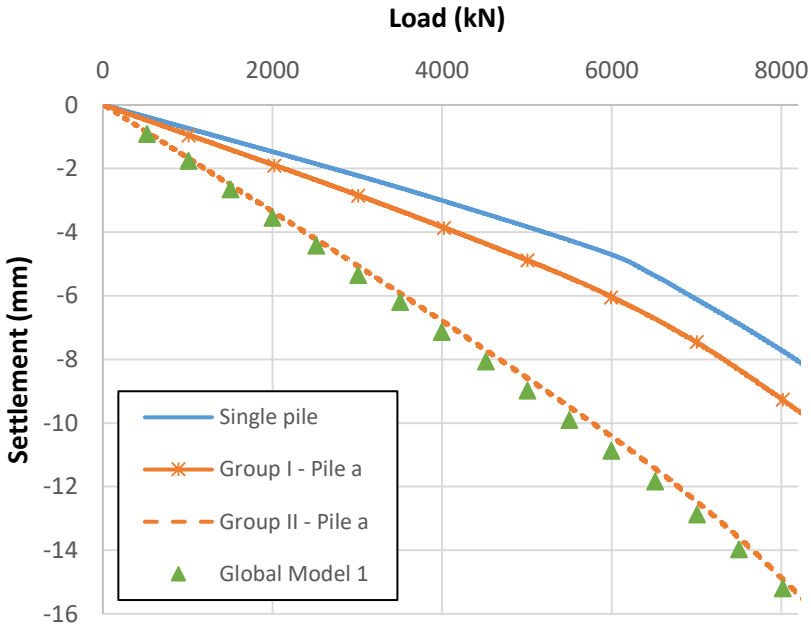

Figure 4.26 Load settlement curves obtained from different geometries

The global model considers the group effect between the piles; thus, the settlement of each pile is the result of its own axial load and the load applied at the nearby piles. It is known that in a pile group the ultimate shaft resistance is reduced leading to a higher tip load and a higher settlement.

It can be noticed that the pile in "Pile Group II" showed the same behavior as in the Global model which means that the symmetry axes implemented in that model allowed to represent the group effect that occurs in case of many surrounding piles.

On the other hand, these results were compared with Plaxis 3D results that were presented earlier (Table 4.16) knowing that the models have the same parameters in an attempt to compare the two different numerical methods (FDM and FEM). However, it should be noted that the FEM results were obtained from Plaxis3D using a Plastic-Hardening Model. Two points were added in orange to the curves, which correspond to two different loads from Table 4.16 (SLS Char.). The results are shown in Figure 4.27.

Although the two added points match well with the Global model 1 performed in FLAC3D using the same parameters, no conclusion can be drawn here because the FEM model took the loading history of the site and the nearby structures into account.

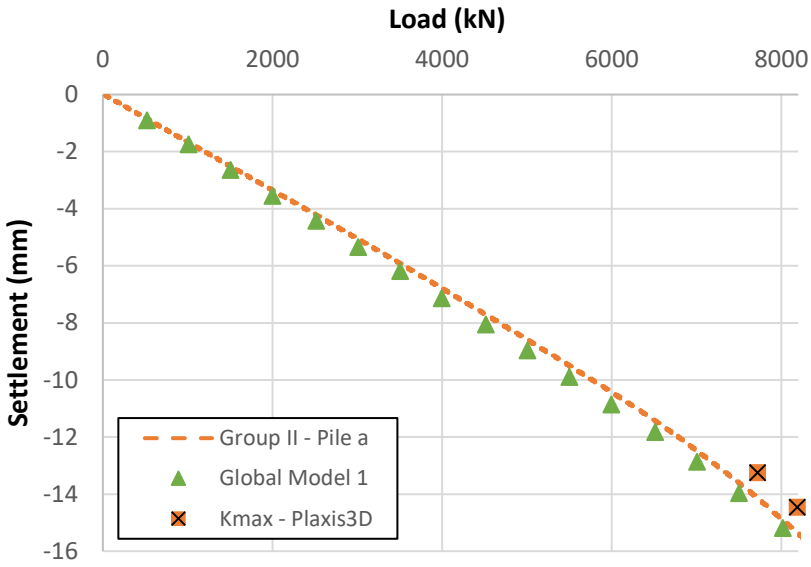

Figure 4.27 Load settlement curves in FLAC3D compared to Plaxis3D results

5-3- Analysis of the global model in FLAC3D

Identically to the analysis in Section 5-1, different sets of parameters and constitutive laws were tested. Along with Model 4.1, only the models "a" with a cohesion equal to 5 kPa were chosen since at a load smaller than 3 000 kN, the cohesion had no influence.

The characteristics of these models are shown in Table 4.17.

Table 4.17 Parameters used in the analysis of the "Global models"

	Global model 4.1	**Global model 4.2-a**	**Global model 4.3-a**	**Global model 4.4-a**
Alluviums				
➢ **Law**	Elastic perfectly plastic model with a MC failure criterion			
➢ **Parameters**	Parameters of Table 3.1: • c = 50 kPa • ϕ = 35° / ψ = 5° • Young modulus: • $\begin{cases} 135\ MPa & Alluv.1 \\ 20\ MPa & Alluv.2 \\ 150\ MPa & Alluv.3 \end{cases}$	• c = 5 kPa • ϕ = 36° / ψ = 5° • $E = \begin{cases} 245\ MPa & Alluv.1 \\ 32\ MPa & Alluv.2 \\ 264\ MPa & Alluv.3 \end{cases}$		
Molasse				
➢ **Law**	Elastic perfectly plastic model with a MC failure criterion	Elastic perfectly plastic model with a MC failure criterion	Plastic Hardening Model	Plastic Hardening Model
➢ **Parameters**	• c = 50 kPa • ϕ = 35° / ψ = 5° • E = 300 MPa	• c = 25 kPa • ϕ = 35° / ψ = 5° • E = 375 MPa *(shaft)* • E = 326 MPa *(tip)*	Parameters inspired from Global model 4.2 (Table 4.14)	Parameters obtained from the experimental tests (Table 4.14)

In this analysis, the loads measured using the CPC on the 3/9/20 were applied on the head of the piles (2 960, 2 435 and 2 750 kN for the piles 17, 18 and 19 respectively).

The largest part of the soil mass remains in the elastic domain. The vertical displacement contours of the four models are presented in Figure 4.28 and Figure 4.29, with the detailed values shown in Table 4.18. The pile 17A, which is the most loaded among the others, is subjected to the largest settlement. The comparison between the four models shows that the displacement is bigger in Global model 4.1 (5.2 mm) while it is the lowest in Global model 4.3-a (1.9 mm) which is very consistant with the parameters chosen for the models.

It can be noticed that there is no significant difference between Global model 4.2-a and 4.4-a. This needs to be verified for higher loads.

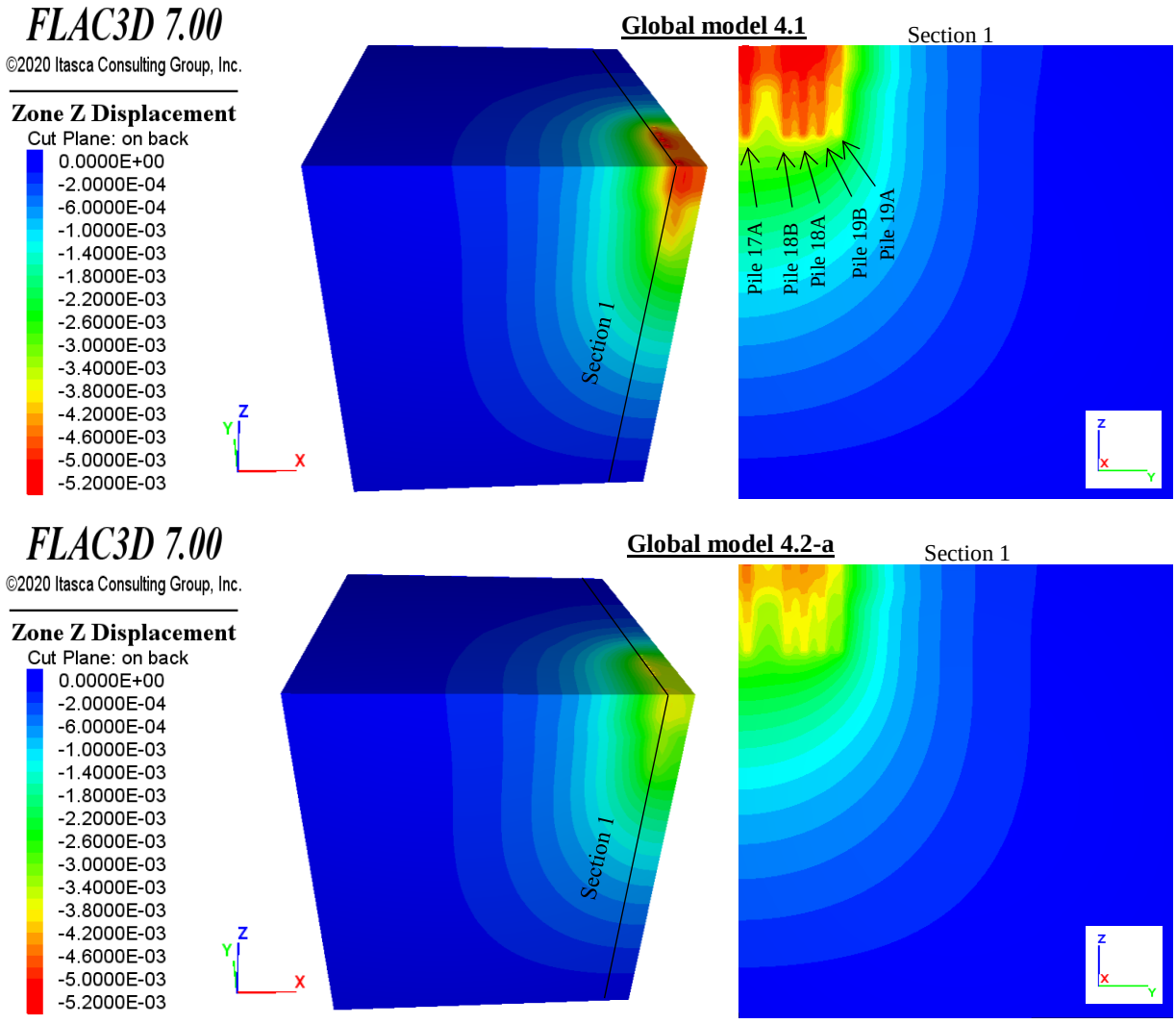

Figure 4.28 Displacement contours at the end of the calculation for Global models 4.1 and 4.2-a

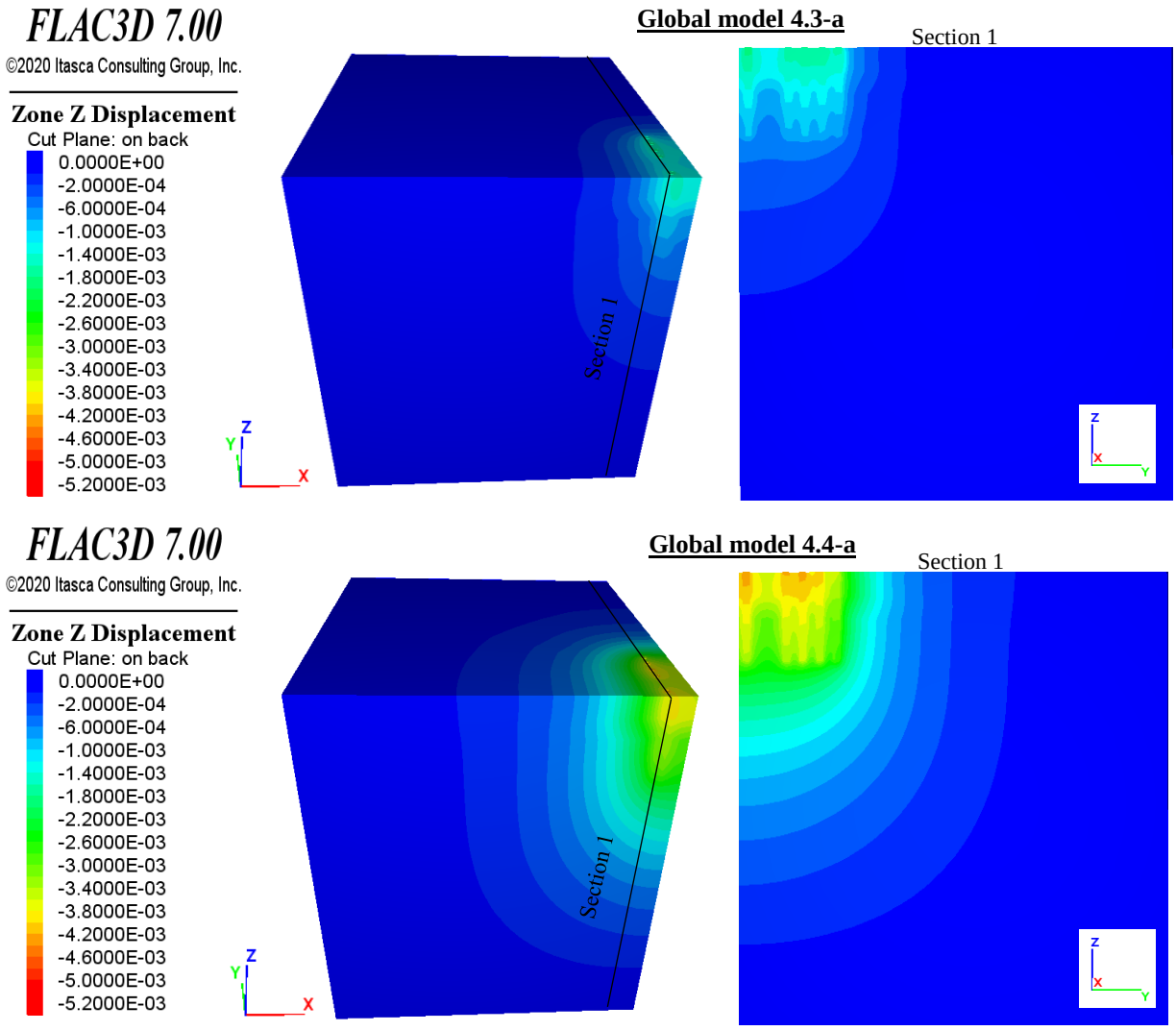

Figure 4.29 Displacement contours at the end of the calculation for Global model 4.3a and 4.4-a

Table 4.18 Summary of the pile settlements in the four global models

Pile number	Vertical displacement at the head of the piles (mm)			
	Global model 4.1	Global model 4.2-a	Global model 4.3-a	Global model 4.4-a
Pile 17A (Q = 2 960 kN)	5.2	4.5	1.9	4
Pile 18A/B (Q = 2 435 kN)	5.1/5	4.3	1.8	4.1/4
Pile 19A/B (Q = 2 750 kN)	4.4/4.9	3.8/4.2	1.7/1.8	3.5/3.9

Figure 4.30 presents a comparison between the pile deformation obtained by these models and the results of the instrumentation. Identically to the results of the single pile models, the curves showed the same deformation range without a negative skin friction in the upper part.

The settlement of the soil at the location of the fiberglass extensometer is shown in Figure 4.31.

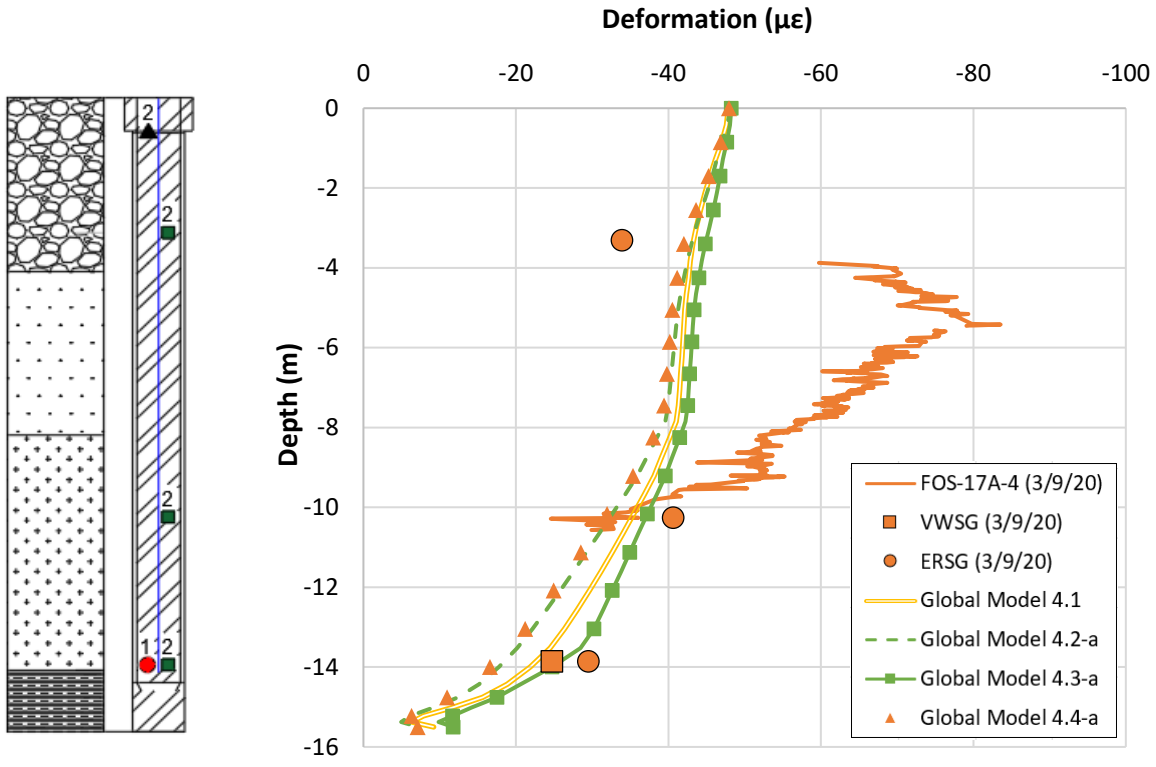

Figure 4.30 Comparison between the deformation curves of the global models

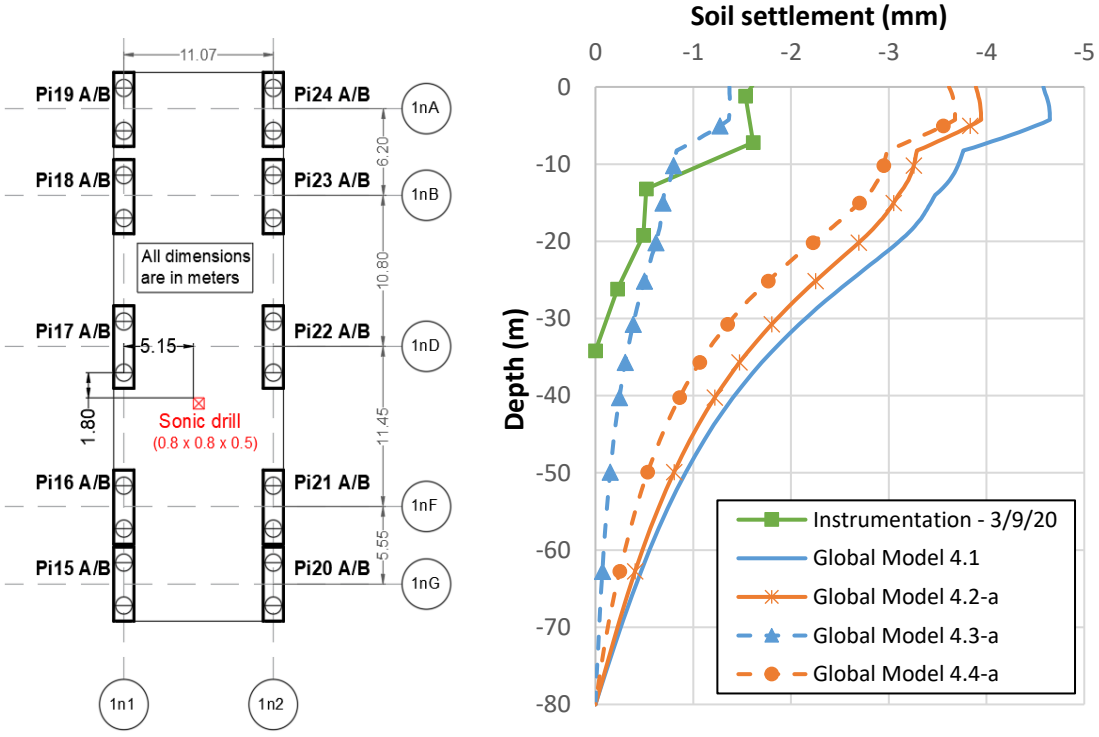

Figure 4.31 Location of the fiberglass rod extensometer and soil settlement curves of different numerical models

It can be noticed that only the settlement of the soil in Global model 4.3-a matches well the experimental result while it is overestimated in Global models 4.1, 4.2-a and 4.4-a with a value between 3.6 and 4.6 mm at the top of the soil and between 2.6 and 3.4 at the pile's tip. The displacement at -35 m is in the range 1 – 1.8 mm which is considered high compared to the depth below the pile. This can be caused by the parameters of the molasse layer that do not reflect its real behavior at high depths.

Although the pile in the four different models exhibited the same behavior in this analysis, Global model 4.2-a and 4.4-a were considered to be the most appropriate and more particularly the latter since the parameters were chosen based on experimental tests of the alluviums and the molasse. This needs however to be validated for higher loads.

On the other hand, since the settlement of the soil should be diminished at high depth in the molasse due to its stiffness, especially after 35 m, it was suggested to change the parameters at this level. With the aim to improve the previous analysis, two additional models were tested by taking the parameters of Model 4.2-a and Global model 4.2-a as references but with some modifications as follows:

- Global model 4.5-a:
  - Using a Young modulus E_s = 3 000 MPa for the molasse layer after 23 m depth in order to represent a stiffer layer and thus reduce the settlement at high depths
- Global model 4.6-a:
  - E_s = 3 000 MPa for the molasse after 23 m depth
  - The substitution of the alluviums 2 layer by an extension of the alluviums 1 having a modulus E_s = 245 MPa and this because it was believed that this layer could not be clearly observed in the FOS strain profiles

The soil settlement profiles were compared in Figure 4.32.

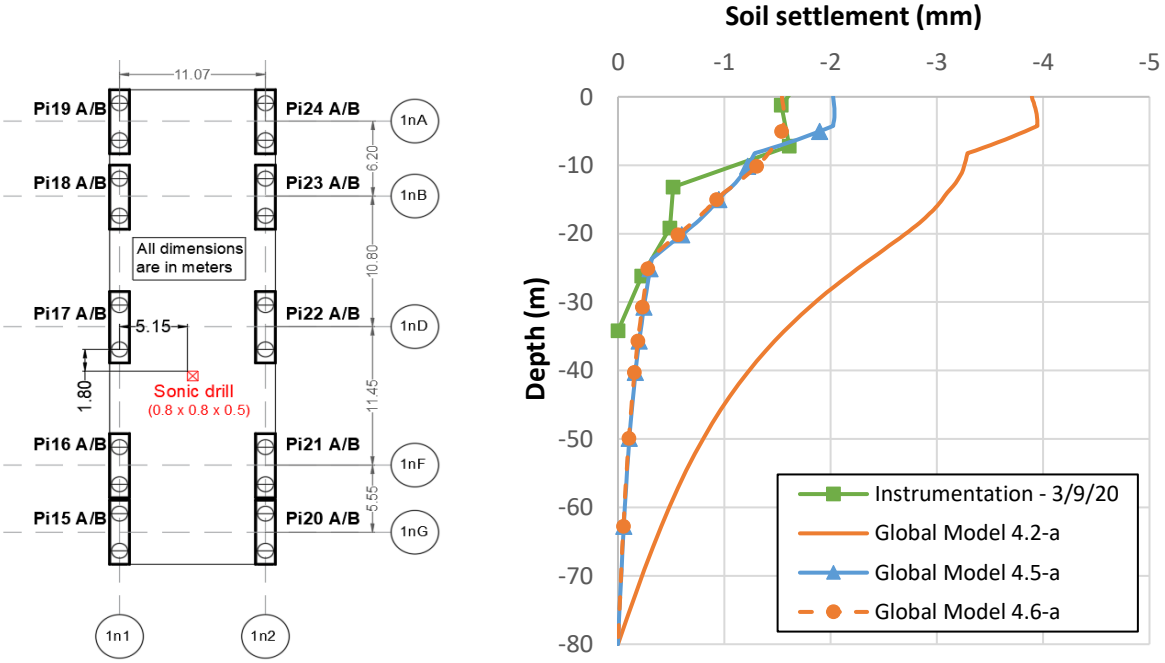

Figure 4.32 Comparison of the soil settlement in experimental and numerical models

The new molasse parameters allowed the soil settlement to become closer to the experimental curves (Global model 4.5-a and 4.6-a).

Besides, the displacement contours in Figure 4.34 and 4.34 show that the pile settlement decreased from 4.5 mm to 2.9 and 2.7 mm in Global model 4.5-a and 4.6-a respectively.

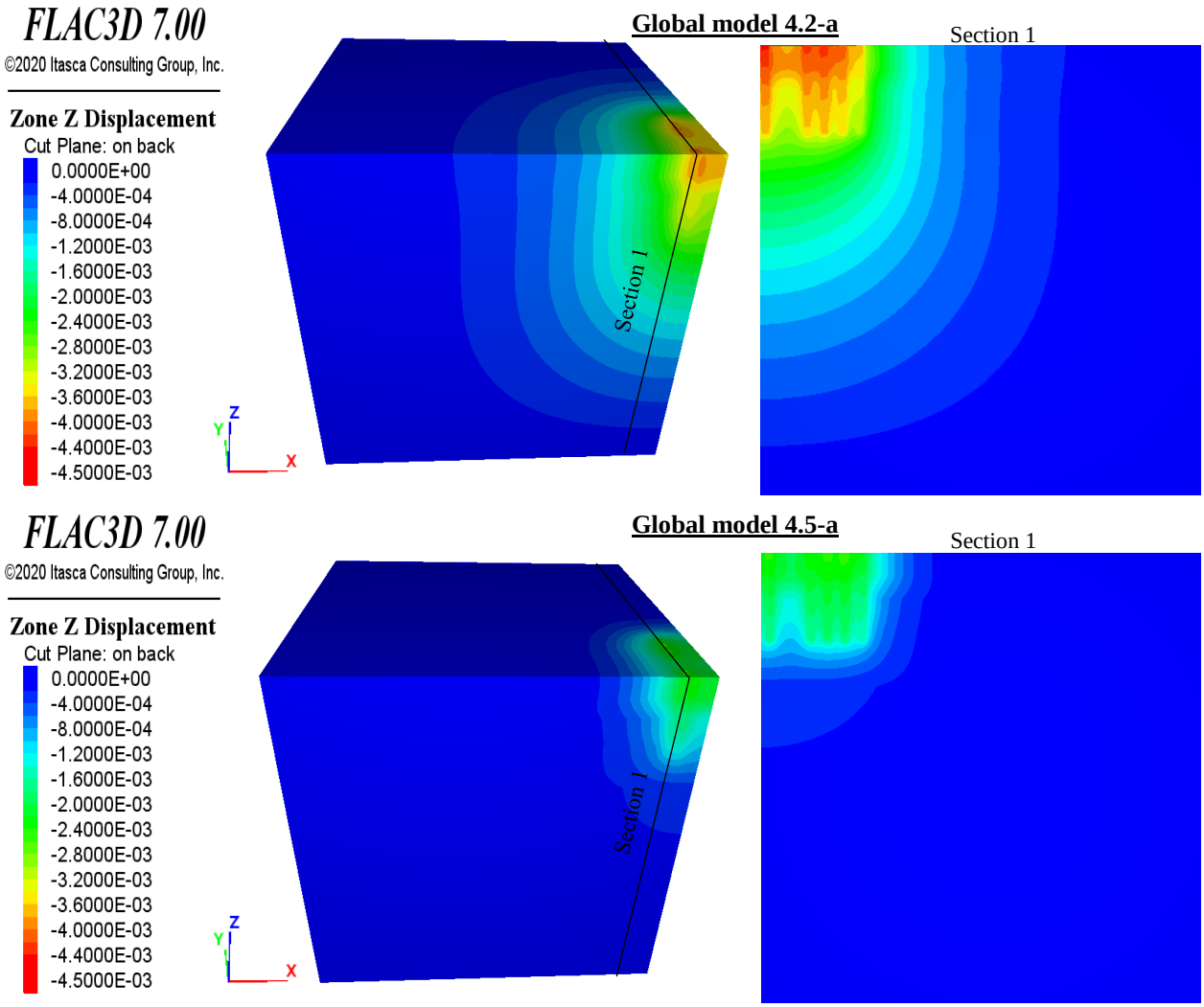

Figure 4.33 Displacement contours at the end of the calculation (Global models 4.2-a and 4.5-a)

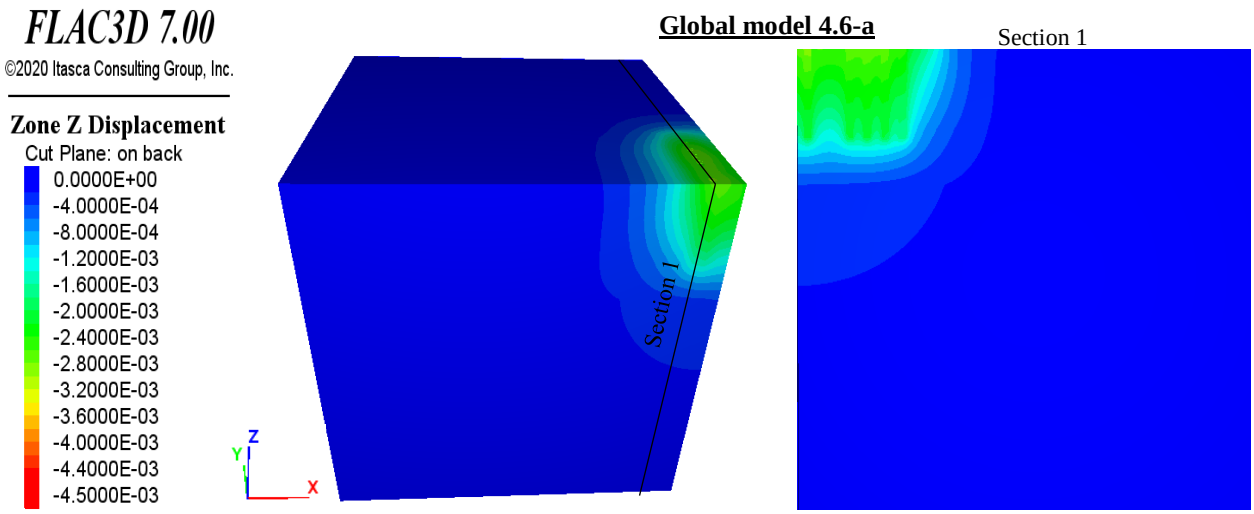

Figure 4.34 Displacement contours at the end of the calculation (Global models 4.6-a)

The deformation along the piles in these three models is presented in Figure 4.35. The change that was done to the Young modulus of the alluviums 2 layer in Global model 4.6-a shows in the shape of the curve. This results in an even distribution of the mobilized skin friction along the pile, since the layers are quite similar.

Based on the same previous approach, a surface load of 30 kPa was applied at the surface of the soil in all these models. The deformation curves obtained before and after this modification are compared to the FOS curves in Figure 4.35.

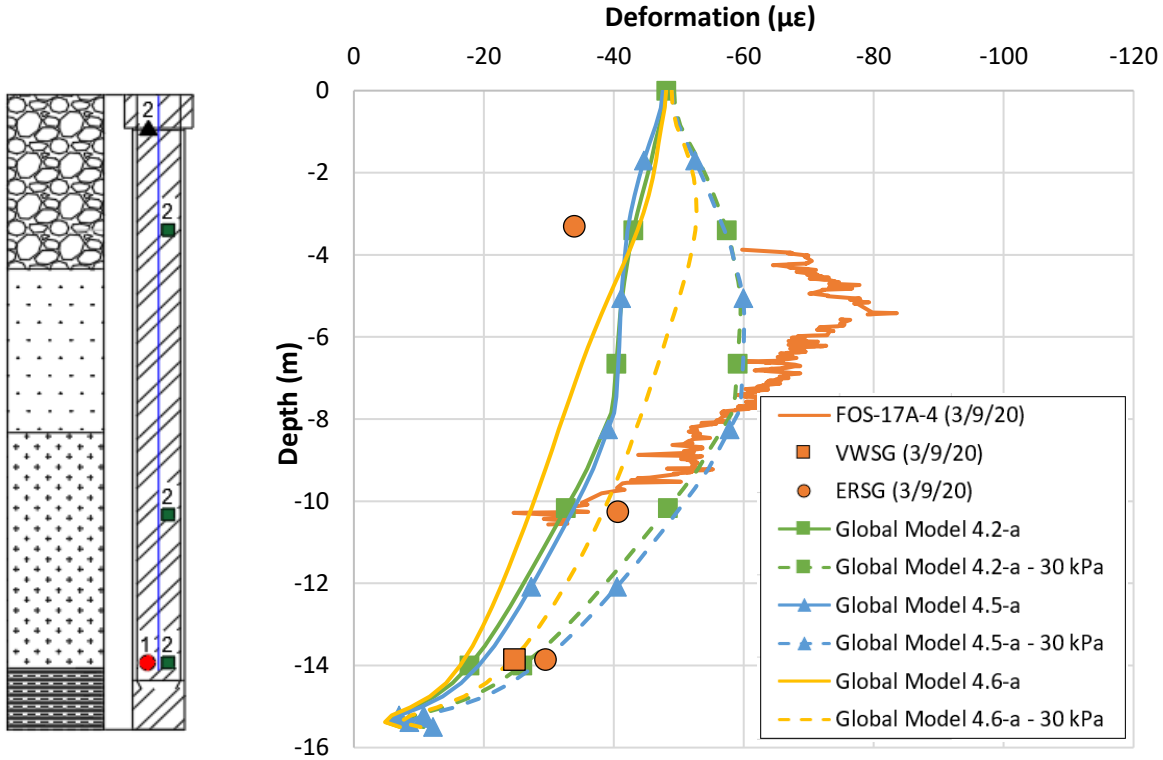

Figure 4.35 Comparison between the strain distribution before and after correction

By comparing Global model 4.2-a to Global model 4.5-a, one can say that the Young modulus of the deep molasse has no influence on the pile's deformation.

After applying 30 kPa on the top of the soil, the load transferred at the shaft of the pile "Q_s" in the range 5.5 – 10.5 m was around 640, 600 and 500 kN in Global models 4.2-a, 4.5-a and 4.6-a respectively.

The dotted curves (after 30 kPa) of Global model 4.2-a and 4.5-a show well a negative skin friction, which is more pronounced than in Global model 4.6, but is still far from the behavior observed in-situ.

The last model (4.6-a) presented a special behavior due to the high Young modulus of the alluviums 2. A load which is higher than 30 kPa is thus needed to reach the negative skin friction observed in-situ.

The skin friction profile is also shown in Figure 4.36.

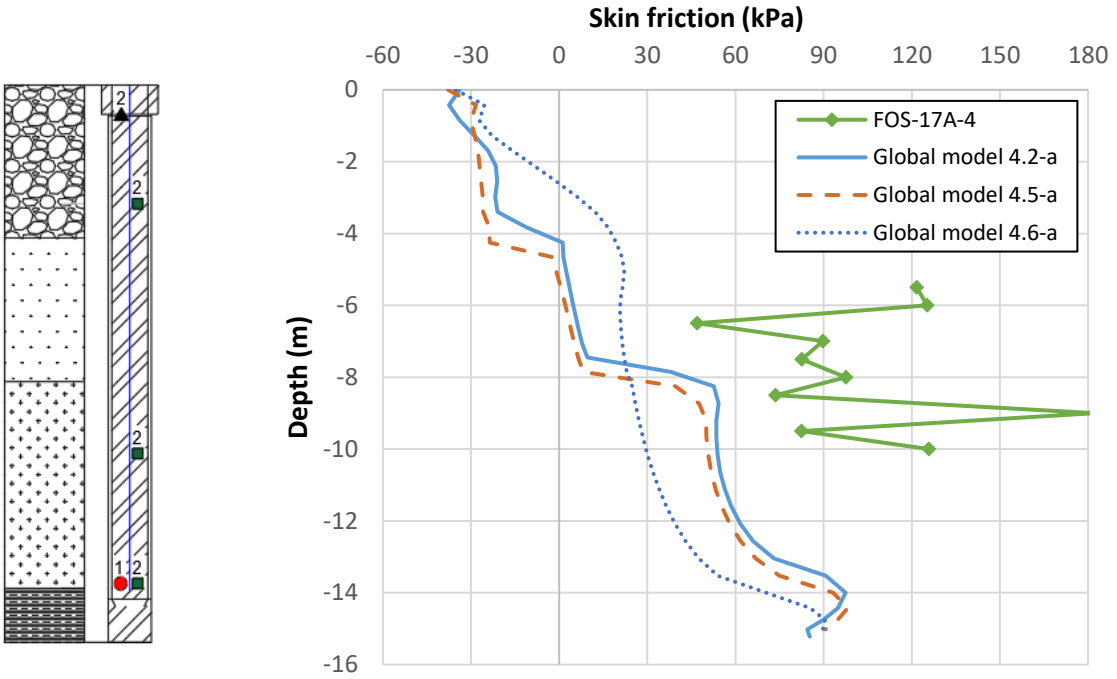

Figure 4.36 Comparison between the skin friction distribution along the pile

However, it should be noted that the obtained curves in the previous section were not completely accurate since the load that was applied to the soil should not be equally distributed in order to give a better representation of the reality. This load depends among others on the concrete slab, the applied load on the piles and the soil properties. In order to get a better perspective of the negative skin friction that had occurred in reality on site, additional models have been tried in which the concrete slab and the transfer structure were modeled. These models have not borne the desired fruit in terms of the deformation profile, without forcing an additional displacement on the soil. It came back to the previous models where the concrete slab and the transfer structure were not modeled.

Besides, we must understand that the simplifying hypothesis assumed in the beginning of the thesis, which helped us in terms of reducing the computation time, may also result in such a difference in the results when

compared with the experimental data. At the same time, due to the low applied load, it is hard to evaluate their accuracy, with respect to the sensors' resolution.

On the other hand, the parameters of Global model 4.4-a were obtained from experimental tests performed on few samples of molasse. The experience showed that the characteristics of this soil may differ according to the depth and location. This should be also considered in the future projects.

Despite the many efforts deployed in this regard, the behavior of the pile-soil interface could not be well represented in all the FLAC3D models although different set of parameters were employed. It must not be forgotten that the interface elements were assigned an elastic perfectly plastic model with Mohr-Coulomb failure criterion which may limit the mobilized skin friction compared to other models which uses a hyperbolic elastic section for example instead of a linear one. However, the implementation of such laws in FLAC3D needs further work.

Finally, it was concluded that this effect may be also due to a local change in the pile's diameter which is also seen in the pile monitoring records or to different soils parameters observed locally. This was hard to be numerically represented in the previous models in the framework of this thesis.

5-4- Use of the Plastic Hardening Soil – small (PH-S model)

Although few experimental tests are available for the alluviums in particular, an attempt was made to calibrate a PH model with small-strain for both soils, based on the Section 4-2-4 of Chapter 1.

The study should start by estimating the deformation level. For a total displacement of 3 mm over a pile's length of 15.5m (as shown in Section 3-4), the deformation is around 0.02% which is considered as small deformation domain according to Figure 1.18. In the following, the parameters of the molasse and the alluviums will be shown in details.

5-4-1- Parameters of the molasse

First, the parameters of the classic PH model are shown in Table 4.19.

Table 4.19 Parameters obtained from the molasse from experimental tests for p_{ref} = 100 kPa

Parameters	
c (kPa)	25
ϕ (°)	35
$\mathbf{E_{50}^{ref}}$ **(MPa)**	12.46
$\mathbf{E_{oed}^{ref}}$ **(MPa)**	17
$\mathbf{E_{ur}^{ref}}$ **(MPa)**	= 4 E_{50}^{ref} (default)
$\mathbf{R_f}$	0.8
m	0.5

Based on Figure 4.4, the Young modulus is 150 MPa for an axial deformation around 0.02 %, while the maximum modulus is around 460 MPa. This value will be assigned to E_0^{ref}.

The shear modulus for both deformation levels is 57 and 177 MPa respectively. The shear strain was also calculated for this triaxial test. This analysis allowed to plot the shear stiffness degradation curve which shows that at a shear strain equal to 0.02%, G/G_{max} is 0.32 (Figure 4.37).

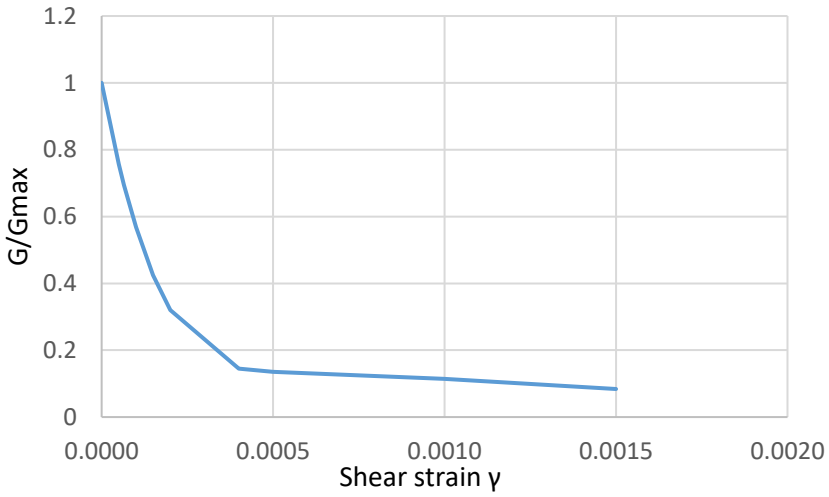

Figure 4.37 G/G_{max} versus shear strain for the molasse

Based on this curve, $\gamma_{0.7}$ was estimated at 0.0065%.

A quick verification was made with the tests obtained for the molasse at Bugey showed the following results:

- E_0^{ref} = 483.6 MPa
- G/G_{max} = 0.38 at 0.02%

These are consistent with the previous results.

5-4-2- Parameters of the alluviums

There are in the literature plenty of laboratory tests (such as those cited in Table 1.2) performed on sandy soil, which give the values of the stiffness with respect to the confining pressure and shear strain. However, these are hard to be performed on gravels due to the big grain size and because undisturbed samples are hard to be extracted from gravelly soils. Therefore, assumptions were made and theoretical equations were used in order to estimate the Plastic Hardening parameters.

First, in this paragraph, the cohesion and the friction angle were estimated at 5 kPa and 35°. Using these two values, the Mohr-Coulomb failure criterion can be used to estimate the deviator and mean stress at failure (q and p'). The triaxial stress path starts for an initial mean stress based on the initial state of the soil, for a $p_{ref} = \sigma_h$ in PH model. The pressuremeter moduli determined at the center of the soil layers were used. The values are presented in Table 4.20 and 4.21.

Table 4.20 Initial parameters based on initial state

Soil layer	Depth at the center of the layer (m NGF)	Initial parameters			E_M (MPa)	E (MPa)
		σ_v (kPa)	σ_h (kPa)	p' (kPa)		
Alluviums 1	159.875	21.25	9	13	62	245
Alluviums 2	155.75	62.5	26.75	39	8	32
Alluviums 3	150.875	111.25	47.6	69	67	264

Table 4.21 Additional parameters for the alluviums

Soil layer	Depth at the center of the layer (m NGF)	Parameters for a virtual triaxial test		
		p'_{max} (kPa)	q_{max} (kPa)	$q_{max}/2$ (kPa)
Alluviums 1	159.875	31	53	26.5
Alluviums 2	155.75	79.5	121	60.5
Alluviums 3	150.875	136	200	100

E_{50}^{ref} in the PH model is defined as the secant modulus at 50% q, which corresponds to the intersection level between the PH and MC stress-strain curve in a triaxial test. Therefore, as an approximation, the MC modulus was estimated using Eq. 1.134. The values were also shown in Table 4.20.

The stress-strain curves for each of the alluvium layer was reconstructed based on the foregoing and on Eq. 1.103 and 1.107 of Chapter 1.

A value of 0.8 was chosen for the failure ratio R_f.

$\gamma_{0.7}$ was determined as the shear strain for $G = 70\%G_{max}$.

Although no tests were performed that include bender elements or resonant column, a first estimation of $\gamma_{0.7}$ was made based on results from the bibliography. Rollins et al. (1998) combined the results of around 15 studies performed between 1984 and 1998 on gravelly soils (Figure 4.38). According to this paper, $\gamma_{0.7}$ varies from 0.008% to 0.027%, with a mean value of 0.0175%.

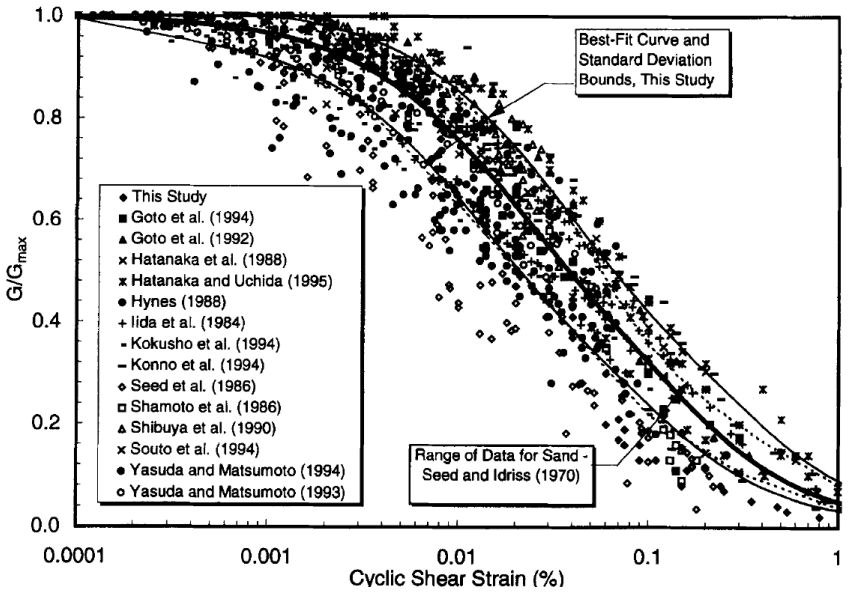

Figure 4.38 G/G_{max} versus shear strain for gravelly soils based on 15 studies (Rollins et al., 1998)

Table 4.22 Additional parameters for the alluviums used in PH-S model

Soil layer	Estimated parameters					
	P_{ref} (kPa)	E_0^{ref} (MPa)	$q_{max}/2$ (kPa)	ε (at $q_{max}/2$)	E_{50}^{ref} (MPa)	$\gamma_{0.7}$
Alluviums 1	13	460	26.5	0. 008955 %	140	0.000175
Alluviums 2	39	202	60.5	0.0472 %	62	0.000175
Alluviums 3	69	354	100	0.0444 %	148	0.000175

Despite the values of E_0^{ref} determined in the previous table, they could not be used in FLAC3D since it requires a value which is greater than E_{ur}^{ref}. Therefore, the maximum modulus used is 560, 248, 592 and 460 MPa respectively.

5-4-3- FLAC3D modeling and results

The previously determined parameters were now employed in the single pile models in FLAC3D. The list of new models and parameters is shown in the following table.

It should be recalled that the following parameters are used in all models:

- Alluviums: c' = 5 kPa; ϕ' = 36°
- Molasse: c' = 25 kPa; ϕ' = 35°

Table 4.23 New models and parameters used in FLAC3D

Model	Alluviums 1	Alluviums 2	Alluviums 3	Molasse
Model 4.7-a (E_p=34.5 GPa)	P_{ref} = 13 kPa E_{50}^{ref} = 140 MPa $E_{oed}^{ref} = E_{50}^{ref}$ $E_{ur}^{ref} = 4\ E_{50}^{ref}$ E_0^{ref} = 560 MPa $\gamma_{0.7}$ = 0.000175	P_{ref} = 39 kPa E_{50}^{ref} = 62 MPa $E_{oed}^{ref} = E_{50}^{ref}$ $E_{ur}^{ref} = 4\ E_{50}^{ref}$ E_0^{ref} = 248 MPa $\gamma_{0.7}$ = 0.000175	P_{ref} = 69 kPa E_{50}^{ref} = 148 MPa $E_{oed}^{ref} = E_{50}^{ref}$ $E_{ur}^{ref} = 4\ E_{50}^{ref}$ E_0^{ref} = 592 MPa $\gamma_{0.7}$ = 0.000175	P_{ref} = 100 kPa E_{50}^{ref} = 12.46 MPa E_{oed}^{ref} = 17 MPa $E_{ur}^{ref} = 4\ E_{50}^{ref}$ E_0^{ref} = 460 MPa $\gamma_{0.7}$ = 0.000065
Model 4.7'-a (E_p=15.7 GPa)				
Model 4.8-a (E_p=34.5 GPa)	$E_0^{ref} = 3\ E_{ur}^{ref}$ (default value in FLAC3D)	$E_0^{ref} = 3\ E_{ur}^{ref}$ (default value in FLAC3D)	$E_0^{ref} = 3\ E_{ur}^{ref}$ (default value in FLAC3D)	$E_0^{ref} = 3\ E_{ur}^{ref}$ (default value in FLAC3D)
Model 4.8'-a (E_p=15.7 GPa)				

The deformation profiles obtained in these models are shown in Figure 4.39. They were compared to the results of Section 5-1. Besides, Figure 4.40 shows the curves obtained after applying a uniform stress at the soil similarly to the previous sections.

It can be seen that there is a big difference between the results obtained for the different models. Models 4.1, 4.2-a and 4.3-a gave close results to the experimental values measured using the VWSG and the ERSG, while it seemed that the FOS profile is closer to the model 4.7'-a.

A negative skin friction was not shown in these curves even in the curves of Figure 1.4 where a stress was applied on the top of the soil. Unfortunately, the small-strain feature that was added to this work could not show the real behavior of the foundation.

These parameters were also tried on Global Models that include all the piles. The results are similar to those for single piles models as shown in Figure 4.41.

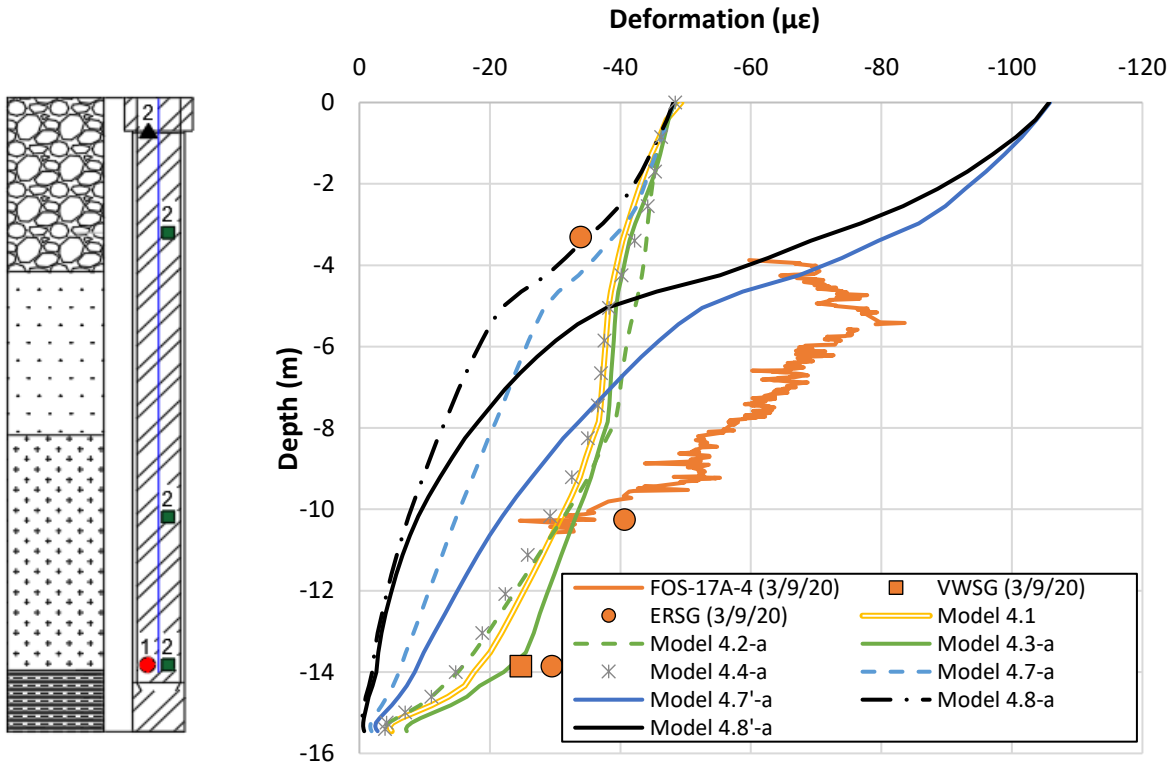

Figure 4.39 Numerical and in-situ deformation curves

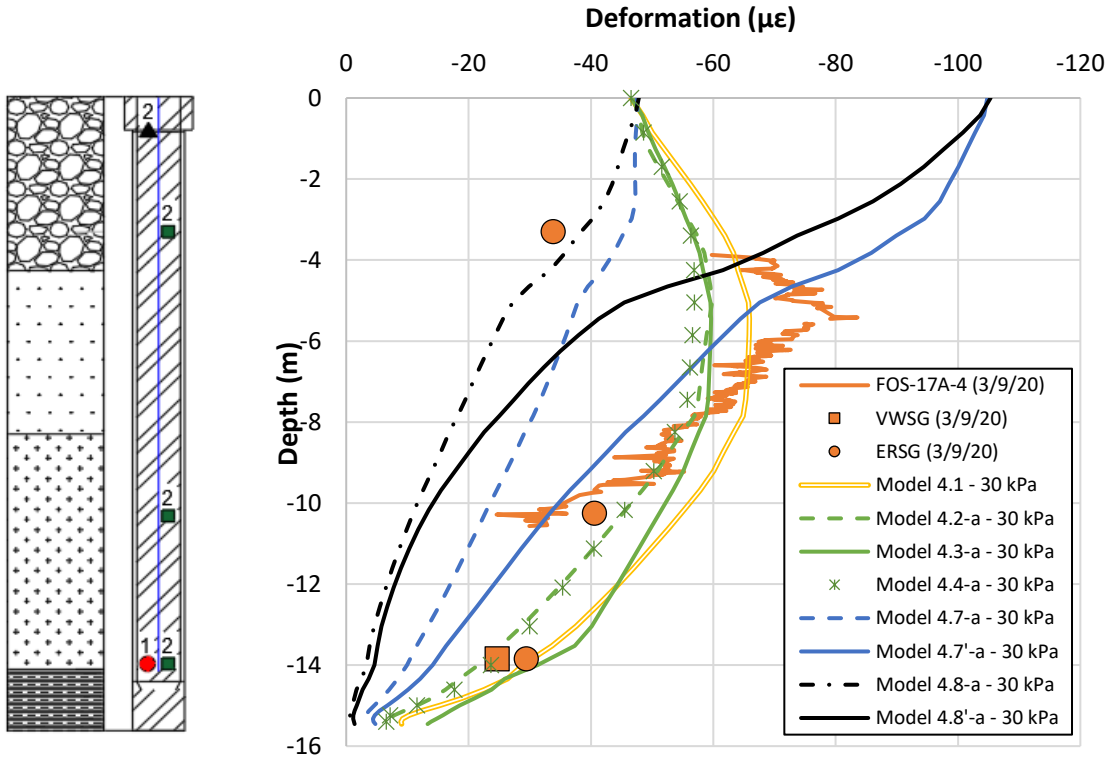

Figure 4.40 Numerical and in-situ deformation curves after correction

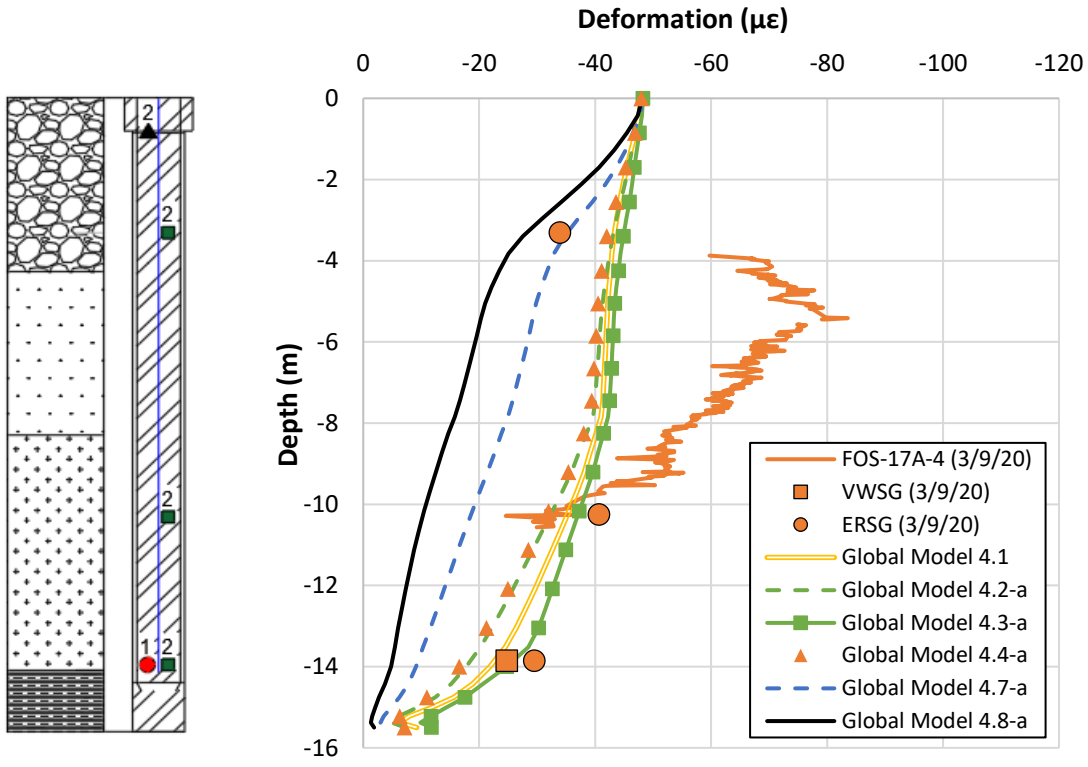

Figure 4.41 Numerical and in-situ deformation curves for global models

6- Observations and conclusions

With all these endeavors, it was possible to validate the measured deformations along the pile. All numerical examples, be it with single pile or the Global model versions showed the same range of deformation which was also compatible with the applied load measured in-situ and estimated numerically.

Model 4.2-a and Model 4.4-a were considered to be the most appropriate and more particularly the latter since the parameters were chosen based on experimental tests of the alluviums and the molasse. The results are summarized in Table 4.24.

In Model 4-7 and Model 4-8, the PH-S model was assigned to the soil layers but due to the absence of advanced tests (particularly for the alluviums due to the big grain size), the parameters could not be well defined and the results were not validated.

However, certain aspects of the piles' behaviors could not be modeled in an accurate way such as the negative skin friction observed on the first 5.5 meters of the piles. In fact, this can be due to several causes such as the water table fluctuation which was not modeled in this work. Furthermore, the numerical model using the habitual parameters cannot necessarily reproduce the load transfer between the soil and the pile. For example, the actual mobilized skin friction along the pile between 26/2/20 and 3/9/20 is higher than the values estimated numerically and even in some location it exceeds the upper limit values imposed by assigning to the interface a zero friction angle and a cohesion equal to "q_s".

This can be due also to an underestimation of the Young modulus of the soil layers as seen in Chapter 3 or in paragraph 5-3 5-3- of Chapter 4, especially for the Alluviums 2 layer. The deformation profile of Pile 17A showed indeed as if this layer was not present on site in this particular location. The important role of the constitutive law of the soil and the interface in predicting their response should be remembered as well.

Besides, this deformation variation may be caused by a difference in the pile's diameter at this level.

On the other hand, the analytical methods showed that compared with the small applied loads, the piles were overdesigned in the project. It should be recalled in this context that at the beginning of the project, a 7-m length piles were suggested by the company but then for safety reasons this option was rejected in order to ensure a 1.5m embedment in the rigid stratum (the molasse layer). This was validated after analyzing the deformation measurements in Pile 17A.

Therefore, it is recommended to investigate more about the characteristics of the alluviums so that other parameters and maybe other constitutive laws can be employed in future projects.

On the other hand, some of the following improvements of the numerical model can be performed:

- Model the load history in the Part-Dieu neighborhood and the nearby structures (paragraph 2-2 of Chapter 2)
- Use the real geometry of the model without the simplifying hypotheses, especially with the piles having different top levels and different level of concrete slabs
- Implement in FLAC3D a more advanced constitutive law for the interface

This work has also allowed to highlight the importance of performing a pile load test since the lithography is prone to changing from a location to another. This may save time and money in any project.

All these conclusions have yet to be discussed and validated later after comparing the long-term behavior of the structure and the soil, especially if higher loads were detected at the head of the piles. This will allow to validate or not the soils parameters determined experimentally.

Table 4.24 Selected parameters for the Global models with some results

	Global model 4.2-a	**Global model 4.4-a**
Alluviums		
➢ **Law**	Elastic perfectly plastic model with a MC failure criterion	
➢ **Parameters**	• c = 5 kPa • ϕ = 36° / ψ = 5° • $E = \begin{cases} 245\ MPa & Alluv.1 \\ 32\ MPa & Alluv.2 \\ 264\ MPa & Alluv.3 \end{cases}$	
Molasse		
➢ **Law**	Elastic perfectly plastic model with a MC failure criterion	Plastic Hardening Model
➢ **Parameters**	• c = 25 kPa • ϕ = 35° / ψ = 5° • E = 375 MPa *(shaft)* • E = 326 MPa *(tip)*	See Table 4.14
Concrete	E_p = 34.5 GPa	E_p = 34.5 GPa
Results	• Good representation of the deformation range measured experimentally • Comparibility between the deformation and the applied load	
Limitations	• They could not represent the negative skin friction that exists at the first meters of the pile ⇨ *This aspect can be shown when a stress of 30 kPa is applied on the soil* • The mobilized skin friction is small compared to the one determined experimentally ⇨ *Due to the choice of the constitutive law assigned to the interface* • The molasse layer at high depth is underestimated using the previously mentioned parameters ⇨ *Improvements in Model 4.5-a*	

Conclusions and perspectives

General conclusion

This thesis was done in the framework of the project "Fondasilex" funded by the region "Auvergne-Rhône-Alpes" whose objective was to study the behavior of the foundations of the tower Silex^2 located in Part-Dieu, Lyon and the soil present in the site location. This tower is founded on 20 piles of 1.22-m diameter that are subjected to different loads based on a load transfer schedule provided by the construction company. The soil in Lyon and in Part-Dieu district in particular is characterized by three different layers of alluviums (labeled from 1 to 3 in this thesis) on top of a deep molasse layer dating from the Miocene period, which consists of sandy-silty to sandy-gravelly beige sands. In order to understand the load transfer mechanism and the behavior of the soil and the piles, experimental and numerical techniques were employed simultaneously. This helped in validating the design and optimizing the dimensions for future projects planned in the same area in the coming few years.

In this project, a geotechnical instrumentation was performed during the early phase of the construction with the aim of getting real-time measurements of the stress transferred to the head of the piles and their deformation as well as the settlement of the soil. Thus, 18 concrete pressure cells were installed on the head of the piles in addition to three different types of deformation sensors: 14 vibrating wire strain gages, 36 electrical resistance strain gages and 6 fiber optic sensors based on reflectometry by Rayleigh scattering. Different technologies were used in the measurement of the deformation in order to ensure redundancy and this has proven to be very successful. The sensors were chosen because of their i) small size, ii) moisture resistance, iii) measuring interval, iv) compatibility with the concrete, v) ease of installation and vi) price. Compared to conventional sensors, the DOFSs have the added advantage of giving the overall behavior of the pile.

In total, 78% of these sensors could withstand the harsh environmental conditions of the site, while the others were either broken during the construction or did not show compatible and interpretable results. The deformations and stresses measured between 26/2/20 and 3/9/20 during the construction of the tower were compatible. The calculated loads were in close agreement with the theoretical ones provided by the construction company.

The three types of sensors with the different technologies showed approximately the same deformation range, which reflects a good functioning of the sensors. However, these values were small because of the small applied load and the diameter of the piles. This allows us to think that the piles are overdesigned. Since these sensors are all sensitive to temperature changes, a thermal compensation was needed in order to get the mechanical strain which is the result of pure stress changes. A closer scrutiny on the deformation profiles provided by all types of sensors indicates a negative skin friction in the few meters of the piles, i.e., above 5.5 m.

Despite the difficulty to install FOSs in cast-in-place piles in a real site, the obtained results were interesting in terms of the quality of measurement. The only problem was their fragility. The FOS allows to capture the overall behavior of the pile, unlike the sensors that give single measurements such as the conventional strain gages.

In parallel, a fiberglass rod extensometer was installed in the soil in order to measure its displacement using six sensors at different levels (2, 8, 14, 20, 27 and 35 m which served as a reference). The maximum value detected at the end of the construction was around 1.6 mm, measured above 8 m depth.

At the location of this extensometer, a sonic drill was performed allowing to retrieve samples of alluviums and molasse until a depth of 35 m, on which laboratory tests were performed. Shear box tests were done on alluviums capped samples to determine the shear strength parameters (c and ϕ). On the other hand, triaxial and oedometer tests were used in case of the molasse. These tests were calibrated using numerical tools, which allowed to determine the soil parameters needed in the numerical pile models performed later. Accordingly, an elastic perfectly plastic model was chosen for the alluviums with a cohesion and friction angle equal to (5 – 25 kPa) and 36° respectively. However, for the molasse, a more advanced constitutive law was chosen which is the Plastic Hardening Model that employs a bigger number of parameters.

On the other hand, crushing tests were performed on concrete samples fabricated during the casting of the piles. These tests showed a secant Young modulus equal to 34.5 GPa, which will be used in this study to estimate the load from the measured deformation.

In addition to the experimental part, a major section of this work was accomplished using a numerical modeling software FLAC3D, based on the finite difference method which allowed to model the foundations and to predict their response and that of the soil when subject to axial loads.

This required in the first place to perform a sensitivity analysis on single pile models in which the influence of each parameter was studied separately. This study presented in Chapter 3 allowed to conclude that some parameters showed a minor influence on the behavior of the piles when the applied load is in the range (0 – 3 000 kN) such as the presence of the water table, and some soil parameters (cohesion, friction angle, dilatancy angle). It should be noted that the influence of the cohesion and the friction angle was analyzed by assigning to the interface elements the same parameters of the adjacent soil in order to prevent their early failure. Other parameters had a direct influence on the mobilized skin friction along the pile and thus on its settlement.

- The parameters of the interface and in particular the cohesion and the friction angle played a major role in determining the response of the pile, when the skin friction is fully mobilized. When these parameters were increased, the ultimate skin friction increased generating a lower settlement. However, the initial elastic section of the load transfer curves is not affected.
- The Young modulus of the soil is also of high importance. It was tested on the alluviums 2 and the molasse layers. The analysis showed that when the modulus of the alluviums 2 was increased, the mobilized skin friction increased and the settlement decreased. However, for the molasse layer, both the skin friction and the end-bearing pressure were affected but the latter took precedence over the former. Therefore, when its modulus was increased, the load at the pile's tip increased but the settlement decreased.
- The influence of the Young modulus of the pile is also important. The pile settlement decreases when it increases.
- The constitutive law assigned for the soil affects a lot the behavior of the piles.

On the other hand, three different geometries of pile group models were studied as follows:

- Pile Group I: Two equally loaded piles were considered to be isolated from the rest of the piles. For the same axial load, this model showed that the settlement of the pile group is 27.5% higher than the settlement of a single pile when 5 000 kN was applied for the case of E_p = 34.5 GPa.
- Pile Group II: The interaction between Pile 17A/B and the rest of the groups was modeled by imposing different symmetry axes at the boundaries. The settlement of the pile group II is 123.8% higher than the settlement of a single pile when 5 000 kN was applied (E_p = 34.5 GPa).
- Global model: All the piles were modeled in an attempt to make an overall analysis of the pile-soil system. Compared to the previous models, the settlement was close to the one in Group II.

In the pile group models, the Young modulus of the pile was of a high influence on the final response of the piles while the water table showed no impact for a range (0 – 3 000 kN).

Aside from the sensitivity analysis, the main objective of the numerical work was to be able to represent the experimentally observed behavior of the pile and thus to be able to validate the chosen parameters and constitutive laws. Therefore, in the final models, the load measured by the CPCs was applied on the top of the piles, allowing to analyze the induced deformation and to compare it with the experimental values.

Different sets of parameters and constitutive laws were used based on the literature and on laboratory tests performed on the alluviums and molasse samples. While the cohesion of the soil layers showed a minor influence in this load range, the role of the Young modulus was found very important. Four different global models were established. An elastic perfectly plastic model with a Mohr-Coulomb failure criterion was first assigned to all layers using two different sets of Young moduli (Global model 4.1 and 4.2). These models were then improved by assigning a PH model to the molasse (Global model 4.3 and 4.4) and then a PH-S model to all soil layers (Global model 4-7 and 4-8).

In Global model 4.4, the molasse's parameters were determined from triaxial and oedometer tests. The four models showed a good deformation range but the negative skin friction could not be observed obviously because no load was transferred to the soil. Therefore, a stress was applied on the top of the soil in order to force additional displacements. This allowed to observe the desired behavior but with different values that can be also caused by local variation in the modulus or the section of the piles.

Besides, in Global Model 4-7 and 4-8, the PH-S was assigned to the alluviums and the molasse and the parameters were defined based on the literature and some recent experimental tests. However, this did not improve the results. In future projects, more advanced tests need to be performed.

Based on this section, Model 4.2 and 4.4 (and the corresponding global model versions) were chosen to represent the behavior of the existing soil. These models were later improved by assigning to the deep molasse better parameters reducing its settlement. However, all these findings need to be checked for higher loads in order to be able to validate definitely the chosen parameters and laws.

In parallel to the experimental and numerical study, a comparison was made with two analytical methods:

- Elastic theory (Poulos and Davis, 1980): Although this method reflects well the behavior of the pile when in the elastic domain, it was found not suitable in this project. It actually underestimated the pile's settlement due to the contrast between the Young moduli of the different layers

- Load transfer method (Frank and Zhao, 1982): Based on previous experience, this method gives realistic results for a load which is less than 70% of the creep resistance. In this project, it was used to validate the choice of the parameters that govern the pile load settlement curve.

This work allowed to validate the importance of the instrumentation in the analysis of piles and pile groups. What makes this instrumentation unique is that it has shifted outside the framework of a typical instrumented pile load test by providing measurements during the installation of the structure. The installed sensors in the piles allowed to measure the actual stresses and to compare it with the theoretical values. Besides, the deformation was measured in different technologies which helped in estimating the load mobilized at the pile shaft. This work is one of the few projects that installed fiber optic sensors using a reflectometry by Rayleigh scattering in CFA piles. In fact, this technique allowed to measure the distributed deformation and allowed thus to visualize the global behavior of the pile. In addition, what is also of high importance in such studies is the calibration of the numerical models based on real behavior of the structure and the soil. However, this does not always give the expected results because of the simplifying hypotheses imposed by the computation time and cost. Unfortunately, this work was also limited to the domain of the applied load which was not enough to visualize the plastic behavior of the soil especially that the piles were initially overdesigned. This reminds us of the importance of pile load tests in such projects.

On the other hand, although the elastic theory was supposed to be suitable for elastic domain, it did not show good results in this project for the previously cited reasons. This reminds us on the limitations of analytical methods.

Perspectives

In this thesis, a geotechnical instrumentation and a numerical modeling were performed to understand better the behavior of pile foundations. However, this work opens up several new perspectives:

- Instrumentation:

Despite the good results obtained experimentally, we could not observe well the behavior of the piles and the soils due to the small applied load. As a result, it was hard to calibrate these models numerically during the thesis. However, the monitoring will continue in the next few months.

We suggest to perform a pile load test in one of the future projects of the Part-Dieu. The pile load test may cause extra costs but at the same time will surely bring many benefits. This avoids the overdesign caused sometimes by a mis-evaluation of the soil's characteristics.

- Experimental tests:

In the same context, it is recommended to investigate more about the characteristics of the alluviums by performing additional laboratory or in-situ tests. It has long been assumed that the rigid stratum is defined by the molasse's altitude, while in fact the alluviums may be really underestimated.

- Numerical modeling:

In order to obtain a reliable modeling in FLAC3D, some improvements were suggested:

  - In this thesis, several simplifying hypotheses were assumed in order to save computation time in FLAC3D, especially in the Global model. It is recommended thus to verify their influence on the behavior of the model.
  - It is also as important to model the load history in the Part-Dieu neighborhood since it may highly affect the response of the soil and the piles. The same applies to the existing nearby structures (Silex[1], EDF and RTE buildings)
  - Based on the results of additional experimental tests suggested on the alluviums and the molasse, it may be helpful to investigate for more advanced constitutive laws to be used for the soil.
  - The parameters of the interface chosen in this thesis were based on previous experience or on values obtained experimentally. The ultimate skin friction was not reached due to the small loads and thus the chosen parameters did not highly affect its response. However, if higher loads need to be considered later for further projects, a good characterization of the interface is essential.

References

Abalde-Cela, S., Aldeanueva-Potel, P., Mateo-Mateo, C., Rodriguez-Lorenzo, L., Alvarez-Puebla, R. A., Liz-Marzán, L. M. (2010). Surface-enhanced Raman scattering biomedical applications of plasmonic colloidal particles. *Journal of the Royal Society Interface*, *7*, S435–S450.

Abchir, Z., Habert, J., Legrand, S., Burlon, S. (2014). Analyse de la base d'essais de chargement de l'IFSTTAR pour le calcul du tassement des pieux.

ACI Committee 543R-12. (2012). Recommendations for Design, Manufacture, and Installation of Concrete Piles. *American Concrete Institute, Detroit*, 34.

Ahlund, R., Ögren, O. (2016). Pore pressures and settlements generated from two different pile drilling methods.

Al-Obaidi, A. A., Mahmood, P. N., Al-Karawi, A. A. (2016). Assessment of vertical pile capacity in coil with weak layers and cavities. In *Proceedings of the 2nd International Conference on Developments in Civil and Computer Engineering Applications*.

Allagnat, D. (2005). La méthode observationnelle pour le dimensionnement interactif des ouvrages. *Guide Technique, Presses de l'ENPC (The Observational Method for the Interactive Design of Structures)*.

Alnuaim, A. M., El Naggar, H., El Naggar, M. H. (2013). Performance of piled-raft system under axial load. In *Proceedings of the 18th International Conference on Soil Mechanics and Geotechnical Engineering, Paris, France, 02-06 September 2013* (pp. 2663–2666).

Atkinson, J. H., Sallfors, G. (1991). Experimental determination of stress-strain-time characteristics in laboratory and-in-situ tests. In *Proceedings of the 10th European Conference on Soil Mechanics and Foundation Engineering, Florence, Rotterdam: Balkema* (Vol. 3, pp. 915–956).

Balaam, H. P., Poulos, H. G., Booker, J. R. (1975). Finite element analysis of the effects of installation on pile load-settlement behaviour. *Géotechnical Engineering*, *6*(1), 33–48.

Banerjee, P. K., Davies, T. G. (1978). The behaviour of axial and laterally loaded single piles embedded in nonhomogeneous soils. *Geotechnique*, *28*(3), 309–326.

Bao, X., Chen, L. (2012). Recent Progress in Distributed Fiber Optic Sensors. *Sensors (Switzerland)*, *12*(7), 8601–8639.

Bao, X., Dhliwayo, J., Heron, N., Webb, D. J., Jackson, D. A. (1995). Experimental and theoretical studies on a distributed temperature sensor based on Brillouin scattering. *Journal of Lightwave Technology*, *13*(7), 1340–1348.

Barbas, A., Frank, R. (1982). *Utilisation de la méthode des éléments finis en mécanique des sols dans le domaine de l'élastoplasticité*. Rapport de recherche, 116, Laboratoire Centrale des ponts et Chaussées, Paris.

Barrias, A., Casas, J. R., Villalba, S. (2016). A review of distributed optical fiber sensors for civil engineering applications. *Sensors (Switzerland)*, *16*(5), 748.

Bastianini, F., Matta, F., Rizzo, A., Galati, N., Nanni, A. (2007). Overview of recent bridge monitoring applications using distributed Brillouin fiber optic sensors. *J. Nondestruct. Test*, *12*(9), 269–276.

Benz, T. (2007). *Small-strain stiffness of soils and its numerical consequences* (Vol. 5). Univ. Stuttgart, Inst. f. Geotechnik Stuttgart.

Berezantsev, V. G., Khisttoforov, V. S., Golubkov, V. N. (1961). Load bearing capacity and deformation of pile foundations. *5º Congrès International de Mécanique Des Sols et Des Travaux de Fondations, Paris.*

Bersan, S., Bergamo, O., Palmieri, L., Schenato, L., Simonini, P. (2018). Distributed strain measurements in a CFA

pile using high spatial resolution fibre optic sensors. *Engineering Structures*, *160*(May), 554–565.

Bica, A. VD, Prezzi, M., Seo, H., Salgado, R., Kim, D. (2014). Instrumentation and axial load testing of displacement piles. In *Proceedings of the Institution of Civil Engineers: Geotechnical Engineering* (Vol. 167, pp. 238–252).

Billaux, D., Cundall, P. (1993). Simulation des géomatériaux par la méthode des éléments Lagrangiens. *Revue Française de Géotechnique*, (63), 9–21.

Bjerrum, L., Johannessen, I. (1960). Pore pressures resulting from driving piles in soft clay. Pore pressure and suction in soils.

Bohn, C. (2015). *Serviceability and safety in the design of rigid inclusions and combined pile-raft foundations*. Doctoral dissertation, Paris Est.

Bolton, M. D. (1986). The strength and dilatancy of sands. *Geotechnique*, *36*(1), 65–78.

Bordes, J. L., Debreuille, P. J. (1985). Some Facts About Long-Term Reliability of Vibrating Wire Instruments. *Transportation Research Record*, (1), 20–27.

Bourdeau, Y. (1997). Le comportement des alluvions du Rhône dans une grande boite de cisaillement direct. *Revue Française de Géotechnique*, (79), 45–57.

Bourdeau, Y., Lareal, P., Marchal, J. (1989). Résistance au cisaillement des alluvions du rhone. In *Congrès international de mécanique des sols et des travaux de fondations. 12* (pp. 695–696).

Bowles, J. E. (1996). *Foundation analysis and design* (5th editio). McGraw-Hill, New York.

Boyce, J. R. (1980). A non-linear model for the elastic behaviour of granular materials under repeated loading. In *Proceedings of the International Symposium on Soils under Cyclic and Transient Loading, Swansea, 7-11 January 1980*.

Briançon, L., Cazeaudumec, B., Pincent, B. (2016). Auscultation géotechnique. *Techniques de l'ingénieur Géotechnique, base docum*(ref. article : c229).

Brinkgreve, R. B. J., Bakker, K. J., Bonnier, P. G. (2006). The relevance of small-strain soil stiffness in numerical simulation of excavation and tunneling projects. In *Proceedings of 6th European Conference in Geotechnical Engineering, Graz, Austria, 6–8 September 2006* (pp. 133–139).

Brinkgreve, R. B. J., Swolfs, W. M., Engin, E., Waterman, D., Chesaru, A., Bonnier, P. G., Galavi, V. (2010). PLAXIS 2D 2010. *User Manual, Plaxis Bv*.

Burland, J. B. (1989). Small is beautiful - the stiffness of soils at small strains. *Canadian Geotechnical Journal*, (26), 499–615.

Burns, S. E., Mayne, P. W. (1999). Pore pressure dissipation behavior surrounding driven piles and cone penetrometers. *Transportation Research Record*, *1675*(1), 17–23.

Butterfield, R., Banerjee, P. K. (1971). The elastic analysis of compressible piles and pile groups. *Geotechnique*, *21*(1), 43–60.

Butterfield, R., Douglas, R. A. (1981). *Flexibility coefficients for the design of piles and pile groups*. No. 108 Monograph. 1981.

Byrne, B. W., McAdam, R. A., Burd, H. J., Houlsby, G. T., Martin, C. M., Gavin, K., … SkovGretlund, J. (2015). Field testing of large diameter piles under lateral loading for offshore wind applications. In *Proceedings of the 16th European Conference on Soil Mechanics and Geotechnical Engineering, Edinburgh, UK, 13-17 September 2015*.

Cambou, B., Jafari, K. (1988). Modèle de comportement des sols non cohérents. *Revue Française de Géotechnique*, (44), 43–55.

Caputo, V. (1984). Pile foundation analysis: a simple approach to nonlinerity effects. *Rivista Italiana Di Geotecnica*,

18(1), 32–51.

Caquot, A., Kerisel, J. (1953). Sur le terme de surface dans le calcul des fondations en milieu pulvérulent. In *Proceedings of the 3rd International Conference on Soil Mechanics and Foundation Engineering, Zurich, Switzerland, 16-27 August, 1953* (Vol. 1, pp. 336–337).

Cazacliu, B., Di Benedetto, H. (1998). Behavior of sand in the small strain domain observed with a hollow cylinder apparatus. In *European Conference on Earthquake Engineering, Paris*.

Çelik, S. (2017). Comparison of mohr-coulomb and hardening soil models' numerical estimation of ground surface settlement caused by tunneling. *Iğdır University Journal of the Institute of Science and Technology*, 96–102.

CGS. (1992). *Canadian Foundation Engineering Manual.* (3rd Editio). Canadian Geotechnical Society, Ottawa, 512 p.

Chan, K. S., Karasudhi, P., Lee, S. L. (1974). Force at a point in the interior of a layered elastic half space. *International Journal of Solids and Structures*, *10*(11), 1179–1199.

Chan, S. F. (2004). Special Lecture, Design and Construction of Foundations for Suntec City. In *Proceedings of the Malaysian Geotechnical Conference, Malaysia* (pp. 21–43).

Chan, S. F., Lee, P. C. S. (1990). The Design of Foundations for Suntec City, Singapore. In *Proceedings of Conference on Deep Foundation Practice, Singapore*.

Cheng, J.-X., Xie, X. S. (2004). Coherent anti-Stokes Raman scattering microscopy: instrumentation, theory, and applications. ACS Publications.

Cheung, Y. K., Tham, L. G., Guo, D. J. (1988). Analysis of pile group by infinite layer method. *Géotechnique*, *38*(3), 415–431.

Chow, Y. K. (1986a). Analysis of vertically loaded pile groups. *International Journal of Numerical and Analytical Methods in Geomechanics*, *10*(1), 59–72.

Chow, Y. K. (1986b). Discrete element analysis of settlement of pile groups. *Computers and Structures*, *24*(1), 157–166.

Christian, J. T., Desai, C. S. (1977). *Numerical methods in geotechnical engineering*. New York, McGraw-Hill.

Clayton, C. R. I., Heymann, G. (2001). Stiffness of geomaterials at very small strains. *Géotechnique*, *51*(3), 245–255.

Clough, G. W., Duncan, J. M. (1971). Finite element analyses of retaining wall behavior. *Journal of Soil Mechanics & Foundations Div*.

Combarieu, O. (1985). *Frottement négatif sur les pieux.* Rapport de recherche LPC No.136, Laboratoire Centrale des ponts et Chaussées, Paris.

Combarieu, O. (2006). L'usage des modules de déformation en géotechnique. *Revue Française de Géotechnique*, (114), 3–32.

Comodromos, E. M., Bareka, S. V. (2005). Evaluation of negative skin friction effects in pile foundations using 3D nonlinear analysis. *Computers and Geotechnics*, *32*(3), 210–221.

Comodromos, E. M., Papadopoulou, M. C., Rentzeperis, I. K. (2009). Pile foundation analysis and design using experimental data and 3-D numerical analysis. *Computers and Geotechnics*, *36*(5), 819–836.

Coyle, H. M., Reese, L. C. (1966). Load transfer for axially loaded piles in clay. *Journal of the Soil Mechanics and Foundations Division*, *92*(2), 1–26.

Coyle, H. M., Sulaiman, I. H. (1967). Skin friction for steel piles in sand. *Journal of Soil Mechanics and Foundations Division, ASCE*, *92*, *SM5*,(Proc Paper 490).

D'Appolonia, E., Romualdi, J. P. (1963). Load Transfer in End Bearing Steel H-Piles. *Journal of the Soil Mechanics*

and Foundations Division, ASCE, *89*,*SM2*, 1–25.

Das, B. M. (2007). *Principles of Foundation Engineering* (6th Editio). Thomson.

David, L. (1967). Formations glaciaires et fluvio-glaciaires de la région lyonnaise. In *Document du Laboratoire de géologie Faculté des sciences, Lyon n22* (p. 159).

David, L. (1973). *Eléments de géologie régionale lyonnaise*. Centre régional de recherche et de documentation pédagogique.

Davis, C., Knowles, M., Rajic, N., Swanton, G. (2016). Evaluation of a Distributed Fibre Optic Strain Sensing System for Full-Scale Fatigue Testing. *Procedia Structural Integrity*, *2*, 3784–3791.

De Gennaro, V. (1999). *Etude du comportement mecanique des interfaces sol-structure. Application a l'analyse du comportement des pieux. Thèse de Docteur de l'Ecole Nationale des Ponts et Chaussées, Spécialité: Géotechnique*.

De Mello, V. F. B. (1969). Foundations of buildings on clay. In *State of the Art Report, Proceedings of the 7th International Congress on Soil Mechanics and Foundation Engineering, Mexico City, Mexico* (Vol. 1, pp. 49–136).

Desai, C. S., Johnson, L. D., Hargett, C. M. (1974). Analysis of pile-supported gravity lock. *Journal of the Geotechnical Engineering Division*, *100*(9), 1009–1029.

Dibiagio, E., Myrvoll, F. (1981). Field instrumentation for soft clay. In *Soft Clay Engineering, R.P. Brenner and E.W. Brands* (pp. 699–736). Elsevier Publishing, Amsterdam.

Ding, X., Qin, H. (2000). Geotechnical instruments in structural monitoring. *Journal of Geospatial Engineering*, *2*(1), 45–56.

DuBose, L. A. (1956). *A comprehensive study of factors influencing the load carrying capacities of drilled and cast-In-place concrete piles*. Texas Transportation Institute.

Dumollard, M. (1963). *Contribution à l'étude des sols de la région lyonnaise. Thèse Faculté des Sciences, Lyon*. Université, Faculté des Sciences.

Duncan, J. M., Chang, C.-Y. (1970). Nonlinear analysis of stress and strain in soils. *Journal of Soil Mechanics and Foundations Division*.

Dunnicliff, J. (1988). *Geotechnical instrumentation for monitoring field performance*. John Wiley & Sons, 1988.

Dunnicliff, J., Powderham, A. (2001). Recommendations for procurement of geotechnical instruments and field instrumentation services. *Geotechnical Instrumentation News*, 30–35.

Eberhardt, E., Stead, D. (2011). Geotechnical instrumentation. *SME Mining Engineering Handbook*, *1*(8.5), 551–572.

Eickhoff, W., Ulrich, R. (1981). Optical frequency domain reflectometry in single-mode fiber. *Applied Physics Letters*, *39*(9), 693–695.

Ellison, R. D., Dappolinia, E., Thiers, G. R. (1971). Load-deformation mechanism for bored piles. *Journal of Soil Mechanics and Foundations Division*.

Esterhuizen, J. J. B., Filz, G. M., Duncan, J. M. (2001). Constitutive behavior of geosynthetic interfaces. *Journal of Geotechnical and Geoenvironmental Engineering*, *127*(10), 834–840.

Eurocode 2. (2005). Design of concrete structures - Part 1-1: General rules and rules of buildings. NF EN 1992-1-1, Brussels, Belgium.

Eurocode 7. (2005). Partie 1 (NF EN 1997-1). Calcul Géotechnique – Partie 1 : Règles Générales, EN 1997-1 Comité Européen de Normalisation (CEN), Bruxelles.

Fahey, M., Carter, J. P. (1993). A finite element study of the pressuremeter test in sand using a nonlinear elastic plastic

model. *Canadian Geotechnical Journal*, *30*(2), 348–362.

Faisal, H. A., Lee, S. K. (2008). Recent development in pile instrumentation technique for prestressed spun concrete piles. *Geotechnical Engineering*, *39*(2), 87–95.

Fajkus, M., Nedoma, J., Mec, P., Hrubesova, E., Martinek, R., Vasinek, V. (2017). Analysis of the highway tunnels monitoring using an optical fiber implemented into primary lining. *Journal of Electrical Engineering*, *68*(5), 364–370.

Fakharian, K., Ahmari, S., Amiri, A., others. (2008). 3-D Numerical Investigation of Piles under Monotonic and Cyclic Lateral Loads in Clay. In *The Eighteenth International Offshore and Polar Engineering Conference*.

Fellenius, B H. (1969). Negative skin friction on piles in clay. A literature survey. In *Proceedings of the 7th International Conference on Soil Mechanics and Foundation Engineering, Mexico City, Mexico* (pp. 93–98).

Fellenius, Bengt H. (2002). Determining the true distributions of load in instrumented piles. *Geotechnical Special Publication*, *2*(116 II), 1455–1470.

Fellenius, Bengt H, Asce, M., Kim, S., Ph, D., Chung, S., Ph, D., Asce, M. (2009). Long-Term Monitoring of Strain in Instrumented Piles, *135*(November), 1583–1595.

Fleming, K. (1996). Talking Point: Ken Fleming assesses the present major issues in the pile testing industry. *Ground Engineering*, 3.

Fleming, K., Weltman, A., Randolph, M., Elson, K. (2008). *Piling engineering*. CRC press.

Focht, J. A. (1967). Discussion to paper by Coyle and Reese. *Journal of Soil Mechanics and Foundation Engineering, ASCE*, *93*(SM1), 133–138.

Foucault, A. (2010). *Modélisation du comportement cyclique des ouvrages en terre intégrant des techniques de régularisation*. Châtenay-Malabry, Ecole centrale de Paris.

Frank, R. (1999). *Calcul des fondations superficielles et profondes*. Presses de l'Ecole Nationale des Ponts et Chaussées, Paris.

Frank, R., Cuira, F., Burlon, S. (2019). Fondations profondes. *Techniques de l'ingénieur Stabilité Des Sols, Fondations, base docum*(ref. article : c248). Retrieved from https://www.techniques-ingenieur.fr/base-documentaire/construction-et-travaux-publics-th3/stabilite-des-sols-fondations-42219210/fondations-profondes-c248/

Frank, R., Zhao, S. R. (1982). Estimation par les paramètres pressiométriques de l'enfoncement sous charge axiale de pieux forés dans des sols fins. *Bulletin de Liaison Des Laboratoires Des Ponts et Chaussées 119*, 17–24. Retrieved from http://trid.trb.org/view.aspx?id=1044395

Fry, J. J., Mamba, M., Flavigny, E. (1989). Classification et propriétées des enrochements: Le cas d'un grès. In *Congrès international de mécanique des sols et des travaux de fondations. 12* (pp. 713–714).

Geoffroy, H., Di Benedetto, H., Duttine, A., Sauzéat, C. (2003). Dynamic and cyclic loadings on sands: results and modelling for general stress-strain conditions. In *Deformation characteristics of geomaterials, IS Lyon 2003* (pp. 353–363).

Geotechnical Engineering Office. (2006). *Foundation design and construction*. *GEO Publication No. 1/2006, The Geotechnical Engineering Office of HKSARG, Hong Kong*.

Ghee, E. H., Guo, W. D. (2011). FLAC3D analysis on soil moving through piles.

Giallorenzi, T. G., Bucaro, J. A., Dandridge, A., Sigel, G. H., Cole, J. H., Rashleigh, S. C., Priest, R. G. (1982). Optical fiber sensor technology. *IEEE Transactions on Microwave Theory and Techniques*, *30*(4), 472–511.

Gowthaman, S., Nasvi, M. C. M. (2017). 2D and 3D Numerical Simulation of Load-Settlement Behaviour of Axially Loaded Pile Foundations. *American Journal of Civil Engineering and Architecture*, *5*(5), 187–195.

Guan, Y. Y., Li, C., Cai, Z. C., Guo, L., Chen, W., Zhao, Z., … Wu, S. (2014). Monitoring research of fiber Bragg grating strain sensors embedded in tunnel secondary lining. *Opt. Tech*, *40*, 547–550.

Gudefin, H., Rousselot, D. (1974). Synthèse des études géologiques et hydrogéologiques du BRGM en vue de la création d'un réseau métropolitain dans l'agglomération lyonnaise. *BRGM, Orleans, France*.

Guo, D. J., Tham, L. G., Cheung, Y. K. (1987). Infinite layer for the analysis of a single pile. *Computers and Geotechnics*, *3*(4), 229–249.

Guo, W D. (1997). *Analytical and numerical analyses for pile foundations*. *Thesis presented to the University of Western Australia for the degree of Doctor of Philosophy*.

Guo, Wei Dong, Randolph, M. F. (1997). Vertically loaded piles in non-homogeneous media. *International Journal for Numerical and Analytical Methods in Geomechanics*, *21*(8), 507–532.

Habel, W. R., Krebber, K. (2011). Fiber-optic sensor applications in civil and geotechnical engineering. *Photonic Sensors*, *1*(3), 268–280.

Hajduk, E. L., Paikowsky, S. G. (2000). Performance evaluation of an instrumented test pile cluster. In *Performance Confirmation of Constructed Geotechnical Facilities* (Vol. 300, pp. 124–127).

Hansen, J. B. (1970). A revised and extended formula for bearing capacity.

Hardin, B. O., Drnevich, V. P. (1972). Shear modulus and damping in soils: design equations and curves. *Journal of Soil Mechanics and Foundations Division*, *98*(sm7).

Hardin, B. O., Richart Jr, F. E. (1963). Elastic wave velocities in granular soils. *Journal of the Soil Mechanics and Foundations Division*, *89*(1), 33–65.

Hawkes, I., Bailey, W. V. (1973). *Design, develop, fabricate, test, and demonstrate permissible low cost cylindrical stress gages and associated components capable of measuring change of stress as a function of time in underground coal mines. Open file report*.

Hayes, J., Simmonds, T. (2002). Interpreting strain measurements from load tests in bored piles. In *Proceedings of the 9th International Conference on Piling and Deep Foundations, Nice, France* (pp. 663–669).

Hemaida, A. A. (2007). *Numerical Modelling of Vertically Loaded Piled Raft Foundation,PhD thesis*. Cairo University, Egypt.

Hill, R. (1950). The mathematical theory of plasticity, Clarendon. *Oxford*, *613*, 614.

Hirayama, H. (1990). Load-settlement analysis for bored piles using hyperbolic transfer functions. *Soils and Foundations*, *30*(1), 55–64.

Hoang, M. T., Cuira, F. ., Dias, D., Miraillet, P. (2018). Estimation du rapport E/EM : application aux Radiers de grandes dimensions. In *Journées Nationales de Géotechnique et de Géologie de l'Ingénieur - Champs-sur-Marne* (pp. 1–8).

Hong, S. H., Lee, F. H., Yong, K. Y. (2003). Three-dimensional pile-soil interaction in soldier-piled excavations. *Computers and Geotechnics*, *30*(1), 81–107.

Horikoshi, K., Matsumoto, T., Hashizume, Y., Watanabe, T. (2003). Performance of piled raft foundations subjected to dynamic loading. *International Journal of Physical Modelling in Geotechnics*, *3*(2), 51–62.

Hsiung, B. B. C. (2009). A case study on the behaviour of a deep excavation in sand. *Computers and Geotechnics*, *36*(4), 665–675.

Hsiung, B. C. B., Dao, S. D. (2014). Evaluation of constitutive soil models for predicting movements caused by a deep excavation in sands. *Electronic Journal of Geotechnical Engineering*, *19*(Z5), 17325–17344.

International Organization for Standardization. (2005). *ISO/DIS 22477-1, Geotechnical and testing - testing of geotechnical structures - part 1 : pile load test by static axially loaded compression. International Organization*

for Standardization, Geneva.

Itasca, F. (2019). Fast Lagrangian Analysis of Continua in 3 Dimensions, Version 7.0. *Minneapolis, Minnesota, Itasca Consulting Group*.

Jaky, J. (1944). The coefficient of earth pressure at rest. *Journal of the Society of Hungarian Architects and Engineers*, *8*(22), 355–358.

Janbu, N. (1976). Static bearing capacity of friction piles. In *Sechste Europaeische Konferenz Fuer Bodenmechanik Und Grundbau* (Vol. 1).

Jardine, R. J. (1992). Some observations on the kinematic nature of soil stiffness. *Soils and Foundations*, *32*(2), 111–124.

Jardine, R. J., Potts, D. M., Fourie, A. B., Burland, J. B. (1986). Studies of the influence of non-linear stress--strain characteristics in soil--structure interaction. *Geotechnique*, *36*(3), 377–396.

Jenck, O. (2005). *Le renforcement des sols compressibles par inclusions rigides verticales. Modélisation physique et numérique.*

Jeremic, B., Yang, Z., Cheng, Z., Jie, G., Sett, K., Taiebat, M., … Tasiopoulou, P. (2009). *Lecture notes on computational geomechanics: Inelastic finite elements for pressure sensitive materials*. *Department of Civil and Environmental Engineering, University of California, Davis*.

Jimenez, G. A. L. (2019). *Static and Dynamic behaviour of pile supported structures in soft soil*.

Johannessen, I. J., Bjerrum, L. (1965). Measurement of the compression of a steel pile to rock due to settlement of the surrounding clay. In *Soil Mechanics and Foundation Engineering, Canada* (pp. 261–264).

Ju, J. (2015). Prediction of the settlement for the vertically loaded pile group using 3D finite element analyses. *Marine Georesources and Geotechnology*, *33*(3), 264–271.

Kania, J. G., Sorensen, K. K., Fellenius, B. H. (2020). Application of distributed fibre optic cables in piles. *Geotechnical Engineering*, *51*(1), 94–102.

Karthigeyan, S., Ramakrishna, V. V., Rajagopal, K. (2006). Influence of vertical load on the lateral response of piles in sand. *Computers and Geotechnics*, *33*(2), 121–131.

Kastner, R. (1974). *Mise hors d'eau des fouilles à l'abri d'écrans étanches - Comparaison des débits théoriques et expérimentaux. Thèse présentée devant l'université Claude-Bernard Lyon pour obtenir le titre de Docteur-Ingénieur*.

Kastner, R. (1982). *Excavations profondes en site urbain: problèmes liés à la mise hors d'eau. dimensionnement des soutènements butonnés.* Thèse de Docteur ès Sciences, 409 pp, INSA Lyon, Université Claude Bernard Lyon I.

Kastner, R., Lareal, P. (1975). *Experimental excavation of length 50 m supported by strutted cast diaphragm walls: an analysis of stress distribution in the struts*. *Diaphragm walls and Anchorages*. Thomas Telford Publishing.

Kechavarzi, C., Pelecanos, L., de Battista, N., Soga, K. (2019). Distributed fibre optic sensing for monitoring reinforced concrete piles. *Geotechnical Engineering*, *50*(2), 43–51.

Kerisel, J., Ferrand, J., Lareal, P., Clement, P. (1972). Mesures de poussée et butée faites avec 42 paires de butons asservis. In *Proceedings of the European Conference on Soil Mechanics, Madrid* (pp. 265–273).

Kerisel, J., Lareal, P. (1971). Essai d'arrachement d'un élément de paroi moulée dans les alluvions sablo-graveleuses. In *Journées nationales du CFMS, Paris 1971. Bull. Livraison du Laboratoire des Pont et Chaussées, numéro spécial, Juin 1972* (pp. 219–228).

Khoiri, M., Ou, C.-Y. (2013). Evaluation of deformation parameter for deep excavation in sand through case histories. *Computers and Geotechnics*, *47*, 57–67.

Kondner, R. L. (1963). Hyperbolic stress-strain response: cohesive soils. *Journal of the Soil Mechanics and*

Foundations Division, *89*(1), 115–144.

Kraft, L. M., Ray, R. P., Kagawa, T. (1981). Theoretical tz curves. *Journal of Geotechnical and Geoenvironmental Engineering*, *107*(11), 1543–1561.

Kulhawy, F. H., O'Rourke, J. P., Stewart, J. P., Beech, J. . (1983). *Transmission line structure foundations for uplift-compression loading: Load test summaries*. *Rep. No. EL-3160, Electric Power Research Institute, Palo Alto, CA, June*.

Kurashima, T., Horiguchi, T., Tateda, M. (1990). Distributed-temperature sensing using stimulated Brillouin scattering in optical silica fibers. *Optics Letters*, *15*(18), 1038–1040.

Kwon, S. Y., Kim, M. M., Kim, S. H., Choi, J. I. (2013). 3D dynamic numerical modeling for soil-pile-structure interaction in centrifuge tests. In *Proceedings of the 18th International Conference on Soil Mechanics and Geotechnical Engineering, Paris*.

Lade, P. V. (2005). Overview of constitutive models for soils. In *Soil constitutive models: Evaluation, selection, and calibration* (pp. 1–34).

Lambe, T. W., Horn, H. M. (1964). *The influence on an adjacent building of pile driving for the MIT Materials Center*. Department of Civil Engineering, Massachusetts Institute of Technology.

Lareal, P. (1975). *Sols de la région lyonnaise: prévision de leur comportement mécanique à l'aide d'essais in situ et en vraie grandeur*. Université Claude-Bernard-LYON.

Lareal, P., Bourdeau, Y., Lambert, P., Cottereau, C. (1973). Essais de cisaillement "in-situ" sur des sols alluvionnaires de la Vallée du Rhône. *Travaux*, *55*, 52–59.

Lee, C. Y. (1991). Discrete layer analysis of axially loaded piles and pile groups. *Computers and Geotechnics*, *11*(4), 295–313.

Lee, C. Y. (1993). Settlement of pile groups—practical approach. *Journal of Geotechnical Engineering*, *119*(9), 1449–1461.

Leung, C. K. Y., Wan, K. T., Inaudi, D., Bao, X., Habel, W., Zhou, Z., … Imai, M. (2015). Review: optical fiber sensors for civil engineering applications. *Materials and Structures/Materiaux et Constructions*, *48*(4), 871–906.

Li, S., Ma, J., Hu, J. (2015). Rockfall hazard alarm strategy based on FBG smart passive net structure. *Photonic Sensors*, *5*(1), 19–23.

Liew, S. S., Kowng, Y. W., Gan, S. J. (2004). Interpretations of instrumented bored piles in Kenny Hill Formation. In *Proceedings of the Malaysian Geotechnical Conference, Petaling Jaya, Malaysia,16-18 March, 2004* (pp. 16–18).

Liu, J., Xiao, H. B., Tang, J., Li, Q. S. (2004). Analysis of load-transfer of single pile in layered soil. *Computers and Geotechnics*, *31*(2), 127–135.

Liu, Q., Meyerhof, G. G. (1987). New method for non-linear analysis of rigid piles in clay. *Computers and Geotechnics*, *3*(4), 185–212.

Luna Innovations Incorporated. (2013). Distributed fiber optic sensing: temperature compensation of strain measurement (Engineering note EN-FY1402), 1–7.

Ma, J., Aziz, H. Y., Su, C., Shi, C. (2014). Settlement prediction and behaviour of pile foundations in deep clayey soil deposits. *Journal of Central South University*, *21*(4), 1554–1564.

Madabhushi, S. P. G., Haigh, S. K. (1998). Finite element analysis of pile foundations subject to pull-out. In *Application of Numerical Methods to Geotechnical Problems* (pp. 131–140). Springer.

Magnan, J.-P. (1997). *Description, identification et classification des sols*. Ed. Techniques Ingénieur.

Maheshwari, B. K., Watanabe, H. (2006). Nonlinear dynamic behavior of pile foundations: Effects of separation at the soil-pile interface. *Soils and Foundations*, *46*(4), 437–448.

Mandolini, A., Viggiani, C. (1997). Settlement of piled foundations. *Géotechnique*, *47*(4), 791–816.

Mattes, N. S., Poulos, H. G. (1969). Settlement of single compressible pile. *Journal of the Soil Mechanics and Foundation Division, ASCE, No. SM1*, 189–207.

Mattsson, N., Menoret, A., Simon, C., Ray, M. (2013). Case study of a full-scale load test of a piled raft with an interposed layer for a nuclear storage facility. *Géotechnique*, *63*(11), 965–976.

McCabe, B. A., Lehane, B. M. (2006). The behaviour of axially loaded pile groups driven in clayey silt. *Journal of Geotechnical and Environmental Engineering, ASCE*, *132*(3), 401–410.

McRae, J. B., Simmonds, T. (1991). Long-term stability of vibrating wire instruments: one manufacteur's perspective. In *International Symposium on field measurements in geomechanics* (pp. 283–293).

Meyerhof, G. G. (1959). Compaction of sands and bearing capacity of piles. *Journal of Soil Mechanics and Foundation Engineering, ASCE*, *85*(SM6), 1–27.

Meyerhof, G. G. (1963). Some recent research on the bearing capacity of foundations. *Canadian Geotechnical Journal*, *1*(1), 16–26.

Meyerhof, G. G. (1976). Bearing capacity and settlements of piled foundations. *Journal of the Geotechnical Engineering Division, ASCE*, *102*, 197–228.

Mindlin, R. D. (1936). Force at a point in the interior of a semi-infinite solid. *Physics*, *7*, 197–202.

Mishra, D., Tutumluer, E., Stark, T. D., Hyslip, J. P., Chrismer, S. M., Tomas, M. (2012). Investigation of differential movement at railroad bridge approaches through geotechnical instrumentation. *Journal of Zhejiang University: Science A*, *13*(11), 814–824.

Moayedi, H., Kalantar, B., Abdullahi, M. M., Rashid, A. S. A., Nazir, R., Nguyen, H. (2019). Determination of young elasticity modulus in bored piles through the global strain extensometer sensors and real-time monitoring data. *Applied Sciences (Switzerland)*, *9*(15).

Moffat, R. A., Beltran, J. F., Herrera, R. (2015). Applications of BOTDR fiber optics to the monitoring of underground structures. *Geomech. Eng*, *9*(3), 397–414.

Mohan, D., Jain, G. S., Kumar, V. (1963). Load-bearing capacity of piles. *Géotechnique*, *13*(1), 76–86.

Monnet, J., Gielly, J. (1979). Détermination d'une loi de comportement pour le cisaillement des sols pulvérulents-Application au calcul d'essais triaxiaux. *Revue Française de Géotechnique*, (7), 45–56.

Motil, A., Bergman, A., Tur, M. (2016). State of the art of Brillouin fiber-optic distributed sensing. *Optics & Laser Technology*, *78*, 81–103.

Muir Wood, A. (1990). The observational method revisited. In *Proceedings of the 10th Southeast Asian Geotechnical Conference, Taipei, ROC,16-20 April 1990* (pp. 37–42).

Nagase, H., Ishihara, K. (1988). Liquefaction-induced compaction and settlement of sand during earthquakes. *Soils and Foundations*, *28*(1), 65–76.

Nejjar, K. (2019, July). *Behavior of retaining walls in an exceptional environment (great deep , deformable formations , sensitive environment). : Application to the station Fort d'Issy-Vanves-Clamart of Grand Paris Express project and comparison with measurements*. Université Grenoble Alpes. Retrieved from https://tel.archives-ouvertes.fr/tel-02414535

Neves, M. Das, Mestat, P., Frank, R., Degny, E. (2001a). Étude du comportement de pieux forés. II. Modélisation par éléments finis. *Bulletin Des Laboratoires Des Ponts et Chaussées*, (231).

Neves, M. Das, Mestat, P., Frank, R., Degny, E. (2001b). Étude du comportement de pieux forés I. Expérimentations

in situ et en laboratoire. *Bulletin Des Laboratoires Des Ponts et Chaussées*, (231), 39–54.

NF EN 1990. (2003). *Eurocodes structuraux, Bases de calcul des structures, mars 2003, AFNOR*.

NF EN ISO 17892-4. (2018). *Reconnaissance et essais géotechniques - Essais de laboratoire sur les sols - Partie 4 : Détermination de la distribution granulométrique des particules, AFNOR, 2018*.

NF P 94-150-1. (1999). Essai statique de pieu isolé sous un effort axial. Norme Française. AFNOR.

NF P 94-156, N. (1995). 94 156. *Mesures à l'inclinomètre--Annexe B: Scellement Des Tubes Inclinométriques Au Coulis*.

NF P 94-262. (2012). *Justification des ouvrages géotechniques, Normes d'application nationale de l'Eurocode 7, Fondations profondes - juin 2012, AFNOR, France*.

NF P94-071-1. (1994). Reconnaissance et essais-Essai de cissaillement rectiligne à la boîte-Partie 1: Cisaillement Direct. AFNOR.

Nicholson, D., Tse, C.-M., Penny, C., O Hana, S., Dimmock, R. (1999). *The observational method in ground engineering: principles and applications* (Vol. 185). Construction Industry Research and Information Association London.

O'Neill, M. W. (1983). Group action in offshore piles. In *Geotechnical Practicein Offshore Engineering: Proceedings of the Geotechnical Practice in Offshore Pilling Conference, Austin, Tex. Edited by S.G. Wright ASCE, NY* (pp. 25–64).

Oakley, L. H., Dinehart, S. A., Svoboda, S. A., Wustholz, K. L. (2011). Identification of organic materials in historic oil paintings using correlated extractionless surface-enhanced Raman scattering and fluorescence microscopy. *Analytical Chemistry*, *83*(11), 3986–3989.

Osgerby, C., Taylor, P. T. (1968). Vibrating-wire load cell for long-term tests. *Experimental Mechanics*.

Ottaviani, M. (1975). Three-dimensional finite element analysis of vertically loaded pile groups. *Géotechnique*, *25*(2), 159–174.

Paikowsky, S. G., Hajduk, E. L. (2004). Design and construction of three instrumented test piles to examine time dependent pile capacity gain. *Geotechnical Testing Journal*, *27*(6), 515–531.

Patel, D., Nicholson, D., Huybrechts, N., Maertens, J. (2007). The observational method in geotechnics. In *Proceedings of the 14th European Conference on Soil Mechanics and Geotechnical Engineering, Madrid, Spain, 01-03 October 2007* (Vol. II, pp. 371–380).

Peck, R. B. (1969). Advantages and limitations of the observational method in applied soil mechanics. *Geotechnique*, *19*(2), 171–187.

Pelecanos, L., Soga, K., Elshafie, M. Z. E. B., de Battista, N., Kechavarzi, C., Ye Gue, C., … Seo, H. J. (2018). Distributed fiber optic sensing of axially loaded bored piles. *Journal of Geotechnical and Geoenvironmental Engineering*, *144*(3).

Pokhrel, A., Kuwano, R., Suwal, L. P. (2015). Development of large size Disk Transducer to evaluate elastic properties of coarse granular materials. In *Deformation Characteristics of Geomaterials* (pp. 366–373). IOS Press.

Poorooshasb, H. B., Alamgir, M., Miura, N. (1996). Negative skin friction on rigid and deformable piles. *Computers and Geotechnics*, *18*(2), 109–126.

Potts, P. J. (2012). Glossary of analytical and metrological terms from the international vocabulary of metrology. *Geostandards and Geoanalytical Research*, *36*(3), 231–246.

Poulos, H. G. (1968). Analysis of the settlement of pile groups. *Geotechnique*, *18*(4), 449–471.

Poulos, H. G. (1979). Settlement of single piles in non-homogeneous soil," Volume 105, No. GTS, May, 1979, pp. 627-641. *Journal of the Geotechnical Engineering Division, ASCE*, *105*(5), 627–641.

Poulos, H. G. (1989). Pile behaviour-theory and application. *Géotechnique*, *39*(3), 365–415.

Poulos, H. G., Davis, E. H. (1968). The settlement behaviour of single axially loaded incompressible piles and piers. *Geotechnique*, *18*(3), 351–371.

Poulos, H. G., Davis, E. H. (1980). Pile foundation analysis and design. John Wiley and sons, Inc. New York.

Poulos, H. G., Mattes, N. S. (1969). Behavior of axially loaded end bearing piles. *Géotechnique*, *19*(7), 285–300.

Poulos, H. G., Mattes, N. S. (1971). Settlement and load distribution of pile groups. Australian Geotechnical Journal. G1.

Powderham, A. J. (1994). An overview of the observational method: development in cut and cover and bored tunnelling projects. *Géotechnique*, *44*(4), 619–636.

Powderham, A. J. (2002). The observational method—learning from projects. *Proceedings of the Institution of Civil Engineers-Geotechnical Engineering*, *155*(1), 59–69.

Powderham, A. J., Nicholson, D. P. (1996). *The way forward. The observational method in geotechnical engineering*. Thomas Telford, London.

Pra-Ai, S. (2013). Behaviour of interfaces subjected to a large number of cycles. Application to piles, 353.

Puzrin, A. M., Burland, J. B. (1996). A logarithmic stress--strain function for rocks and soils. *Geotechnique*, *46*(1), 157–164.

Qiu, H. T., Li, C., Cui, H. L., Zhang, D., Ding, Y. (2008). Stain monitoring for tunnel using distributed optical fiber BOTDR sensors. In *Boundaries of Rock Mechanics* (pp. 47–50). CRC press.

Rajapakse, R. A. (2016). *Pile design and construction rules of thumb*. Butterworth-Heinemann.

Rajapakse, R. K. N. D. (1990). Response of an axially loaded elastic pile in a Gibson soil. *Géotechnique*, *40*(2), 237–249.

Randolph, M. . (2003). Load transfer analysis of axially loaded piles, RATZ manual version 4.2. University of Western Australia.

Randolph, M. ., Wroth, C. . (1978). Analysis and deformation of vertically loaded piles. *Journal of Geotechnical Engineering*, *104*(12), 1465–1487.

Randolph, M. ., Wroth, C. P. (1979a). An analysis of the vertical deformation of pile groups. *Geotechnique*, *29*(4), 423–439.

Randolph, M. F. (1986). RATZ-load transfer analysis of axially loaded piles. *Report No. Geo*, *86033*.

Randolph, M. F. (1994). Design methods for pile groups and piled rafts. In *International conference on soil mechanics and foundation engineering* (pp. 61–82).

Randolph, M. F., Wroth, C. P. (1979b). A simple approach to pile design and the evaluation of pile tests. In *Behavior of Deep Foundations*. ASTM International.

Rayhani, M. H., El Naggar, M. H. (2008). Numerical modeling of seismic response of rigid foundation on soft soil. *International Journal of Geomechanics*, *8*(6), 336–346.

Reese, L.C. (1979). Design and construction of drilled shafts. *Journal of Geotechnical and Geoenvironmental Engineering*, *104*(ASCE 14599 Proceeding), 95–116.

Reese, L C, Hudson, W. R., Vijayvergiya, V. N. (1969). An investigation of the interaction between bored piles and soil. In *Proceedings of the Seventh International Conference on Soil Mechanics and Foundation Engineering, Mexico*.

Reese, L C, Isenhower, W. M., Wang, S.-T. (2005). *Analysis and design of shallow and deep foundations* (Vol. 10). John Wiley & Sons.

Reese, Lymon C. (1969). Instrumentation for measurement of axial load in drilled shafts, (November).

Rollins, K. M., Evans, M. D., Diehl, N. B., III, W. D. D. (1998). Shear modulus and damping relationships for gravels. *Journal of Geotechnical and Geoenvironmental Engineering*, *124*(5), 396–405.

Rousset, B. (2013). La Molasse grise de Lausanne. De la roche sédimentaire détritique au matériau de construction séculaire.

Said, I. (2006). *Comportement des interfaces et modélisation des pieux sous charge axiale*.

Santos, J. A., Correia, A. G. (2001). Reference threshold strain of soil. Its application to obtain an unique strain-dependent shear modulus curve for soil. In *International Conference on soil mechanics and geotechnical engineering* (pp. 267–270).

Sauzéat, C., Di Benedetto, H., Chau, B., Pham Van Bang, D. (2003). A rheological model for the viscous behaviour of sand. In *Deformation characteristics of geomaterials, IS Lyon 2003* (pp. 1201–1209).

Schanz, T., Vermeer, P. A. (1998). On the stiffness of sands. In *Pre-failure deformation behaviour of geomaterials* (pp. 383–387). Thomas Telford Publishing.

Schanz, T., Vermeer, P. A., Bonnier, P. G. (1999). The hardening soil model: formulation and verification. *Beyond 2000 in Computational Geotechnics*, 281–296.

Schlosser, F., Guilloux, A. (1981). Le frottement dans le renforcement des sols. *Revue Française de Géotechnique*, (16), 65–77.

Schweiger, H. F. (2009). Influence of constitutive model and EC7 design approach in FE analysis of deep excavations. *Proceeding of ISSMGE International Seminar on Deep Excavations and Retaining Structures, Budapest*, 99–114.

Seed, H. B., Reese, L. C. (1955). The action of soft clay along friction piles. *American Society of Civil Engineers Transactions*.

Seed, H. B., Reese, L. C. (1957). The action of clay along friction piles. *Journal of Geotechnical Engineering*, *504*, 92.

Seif El Dine, B. (2007). *Etude du comportement mécanique de sols grossiers à matrice*.

Seiler, J. F., Keeney, W. D. (1944). The efficiency of piles in groups. *Wood Preserving News*, *22*(11), 109–118.

Seo, H., Prezzi, M. (2007). Analytical solutions for a vertically loaded pile in multilayered soil. *Geomechanics and Geoengineering*, *2*(1), 51–60.

Shi, B., Xu, X. J., Wang, D., Wang, T., Zhang, D., Ding, Y., … Cui, H. (2005). Study on BOTDR-based distributed optical fiber strain measurement for tunnel health diagnosis. *Chinese Journal of Rock Mechanics and Engineering*, *24*(15), 2622–2628.

Shirley, D. J., Hampton, L. D. (1978). Shear-wave measurements in laboratory sediments. *The Journal of the Acoustical Society of America*, *63*(2), 607–613.

Sikali Mamdem, Y. (2012). *Capteurs à fibres optiques répartis par effet Brillouin: séparation de la dépendance à température et à la déformation*. Paris, ENST.

Skempton, A. W. (1959). Cast in-situ bored piles in London clay. *Geotechnique*, *9*(4), 153–173.

Song, S., Wu, Z., Yang, C., Wan, C., Shen, S. (2011). Deformation monitoring of shield tunnel based on distributed optical fiber strain sensing technology. *Structural Health Monitoring 2011*, *2*, 2058–2066.

Souley, M., Su, K., Ghoreychi, M., Armand, G. (2003). Constitutive models for rock mass: numerical implementation, verification and validation. In *FLAC and numerical modelling in geomechanics-2003* (pp. 71–80).

Teachavorasinskun, S. (1989). Stress-strain and strength characteristics of granular materials in simple shear. *MEng*

Thesis, University of Tokyo.

Terzaghi, K. (1943). *Theoretical Soil Mechanics*. New York: Wiley.

Tomlinson, M. J. (1986). *Foundation design and construction.* (L. Pitman, Ed.). Pitman, London.

Tomlinson, M., Woodward, J. (2014). *Pile design and construction practice*. *Pile Design and Construction Practice*.

Tuan, P. A. (2016). A simplified formular For analysis group efficiency of piles in granular soil, *7*(7).

Udd, E., Spillman Jr, W. B. (2011). *Fiber optic sensors: an introduction for engineers and scientists*. John Wiley & Sons.

Vesić, A. (1967). A study of the bearing capacity of deep foundations.

Vesić, A. (1969). Experiments with instrumented pile groups in sand. In *ASTM Special Technical Publication No. 444, Performance of Deep Foundations* (pp. 177–222). ASTM International.

Vesić, A. (1973). Analysis of ultimate loads of shallow foundations. *Journal of Soil Mechanics & Foundations Div*, *99*(sm1).

Vesić, A. (1977). Design of pile foundations. *NCHRP Synthesis of Highway Practice*, (42).

Viggiani, C., Mandolini, A., Russo, G. (2012). Piles and pile groups. *Applied Soil Mechanics*, 286–331.

Waldmann, R., Ferrand, J. (1970). Essais de parois moulées à Lyon. *Revue Travaux*, 73–80.

Waldmann, R., Gonin, H., Clement, P. (1971). *Section expérimentale du métro de Lyon - Principe et technologie des mesures. Travaux, Janv. 1971*.

Wang, Y., Liu, X., Zhang, M., Yang, S., Sang, S. (2020). Field Test of Excess Pore Water Pressure at Pile--Soil Interface Caused by PHC Pipe Pile Penetration Based on Silicon Piezoresistive Sensor. *Sensors*, *20*(10), 2829.

Whitaker, T., Cooke, R. W., Clarke, G. W. L. (1962). Loading test on a bored pile with a load cell for measuring base resistance. Engineering.

Wu, H. M., Shu, Y. M., Zhu, J. G. (2011). Implementation and verification of interface constitutive model in FLAC3D. *Water Science and Engineering*, *4*(3), 305–316.

Wu, J. J., Li, Y., Cheng, Q. G., Wen, H., Liang, X. (2016). A simplified method for the determination of vertically loaded pile-soil interface parameters in layered soil based on FLAC3D. *Frontiers of Structural and Civil Engineering*, *10*(1), 103–111.

Xie, Q., Da Gama, C. D., Yu, X., Chen, Y. (2013). A parametric study of interface characteristics in a buttress retaining wall. *Electronic Journal of Geotechnical Engineering*, *18 G*, 1477–1492.

Xue, F., Ma, J., Yan, L. (2011). Three-dimensional FEM analysis of bridge pile group settlement in soft soils. In *Advances in Pile Foundations, Geosynthetics, Geoinvestigations, and Foundation Failure Analysis and Repairs* (pp. 135–143).

Yang, Q., Leng, W. M., Zhang, S., Nie, R. S. (2013). Experimental study on compression modulus of sandy soil. *Geotechnical Special Publication*, (232 GSP), 287–296.

Yoshimi, Y., Kishida, T. (1981). A ring torsion apparatus for evaluating friction between soil and metal surfaces. *Geotechnical Testing Journal*, *4*(4), 145–152.

Zeng, X., Bao, X., Chhoa, C. Y., Bremner, T. W., Brown, A. W., DeMerchant, M. D., … Georgiades, A. V. (2002). Strain measurement in a concrete beam by use of the Brillouin-scattering-based distributed fiber sensor with single-mode fibers embedded in glass fiber reinforced polymer rods and bonded to steel reinforcing bars. *Applied Optics*, *41*(24), 5105–5114.

Zhang, Q. Q., Li, S. C., Liang, F. Y., Yang, M., Zhang, Q. (2014). Simplified method for settlement prediction of single pile and pile group using a hyperbolic model. *International Journal of Civil Engineering*, *12*(2 B), 179–

192.

Zhang, Q. Q., Liu, S. w, Zhang, S. m, Zhang, J., Wang, K. (2016). Simplified non-linear approaches for response of a single pile and pile groups considering progressive deformation of pile–soil system. *Soils and Foundations*, *56*(3), 473–484.

Zhang, Q. Q., Zhang, Z. M. (2012). Simplified calculation approach for settlement of single pile and pile groups. *Journal of Computing in Civil Engineering*, *26*(6), 750–758.

Zhou, A., Lu, T. (2009). Elasto-plastic constitutive model of soil-structure interface in consideration of strain softening and dilation. *Acta Mechanica Solida Sinica*, *22*(2), 171–179.

Appendix – Loads and load combinations

1- Loads

The loads transferred to the piles were estimated by the company "BET RBS". Two categories of loads were defined as follows:

- Static loads
  - G: permanent load
    1. Self-weight
    2. RC slab (15 cm)
    3. Permanent loads of roof
    4. Weight of the facade
  - Q: Variable load
    5. Offices ($\Psi_0 = 0.7$; $\Psi_1 = 0.5$; $\Psi_2 = 0.3$, Category B)
    6. Technical room ($\Psi_0 = 1.0$; $\Psi_1 = 0.5$; $\Psi_2 = 0.9$)
  - Other loads
    7. Wind North/South $C_{p,i}$ + ($\Psi_0 = 0.6$; $\Psi_1 = 0.2$; $\Psi_2 = 0$)
    8. Wind North/South $C_{p,i}$ – ($\Psi_0 = 0.6$; $\Psi_1 = 0.2$; $\Psi_2 = 0$)
    9. Wind South/North $C_{p,i}$ + ($\Psi_0 = 0.6$; $\Psi_1 = 0.2$; $\Psi_2 = 0$)
    10. Wind South/North $C_{p,i}$ – ($\Psi_0 = 0.6$; $\Psi_1 = 0.2$; $\Psi_2 = 0$)
    11. Wind East/West $C_{p,i}$ + ($\Psi_0 = 0.6$; $\Psi_1 = 0.2$; $\Psi_2 = 0$)
    12. Wind East/West $C_{p,i}$ – ($\Psi_0 = 0.6$; $\Psi_1 = 0.2$; $\Psi_2 = 0$)
    13. Wind West/East $C_{p,i}$ + ($\Psi_0 = 0.6$; $\Psi_1 = 0.2$; $\Psi_2 = 0$)
    14. Wind West/East $C_{p,i}$ – ($\Psi_0 = 0.6$; $\Psi_1 = 0.2$; $\Psi_2 = 0$)

Where the Cpi is the internal pressure coefficient

- Seismic loads
    15. EX: seismic load – X direction
    16. EY: seismic load – Y direction

2- Load combinations

Load combinations are calculated based on the Eurocode 0 (NF EN 1990, 2003) and NF P 94-262 (2012). They are presented in the following table.

Table 0.1 Definition of load combinations

Combination	$G_{kj,sup}$	$G_{kj,inf}$	$Q_{k,1}$	$Q_{k,i}$	A_{Ed}
ULS D&T	1.35	1	1.5 or 0	1.5 $\Psi_{0,i}$ or 0	-
ULS seismic	1	1	$\Psi_{2,1}$	$\Psi_{2,i}$	1
SLS Char.	1	1	1	$\Psi_{0,i}$	-
SLS QP	1	1	$\Psi_{2,1}$	$\Psi_{2,i}$	-

Six different cases were used to calculate the load transfer at the head of the pile. They either analyze the towers as coupled or consider Silex^2 alone. The maximum and the minimum stiffnesses were defined for both towers and were used in the configurations. For example, for the EDF tower they were estimated for two cracking hypotheses (0.2 and 1) and for the new Silex^2 tower, $k_{Silexmin}$ and $k_{Silexmax}$ were determined from 3D models using different soil parameters (Young moduli of the soil layers were calculated based on $E_M/2$ for k_{max} or E_M for k_{min}, where E_M is the pressuremeter moduli of the soil layers).

The cases are as follows:

- "Coupled towers" configurations with different combinations of stiffnesses
  - $K_{EDFmin}/K_{Silexmax}$
  - $K_{EDFmin}/K_{Silexmin}$
  - $K_{EDFmax}/K_{Silexmin}$
  - $K_{EDFmax}/K_{Silexmax}$
- "Silex^2 only" configurations
  - $K_{Silexmin}$
  - $K_{Silexmax}$

Several load combinations were evaluated for the previous configurations using a numerical tool. The envelopes for the six load transfer cases, presented earlier in Chapter 2, are given for different limit states in the following tables.

Table 0.2 Loads: Coupled towers – k_{max}/k_{min}

Pile Number	SLS QP	SLS Char.	ULS D&T	ULS seismic
15	5 900	7 477	10 506	6 955
16	6 001	7 356	10 336	6 326
17	6 707	8 159	11 448	6 889
18	5 572	6 943	9 732	5 904
19	5 592	7 163	10 050	6 552
20	5 540	6 928	9 756	6 595
21	5 887	7 128	10 028	6 210
22	6 436	7 757	10 890	6 670
23	5 447	6 703	9 393	5 772
24	5 156	6 499	9 118	6 102

Table 0.3 Loads: Coupled towers – k_{max}/k_{max}

Pile Number	SLS QP	SLS Char.	ULS D&T	ULS seismic
15	5 863	7 467	10 499	6 918
16	5 889	7 281	10 233	6 214
17	6 706	8 194	11 500	6 887
18	5 528	6 936	9 726	5 860
19	5 504	7 092	9 954	6 465
20	5 992	7 458	10 497	7 047
21	5 807	7 069	9 945	6 130
22	6 338	7 658	10 753	6 572
23	5 401	6 673	9 355	5 727
24	5 394	6 816	9 565	6 341

Table 0.4 Loads: Coupled towers – k_{min}/k_{max}

Pile Number	SLS QP	SLS Char.	ULS D&T	ULS seismic
15	5 834	7 544	10 615	6 889
16	5 871	7 330	10 307	6 196
17	6 695	8 233	11 558	6 877
18	5 516	6 989	9 807	5 848
19	5 484	7 172	10 075	6 445
20	6 014	7 557	10 643	7 069
21	5 820	7 130	10 036	6 144
22	6 349	7 704	10 821	6 583
23	5 420	6 740	9 454	5 746
24	5 420	6 913	9 709	6 366

Table 0.5 Loads: Coupled towers – k_{min}/k_{min}

Pile Number	SLS QP	SLS Char.	ULS D&T	ULS seismic
15	5 871	7 547	10 612	6 926
16	5 984	7 395	10 396	6 309
17	6 695	8 190	11 496	6 876
18	5 560	6 989	9 801	5 892
19	5 571	7 237	10 163	6 532
20	5 543	7 000	9 866	6 598
21	5 901	7 186	10 114	6 225
22	6 447	7 802	10 957	6 681
23	5 463	6 763	9 482	5 789
24	5 183	6 593	9 257	6 130

Table 0.6 Loads: Silex^2 only – k_{min} and k_{max}

Pile Number	Silex^2 only – k_{min}				Silex^2 only – k_{max}			
	SLS QP	SLS Char.	ULS D&T	ULS seismic	SLS QP	SLS Char.	ULS D&T	ULS seismic
15	3 866	7 586	10 829	0	3 901	7 522	10 730	0
16	4 037	6 233	8 782	0	3 990	6 288	8 870	0
17	4 638	6 330	8 842	0	4 660	6 394	8 934	0
18	3 844	6 007	8 463	0	3 828	6 075	8 568	0
19	3 679	7 151	10 199	0	3 685	7 028	10 013	0
20	3 641	7 216	10 314	0	3 757	7 354	10 506	0
21	3 730	5 971	8 436	0	3 653	5 921	8 372	0
22	4 182	5 939	8 320	0	4 096	5 805	8 131	0
23	3 607	5 835	8 240	0	3 536	5 770	8 152	0
24	3 329	6 636	9 479	0	3 519	6 819	9 726	0

FOLIO ADMINISTRATIF

THESE DE L'UNIVERSITE DE LYON OPEREE AU SEIN DE L'INSA LYON

NOM : MILANE DATE de SOUTENANCE : 27/05/2021

Prénoms : Rosy

TITRE : Deep foundations of a high-rise building: an *in situ* testing and numerical study.

NATURE : Doctorat Numéro d'ordre : 2021LYSEI028

Ecole doctorale : MEGA (Mécanique, énergétique, génie civil, acoustique)

Spécialité : Génie Civil

RESUME :

Le dimensionnement des grandes constructions fondées sur des pieux exigent une bonne compréhension du comportement du sol, des pieux ainsi que l'interface sol-pieu. Cette analyse se base sur une évaluation de la capacité portante et du tassement de ces fondations.
Dans le cadre du projet « Fondasilex », cette thèse propose l'étude des fondations de la tour Silex2 qui est construite à Lyon. Celle-ci est fondée sur 20 pieux de 1.22 m de diamètre. L'absence de caractérisation précise des alluvions du Rhône et de la couche de molasse rencontrées peut entraîner un surdimensionnement des fondations et par conséquent une augmentation des coûts de construction.
Cette thèse présente l'instrumentation et la modélisation numérique réalisées pour mieux comprendre le mécanisme de transfert des charges dans le cas de pieux, pour caractériser le sol lyonnais et l'interaction pieux-sol et prédire le comportement à long terme de la structure, des fondations et du sol.
En première partie, une instrumentation des fondations et du sol a été mise en place afin de suivre en temps réel leur comportement. Elle est constituée d'un extensomètre multipoint pour mesurer le tassement du sol, de capteurs de pression totale et de capteurs de déformation qui ont mesuré respectivement la contrainte sur la tête des pieux et la déformation qui en résulte sur toute la longueur du pieu.
En deuxième partie, un modèle numérique a été réalisé sur FLAC3D. Il a permis d'étudier le comportement de la structure, du sol et de l'interface sol-structure. Une loi élastique parfaitement plastique avec un critère de Mohr- Coulomb et le Plastic-Hardening Model ont été jugés bien adaptées aux alluvions et à la molasse respectivement. Ces lois ont été confrontés et validés à partir des résultats de l'instrumentation et des essais de laboratoire réalisés sur des échantillons de sol.

MOTS-CLÉS :
Pieux, interface sol-structure, alluvions du Rhône, molasse du miocène, instrumentation, extensomètre multipoint, fibre optique, jauges de déformation, extensomètre à corde vibrante, capteur de pression totale, différences finies, FLAC3D, Mohr-Coulomb, Plastic-Hardening Model.

Laboratoire (s) de recherche : GEOMAS

Directeur de thèse: DAOUADJI Ali

Président de jury :

Composition du jury :
Ali Daouadji, Laurent Briançon, Roger Frank, Richard Jardine, Diana Salciarini, Lionel Manin